Technische Universität München
Fakultät für Chemie
- Lehrstuhl II für Physikalische Chemie -

Spectroscopy of Unstable and Charged Species in Cryogenic Solids

Marcin Frankowski

Vollständiger Abdruck der von der Fakultät für Chemie
der Technischen Universität München zur Erlangung des akademischen Grades eines

Doktors der Naturwissenschaften

genehmigten Dissertation.

Vorsitzender: Univ.-Prof. Dr. Dr.h.c. St. Veprek

Prüfer der Dissertation:

1. Univ.-Prof. V. E. Bondybey, Ph.D. (Univ. of California, Berkeley, USA)
2. Univ.-Prof. Dr. J. Friedrich
3. Univ.-Prof. Dr. F. von Feilitzsch

Die Dissertation wurde am 06.05.2004 bei der Technischen Universität München
eingereicht und durch die Fakultät für Chemie am 16.06.2004 angenommen.

to my Parents,
Ania and Natalia

> *"Deep in the human unconscious is a pervasive need for a logical universe that makes sense. But the real universe is always one step beyond logic."*
>
> — FRANK HERBERT from "*The Sayings of Muad'Dib* by the Princess Irulan"

Contents

PART I: THEORETICAL, METHODICAL AND EXPERIMENTAL BACKGROUND

PART II: MATRIX-ISOLATION STUDIES OF NEUTRAL MOLECULES

PART III: MATRIX-ISOLATION INFRARED SPECTROSCOPY OF MASS-SELECTED IONS

PART IV: ACTIVATION SPECTROSCOPY OF RARE GAS SOLIDS

Introduction

At extremely low temperatures, rare gas atoms constitute the simplest solids. In these structures, classified as cryogenic or low-temperature solids, closed shell atoms are ordered into cubic arrays by weakly binding *van der Waals* forces.[1] In order to emphasize their role in physics and chemistry one can cite *Song* and *Williams* [2]: “if rare gas crystals did not actually exist, condensed matter theorists would have invented them”. Spectroscopists would likely agree, bearing in mind their importance in molecular physics. This is because the cryogenic solids serve as inert host materials or matrices, for studies of highly reactive and transient species.[3] Thus, unstable, short-lived species including molecular ions can be trapped and accumulated in barely interacting matrices to be studied via various spectroscopic methods. *Matrix-isolation* was introduced fifty years ago by *Pimentel* [4] and independently by *Porter* [5] starting a new field in spectroscopy. Years of experience and modern developments made it a well-established and very productive technique.[6-9] This fact is best reflected in a large and increasing number of scientific publications in highly rated journals as well as in growing interest in international meetings and conferences.

Isolation of the species in low temperature matrices provided a very reliable method to obtain first information on ground-state vibrational frequencies of unstable molecules.[10] However, in many cases the observed, in particular electronic spectra, structure and dynamics reveal appreciable perturbations by the host environment. Although, at the first stage of development of matrix isolation it has been seen as rather undesirable drawback, a few years later it turned out to be an important advantage. Indeed, a breakthrough in this approach was caused by the discovery of the first rare-gas compound by *Bartlett*.[11] This triggered the idea of using rare-gas matrices as reactive media for formation of new rare-gas species.[12,13] Recently, a series of experiments have been carried out on rare-gas hydrides HRgY by *Räsänen et al.*,[14] where Rg is a rare-gas atom, and Y is an electronegative fragment. Those species were initially prepared in xenon matrices using UV-laser photolysis of an HY precursor and subsequent mobilization of hydrogen atoms. Quite recently in cooperation with *Bondybey* and *Lorenz* [15] HRgY were stabilized in the strongly less interacting neon matrix. Successful studies in this field together with theoretical predictions [16] were motivation to produce HXeCCH in a Xe matrix. As demonstrated in *chapter 3*, besides a small amount of the expected HXeCCH, formation of the novel XeC_2 species [17] is definitely favored, which appears to be the reason for the absence of C_2 absorptions in Xe matrices. Besides FT-IR and density functional theory (DFT) ground-state studies, this work is aimed to elucidate the electronic spectra of this unique molecule. Observations of XeC_2 done in Ar and Kr matrices address the important question of solvent effects, since XeC_2 is predicted to be highly polar with a strong charge-transfer character in the Xe–C bond.

Apart from the search for novel rare gas compounds, the use of weakly interacting matrices gives, nowadays, a still unique opportunity for spectroscopic survey of transient and ionic species. Their accumulation result in number densities, which are not available via modern, sophisticated gas-phase methods, such as supersonic beams, providing truly free, cold molecular species.[18] This often allows to overcome the main obstacle in their identification through IR spectra, which is the lower absorption cross-section in this range. Study of highly reactive organic azides, carried out in the framework of the *EU* project on *"Reactive intermediates"* in collaboration with group of *Prof. M. L. Costa* from the *New University of Lisbon* is the subject of *chapter 4*. Investigation of infrared absorptions in various matrices and DFT computations of azidoacetonitrile, N_3CH_2CN, and azidoacetone, $N_3CH_2COCH_3$ is undertaken in order to provide complementary information to decomposition and conformational studies.[19,20]

A milestone in matrix-isolation spectroscopy of molecular ions was the implementation of mass-selective deposition. In spite of several problems involving the intensity of ion beam, deceleration of ions prior to deposition and building up of space charge in hosts, a number of successful experiments have been reported so far.[21] The first isolation of mass-selected cations was reported almost at the same time by the groups of *Rivoal* [22] and *Maier*.[23] Recent experiments in our group [24] focused on ionic cyano-compounds which are of special astrophysical interest.[25,26] Following the project on cyano-ions, FT-IR mass-selected studies in neon matrices, together with DFT computations, presented in *chapters 5* and *6* allow for direct survey of structure of previously unknown molecular ions. The species are generated upon electron impact (EI) ionization of tetracyanoethylene, C_6N_4 and acetonitrile CH_3CN precursors. The former precursor gave an opportunity to deposit and characterize the parent and several fragment cations, $C_6N_4^+$, C_2N^+, $C_4N_2^+$, $C_3N_2^+$, $C_5N_3^+$, and $C_6N_3^+$. New insight into the spectroscopy of protonated acetonitrile, CH_3CNH^+ has been gained upon EI ionization of the acetonitrile precursor. Selective deposition of the cyanomethyl radical cation $C_2H_2N^+$ provided new data on vibrational spectroscopy of its H_2CCN^+, H_2CNC^+, $HCCNH^+$ isomers. Isotopic study and DFT computations appreciably support interpretation of spectra. The obtained information will hopefully facilitate high resolution gas-phase studies and subsequently astronomical searches, which in turn are essential for a better understanding of physics and chemistry of interstellar space.

Due to their simplicity, rare gas solids, as the widest energy-band gap insulating materials, represent model systems for the investigation of stability and dynamics of trapped charged species. [2,27,28] Additional insight into the processes involving those species can be gained from activation spectroscopy studies, [29] as discussed in *chapter 8*. Besides molecular ions, also electrons can be efficiently trapped in the defects or imperfections of the matrix structure as well as by guest species.[27,30] In this work nominally pure neon and argon solids as well as doped argon samples are irradiated with electrons during or after deposition. Subsequent extraction of the electrons from such pre-irradiated matrices upon heating or laser irradiation provides information on trapping mechanisms.[27] Therefore, the analysis of the data obtained on thermally stimulated exoelectron emission (TSEE) and emitted photons (Thermally Stimulated Luminescence) in comparison with the yields of photon-stimulated exoelectrons (PSEE) makes it possible to discriminate between reactions of neutral species and charge carriers, and to some extent elucidate their interconnection. This work is performed in collaboration with *Prof. E.V. Savchenko* from the *Verkin Institute for Low Temperature Physics and Engineering* of the *National Academy of Sciences of Ukraine.*

This thesis is divided in four major parts. After a detailed survey of fundamental aspects of matrix-isolation and activation spectroscopy, experimental and computational methods are described. The results on spectroscopy of unstable molecules (*chapters 3, 4*), mass-selected molecular ions (*chapters 5, 6, 7*) and activation spectroscopy of solid neon and argon (*chapter 8*) provide new information on processes involving neutral and charged guest-species in cryogenic solids. A brief summary ends with an outlook for future studies.

References

[1] M.L. Klein, J.A. Venables, Eds. *Rare Gas Solids,* vol. 1, Academic, New York, 1976.

[2] K.S. Song and R.T. Williams, *Self-Trapped Excitons*, Springer Series in Solid State Science, vol. 105, Springer-Verlag, Berlin, 1996.

[2] B. Meyer, *Low Temperature Spectroscopy*, American Elsevier Publishing Company, New York, 1971.

[4] E. Whittle, D.A. Dows, G.C. Pimentel, *J. Chem. Phys.* **22**, 1943 (1954).

[5] I. Normann, G. Porter, *Nature* **174**, 508 (1954).

[6] V.E. Bondybey, T.A. Miller, *Vibronic Spectroscopy And Photophysics Of Molecular Ions In Low Temperature Matrices* in T.A. Miller, V.E. Bondybey, Eds. *Molecular Ions: Spectroscopy, Structure and Chemistry*; North Holland, Amsterdam, 1983.

[7] L. Andrews, M. Moskovits, Eds., *Chemistry and Physics of Matrix-isolated Species*; North Holland: Amsterdam, 1989.

[8] V.E Bondybey, L. E Brus, *Nonradiative Processes In Small Molecules In Low-Temperature Solids* in *Advances in Chemical Physics*, vol. 41, Ed. R. Prigogine, S.A. Rice, John Wiley & Sons, New York, 1980.

[9] I.R. Dunkin, *Matrix-isolation techniques*, *A practical approach*, Oxford University Press, New York, 1998.

[10] M.E. Jacox, *Chem. Phys.*, **189**, 149 (1994).

[11] N. Bartlett, *Proc. Chem. Soc.* 218 (1962).

[12] K.O. Chrisite, *Angew. Chem. Int. Ed.* **40**, 1419 (2001).

[13] V.E. Bondybey, M. Räsäanen, A. Lammers, *Ann. Rep. Prog. Chem., Sect. C* **95**, 331 (1999); and references therein.

[14] L. Khriachtchev, M. Pettersson, N. Runeberg, J. Lundell, M. Räsänen, *Nature* **406**, 864 (2000).

[15] M. Lorenz, M. Räsänen, V.E. Bondybey, *J. Phys. Chem. A* **104**, 3770 (2000).

[16] J. Lundell, A. Cohen, R.B. Gerber, *J. Phys. Chem. A* **106**, 11950 (2002).

[17] G. Maier, Ch. Lautz, *Eur. J. Org. Chem.* **769** (1998).

[18] G. Scoles, *Atomic and Molecular Beam Methods*, Oxford University PressNew York, 1988.

[19] J. M. Dyke, A.P. Groves, A. Morris, J. S. Ogden, M.I. Catarino, A. A. Dias, A. M. S. Oliveira, M. L. Costa, M. T. Barros, M. H. Cabral, A. M. C. Moutinho, *J. Chem. Phys. A* **103**, 8239 (1999).

[20] M. I. Catarino, B. J. Costa Cabral, M. L. Costa, *J. Mol. Struct. (Theochem)* 397, 223 (1997).

[21] V.E. Bondybey, A.M. Smith, J. Agreiter, *Chem. Rev.* 96 (6), 2113 (1996).

[22] J. C. Rivoal, C. Grisolia, J. Lignieres, D. Kreisle, P. Fayet, L. Wöste, *Z. Phys. D* 12, 481 (1989).

[23] D. Forney, M. Jakobi, J.P. Maier, *J. Chem. Phys.* **90**, 600 (1989).

[24] A.M. Smith-Gicklhorn, M. Lorenz, R. Kołos V.E. Bondybey, *J. Chem. Phys.* **115**, 7534 (2001).

[25] E. Herbst, *Annu. Rev. Phys. Chem.* **46**, 27 (1995).

[26] D. Smith, *Chem. Rev.* **92**, 1473 (1992).

[27] E.V. Savchenko, A.N. Ogurtsov, O.N. Grigorashchenko, S.A. Gubin, *Chem.Phys.* **189** (1994) 415.

[28] Chun-rong Fu and K.S. Song, *J. Phys.: Condens. Matter* **9**, 9785 (1997).

[29] D.R. Vij, in: *Luminescence of Solids*, D.R. Vij, ed.., Plenum Press, New York,1998.

[30] A. Schrimpf, C. Boekstiegel, H.-J. Stockman, T. Bornemann, K. Ibbeken, J. Kraft, and B. Herkert, *J. Phys.: Condens. Matter* **8**, 3677 (1996).

PART I

Theoretical, Methodical and Experimental Background.

The first chapter concentrates on fundamental aspects of matrix-isolation spectroscopy of neutral and ionic species as well as thermally and photon-activated processes in rare gas solids.

In the second, experimental and methodical part, apparatus and specific methods applied in this work are discussed. Sample preparation procedures include deposition of mass-selected ions and sources of transient and ionic species. These are investigated by Fourier-transform absorption and emission spectroscopy as well as measurements of activated exoelectron current.

Principles of computational methods, based on Density Functional Theory, applied to predictions of structure and vibrational spectra are discussed in the last section.

1 Theoretical Basis

1.1 Spectroscopy of Matrix-Isolated Molecules

The term "matrix isolation" was coined 50 years ago by *Pimentel* and co-workers [1], after the discovery that cryogenic solids, bound by *van der Waals* attraction, can be effectively used to isolate and study free radicals and other unstable or transient species. In spite of the emergence of alternative methods for studying low temperature spectra, like adiabatic supersonic expansion, matrix isolation is still useful nowadays as a powerful tool for spectroscopy [2-6].

Properties of rare gas as well as nitrogen solid matrices are summarized in Table 1.1. Cryogenic matrices are typically grown in a high vacuum environment, by condensation from the gas phase at a temperature which is slightly higher than about two thirds of the sublimation temperature [7]. In view of their extremely broad optical transmission range, these solids constitute ideal host materials for spectral survey of embedded species. The low frequency limit, extending to the far infrared region, is determined by the Debye energy below which photons are absorbed via excitation of lattice phonons. The upper limit of the optical transparency, lying in the vacuum UV region, results from the width of the energy-band gap beyond which electrons can be optically excited from the valence to the conduction band, leading to the formation of excitons.

Absence of “hot bands” and rotational structure in absorption spectra observed at cryogenic temperatures facilitates assignment [3]. On the other hand, though cryogenic hosts interact relatively weakly with embedded molecules, their spectra are slightly perturbed by the solid medium and “matrix effects” are usually observed. Isolated species can be located in slightly different local environments, so-called “matrix sites” that contribute to the overall absorption spectrum resulting in observation of several maxima.

Although some of the metastable sites and lattice defects can be relaxed by annealing, the barriers between the minima are too high, especially for larger species, and molecular rotations are usually not observed. Studies of nonradiative processes occurring in the solid matrix have shown that electronic relaxation often proceeds via a complicated interelectronic cascade involving two or more electronic states [8,9]. This gives an advantage of understanding of the relaxation pathways and mechanisms. By exciting higher-lying levels, a "forbidden" state can be populated by the nonradiative relaxation process and studied spectroscopically. The selection rules are often relaxed in the matrix, making it possible to study directly those processes which are rigorously forbidden in the gas phase.

Table 1.1. Atomic/molecular and solid-state properties of used matrix materials [7,10]

	matrix				
	Ne	Ar	Kr	Xe	N_2
diameter [Å]	3.0	3.8	4.2	4.6	4.34 3.39
bondlength [Å]					1.09
polarizability [$Å^3$]	0.39	1.63	2.46	4.02	1.76
ionization energy [eV]	21.56	15.8	14.0	12.1	15.6
lattice constant [Å]	4.47	5.31	5.65	6.13	5.66
binding energy [eV/atom]	0.02	0.08	0.116	0.17	
Debey frequency at $T = 0$ K [cm^{-1}]	75	93	72	64	69
energy band gap [eV]	21.69	14.15	11.60	9.28	
refractive index	1.28	1.29	1.28	1.49	1.22
melting point [K] (~ 1013 mbar)	24.6	83.3	115.8	161.4	
sublimation temperature (~ 10^{-6} mbar) [K]	9	31	42	58	
thermal conductivity (at 20 K) [$Wm^{-1}K^{-1}$]	0.4	1.3	1.2	2	0.4

For most electronic transitions between valence states of neutral molecules the bond energies within the guest are large with respect to the guest-host interactions. Under these circumstances the guest potential function including the anharmonic parts, is not significantly perturbed by the solid. In special cases where either the guest-host interactions are particularly large, or where the guest itself is only weakly bound, this may not be true, resulting in some interesting spectroscopy and dynamics [11]. For instance, much stronger interactions between the matrix and the guest can be expected for molecules in Rydberg states, and also, in general, for ionic guests. Similarly, very strongly polar molecules, such as alkali halides, are known to interact rather strongly with the lattice [12]. Conversely, even a relatively weak interaction with the host can lead to rather strong perturbations of the guest spectrum if the guest itself is a weakly bound dimer or a van der Waals complex.

1.1.1 Electronic Spectra and Molecular Line Shapes

The atoms of the rare gas lattice are bound by very weak van der Waals forces. Thus the pairwise interaction energy is only ~ 60 cm^{-1} for two Ne atoms and ~ 400 cm^{-1} for the more polarizable Xe atoms [13]. The acoustical lattice phonons are therefore of low frequency, and the Debye cutoff for the rare gas solids (RGS) is near 64 cm^{-1}. The energies associated with the internal bonds in the covalently bound molecules are of the order of several eV and their vibrational frequencies are correspondingly higher. *Rebane* [14,15] therefore proposed that to a good approximation a Born-Oppenheimer type separation of the internal molecular vibrations from the low-frequency lattice modes exists.

For each internal vibronic state of the guest, there exists a separate multidimensional potential surface describing the equilibrium positions and motion of the host atoms. These potential surfaces determine the spectral line shapes associated with the vibronic transitions in the guest molecule. The origin of the line shapes is schematically shown for typical one-dimensional potential curves in Figure 1.1 [11]. If there is no change in the shape or equilibrium position of the potential surface between the lower and upper guest internal states, then processes conserving the number of phonons are favored (Figure 1.1a). Only a single sharp line is observed for each vibronic band and the spectrum of the guest resembles that of a nonrotating gas-phase molecule. When on the other hand, a displacement along some normal coordinate accompanies the absorption or emission process, Franck-Condon type considerations will dictate the appearance of a progression in that particular phonon mode as shown in Figure 1.1b. Since the problem is not restricted to one dimension and a large number of phonon modes may couple to the electronic transition, there is a large number of such progressions. This is depicted for several lattice modes in Figure 1.1b. The 0–0 origins of all these progressions are coincident and give rise to a sharp line in the spectrum — the zero phonon line (ZPL). This corresponds physically to the adiabatic process connecting the fully relaxed equilibrium geometry in the lower state with the new equilibrium around the upper level. The higher members of these progressions will, in general, not overlap exactly due to the varying magnitudes of the individual lattice vibrations. The envelope of all these lines will give rise to a relatively broad and usually continuous wing which is called the phonon sideband. Physically, the maximum of the phonon sideband corresponds to the vertical Franck-Condon process which leaves the geometry around the initial state unchanged. This is then followed by fast, $\leq 10^{-12}$ s time scale resolvation of the final state. It should be emphasized that a particular line profile is not a property of a particular guest state but instead of a transition between the initial and the final state. It should also be noted that the appearance of sharp zero phonon lines and absence of appreciable phonon sidebands does not necessarily imply a weak interaction between the guest and the solvent. It simply means that no change in this interaction occurs during the transition. Thus numerous molecular cations exhibit sharp, zero-phonon type spectra, with little evidence for phonon wings, although ion solvation energies [16] are often in excess of 1 eV.

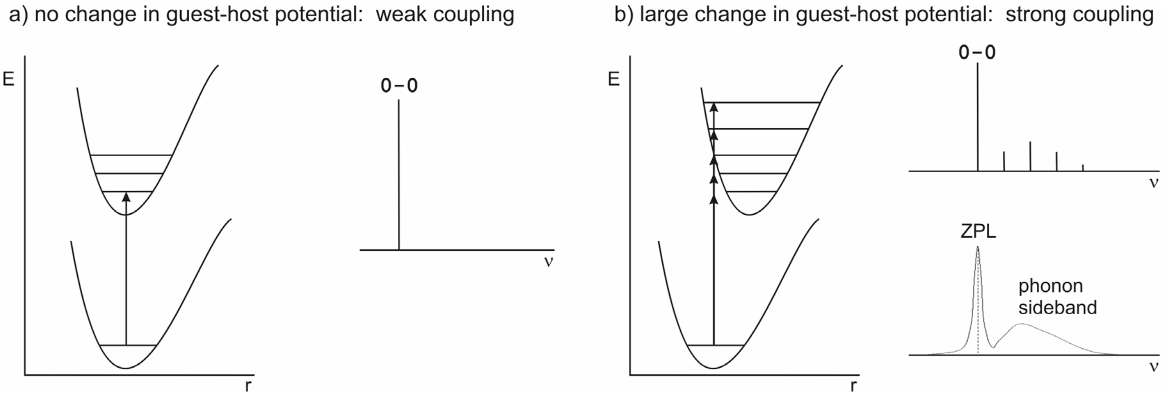
a) no change in guest-host potential: weak coupling

b) large change in guest-host potential: strong coupling

Figure 1.1. Figure explaining schematically the origin of matrix line shapes. (a) If the guest host potential remains unchanged, transitions conserving the number of phonons are favored and single line results. (b) If shift in the lattice atom positions occurs, a Franck-Condon progression will appear. Convolution of many such progressions gives a sharp ZPL containing their common 0–0 origins, and a broad phonon sideband; based on [11].

Experiments reveal that only the ZPL generally appear in infrared and Raman spectra. Under normal circumstances the guest-host interaction is insensitive to the vibrational state of the guest, and so the vibrational transitions are in the weak coupling limit. Electronic transitions are usually more strongly coupled to the phonons as evidenced by the more or less intense phonon wings in the guest spectra, reflecting the extent to which the solvent geometry changes during the transition. Different vibronic bands of the same electronic transition generally display similar line shapes, again reflecting the insensitivity of potentials to the vibrational state of the guest. The guest-host interaction is controlled by the electron density distribution rather than by the bond lengths and nuclear geometry of the guest.

The electronic transition will couple preferentially to those lattice modes (phonon sideband) having a large amplitude in the neighbourhood of the guest. In particular, the introduction of the molecular impurity itself introduces several low-frequency vibrations associated with its rotational and translational degrees of freedom. Preferential coupling to these pseudolocalized modes is particularly apparent in the spectra of some diatomic hydrides, which exhibit a discrete structure in their phonon sidebands resembling the gas phase rotational spectrum [17,18].

1.1.2 Vibrational Spectroscopy

The guest-host interaction potentials are usually not strongly sensitive and specific to the vibrational state of the guest and the line broadening mechanisms are therefore less important in pure vibrational spectroscopy [19-23]. For most molecules vibrational absorptions in inert matrices lie close to the gas-phase band centers and as mentioned above only the ZPL are generally observed in those spectra. The major obstacles to IR studies are rather connected with much lower absorption cross-sections in the corresponding frequency region. In rare gas and nitrogen matrices, infrared absorptions are typically sharp, with FWHM (full width at half-maximum) between 0.1 and 1 cm^{-1} [6]. Any rotational structure is, with few exceptions, quenched. Occurrence of multiple matrix sites, results often in the appearance of several absorption maxima — usually one or two of which predominate — over a range of a few cm^{-1}. A comparison of ground state vibrational frequencies for transient molecules (2 – 16 atoms) in Ne and Ar matrices with corresponding values obtained from gas-phase measurements, reviewed by *Jacox* [6] is shown in Figure 1.2.

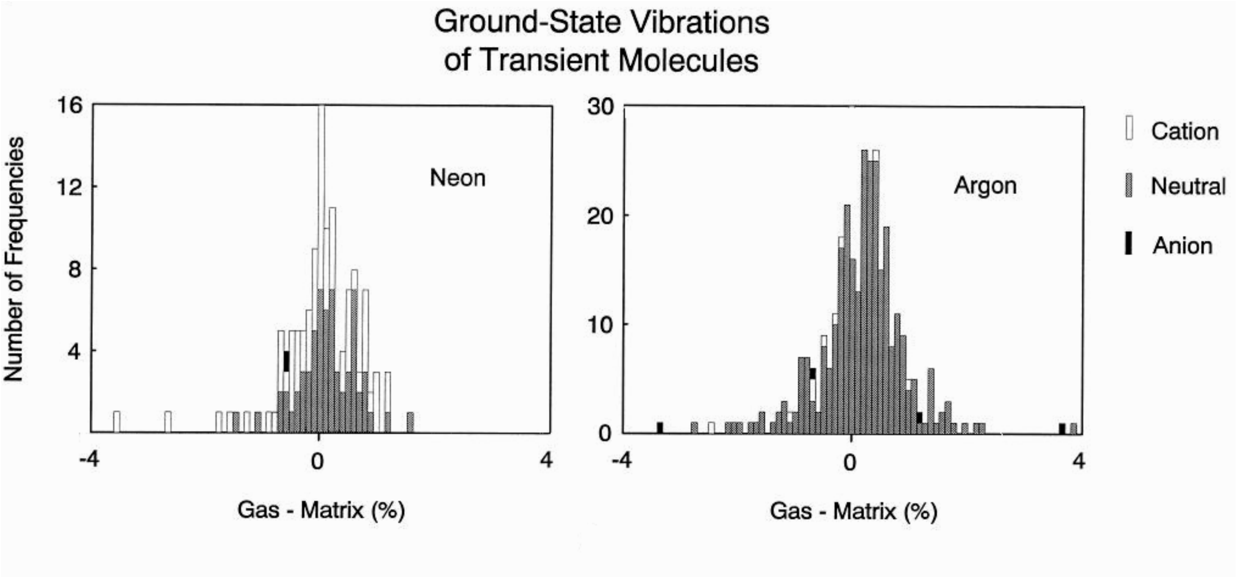

Figure 1.2 Distribution of shifts, expressed as $100(\nu_{gas} - \nu_{matrix})/\nu_{gas}$ for ground state vibrations of free radicals, molecular ions, and other transient molecules isolated in neon and argon matrices, from [6].

Matrix shifts for covalently bound molecules isolated in solid Ne or Ar often are quite small. A comparison of positions of the ground-state vibrational fundamentals of over two hundred diatomic molecules observed in the gas phase and in N_2 and rare-gas matrices has shown that, typically, the smallest matrix shift occurs for Ne matrix observations, with successively increased matrix shifts for the heavier rare gases and for nitrogen. Except for very weakly bound molecules and for the alkali metal and group IIIa halides, matrix shifts of most diatomic molecules isolated in solid argon are smaller than 2 %. Similar conclusions resulted from a comparison of neon- and argon-matrix shifts for the ground-state vibrational fundamentals of larger molecules. In general, experimental data on larger molecules also show that matrix interactions are minimal for Ne, increase with the mass of the rare gas atoms and become even more important for N_2 and most other small molecule matrices. For Ne matrices, the maximum in the distribution lies near 0.0 %, and for Ar matrices, near 0.2 %. For Ne and Ar matrices, less than one-tenth of the matrix shifts are larger than 1 %.

1.1.3 Positive Ions in Rare Gas Matrices

Due to weaker solvent interaction in the ground states of molecular cations, more polarizable matrices as Ar and Kr may be adequate in ground state vibrational spectroscopy studies. On the other hand, one of the key factors in obtaining sharp and unperturbed electronic spectra for ionic guests appears to be a large difference between the guest electron affinity and the host conduction band which is closely related to the bare atom's ionization potential. This condition is well fulfilled for most organic and inorganic cations in solid Ne. Ne is thus clearly the preferred medium for matrix molecular ion studies. The ionization potentials of Ar and the heavier rare gases are much lower and are often close to the electron affinities of organic ions.

As discussed above, in addition to gas-to-matrix vibrational shifts, the entire electronic transition is slightly shifted in the solid medium, reflecting small differences in the absolute depth of the guest-host interaction potentials between the ground and the excited electronic state of the ion. The comparisons between the gas phase and the matrix are more difficult to make due to inhomogeneous broadening. The inhomogeneous distribution for each vibronic band spans a certain frequency range (even extending over 100 cm^{-1}), often with several sharp and well defined "sites" or maxima.

The electronic and vibrational data seem to indicate that most molecular ions in solid Ne are only very weakly perturbed by the solid medium. The gas-to-matrix shifts observed for a wide variety of molecular guests in Ne are of comparable magnitude and sometimes even smaller than those experienced by the parent compounds and similar neutrals. The valence electrons of cations are more tightly held because of the excess positive charge on the nuclei, resulting in more compact electronic wavefunctions. The guest solvation energy while much larger in the absolute sense, consists mainly in polarization of the lattice atoms by the ionic charge. Such an electrostatic interaction is not very state specific, i.e. it does not depend strongly on a particular state of the ion, and does not lead to significant phonon broadening and perturbation of the guest spectra. Very little chemical, charge transfer, interaction seems to occur in solid Ne.

1.1.4 Relaxation Processes

As it was already mentioned the interaction of the vibrational and electronic states of guest species with the lattice vibrations of the host cause an occurrence of complex interelectronic cascades of relaxation processes involving two or more electronic states. This can result in softening of selection rules and emission of radiation in "forbidden" transitions. Such "forbidden" states can be populated after excitation of higher electronic levels via nonradiative relaxation processes. Considering nonradiative processes the internal energy of the guest is relatively rarely transferred directly to the delocalized lattice phonons of the host [5]. Depending on the specific nature of the guest, of its excited state (rotational, vibrational or electronic) and on the strength of the guest-host coupling, the relaxation may proceed by a number of different mechanisms, and the rates may span many orders of magnitude. The simplest nonradiative process, relaxation between two levels of the guest, converting the internal guest energy into delocalized lattice vibrations, can be seen when the level spacing is relatively small in molecules in highly diluted matrices, but is most often accompanied or masked by other, more efficient processes, such as intramolecular V–V (vibration–vibration) energy transfer, transfer of energy to rotational mode (V–R transfer), or transfer of vibrational or electronic energy to other guest molecules [5,24-27]. In large, vibrationally excited molecules, the density of vibrational levels is relatively high. In such species relaxation to the lowest vibrational level proceeds very fast while for smaller ones with vibrational spacing higher than $500 - 1000\ \mathrm{cm}^{-1}$ relaxation takes place via multi-phonon processes.

1.2 Activation Spectroscopy of Solids — Selected Concepts

Rare gas crystals, neon, argon, krypton and xenon condense into stable structures ordered in a face centered cubic (fcc) lattice [28]. In some cases of non-optimal crystal growth, a hexagonal close-packed (hcp) phase may be found as a stable admixture. Crystal growth and their structure and defects have been thoroughly reviewed by *Venables* and *Smith* [29]. RGS are typically deposited in form of a thin film (~ 100 µm). A deposition temperature higher than 2/3 of the sublimation temperature T_{subl} yields the best films, with fcc grains of about 100 nm size. The density of lattice defects decreases as a function of increasing condensation temperature or sample thickness. Lowering the deposition temperature to 1/3 of T_{subl} value diminishes grain size 10-fold and increases density of lattice defects revealing also the hcp minority phase [28].

In all RGS, except helium, the valence band — relatively narrow, consistent with weak bonding of atoms — is derived from the highest occupied atomic *p* orbitals. The conduction bands are wide and nearly free-electron like, and band gaps are very large (Table 1.1). Due to the negative electron affinity E_a, in condensed Ne and Ar conduction electrons repel surrounding rare gas atoms creating a lattice expansion or "bubble" around the electron [28,30]. Electrons occupying the bottom of the conduction band are at higher potential than the vacuum, and can escape from the solid with finite kinetic energy (~ 1 eV from Ne). With the exception of interstitials (negative E_a), electrons in Ne and Ar solids can be trapped (excluding impurities, so-called self-trapping) in such a kind of defects like vacancies, vacancy clusters or pores. On the other hand, the holes in RGS can be self-trapped by rare gas dimer ions Rg_2^+ (STH, self-trapped holes).

1.2.1 Defects in RGS — Formation and Annealing

Exposing RGS to high energy, ionizing radiation — VUV photons, X-rays or electron bombardment, results in large displacements of a small number of atoms accompanied by formation of a variety of persistent lattice defects including vacancies, interstitial atoms or intrinsic ionic centers. The phenomenon of electronically induced lattice defect formation (LDF) is based on energy transport in the electron-nuclear subsystem. The mobile band excitations (free electrons, holes, excitons) cannot provoke immediately lattice destruction because their lifetime at a lattice site $\tau_s \sim B^{-1}$ (B is the half-width of the corresponding band) is much shorter than the characteristic time of atomic displacement, $\tau_{\mathrm{D}} \sim \omega_{\mathrm{D}}^{-1}$ (ω_{D} – Debye frequency) [31]. On trapping, the situation changes essentially and τ_s becomes equal to the total lifetime of the trapped electronic excitation in the crystal. If the energy ΔE released in the vicinity of the trapped excitation on its decay or transformation is higher than the threshold energy E_d for the atom to be displaced to an interstitial position, a stable long-lived defect may be generated in the lattice. It must be noted that only point defects are formed on electronic excitation trapping. In the bulk of sample these are Frenkel pairs (vacancies and interstitials) with different separations between their coupled components. Thus, the energy and time criteria of the electronically induced LDF are [31]: $\Delta E > E_d$ and $\tau_s >> \tau_D$.

The efficient processes of exciton self-trapping (STE) into atomic and molecular states accompanied by a considerable energy release to the lattice contribute to electronic energy dissipation in RGS [32-34]. Electronically induced LDF were found, using spectroscopic methods, in Ne, Ar, Kr and Xe solids excited by a low energy electron beam [31,35]. These studies suggest that the stimulating factor is the self-trapping of excitons either into molecular-type (m-STE) or atomic-type (a-STE) states. In fact, both intrinsic and extrinsic self-trappings are possible, and although some explanations have been proposed, the exact mechanisms of LDF via self-trapping of excitation, and the sites at which LDF occurs are still under investigation. One possibility is that the defects are formed after the radiative decay of excimer molecules. Theoretical considerations also imply a possible permanent LDF in the excited state [31,36]. Based on a qualitative analysis of radiation-induced modification in the luminescence spectra, a simple model was proposed which consists in a displacement of the excited molecular center from the centrosymmetric position in the lattice by overcoming the potential barrier.

Theoretical, molecular dynamics study of the possible evolution of the atomic-type self trapped exciton (a-STE) into stable lattice defects in solid Ne have been carried out by *Fu* and *Song* [30] (Figure 1.3) demonstrating that some of the STE bubbles (lattice expansion around exited center) accompanied with a plastic deformation are at lower energies than a pure STE bubble. The lowest energy species correspond to those with two vacancies in the first atomic shell. Some Frenkel pairs remained stable in the recombined electronic ground state, thereby creating stable lattice defects, but others relaxed back to the perfect lattice after recombination. This study gave indications that in solid Ne, a-STE can lead to permanent defects which survive recombination.

The effects of the radiation damage can be reversed for instance by annealing the samples, or by subjecting them to lower energy irradiation (optical range). Kinetics of defect annealing reflect the existence of the process involved in the annealing (at least the dominant one), the initial distribution of the defects, and the distribution of the various

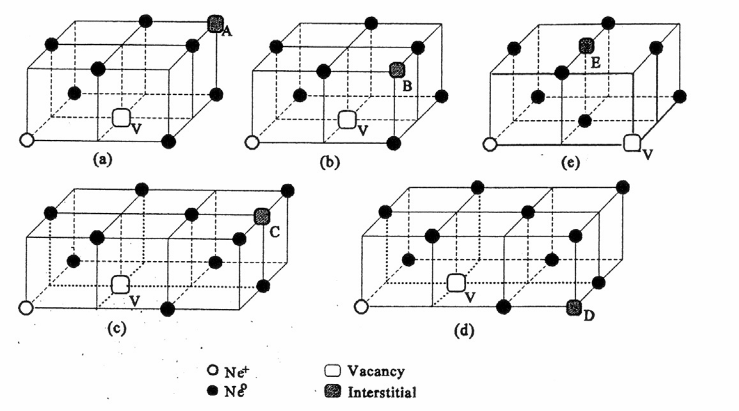

Figure 1.3. Sketches of models used for the representation of vacancy-interstitial pairs. V is vacancy, A-E are interstitials. The interstitial is originally located at the vacancy position. (a)-(d) are the vacancy-associated STEs, while (e) is the interstitial-associated one. (a), (b), and (e) are the second-nearest neighboring Frenkel pairs, (c) and (d) the third-nearest neighboring ones; taken from [30].

sinks (surfaces, grain boundaries, etc.) which take part in the annealing. Therefore, knowledge of annealing kinetics provides information on the defect distribution and their nature. By heating, thermodynamic driving forces reduce the concentration of the defects to the equilibrium concentration characteristic of the material and of the temperature. Considering various mechanisms, the defects can become mobile, migrate to sinks and can recombine with their counterpart, e.g. an interstitial recombines with a vacancy or form new defects by association between themselves or with other types of defects or impurities. Complexes of defects can dissociate. Each of the processes: migration, recombination, complex formation and complex dissociation is characterized by an activation energy (E_m, E_f, E_b) [37], illustrated in Figure 1.4.

This may stimulate diffusion, recombination of the atoms or charged centers, and in general, relaxation of the high energy defects. Such a healing of the defects is often accompanied by spectral changes, light emission or electron emission. Pure or doped RGS with low concentrations of suitable guest atoms or molecules, provide very convenient model systems for studying defect formation, and the reactions and energy conversion processes accompanying their relaxation. Luminescence which may result from defect relaxation, whether thermally or photon stimulated, is a sensitive tool for its monitoring, as demonstrated by numerous studies of **T**hermally **S**timulated **L**uminescence (TSL) [38].

This technique was also employed for the study of nominally pure [39-41] and doped [42-47] RGS. Defect relaxation can also cause promotion of electrons into the conduction band, or electron emission from the sample surface. The former process forms the basis for **T**hermally **S**timulated **C**onductivity (TSC) experiments while the latter one, for **T**hermally **S**timulated **E**xoelectron **E**mission (TSEE).

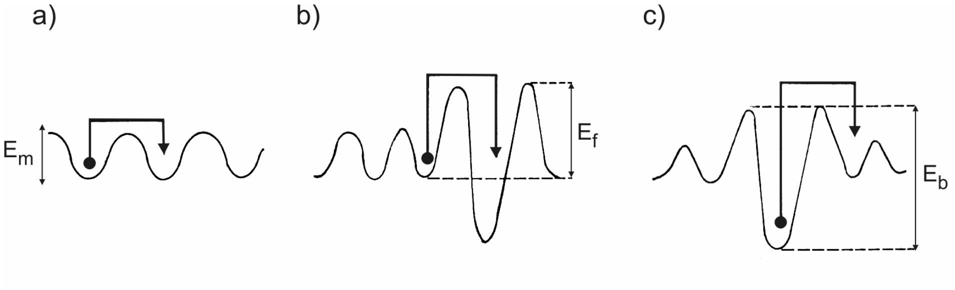

Figure 1.4. Schematic representation of the mechanism of defect migration (a), complex formation (b), and complex dissociation (c) showing the corresponding activation energies involved in the process; from [37].

1.2.2 Thermally Activated Processes

Thermoluminescence (more precisely thermally stimulated luminescence — TSL) in solids, is the light emission that takes place during heating of a sample following earlier absorption of energy from radiation (*Vij* [38]). In this process, previously absorbed energy is released in the form of light. This is quite different from incandescence light emitted by a substance that is heated to a high temperature. The essential condition for TSL to occur is that the material, e.g. insulator or semiconductor have been previously exposed to radiation, i.e. they have been preexcited or preirradiated. Once it has been observed, the material will not show TSL again after cooling and reheating the sample again, unless the sample is again irradiated. One can conclude that though TSL is based on the same fundamental principles as other luminescence processes, the name is misleading since the heating is not responsible for the excitation, but plays the role of a stimulant.

Considering TSL one should also take into account closely related phenomena like thermally stimulated conductivity (or current, TSC), thermally stimulated exoelectron emission (TSEE) and supporting methods such as electron spin resonance (ESR) and optical absorption techniques. The latter method in correlation with TSL contributes to the identification of the type of centers and their relationship with glow peaks after they have been subjected to stepwise annealing. Since trapped electrons give rise to an ESR signal that is directly proportional to the duration and dose rate of the irradiation, and also to the number of traps, this technique provides information regarding charge trapping and its detrapping in TSL. The TSC method is based on changes in conductivity of the preexcited solid sample if the electrons (holes) cross over to the conduction (valence) band due to their thermal detrapping under an electric field applied across the sample. A correlation between TSL and TSC is observed if charge carriers recombine radiatively at the recombination centers and both phenomena occur simultaneously. If TSL emission occurs via detrapping of carriers and their subsequent radiative recombination, through a tunneling process, without the carriers entering either the conduction or the valence band, then TSC will not occur along with TSL. It should be noticed that a TSC peak can occur without carrier detrapping, corresponding to dipole orientation. In this case there is no correlation with the TSL.

Thermally stimulated exoelectron emission (TSEE) is a complementary technique for interpreting the effects underlying TSL and for understanding the nature and distribution of the trapping states from which the electrons are released upon heating of preirradiated solid. Electrons freed from the traps (called exoelectrons) get raised to the conduction band and after they reach energy which is high enough to overcome the potential barrier at the surface and the attraction of the image charges on the surface, they leave the solid sample. However, the negative electron affinity of Ne and Ar causes the opposite situation where electrons experience additional kinetic energy while leaving the surface. Such exoelectrons can be detected, using a Faraday plate, kept under positive potential and placed in the vicinity of the sample. The same thermally detrapped electrons might recombine radiatively at a recombination center giving rise to TSL. A correlation between a TSL peak and a TSEE peak at the same temperature may indicate the presence of electron traps contributing to TSL, at that temperature. Usually, the parameters of the kinetics, such as *Arrhenius* activation energy and frequency factor as well as peak position and shape agree very well for TSL and TSEE, which is strong evidence for an identical origin of emitted and recombined electrons. On the other hand, any absence of correlation between TSL and TSEE could be due to the fact that TSEE is a result of surface traps (arising from adsorbed atoms and molecules and/or surface lattice imperfections) as well as volume traps (existing within the solid), whereas only volume traps contribute to thermoluminescence emission. Both TSEE and TSL yields obtained as a function of temperature are also called glow curves.

1.2.3 Energy-Band Model

Photon- and thermally activated processes can be described in terms of an energy-band model. According to this model, guest species and defects form discrete energy levels within the forbidden energy gap. Other impurities and the presence of vacant lattice sites or other lattice structural defects provide unoccupied energy levels (traps) that have the capability of detaining the charge carriers before their recombination with the luminescent centers, thereby delaying the luminescence. Depending on whether the trapped carriers are holes or electrons these traps are denoted as hole traps or electron traps.

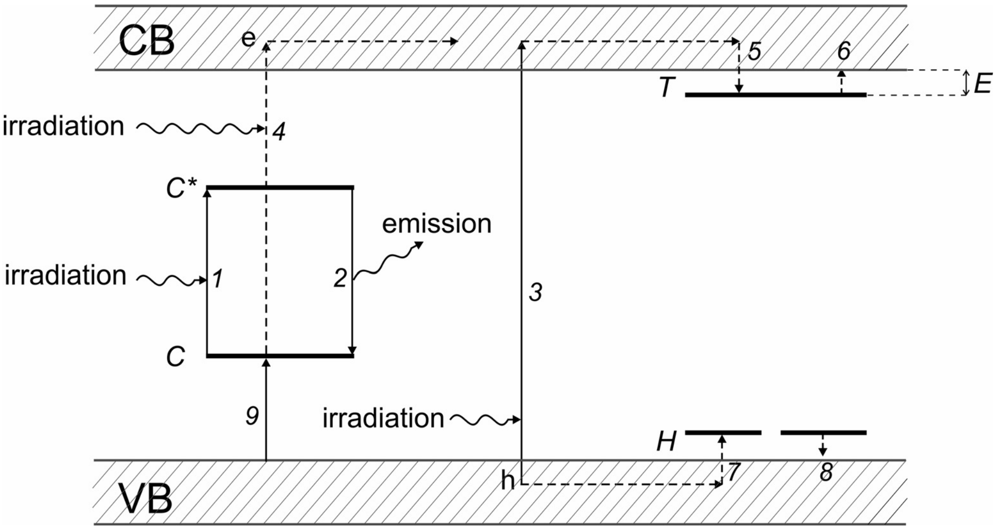

Figure 1.5. Schematic representation of energy-band model; based on [38] (*C* is luminescent center; *T*, *H* – electron and hole trapping states, respectively; e – electron; h – hole; *E* – trap depth; *VB* and *CB* stand for valence and conduction band, respectively).

A simplified energy-band model is illustrated in Figure 1.5. During irradiation, if the luminescent center *C* is raised, via energy absorption (transition *1*), to its excited state *C** without going to the conduction band (*CB*), its return to the ground state will emit a photon — fluorescence, *2*. On the other hand, if the electron is raised to the *CB*, either directly from the valence band (*VB*) by transition *3* or luminescent center *C* via *4*, it will be free to move. With a certain probability it is trapped in the trapping state *T* through the transition *5*. The electron may spend some time τ in the trap before being released to the *CB* via *6* enabling radiative recombination with the luminescent center *C*. Holes play the same role as electrons when they are trapped via *7* and released via *8* to recombine radiatively, *9* at the recombination centers. Direct combination of free electrons and holes across the band gap has much lower probability than indirect, especially in wide-gap semiconductors or insulators, including RGS.

Release of charge carriers from very shallow, small *E* traps, may also occur at the temperature of irradiation (or in case of RGS, deposition) of the sample. Those in deeper traps will be retained for a long period of time even after the irradiation is finished. Upon heating, freed charge carriers may recombine with the luminescent centers, giving rise to TSL. The intensity of TSL increases as the temperature is raised (as the charge carriers start escaping from their traps), reaches a maximum, starts decreasing as the traps are depleted, and reduces to zero when all the traps are empty. The temperature at which the glow curve exhibits a maximum is related to the trap depth *E* below the edge of the conduction band *CB*. The integrated intensity of the glow curve is proportional to the number of populated traps and thus related to the amount of radiation to which the material is initially subjected. A single maximum in the glow curve predicts trapping levels located at a fixed energy *E* below the edge of the *CB* (electron traps) or above the *VB* (hole traps). A set of TSL peaks reveal that the traps are distributed in separate groups at different depths. Each maximum represents a particular set of trapping levels. The trap depth can be calculated based on the temperature at which the TSL maximum occurs.

The energy-band model describes also TSL-related phenomena like TSEE, PSEE (photon-stimulated exoelectron emission) and TSC. In the first two cases, the electrons which gained sufficient energy via the annealing process *6* (TSEE) or photon absorption *6* and *4* (PSEE) can be promoted to the top *CB* and leave the sample, contributing to exoelectron current.

1.2.4 TSL and TSEE — Methods of Analysis

A practical approach in the description of thermally stimulated processes should take into account that the electron released from the trap has a certain probability of getting retrapped. According to *Vij* [38], in general-order kinetics, where a thermoluminescence process follows neither first nor second-order kinetics, its intensity can be expressed by the equation:

$$I_{TSL} = N_{t_0}\ s\exp(-E/kT)\left[\frac{(r-1)s}{\beta}\int_{T_0}^{T}\exp\left(\frac{-E}{kT}\right)dT + 1\right]^{-\frac{r}{r-1}} \qquad (1.1)$$

where N_{t_0} is the number of electrons trapped in initial temperature T_0 and β is the heating rate. The parameter r represents the order of the kinetics and may be non-integer value.

In low temperatures, for no retrapping case of first-order kinetics when all electrons recombine radiatively, one can write:

$$I_{TSL} = N_{t_0}\ s\exp(-E/kT) \qquad (1.2)$$

This relation allows for evaluation of the trap depth E from the initial, ascending part of the glow curve without determining the s parameter — the so-called initial rise method. In the same way the Equations 1.1 and 1.2 can be applied for approximate estimation of E value from TSEE curves, as well as the methods presented below.

There are various methods of TSL and TSEE analysis based on such parameters as heating rate, integrated signal intensity and profile of the glow curve, as mentioned above. However, in most cases TSEE measurements do not provide well-resolved peaks and accurate determination of E is difficult. One of the used technique is based on a series of measurements of the peak locations for different heating rates. This technique of evaluating E is insensitive to retrapping process and is not affected by thermal quenching as for instance, the initial-rise method. Using two different heating rates β_1 and β_2 and the corresponding temperature maxima T_{m1} and T_{m2}:

$$E = \frac{kT_{m1}T_{m2}}{T_{m1} - T_{m2}} \ln\left[\frac{\beta_1}{\beta_2}\left(\frac{T_{m2}}{T_{m1}}\right)^2\right] \tag{1.3}$$

Plotting $\ln(T_m^2/\beta)$ vs. $1/T_m$ yields a straight line with the slope E/k and intersection with the ordinate at $\ln(E/sk)$, which directly gives E and s. Figure 1.6 shows an application example where the E value is determined for the prominent TSEE peak measured from nominally pure Ne at 9.95, 10.28 and 10.57 K for 0.5, 1.0 and 2.0 K/min. heating rate, respectively. As T_m is not very sensitive to changes in β this method is only approximate and results in error of ~ 5 % for T_m accuracy within 1 K (in experiments presented in this work errors do not exceed 20 %).

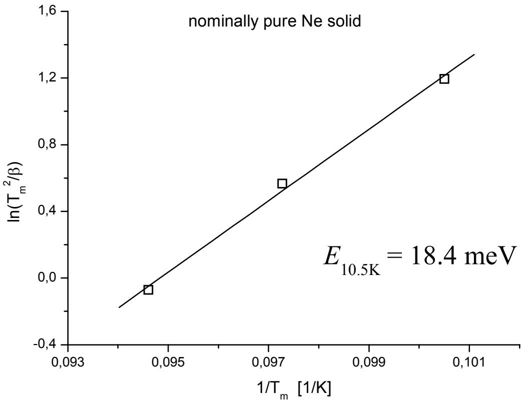

Figure 1.6 E value determined for TSEE Ne peak near 10.5 K using method of different heating rates.

The so-called half-width method allows to determine E from the ascending or descending part of the glow curve. For the latter option, one uses the equation:

$$E = kT_m^2 / \left(T_{half} - T_m\right) \tag{1.4}$$

T_{half} corresponds to the temperature value measured at half of maximum on the descending portion of the glow curve.

By stepwise temperature change in TSEE or TSL measurements one can obtain a set of isothermal-decay (T = const.) curves with different characteristic decay times τ. The time τ can be expressed by $\tau = s\exp(-E/kT)$, enabling determination of E. However, use of this method gives rather ambiguous results since experiments with rare gas solids reveal an almost continuous distribution of electron traps. Usually, an isothermal-decay characteristic, measured at a certain temperature T_2, is affected by process occurring already at lower temperature T_1 ($T_1 < T_2$). Thus, an exponential fitting of such a decay curve is more difficult for higher temperatures, and estimation of characteristic parameters τ for number of traps contributing to the curve is very inaccurate.

2 Experimental and Computational Methods

2.1 Sample Preparation and Sources

2.1.1 Cryostats and Vacuum Systems

Matrix samples are prepared by codeposition of matrix gas (usually rare gas) and vapors of the target molecules on a cooled substrate, whose temperature is typically chosen in the way that diffusion of the host atoms or molecules remains negligible. Besides the analytical instruments and equipment needed for examination of prepared samples, central to matrix-isolation and activation spectroscopy experiments are:

- a refrigeration system (cryostat) with sample holder
- a vacuum-pumping system with pressure monitoring
- a temperature monitoring and regulating system
- sources of species to be examined, e.g. discharge source and electron impact source for radicals and ions

For the experiments presented in this thesis the two experimental setups installed in our laboratory based on closed-cycle helium refrigerators were used. In this type of cryostat the helium is compressed by the compressor unit connected to a compact head module (expander) by high pressure (feed) helium flex-line. The cooling effect is obtained by means of the helium expansion within the head module in two stages after which helium gas returns through the low pressure line to the compressor unit.

The components of both systems are listed in Table 2.1. To facilitate further description as well as discussion of the results in the next sections the two setups will be referred as

LEYBOLD and **APD** correspondingly to the used refrigerators. The choice between one of them depended, in particular on the source of the species which must be used, and the desired matrix. Only the LEYBOLD allows depositing neon matrix since the substrate reaches a temperature of 6 K. For this reason the mass-selection experiment is intended to the LEYBOLD cryostat. Another basic difference between those two arrangements is using of the different type of substrates, and consequently the different way of absorption measurement: in reflection mode — LEYBOLD, and transmission mode — APD. Additionally the LEYBOLD system is equipped with two temperature sensors, one mounted directly on the cold finger of the cryostat (colder one, usually recording temperature in the range of 5.9 – 5.5 K) and the second at the substrate holder (6.4 – 6.6 K). The temperature of the matrix is assumed to be the average of these two values.

Table 2.1 Cryostat systems with temperature control units used in experiments.

cold head	*compressor unit*	*substrate*	*temperature controller*	T_{min}	*temperature sensor*
Leybold RGD 5/100	Leybold RW 6000	mirror: Cu coated by Ag/MgF_2 or Au	Leybold LTC 60	6 K	two Si diodes
APD Cryogenics DE-202	APD Cryogenics HC-2	KCl window	Lakeshore 330	12 K	Si diode

The LEYBOLD and APD vacuum systems are based on standard, O-ring sealed ISO-K components and the cryostat (sample) chambers are pumped by 190 l/s and 230 l/s (given for N_2) turbo-molecular pumps, respectively (Balzers TPH 190, TPH 240 with DUO 1.5a rotary vane pre-pumps). The base pressure under cryo-pumping reaches 6×10^{-8} mbar ($\sim 1.5 \times 10^{-6}$ mbar with the system at room temperature) in LEYBOLD chamber. Correspondingly the pressure value reached for the APD is $\sim 2 \times 10^{-7}$ mbar ($\sim 2 \times 10^{-6}$).

2.1.2 Matrix Deposition

In general the gaseous samples prepared prior for deposition on the cold surface are mixtures of suitable precursors with the matrix gas. Precursor substances in liquid or solid phase must have a sufficient vapor pressure or must be heated in order to obtain desired concentration. The preparation of pre-mixed gas samples is usually done by using the gas handling-mixing systems (at LEYBOLD and APD) equipped with absolute pressure gauges which allow for mixing with arbitrary chosen partial pressure ratios and for control of a pressure drop during matrix deposition. LEYBOLD is independently equipped with a 190 l/s turbo pump which significantly a purification procedure for liquid precursors by means of several pump-freeze-thaw cycles.

Matrices can be deposited continuously by means of the so-called “spray-on” technique [48], which is by far the most widely used method, or by using a pulsed valve. Quite often a pulsed deposition results in more transparent matrices that can be an effect of a slight annealing of the surface layers of the sample. Another advantage of using this technique is the reduction of the concentration of trapped impurities, usually air, carbon dioxide and water vapors, which are rather deposited between gas pulses building thin sub-layers on top of the matrix layer, which are then covered again by the next matrix layer. It is commonly assumed that at base pressures of $10^{-7} – 10^{-6}$ mbar one monolayer of water is deposited per second. Contrary to continuous deposition, building of such a “sandwich” structure at appropriate temperature allows to keep impurities away from the guest species (dopants).

The rare gases, neon (only LEYBOLD), argon, krypton and xenon are used as a matrix gases, as well as N_2. The samples are pre-mixed in glass bulbs or stainless steel containers in ratios from $1/10^2$ to $1/10^5$ (dopant/matrix gas) at a pressure of typically 1 bar. Gas is deposited continuously or by using a pulsed valve (APD, using discharge source) and introduced in the vicinity of the cold substrate by copper tubes at a distance of 2 – 3 cm from its surface. The deposition rate and the amount of sample deposited are determined from the pressure p drop in a known volume V ($pV = nRT$). Typically 4 – 8 mmol of gas are deposited.

2.1.3 Generation of Transient and Ionic Species

Efficient generation of transient or ionic species as well as fragmentation products is of high importance for matrix-isolation spectroscopy. Although modern spectroscopy has developed a host of extremely sensitive methods like laser induced fluorescence (LIF), very often detection and characterization are hampered by difficulties in producing sufficient amounts of the species of interest. This issue turns out to be crucial in the case of mass-selective deposition of ions where the produced species additionally get lost during their passage through a path in the vacuum system.

The choice of the ionization method for a compound depends on the nature of the sample under investigation. Several techniques for the generation of transient or ionic species are available:

- laser vaporization
- photolysis
- microwave discharge
- ion sputtering
- combustion or redox reactions,
- DC discharge
- electron impact (EI) ion source.

DC discharge and EI source are used here and therefore are described in more details. Preliminary results have also been obtained on quadrupole mass spectra of protonated amino acids (L-Arginine, L-histidine) and protonated laser dye molecule Coumarin 120 generated using the electrospray (ESI) ionization technique. However, low efficiency of the source resulted in extremely low ion currents (mass-selected) of the order of pA.

2.1.4 DC-Discharge Source

The electrical DC-discharge (direct current) source with pulsed gas inlet system — implemented in APD system — has been extensively used in our laboratory [49] in a number of experiments producing atoms, ions and radicals. This source was efficiently used in this work to produce XeC_2 molecule by deposition of the discharge products through gaseous mixtures of acetylene with xenon and other matrix gases like argon and krypton.

The source is schematically shown in Figure 2.1. Opening of the electromagnetic valve and introduction of gas is into the space between two aluminum electrodes held under high DC voltage (applied through an electrical circuit, usually about 700 V) ignites the electric discharge. The gas flowing through the discharge fixture expands supersonically into the vacuum chamber and then is intercepted by the cold matrix substrate located at the distance of about 2.5 cm from the nozzle. In the experiments presented in this work the opening time of the valve was in the range of 1 – 2 ms, with a frequency of 10 Hz. The main advantages of this setup are the simplicity of construction and ease in operation. The discharge conditions can be easily optimized for each gas mixture by monitoring the discharge current through the voltage drop across the ballast resistor (in the range of 7 – 12 V) using an oscilloscope and by the control of high voltage and opening time of the valve.

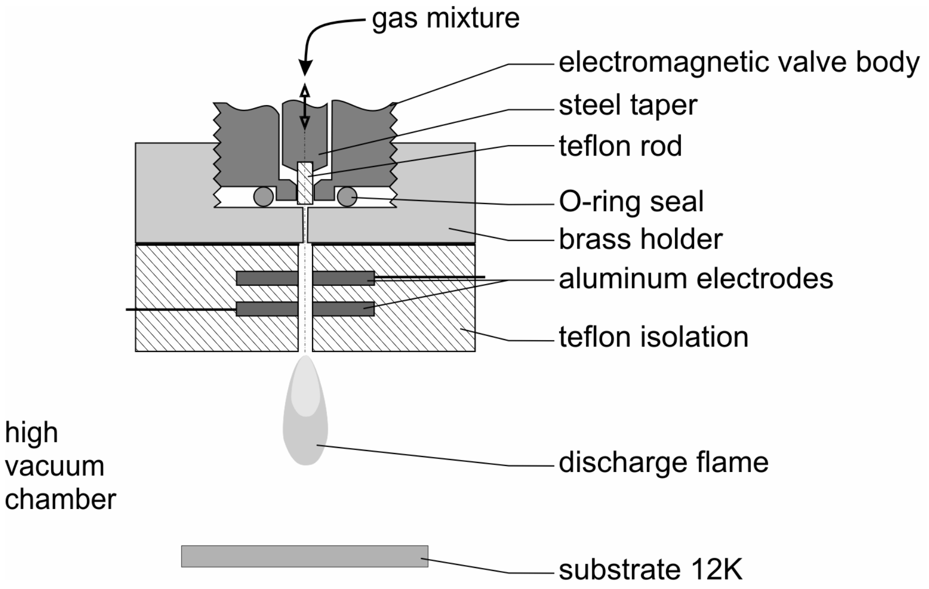

Figure 2.1. DC-electric discharge source with pulsed gas inlet system.

2.1.5 Electron-Impact Ion Source

The electron ionization (EI) is a simple and sensitive method for the analysis of small molecules, well-known in mass spectrometry and also widely employed by spectroscopists. An EI source has been incorporated in our laboratory in the system for mass-selective deposition of ions (LEYBOLD). It is applicable to thermally stable and sufficiently volatile compounds. The upper mass limit considered for this type of ionization is roughly 1000 amu [50], which is much higher that the range of the quadrupole mass filter used for ion deposition.

The precursor substance introduced to the EI source is bombarded with a beam of energetic electrons (with kinetic energy typically of 70 eV) at low pressure conditions of about $10^{-6} – 10^{-5}$ mbar. The collision process detaches an electron from a molecule M of the target compound to convert it to the positive ion M^+:

$$M + e^- \rightarrow M^+ + e^- + e^-$$

In principle the negative ions can be also formed by the capturing of an electron by a neutral molecule but the probability of this process in the EI source is much lower.

Even at such a low pressure the ionization of precursor gas in EI source leads to so-called chemical ionization (CI) [51]. The CI is the process whereby new ionized species are formed when gaseous molecules interact with ions — ion-molecule reactions. The process may involve transfer of an electron, a proton or other charged species between the reactants.

The schematic drawing in Figure 2.2 shows the electron impact source used in our laboratory. The source of electrons are three tungsten filaments heated with a current of ~ 300 mA, mounted between the casing and the cage made of stainless steel mesh. Emitted electrons are accelerated by the negative potentials of the filaments (-50 V) and the casing (-70 V towards the mesh cage kept at positive potential of +40 V. Such a set of adjustable potentials confines the electrons within the casing and allows them to traverse the space within the cage with a kinetic energy in the range of 70 – 100 eV. The collisions of the electrons occasionally hitting the molecules of the precursor gas lead to ionization and/or fragmentation of the molecules. The positive ions are then extracted from the source by an extraction electrode kept at the same potential as the casing and accelerated toward the next stage of the ion transfer setup by an einzel-lens held usually at 400 – 500 V. Test measurements [52] done for N_2 (I_p = 15.6 eV) precursor showed that yield of N_2^+ ions does not change in the range mentioned above but decreases dramatically below an energy of 30 eV. Obviously, production of double charged ions will cost more energy, for example for N_2^{2+} at least 100 eV. The fragmentation of primary ions due to excess of energy gained in collisions with electrons can be followed by further fragmentation processes. The efficiency of such subsequent processes reaches its plateau, similarly to ionization, for energy in the range from 50 to 100 eV at which the EI mass spectrum can be considered as a “fingerprint” of the analyzed compound [50].

Some of the observed ions result from ion-molecule reactions between precursor gas, parent ion and various ionic fragments which can afterwards extracted from the source and deposited in the matrix. As demonstrated in this work EI source can efficiently be used for efficient formation of protonated molecular species (e.g. CH_3CNH^+ and CD_3CND^+).

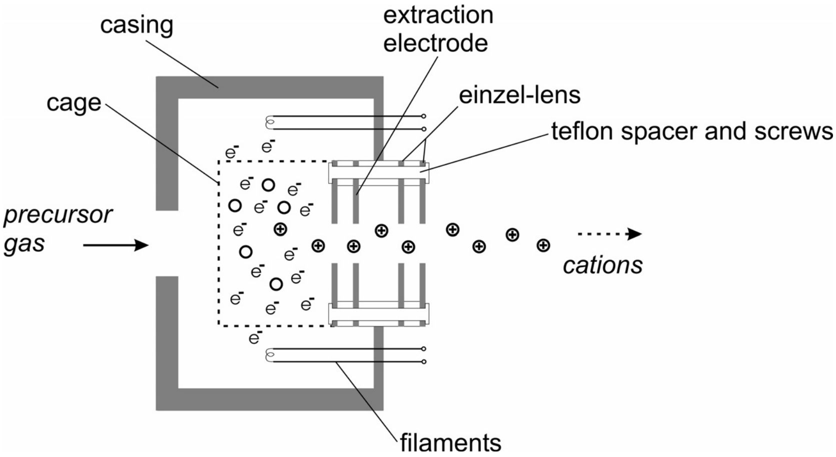

Figure 2.2. Schematic drawing of the electron impact ion source (EI).

The important advantage of using electron impact source is very low consumption of the precursor substance yielding high ion currents, especially if compared with the microwave discharge source applied to the same system. In this case the pressure in the source chamber pumped by a 345 l/s turbo pump usually does not exceed 2×10^{-5} mbar in the experiments and the EI source can operate without a skimmer. In this case the total ion throughput and consequently the mass-selected current, measured in the deposition chamber, is considerably increased by transferring ions from the source chamber to the next stage through the 2 cm (hole) diameter tube. Continued use of less volatile carbon containing precursors significantly shortens the lifetime of the filaments by depositing soot on their surfaces. However, their low cost and easy replacement make this problem acceptable.

2.2 Mass-Selection of Ions

The major disadvantage of the usual approach to matrix-isolation spectroscopy is associated with a large variety of species generated in the sources and directly deposited into the matrices. For instance a discharge through carbon containing precursors produces a large number of carbon compounds that usually results in very complex spectral features. Interpretation of such spectra is a tedious task involving time-consuming correlation studies or experiments with isotopically labeled species. Using the method, in which the ionized molecules of interest are selectively deposited through a mass filter, which is introduced between the ion source and the matrix substrate, is a way to avoid this problem.

The advantages of matrix-isolation studies applying mass-selective ion deposition are:

- efficient elimination of unwanted or disturbing species from deposition process,
- complete information on species generated by ion source via mass spectra,
- appreciable help in identification of spectral features,
- real-time optimization of the ion source and ion transfer parameters with help of mass spectrometer.

However, besides the obvious limitation of the technique to charged species, there are also some significant disadvantages:

- significant looses in ion current: 70 – 95 % in quadrupole mass filter + looses on the tortuous ion path and apertures,
- possible fragmentation and damages caused in the matrix by too high kinetic

energy of the ionic species.

Modern mass spectrometry is largely based on the way with which neutral compounds are transferred into gas-phase ionic species and how those species are efficiently transmitted through a mass filter to a detector. However, state-of-the-art mass spectrometry techniques provide extremely high detection sensitivities (in the attomole, 10^{-18} mol and higher for nanoelectrospray [50]), but the deposition of ions in the cryogenic matrices demands much higher number of species. Consequently in this type of experiments it is necessary to apply ion sources with a high ion current and assure higher ion throughput through the system, often at cost of mass resolution.

2.2.1 Experimental Setup

The schematic of the apparatus for mass-selected ion studies successfully used in our laboratory is shown in Figure 2.3. The setup can be divided in four main sections or stages (chambers) depending on their function in the system:

- the ion source chamber,
- the deflector chamber,
- the quadrupole mass filter (QMS) chamber,
- the sample (cryostat) chamber.

The last stage refers to the LEYBOLD system described in previous sections. The vacuum system containing the whole ion-optics arrangement is based on ISO-K standard components using connecting flanges with diameters of 100 and 160 mm. Each stage is independently pumped. Ion-guiding-optics allow for efficient transfer of the charged species through the different chambers to the substrate (matrix).

The source chamber and the deflector chamber are pumped by 345 l/s turbo-molecular pumps (Leybold Turbovac 361) reaching, without running ion source, pressures of 2×10^{-7} mbar and 1×10^{-7} mbar, respectively. A gate valve mounted between source and deflection chambers allows to cut off the source chamber from the rest of system while cleaning, changing or replacing the ion source, while the other chambers are permanently

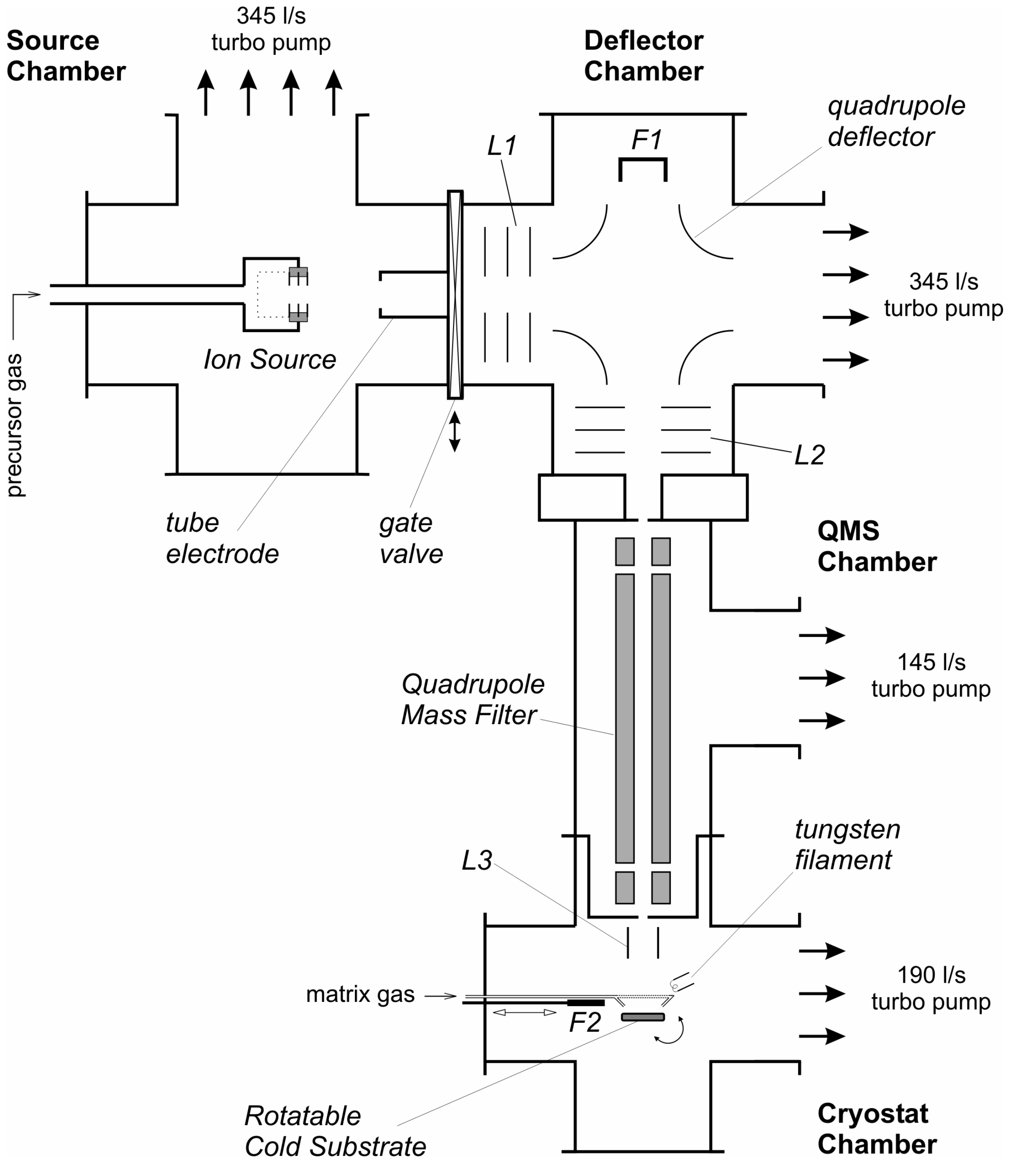

Figure 2.3 Experimental setup for matrix-isolation spectroscopy of mass-selected ions with EI ion source; *F1* – Faraday cup, *F2* – movable Faraday plate, *L1* and *L2* – einzel-lenses, *L3* – cylindrical ion-lens.

pumped. The mass filter compartment is evacuated by a smaller turbo pump 145 l/s (Leybold Turbovac 151) assuring the required conditions for QMS operation.

The ionic species produced in the source chamber are extracted toward the tube-shape electrode and the electrostatic lens (einzel-lens) *L1*, which collimate the ion beam and introduce ions into the deflection unit. Although the EI source operating at lower pressure does not require using a skimmer, for other ion sources it is necessary. The tube-shape electrode, which extracts the ions from the source chamber is held at potential between -400 and -500 V. The potential applied to *L1* typically does not exceed -30 V. In the next step the ion beam is injected to the deflection chamber and deflected at 90° in a quadrupole electric field of the four deflector electrodes (typically the voltages between pairs of electrodes are set within the range 30 – 38 V and 10 – 30 V, respectively). The neutral species which cannot be deflected "fly" directly to the pump and are removed from the system. However, most of the recorded spectra still reveal a considerable amount of precursor substance in the matrix. Apparently, this effect is more pronounced for longer deposition times and depends on the operation pressure in the ion source. The deflected ions are then focused upon the entrance aperture of a quadrupole mass filter (HIDEN HAL/3F) by means of the second einzel-lens *L2*. The potential at *L2* is typically set between -150 and -230 V.

Two current detectors, Faraday cup *F1* and Faraday plate *F2*, permit measurements either of the total ion current (*F1*), or the mass-selected current (*F2*). The mass-selected ion beam is focused, using the cylindrical-ion-lens *L3* onto the matrix substrate, for which the potential is typically fixed at -200 V. Monitoring of the ion currents (usually via the *F2* detector) allows for real time optimization of the source conditions and potentials at the ion guiding elements. Mass spectra are recorded by means of the same Faraday plate *F2* with the quadrupole mass filter operating in scanning mode (QMS).

2.2.2 Quadrupole Mass Filter

For the same reasons, for which quadrupole mass filters are extensively employed in multistage analytical systems as well as in on-line processing applications, it has been incorporated in the matrix-isolation setup. Besides a reasonable cost, its application was determined by several advantages: an ability of operation in continuous and pulsed mode, high transmission, linear mass range, fast scanning capability, electronic adjustment of the parameters via PC-computer controlled interface, and a compact construction, which allowed to include it in a vacuum system based on standard components.

The principle of quadrupole mass spectrometer (QMS) operation is based on control of ion trajectories by a set of direct current (dc) and radio-frequency (rf) potentials applied to two pairs of parallel rod-electrodes, aligned symmetrically in a square array. The ions from the source, which are introduced in one end of the filter in the direction *z* of the rods (see Figure 2.4) experience an oscillating quadrupole electric field. At certain conditions, i.e. time-depended forces within the quadrupole field related to the specific *m/z* (mass/charge) ratio in very narrow range — or in other words, for the certain amplitudes and frequencies applied for the potentials at the electrodes — the ions have stable trajectories whereas others, outside this *m/z* range, unstable ones. In this case, stable trajectories mean a confi-

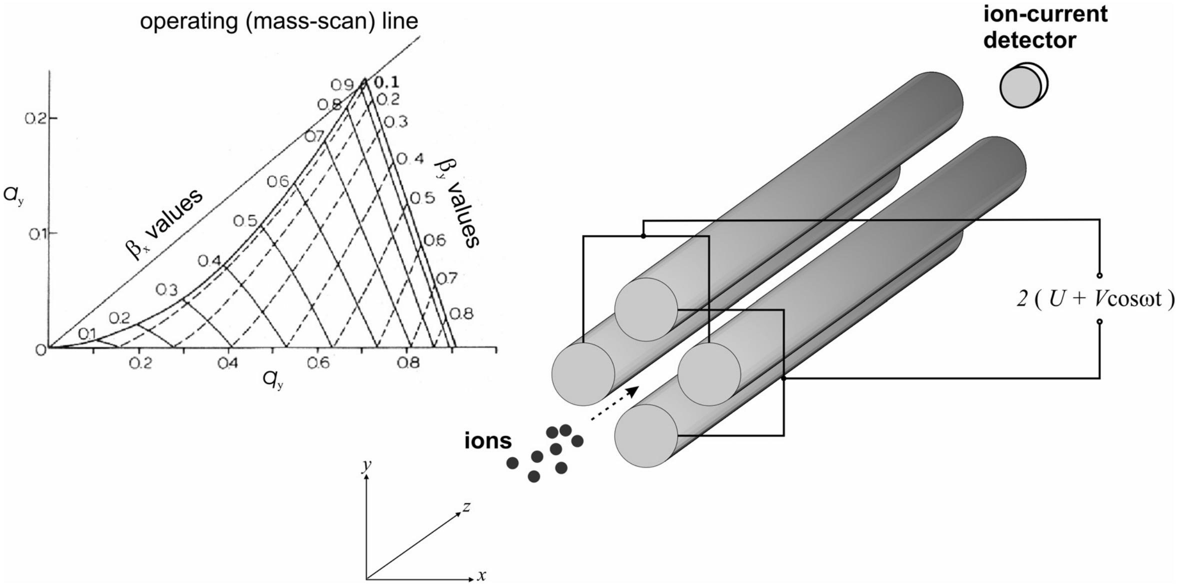

Figure 2.4. Simplified schematic of single-stage quadrupole mass spectrometer (QMS) and the diagram of the lower stability region (inset on the left, taken from [53]) normally used in mass filter operation showing iso-β_y lines for the *x* and *y* direction and a typical operating line (the parameter β is related to the characteristic frequencies of ion trajectory).

nement of the ions within the area among the quadrupole rods. These ions having a certain kinetic energy pass through the filter and reach the detector, while the ions on unstable trajectories are ejected from the quadrupole. Changing the stability conditions by scanning the values of the potentials, the ions characterized by different *m/z* ratio follow the path through the filter and the mass spectrum can be recorded.

The theory of QMS is discussed widely in the literature [50,53] and it is only briefly described in this work. The oscillating quadrupole electric field is a result of the combination of the dc potentials U with the radio-frequency (rf) potentials $V\cos\omega t$ of the opposite sign for both pairs of electrodes, respectively (Figure 2.4). ω is the angular frequency expressed by $\omega = 2\pi f$ (f[Hz].

There are two methods of recording the mass spectra: by varying the frequency ω and holding U and V constant, or varying U and V (keeping U/V fixed) for a constant ω, although the first technique is less common. In principle for a given potential configuration, it is only the mass and ionic charge that determine the stability of an ion trajectory. Theoretically the initial position and velocity in the z direction is not considered for a stable trajectory, however in practice there are limits on the angular divergence of an entering ion beam and its initial x, y and z velocity components. Superimposing of two stability diagrams for x and y directions results in the region shown in left part of Figure 2.4 (so-called: first stability region), representing simultaneous stability conditions for both type of motion. For fixed ω, U, V and r_0 (r_0 is a half of the distance between the opposite quadrupole rods) parameters, all ions of the same *m/z* have the same operating point (a, q). The operating points of all ions lie on the same line of constant a/q called operating line or mass-scan line. Only the ions with operating points between the intersections of the operating line with $\beta_x = 1$ and $\beta_y = 0$ (the parameter β is related to the characteristic frequencies making up an ion trajectory), i.e. the tip of the stability region have trajectories permitting to pass through the quadrupole. This range ensures also the optimal mass resolution. Increasing the U/V ratio operating line approaches closer to the tip and only narrow range of the *m/z* values correspond to stable paths, other ions will strike the electrodes or exit from the field. Adjustment of the U/V ratio changes the resolution decreasing on the other hand, sensitivity or ion throughput.

The mass resolution and range of QMS depend on the amplitude V of the rf signal, rf frequency f, the diameter r_0, length L of the quadrupole rods, and the initial kinetic energy of the ions. Resolution is proportional to the number of rf cycles of an ion within the quadrupole filed and its kinetic energy $E_{kin,z} = zV_z$ along z axis (Figure 2.4):

$$\frac{m}{\Delta m} \propto \frac{mf^2L^2}{E_{kin,z}} \tag{2.1}$$

The upper mass limit can be extended by increasing V and decreasing f and r_0. In view of practical limitations, commercially available QMSs are usually equipped with $2.296r_0$ diameter rods (5 – 20 mm, giving best approximation of the quadrupole field) of a length of 15 – 20 cm, f in the range of 0.5 – 10 MHz and V of the order of 3 kV.

Table 2.2. Specifications of the quadrupole mass analyzer/filter used in laboratory.

mass range	1 – 500 amu
mass resolution	higher than 0.5 amu for entire mass range
quadrupole rods	Ø 12 mm diameter (enhanced transmission)
apertures	Ø 7 mm diameter (entrance and exit)
ion transmission	determined by resolution, up to 30 % (excluding apertures)
scan speed	200 amu/s or 55 mass channels/s
control	PC HAL MASsoft (Windows'95) via controller RS232 interface
ion detector	Au-coated copper Faraday plate (*F2*), Ø 25 mm diameter
signal detection	Femto DLPCA 100 low noise current amplifier (gain 10^9 V/A)

The QMS applied for mass-selective ion deposition is based on the commercial rest gas analyzer (RGA) HAL/3F (HIDEN Analytical Ltd.) equipped with a triple-stage EPIC filter assuring improved line profile, HAL IV controller, separate rf generator, custom modified mounting flange (ISO-K, 160 mm) and electrical feedthroughs. The Faraday plate (*F2*) is used instead of the original detector of the standard RGA. The current from the Faraday plate is amplified by a low noise (FEMTO DLPCA 100) current amplifier which permits for work with very low ion currents down to 100 fA and obtaining mass spectra with S/N ratio better than $10^3/1$. Although the optimal kinetic energy of the ions for the quadrupole mass spectrometer is around 10 eV, there is no significant reduction of resolution for optimized ion currents corresponding to energies up to 30 – 50 eV in the experiments. The efficiency of the ion transfer through the filter reaches 30 % excluding losses on the apertures. The most important parameters of the system used in our laboratory are specified in Table 2.2.

2.2.3 Deposition of Positive Ions

In the deposition of mass selected species one has to deal with two important problems related to the electrical charge carried by the deposited species and their kinetic energy. In general, experimental techniques using mass-selection usually require high kinetic energy of the selected ions in order to obtain ion signal on a reasonable level. In the case of the quadrupole mass spectrometer applied in our system, the optimum range for the kinetic energy of ions lies between 30 and 50 eV and it is thus higher than the recommended 10 eV specified by the manufacturer. Consequently, assuming the neutrality of the solid sample, ions leaving the exit aperture of the mass filter, and focused by lens *L3* reach the matrix substrate with energies above 10 eV.

Decelerating the ions in order to ensure their “soft landing” on the matrix surface is one of the major problems encountered in the mass-selective deposition. It stems from the trade-off between a high ion beam current and low kinetic energy of the arriving ions. Unless the ions impinging on the matrix are sufficiently slowed down, they can fragment hitting the surface. On the other hand, comparison of a kinetic energy as low as 20 eV with the *van der Waals* bond energy of two rare gas atoms being four orders of magnitude lower (3.7 meV for Ne), suggests that even if ions survive fragmentation their kinetic energy can cause melting or evaporation of a number of matrix atoms. Assuming that the energy of incoming ions is in the range of 10 – 50 eV and it is redistributed in the vicinity of the solid neon surface and taking into account the binding energy of a Ne atom in the solid as 20 meV/atom [54] one can estimate that it will result in evaporation of at least a few hundred Ne atoms. An arriving ion can also penetrate the matrix to an appreciable depth resulting in chemical reactions and aggregations of already deposited guest species defeating their isolation in matrix. The problem of “soft landing” and fragmentation was studied in particular for CF_3^+ codeposited with a CO_2/Ne mixture [55] and small metal cluster ions [56]. However, in spite of remarkable problems and obstacles, many successful experiments, including those in our laboratory, have been performed for the last fourteen years since the first experiments by *Rivoal et al.* [57]. Laser excitation spectra of the $C_6F_6^+$ cation, recorded some time ago in our laboratory [52,58] demonstrated that the deposition of ions with high kinetic energy results in a variety of perturbed matrix sites, presumably due to lattice defects and nearby located vacancies, producing different inhomogeneous line profiles in comparison with those obtained from *in-situ* photoionization [59]. Multiple sites were almost absent in the latter case. The same work showed also the dependence of appearance of the excitation spectra on the kinetic energy of $C_6F_6^+$ cations, confirming the damage of the matrix by ion bombardment.

Since rare gas solids serving as matrices are wide band-gap non-conducting materials, the deposition of the charged species builds up a space charge in the matrix structure. The stray electric fields generated by the presence of charged species in a solid sample would deflect the ion beam from the substrate, opposing the goal of accumulating a high number density of ions. *Godbout et al.* [55] proposed a model where the incoming positive ions are alternatively attracted or repelled from the growing matrix, thus leading to a layered deposit. The same concerns negatively charged species emanating from molecules condensed on the cold surfaces. These authors suggested three different ways in which negative charges can be generated in the matrix: via extracting electrons from grounded metal elements being in contact with the sample and trapping them in the matrix; via ionization of some molecular species by incoming ions in front of the sample surface; via collisions with metal surfaces (including some condensed gases) leading to generation of gas phase anions or electrons that are subsequently attracted to the matrix. This model includes rather extreme assumptions. More realistic approach proposed by the same investigators is that some mean, net positive potential of the matrix must be established attracting negative charges. On the other hand, this potential is not sufficient to prevent further accumulation of cations but serves to decelerate incoming ions and consequently in many cases, even increases the efficiency of deposition. This issue is closely related to the problem of "soft landing" of ions, which are slowed down and do not undergo fragmentation. It should be emphasised that the mechanism proposed in [55] implies clearly that full initial kinetic energy of the arriving ions is not relevant to the cation deposition process.

A quite different experimental approach to the cation deposition has been employed in our laboratory, in which an overall neutrality of the sample is maintained by simultaneous irradiation of the growing matrix with electrons generated by a hot filament. The cations are deposited with a significant excess of neon matrix gas, introduced by two copper tubes and deposited simultaneously using the spray-on technique [48]. As it is shown in Figure 2.5, relatively low energy electrons are sprayed from the hot filament, which is kept under a potential for which the electron current exceeds about three to five times the positive ion current. In order to obtain electron current at such a level — usually within the range from a few hundred pA up to a few nA depending on the cation current — the filament potential V_{fil} is typically held in the range of -110 – -130 V. Normally, the potential at *L3* lens does not exceed -200 V to avoid additional acceleration of the ions. The electrons negatively charge the surface of the non-conducting matrix until it reaches

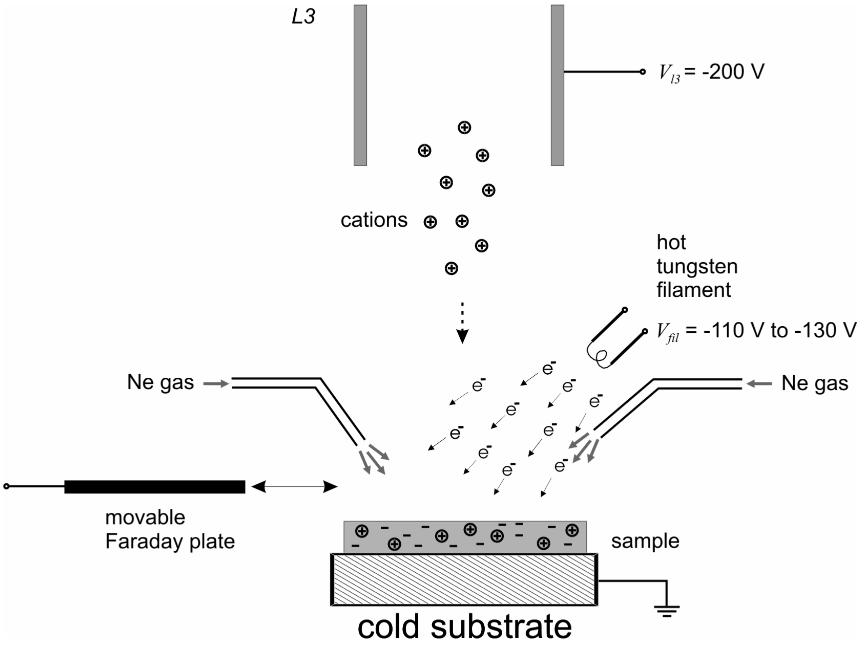

Figure 2.5. Detailed, schematic view of the experimental setup for mass-selective positive ion deposition in the substrate area.

the same negative potential as the filament. In the same time, the arriving cations, which are accelerated toward the matrix, charge it positively. In effect, the kinetic energy of cations hitting the matrix E_{final} is the sum of their initial kinetic energy E_{init} after exiting the *L3* lens area and the energy gained by the negative potential of the matrix surface: $E_{final} = E_{init} + e|V_{fil}|$. Assuming E_{init} energy as 20 eV, the E_{final} for landing ions is in the range of 130 – 150 eV, i.e. fairly high. Regarding the above discussion and a number of successful experiments with mass-selected cations deposition, such a explanation involves rather extreme assumptions. Again, in a more realistic model one could say that the deposition process reaches to some extent a dynamic equilibrium and some mean positive potential of the sample is established, lowering the E_{final} energy of the arriving ions.

An important question is why some cations which can be efficiently generated and transmitted to the cold substrate can be easily detected, even in spite of their weak absorptions, while others not? Series of experiments with our apparatus show that neutralization of ions by spraying the matrix with electrons during depositions is rather inefficient. Following the conclusion derived by *Godbout* and coworkers [55] the crucial role in this type of experiments can be played by an overall averaged matrix potential, which determines the kinetic energy of an ion encountering the matrix surface, which either prevents or favours collision-induced dissociation and charge-transfer processes.

Deposition of Positive Ions – Quantitative Analysis

Some quantitative results on cations deposition using acetylene as precursor gas in the EI source are exemplified in Figure 2.6. Acetylene cations $C_2H_2^+$ (mass 26 amu) were deposited in a neon matrix, in three experiments characterized by different deposition time as well as the value of the ion current. All infrared spectra have been recorded under the same conditions allowing for comparison of line intensities (integrated absorbance). Variations of the ion current during the deposition process were monitored in order to estimate its average value. Thus, average ion current intensities of 3.6 nA, 3.0 nA and 2.9 nA, were obtained for the total deposition times t_{total} = 2 h 30 min., 3 h 30 and 5 h 20 min, respectively for all experiments.

The number of deposited ions (singly charged) calculated from the relation $N_{ion} = (I_{ion} \times t_{total})/e$, where e is the elementary charge, corresponds to the order of 10^2 picomoles. Through the estimation of the approximate amount of deposited rare gas as 10^{-3} mol (from the pressure drop in the gas container), one can obtain a guest/matrix ratio of 10^{-7} for the acetylene cations isolated in neon matrix. Consequently the cation density is usually of the order of $10^{15} - 10^{16}$ per cm^3. Those values are representative for the majority of the performed experiments, although in some cases the ion currents were even one order of magnitude lower. Obviously such an assessment can be done only under the assumption that 100 % of ions reached the matrix, surviving possible recombination and fragmentation during the deposition process. The percentage of successfully deposited cations for

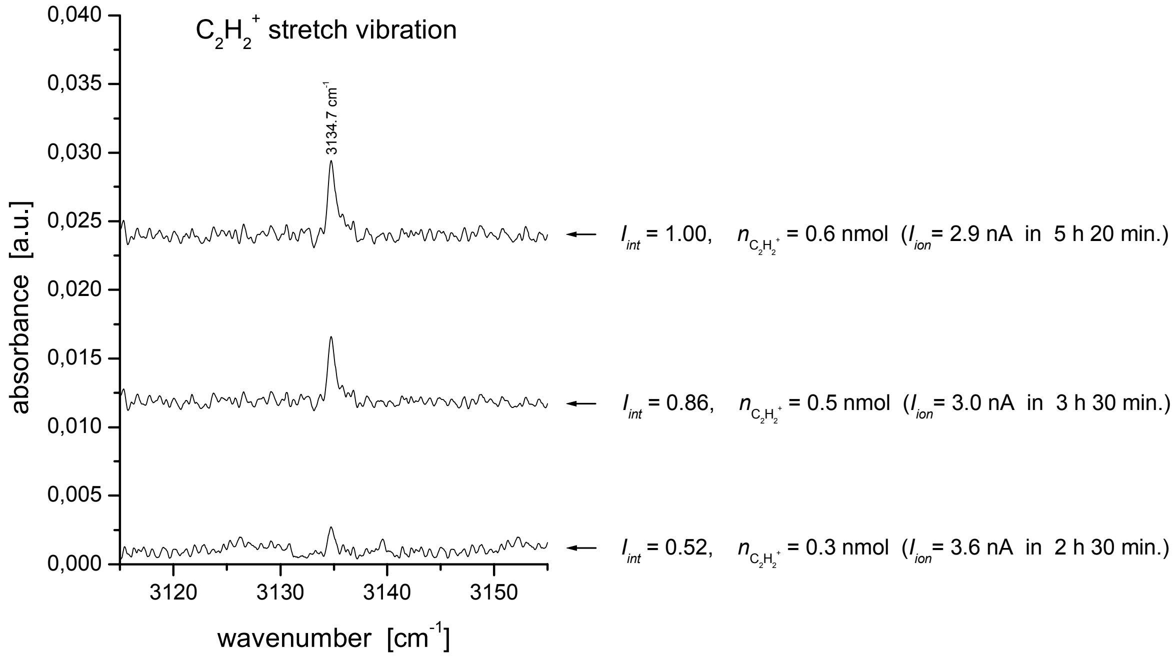

Figure 2.6. Stretching vibration band of acetylene $C_2H_2^+$ cation in Ne matrix observed for different number of mass-selected $C_2H_2^+$ ions (mass 26 amu) deposited from EI source using acetylene precursor gas. Evaluation shows very good correlation between the numbers of deposited ions and integrated intensities (scaled to the most intense line) of the 3134.7 cm^{-1} peak.

$C_6H_3F_3^+$ suggested by *Lorenz* [52] reaches even 80 % confirming the accuracy of the estimation done above at least for the order of magnitude. As expected, the integrated intensities ratio — determined from spectra for the $C_2H_2^+$ stretching band centered at 3134.7 cm^{-1} — is 1.00 : 0.83 : 0.52 (see Figure 2.6) that is in very good agreement with the ratio of the numbers of deposited $C_2H_2^+$ ions of 1.00 : 0.83 : 0.50 evaluated from the measured currents and deposition times.

2.3 Spectroscopy Methods

2.3.1 Fourier-Transform Spectroscopy

Spectral analysis of absorption and emission characteristics of cryogenic matrices is carried out by means of the Fourier-Transform technique. Figure 2.7 shows a schematic drawing of the high resolution BRUKER IFS 120 HR Fourier-Transform Spectrometer, operating in a wide spectral range, which extends from middle infrared up to near UV. The computer-controlled optical bench of the spectrometer allows choosing between two different systems, LEYBOLD and APD equipped with 6 and 12 K cryostats. An internal compartment can be used for additional applications. Spectrometer control, acquisition and data processing are performed by means of a Pentium III computer system (Windows 2000) equipped with OPUS 4.0 (Bruker) software.

The core part of this type of spectrometers is a Michelson interferometer with a movable mirror. By scanning the movable mirror over some distance, an interference pattern is produced that encodes the spectrum of the source. The collimated light beam emitted or partially absorbed by a sample is directed through a selectable aperture to a beam splitter. In this way the interferometer produces and recombines two split light beams (wave trains) of equal intensity with a relative phase difference, depending on the movable mirror displacement x. Finally, the intensity of the infrared beam is detected, yielding maxima or minima of the signal depending on optical retardation of partial waves described by the relation: $2x = n\lambda$ ($n = 0, 1, 2,\ldots$). To control the mirror displacement x and optical path difference, a frequency-stabilized He-Ne laser is used. Both, the laser and the original light beam are coaxially aligned. The complete dependence of $I(x)$ on x is expressed by the cosine function:

$$I(x) = I_{HeNe} \cos(2\pi \tilde{\nu} x) \tag{2.2}$$

where I_{HeNe} is the intensity of He-Ne laser (at 15797.989 cm^{-1}) and $\tilde{\nu} = 1/\lambda$ is given in wavenumbers. The maximum optical path difference Δx_{max} of the beams in the interferometer, related to Δx, determines the maximum resolution which in our case (for $\Delta x_{max} = 6$ m) reaches:

$$\Delta \tilde{\nu} = \frac{1}{N\Delta x} = \frac{1}{\Delta x_{max}} = 0.00167\,\mathrm{cm}^{-1} \tag{2.3}$$

where N is a number of sampled points of the interferogram.

The source interferogram is digitized with 16 bit resolution at the zero crossings of the He-Ne laser interferogram (destructive interference). Procedure, in which the continuous interferogram $I(x)$ is sampled resulting in N discrete, equidistant points, requires replacements of the continuous variables x and $\tilde{\nu}$ by $n\Delta x$ and $k\Delta\tilde{\nu}$ ($k = 0, 1, 2,\ldots$), respectively, giving the relation for discrete Fourier transformation:

$$S(k\Delta\tilde{\nu}) = \sum_{n=0}^{N-1} I(n\Delta x) \exp\left(\frac{i2\pi\, n\, k}{N}\right) \tag{2.4}$$

The routine use of Fourier-Transform spectrometer in mid-infrared region is an effect of the replacement of the highly redundant Equation 2.4 with the Fast-Fourier-Transformation method (FFT), which substantially saves computer time [60]. As a result a spectrum in the range from 0 to $\tilde{\nu}_{\mathrm{HeNe}}$ = 15797.989 cm^{-1} is obtained. Extension to VIS–UV range, for which the sampling frequency is electronically doubled or quadruplicated by a phase-locked loop circuit. Spectroscopy of matrix-isolated species characterized by environmentally broadened lines allows to work with reduced resolution which is typically

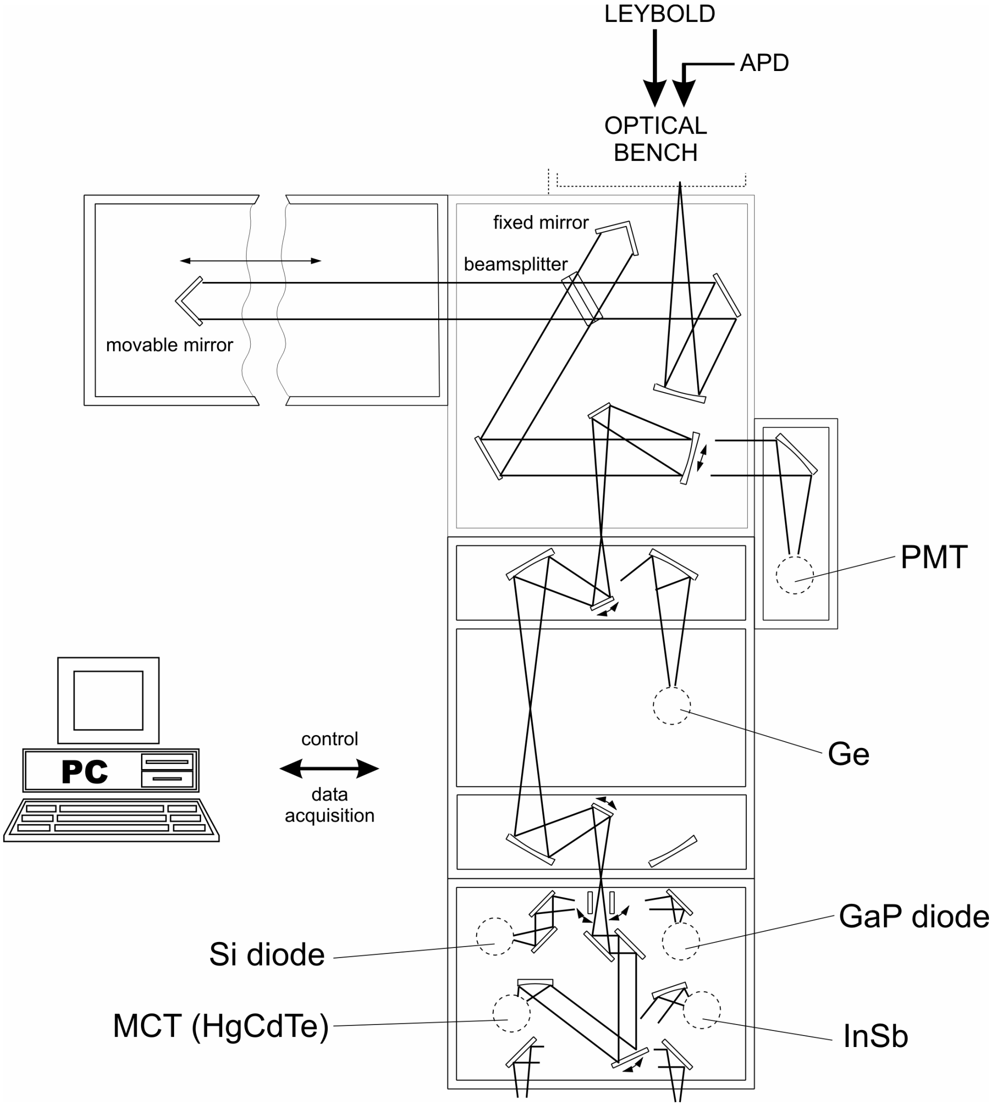

Figure 2.7. Schematic of high-resolution BRUKER IFS 120 HR Fourier-Transform Spectrometer equipped with six selectable detectors covering frequency range of 500 – 30000 cm^{-1}.

0.06 cm^{-1} for IR range and 0.1 – 1 cm^{-1} in VIS–UV region, resulting in shorter scan length and faster scanning. Typical scan times for BRUKER IFS 120 HR are 7.05 sec./scan for measurement with 0.06 cm^{-1} resolution (IR), and 3.96 sec./scan for 1 cm^{-1} resolution (VIS, UV).

Fourier-Transform spectrometers have several significant advantages over conventional, dispersive/grating instruments. The main of them include so-called Jacquinot, Fellgett and Connes advantages:

- Jacquinot – throughput advantage: circular apertures in FT spectrometers have a larger area than the linear slits of monochromators enabling higher throughput of irradiation and markedly better signal-to-noise (*S/N*) ratio;
- Fellgett – multiplex advantage: contrary to conventional method, the spectrum $S(\tilde{\nu})$ is measured simultaneously for all frequencies; considering $N = \tilde{\nu}_{\mathrm{HeNe}}/\Delta\tilde{\nu}$ as a number of frequencies per one interferogram point, *S/N* increases by factor of $\sqrt{N}$;
- Connes advantage: the sampling accuracy, between two zero crossings is determined by the precision of stabilized He-Ne laser (0.001 cm^{-1}) – built in wavenumber calibration.

2.3.2 Absorption Measurements

The entire spectral range for absorption measurement includes regions from middle infrared (MIR) up to UV – from 500 to 31500 cm^{-1} (20 µm – 317 nm). Sensitivity in a specific range depends on the used combination of a broadband light source, beamsplitter, detector and other optical elements like windows (mainly KCl and KBr) and mirrors. The sets of components of the BRUKER IFS 120 HR spectrometer which are usually used in our experiments for different spectral ranges are shown in Table 2.3.

The absorbance spectrum $A(\Delta\tilde{\nu})$ is obtained from the final transmittance spectrum $T(\Delta\tilde{\nu})$. The final transmittance spectrum is obtained from the ratio of the so-called single channel sample spectrum $S(\Delta\tilde{\nu})$ and previously measured single channel reference spectrum $R(\Delta\tilde{\nu})$:

$$A(\nu) = -\log T(\tilde{\nu}), \qquad \text{where:} \qquad T(\Delta\nu) = S(\Delta\tilde{\nu}) / R(\Delta\tilde{\nu}) \qquad (2.5)$$

The reference spectrum $R(\Delta\tilde{\nu})$ is the combined spectral response curve of light source,

Table 2.3 Combinations of light source, beamsplitter and detector used for absorption measurements with BRUKER IFS 120 HR spectrometer.

spectral region	light source	beamsplitter (substrate/coating)	detector	effective spectral range [cm^{-1}]
MIR	glowbar	KBr/Ge	MCT (LN-cooled)	500 – 4000
NIR	glowbar /tungsten lamp	CaF_2/Si	InSb (LN-cooled)	1800 – 15500
VIS	tungsten lamp	quartz/dielectric	Si diode	8000 – 25000
UV		quartz/Al	GaP diode	15800 – 31500

detector and all optical elements like windows, mirrors and filters. In view of the applied optics the main difference between $R(\Delta\tilde{\nu})$ taken for two experimental setups, is the reflectance characteristics of Ag/MgF_2 or Au coated copper substrates mounted on LEYBOLD cryotip and the transmittance characteristic of KCl window-substrate on APD. For mid-IR (MIR) and near-IR (NIR) spectral ranges one has to take into account the atmospheric conditions in the laboratory environment. In this case the background characteristics $R(\Delta\tilde{\nu})$ contain water vapors and CO_2 gas vibrational lines originating mainly from the non-evacuated compartments between cryostat chamber and spectrometer input window (purged with nitrogen continuously flowing through the boxes containing silica gel to absorb H_2O). These lines can appear as "negative" or "positive" with reference to the baseline and depend on the difference in water and carbon dioxide contents present in the atmosphere in the time when reference and sample single channel spectra were measured. A schematic drawing showing absorption measurement for both cryostat systems is presented in Figure 2.8.

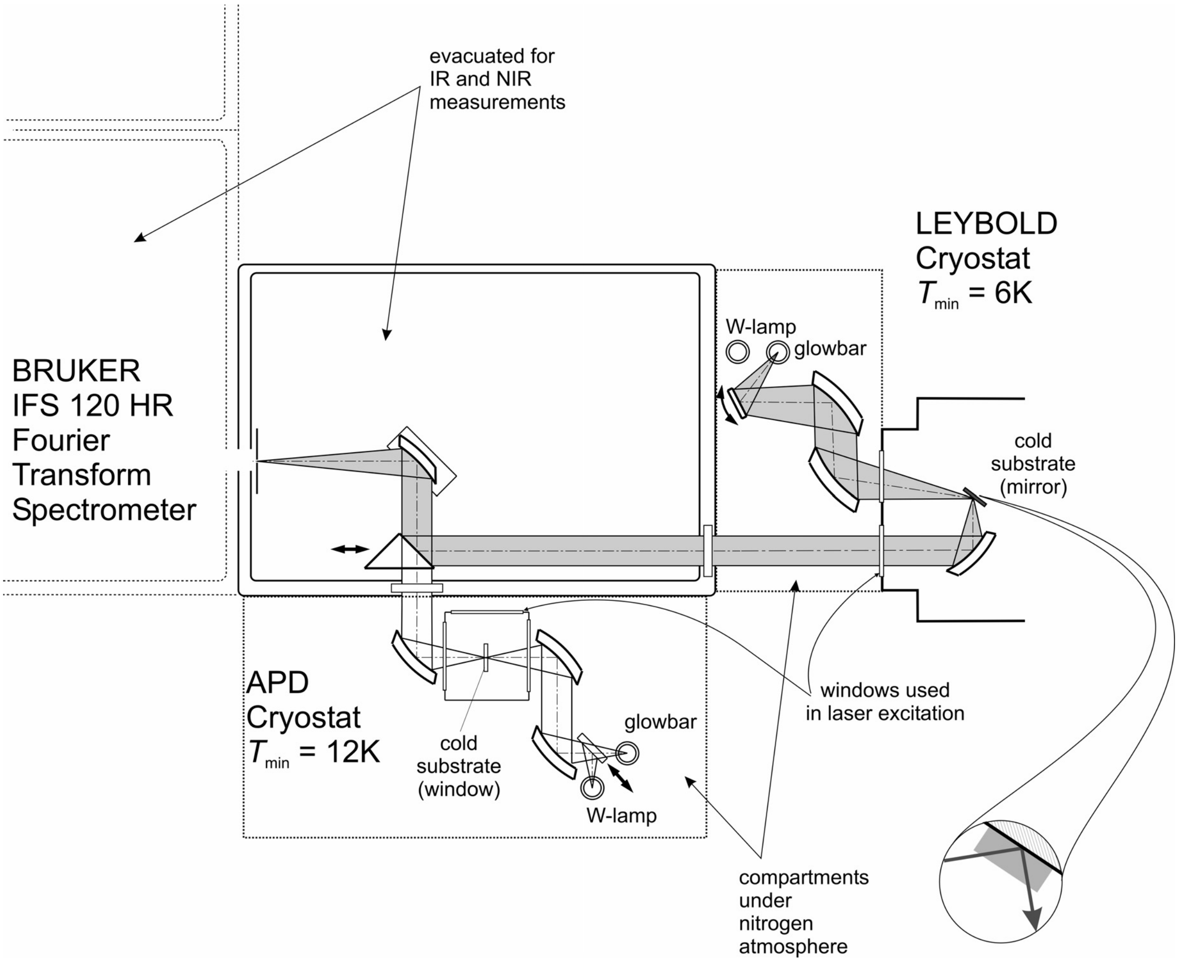

Figure 2.8. Schematic drawing of absorption measurement on Leybold and APD cryostat systems performed in reflection (expanded in the inset) and transmission modes, respectively. When deposition is finished, absorption measurements can be taken after rotation of the substrates (cold heads) for 120º – LEYBOLD and 90º – APD to the position shown above. Flipping mirrors allow selection between the globar and tungsten light sources. The optical path for the substrate mounted on the LEYBOLD cryotip is shaded grey.

2.3.3 Emission Measurements: Laser Spectroscopy Methods

In the spectral region from NIR to UV, which involves transitions between electronic states of molecules, there is a number of complementary, highly sensitive laser-based methods available. Apart from absorption spectroscopy using broadband light sources like a globar or a tungsten lamp, use of the lasers provides powerful tools. Two most commonly used techniques were applied in this work:

- laser excitation technique — based on measurement of a total yield of emission by scanning through an entire excitation region,
- laser-induced fluorescence (LIF) — based on measurement of a spectrally resolved emission (using FT spectrometer) upon a selective excitation.

The list of laser sources used for experiments presented in this work is shown in Table 2.4.

Table 2.4 Laser systems used in laser excitation and LIF experiments.

laser/active medium	pumping source	emission range	
		λ [nm]	ν [cm^{-1}]
ring dye laser/stilbene 3	Ar$^+$ laser: multi-UV mode	465 – 410	21500 – 24400
dye laser/rhodamine 6G	Ar$^+$ laser: multi-VIS mode	625 – 568	16000 – 17600
Ar$^+$ laser: multi-UV mode	—	363.8 – 333.6	27488 – 29976
Ar$^+$ laser: multi-VIS mode	—	514.5 – 457.9	19436 – 21839
Ar$^+$ laser: VIS single line			

Table 2.5 Combinations of light source, beamsplitter and detector used for emission measurements with BRUKER IFS 120 HR spectrometer.

spectral region	beamsplitter (substrate/coating)	detector	effective spectral range [cm^{-1}]
NIR/VIS	CaF$_2$/Si	Ge (LN-cooled)	4000 – 15000
VIS/UV	quartz/dielectric quartz/Al	PMT	8000 – 30000

Since most of the electronically excited states are characterized by short life-times for spontaneous emission, quantum efficiency reaches in many cases 100%. For the emission signal a high sensitivity detectors are used: photomultiplier (PMT) for VIS – UV range and liquid nitrogen cooled germanium (Ge) detector in NIR – VIS, see Table 2.5.

Laser Excitation Technique

The laser excitation method allows reaching extremely high sensitivity of absorption measurements by recording a total yield of emitted photons from fluorescing molecules excited with a laser beam. In fact, it is an extremely sensitive alternative for absorption spectroscopy based on measurement of a total yield of emitted photons by scanning through an entire excitation region. Significant improvement in S/N ratio is achieved by the high power in very narrow frequency range (monochromatic light) aided by so-called lock-in technique. This method is particularly useful for measurements with very low concentrations of matrix-isolated species, for which the sensitivity of traditional absorption technique turns out to be insufficient. In this case sensitivity increases even up to four orders of magnitude. It should be noticed, that although the laser excitation spectra can reproduce absorption spectra with respect to the position (frequency) of the lines, the relative intensities are alike only for the following conditions [61]:

- quantum efficiency must be equal for all excited states;
- quantum efficiency of detector must be constant for entire measurement range or must be compensated by multiplication by spectral response curve;
- spatial distribution of photons emitted form the sample as a fluorescence must be isotropic.

In this type of experiment matrix sample is irradiated using a tunable laser as shown in Figure 2.9. The laser frequency is tuned by the stepper motor turning a three-plate birefringent filter while recording the spectra. Since the dye lasers exhibit significant fluctuations in the beam intensity, it needs to be stabilized at the some expense of the output power. The intensity stabilized laser output is first modulated at 1.4 kHz by a chopper, transmitted through the fiber optics and then focused onto the sample. The fluorescence collected by a parabolic mirror is directed via suitable optical filters to eliminate or reduce the scattered laser light to the PMT or Ge detector. The signal from the detector is filtered in the interesting frequency range by a lock-in amplifier, which uses the reference signal from the chopper. The resulting frequency band-width is approximately 1 Hz, eliminating most of the broadband 1/*f* noise.

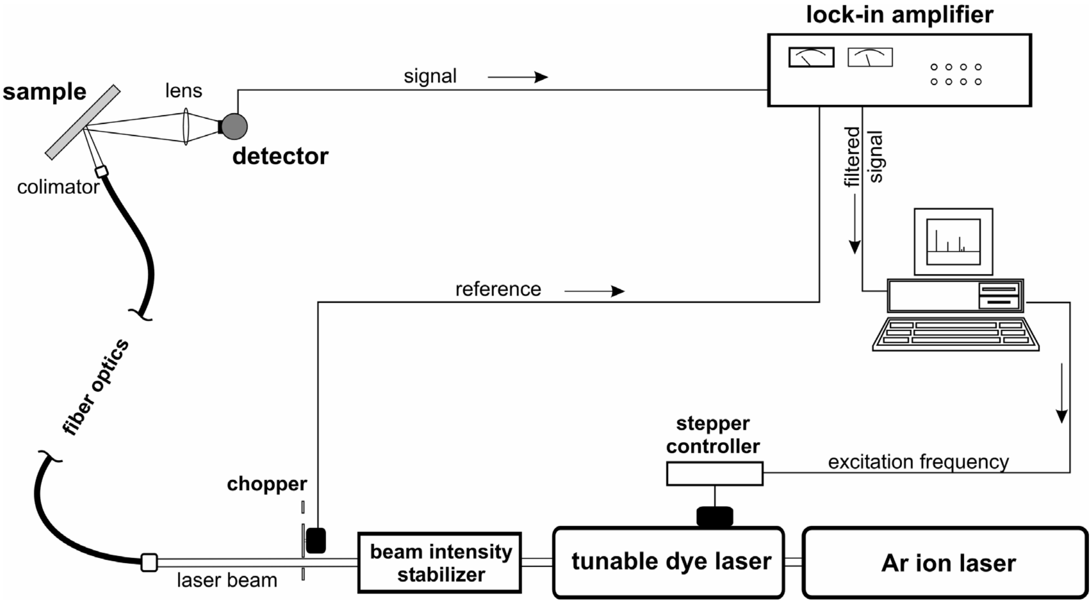

Figure 2.9. Experimental setup for measurement of laser excitation spectra.

Laser-Induced Fluorescence

Laser-induced fluorescence (LIF) technique is based on measurement of spectrally resolved emission from samples selectively excited with laser. In comparison with broadband excitation of polyatomic molecules, a laser source provides a selective excitation which makes the obtained spectra much easier to interpret. Moreover, with high intensities of laser lines one can reach much higher populations of excited states resulting in higher fluorescence intensities. Thus one can observe electronic transitions characterized by low values of Franck-Condon factors. Although in case of the LIF technique the use of single-mode (longitudinal) lasers is more advantageous, the application of multimode lasers is also possible. In most cases, especially in matrix-isolation spectroscopy applications, a jitter of frequency of the beam emitted by the laser is negligible in comparison with absorption line-width, and frequency stabilization is not needed.

2.4 Activation Spectroscopy Methods

2.4.1 Sample Deposition and Charge Center Generation

In a typical experiment the sample is grown from high purity rare gases, in this work neon and argon (99.999%). In case of using dopants their concentrations are estimated from partial pressures in premixed gas samples. All experiments were performed on the LEYBOLD system using the same cryostat chamber arrangement as for mass-selected ions deposition assuring convenient switching between those two experiments.

Samples are deposited onto a solid metal substrate, a gold-coated copper mirror. In earlier experiments the copper substrate was covered by silver and over-coated by very thin insulator layer (MgF_2), but measurements show no difference in yield of electrons emitted from the sample. Continuous deposition of neon at the minimal reachable temperature of 6 K results in transparent films and does not reveal strong dependence on base pressure in the vacuum chamber. Unlike neon deposits, using a pulsed valve for argon samples results in a better optical quality for lower temperatures, but it was found that transparent argon films can be easily obtained from continuous deposition started at a relatively high temperature of 60 – 70 K. A soft sub-layer built at higher temperature fills in micro-pores, scratches or imperfections of the substrate surface, preparing a "smooth" basis for incoming new argon atoms. Practically, in this case the heater is switched off right after the valve is opened and gas starts to flow towards the substrate. The cryostat reaches minimal temperature within a few minutes.

The thickness of solidified rare gas films was estimated from the pressure drop in the known volume of the gas container by the assumption that the sticking coefficient was close to unity. Although such an assumption gave rather approximate values for neon layers for which the pressure monitored during deposition was in the range of $2 – 6 \times 10^{-6}$ mbar, its accuracy is sufficient from the point of view of the presented discussion. The base pressure with cryo-pumping reaches $6 – 8 \times 10^{-8}$ mbar already at $T = 60$ K (argon experiments) and does not change appreciably when the cryostat approaches minimum temperature.

Low energy electrons emanating from a heated tungsten filament, maintained at a constant negative potential — in the range from -100 to -600 V with respect to the grounded substrate — are used for efficient ionization of the sample. Sample preparation is shown schematically in Figure 2.10. As it was already described the filament is mounted off the axis of the ion beam in case of mass-selected deposition and at a distance of a few centimeters away from the substrate surface. The electrons are “sprayed” from the filament and deflected by a cylindrical electrostatic lens (*L3* – tube-shaped ion lens) towards the sample. *L3* is located at about 5 cm distance from the substrate and held at higher negative potential than the filament. Consequently, as it is seen from substrate–filament–*L3* geometry, the energy of electrons in the “beam” is slightly higher than the potential difference between the filament and the substrate.

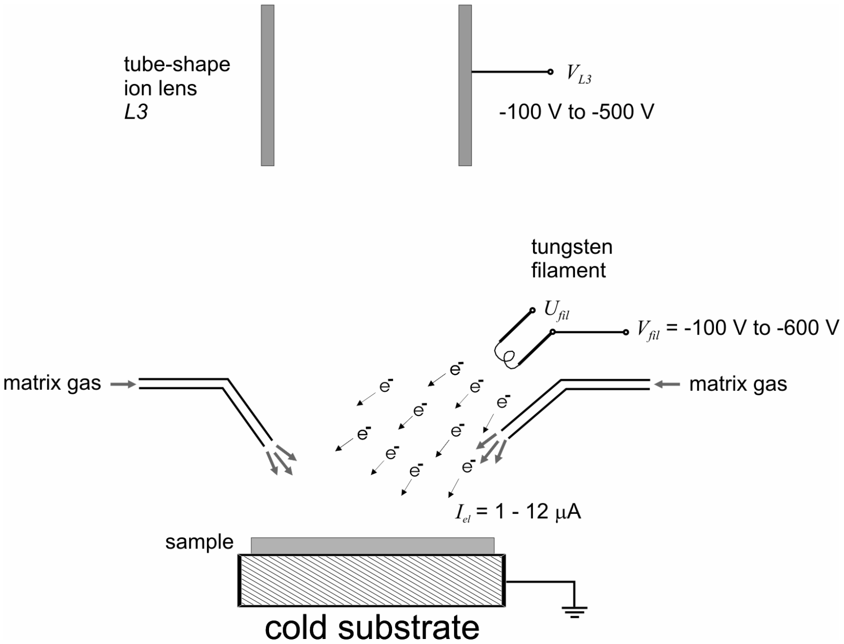

Figure 2.10. Schematic drawing of the sample preparation process: Ne or Ar matrix gas is solidified onto the metal substrate and irradiated by electrons emanating from the heated filament either during or after the deposition. Negative potentials applied to the filament and tube ion lens accelerate and deflects electrons towards the sample.

Charged centers are generated in two ways:

(i) by deposition of the gas under electron bombardment

(ii) by irradiation of the sample after deposition is completed

Technique (i) allows for efficient generation of charged centers across the whole solid through the deposition of electrons layer by layer. Relatively slow electrons are used in this technique, for which the filament potential V_{fil} is typically set between -110 to -130 V with fixed *L3* voltage at -200 V. The intensity of the electron current can be additionally adjusted to some extent by changing the heating voltage of the tungsten filament (U_{fil} = 1.2 –1.8 V). The obtained electron current can be changed in the range from 1 to 12 μA (with an estimated electron density in the range of 0.2 – 2.4 μA/cm^2).

The thickness of the subsurface layer containing charged centers as well as their density obviously depend on the energy of the accelerated electrons. Thus, the second (ii) approach requires higher V_{fil} potential up to 600 V. However, the obtained current density is limited by the used filament type and does not significantly exceed that in technique (i). The trace amounts of nitrogen or oxygen in the solid sample allowed determining the optimum set of V_{fil} and V_{L3} potentials by means of a well visible luminescence spot centered in the middle of the substrate, see Figure 2.11. The experiments with variable irradiation times revealed that ionization can be completed in 15 to 20 minutes after which one seemingly reaches saturation by charging the sample to the potential of the filament.

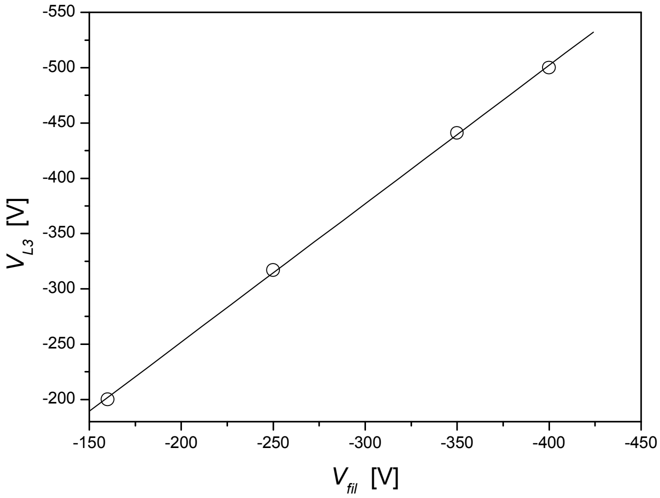

Figure 2.11. Optimized V_{fil} and V_{L3} potentials for maximum electron density.

2.4.2 Electron Current Measurement

The double-side/Au-coated removable Faraday plate serves as universal current detector, which allows measurements of the current intensities of both the electron beam used in irradiation (*F2*, as in case of mass-selected ion deposition) and the emitted exoelectrons (see Figure 2.12). The Faraday plate is inserted parallel to the matrix and about 5 mm above its surface, either to allow detection of any exoelectron emanating from the sample (after completed sample deposition) or to measure the filament current before irradiation is started. During the exoelectron measurements, the Faraday plate is held under a positive potential of $V_F = +9$ V with respect to the grounded substrate. Indeed, it was found that this value seems to be close to optimal for registration of thermally stimulated currents (TSEE) from neon and argon solids. For some experiments variable potentials were applied. Using a Femto DLPCA 100 low noise current amplifier the intensity of the electron current can be measured in a wide range, covering several orders of magnitude. The signal from the amplifier is sampled by an A/D-converter at a rate of ~ 0.9 Hz. With this rate each curve-point is measured 20 times and then averaged. The estimated efficiency of exoelectrons yield in terms of number of deposited electrons is rather low and does not exceed 0.01%.

A different approach has been applied in measurements of photon stimulated exoelectrons (PSEE), schematically shown in lower part of the Figure 2.12. In this case our experimental setup does not allow using closely placed Faraday plate which would effectively conceal the substrate from the exciting laser beam. Instead, photoelectrons emitted from the solid under laser irradiation are efficiently collected by the tube-shape lens *L3* at $V_{L3} = +18$ V.

Recording of TSEE currents is realized by means of a Leybold LTC 60 programmable temperature controller. Through a diode sensor located at the bottom of the cryotip, the controller regulates the voltage of the heater until the temperature readout reaches the desired value. Linear heating characteristic allows to synchronize the controller with the PC acquisitions system and perform continuous measurements with a different rate of temperature raise. The same system facilitates multi-step experiments and recording of the stepwise isothermal exoelectron emission decay.

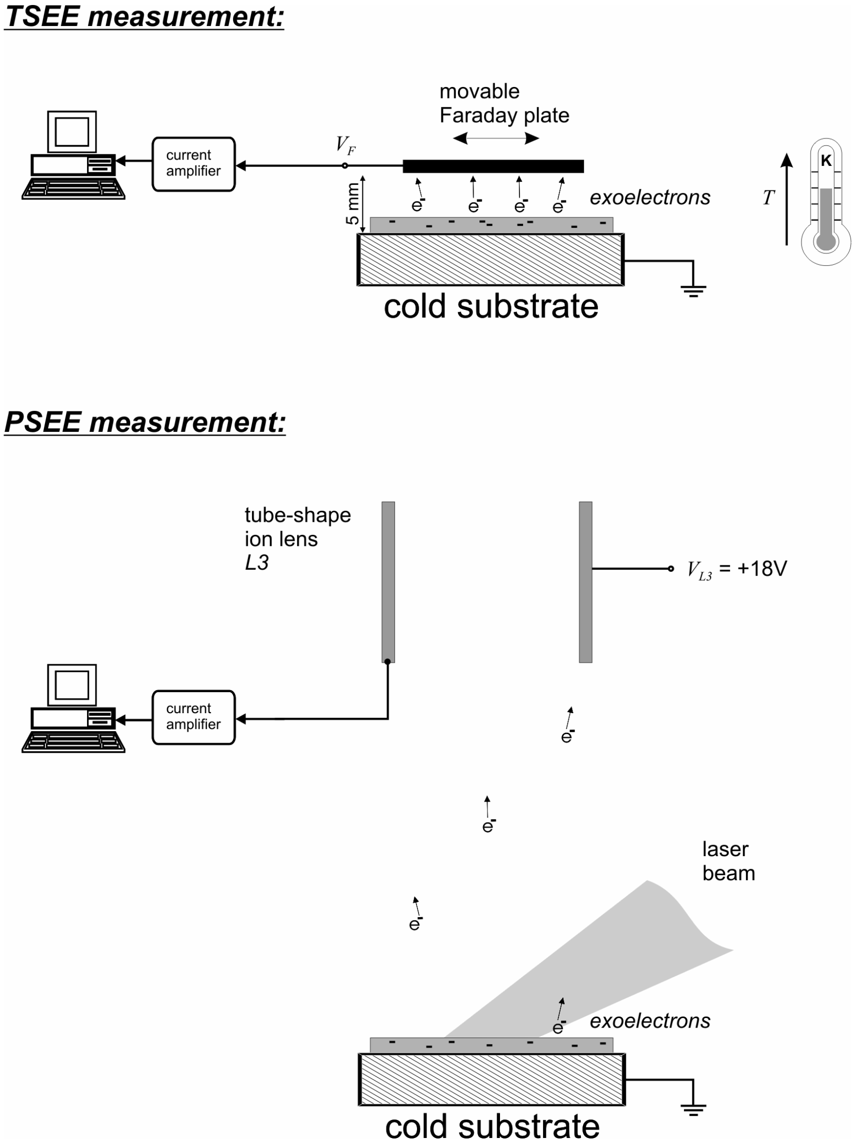

TSEE measurement:

PSEE measurement:

Figure 2.12. Measurement of the exoelectron current: upper part — *Thermally Stimulated Exoelectron Emission* induced by linear heating of the sample is recorded by a closely placed Faraday plate held under positive potential, typically set at V_F = +9 V; lower part — focused laser beam induces *Photon Stimulated Exoelectron Emission* with tube-shape ion lens at +18 V used as current detector. Signal amplified by high sensitivity current amplifier (gain 10^9 V/A) is digitized by the A/D converter on PC and averaged from 20 scans per each curve-point.

The precision of the registration of the exoelectron current curve depends primarily on three factors:

- accuracy of the temperature measurements (estimated as ±0.2 K) determined by averaging of the readouts from two temperature sensors mounted at the top and at the bottom of the substrate holder
- influence of the nonlinearities in the temperature increase
- fluctuations of the temperature — cryostat “breathing” (see Figure 2.13)

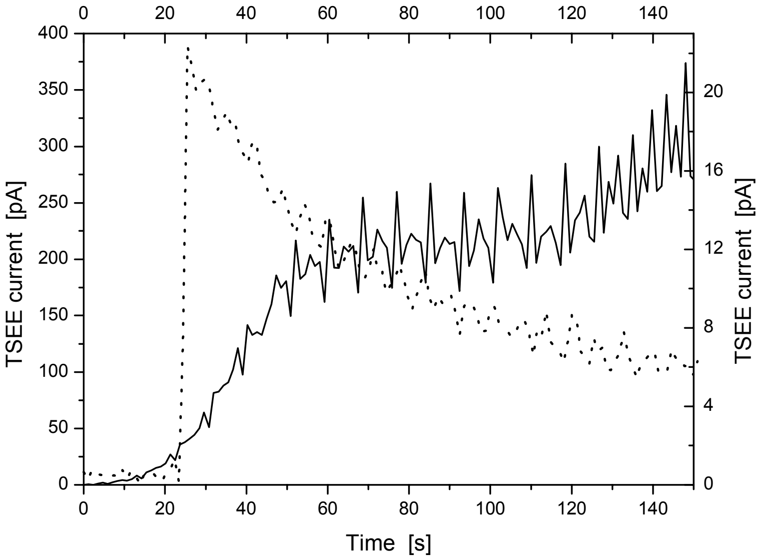

Figure 2.13. Periodical fluctuation of the exoelectron current steaming from the cooling cycles of the refrigerator (“breathing”). Signal was recorded from a nominally pure Ne sample pre-irradiated by electrons: TSEE recorded upon heating with the rate 2 K/min. (solid curve) and isothermal decay at $T = 7$ K (dot curve).

2.5 Quantum Chemical Computations

Theoretical computations of molecular structure and molecular spectra are nowadays no longer reserved for specialists. The available programs allow, in a convenient and easy way, to formulate the needed input and to obtain information about the electronic structure, geometry, and infrared spectroscopy of the species of interest, which is routinely applied in the interpretation of experimental results.

2.5.1 Density Functional Theory and Hybrid Methods

In the last decade, the Density Functional Theory (DFT) developed into a cost effective alternative to correlated *ab initio* methods. In principle, DFT is a theory of ground state electronic structure, expressed in terms of the electronic density distribution $\rho(\vec{r})$. It appeared very useful for the understanding and calculation of the ground state density and energy of molecules, clusters, and solids with or without static perturbations. It is an alternative and complementary approach to the traditional methods of quantum chemistry which are formulated in terms of the many-electron wave function $\Psi(\vec{r}_1,\vec{r}_2,...,\vec{r}_n)$ [62]. *Hohenberg* and *Kohn* [63,64] have shown that, without explicit knowledge of the electronic wave function, the total energy E of an *n* electron system can be expressed as a functional of its electron density $\rho(\vec{r})$. Usually, the total energy is partitioned in the following form [65]:

$$E(\rho) = E^T(\rho) + E^V(\rho) + E^J(\rho) + E^{XC}(\rho) \tag{2.6}$$

where E^T is the kinetic energy of the electrons, E^V the sum of the Coulombic repulsion energy between the atomic nuclei and the attractive Coulombic interaction of the positive nuclei with the negative electron density, E^J the Coulombic repulsion energy between the electrons (Coulombic self-interaction of the electron density), and E^{XC} the exchange-correlation term. $E^T + E^V + E^J$ is the classical, i.e. non-quantum mechanical contribution to the energy, and each contribution can be expressed analytically. However, no analytical expression exists for the exchange-correlation term E^{XC}. *Hohenberg* and *Kohn* [63] state that the energy is determined by the electron density of the system. If $E(\rho)$ is taken as the exact total energy, Equation 2.6 can be regarded as a definition of E^{XC}. The difficulty in the application of density functional theory to chemical problems lies in finding a physically reasonable analytic expression, which is a good approximation for E^{XC}, the exact exchange.

A common approach, incorporated in commercial program packages such as *Gaussian 98* [66], is to approximate E^{XC} as an integral of the spin densities and gradients [65]:

$$E^{XC}(\rho) = \int f(\rho_\alpha(\vec{r}), \rho_\beta(\vec{r}), \nabla\rho_\alpha(\vec{r}), \nabla\rho_\beta(\vec{r}))d^3\vec{r} \qquad (2.7)$$

$\rho = \rho_\alpha + \rho_\beta$ denotes the total electron density composed of the α (spin ↑) and β (spin ↓) spin densities. E^{XC} is then further split up into contributions of same-spin and mixed-spin interactions, which define the terms exchange functional E^X and correlation functional E^C, respectively:

$$E^{XC}(\rho) = E^X(\rho) + E^C(\rho) \qquad (2.8)$$

Functionals which only depend on the electron density ρ are called *local*, while functionals of the electron density ρ and of its gradient $\nabla\rho$ are called *non-local* or *gradient-corrected*. In the development of density funtionals for the calculation of isolated molecules, gradually more refined functionals emerged. The basic local exchange funtional called $E^X{}_{LDA}$ is defined as:

$$E^X_{LDA} = -\frac{3}{2}(\frac{3}{4\pi})^{\frac{1}{3}} \int \rho^{\frac{4}{3}} d^3\vec{r} \qquad (2.9)$$

This functional was developed as the exchange energy of a uniform electron gas [62] Application to molecules and molecular systems, however, leads to significant errors. Therefore, gradient-corrections were introduced, of which the most widely used is the one developed by *Becke* in 1988 [67]. The gradient corrected exchange functional is known as the Becke88 functional, and as “B” part of the method acronyms in *Gaussian 98*:

$$E^X_{Becke88} = E^X_{LDA} - \gamma \int \frac{\rho^4 \left|\nabla\rho\right|^2}{1 + 6\gamma \sinh^{-1}(\rho^{\frac{4}{3}} \left|\nabla\rho\right|)} d^3\vec{r} \tag{2.10}$$

γ is a parameter fitted to the exchange energies of rare gas atoms, and amounts to 0.0042 Hartrees according to Becke. Similarly, various local and gradient-corrected correlation functionals are in use, of which the VWN3 [68] local correlation functional and the Perdew-Wang PW91 [69] and Lee-Yang-Parr LYP [70] gradient corrections are most popular.

DFT methods are sufficiently accurate for certain kinds of molecules, but may lead to significant errors for others, for which Hartree-Fock based methods sometimes seem to be superior. To find density functionals that are reliably applicable to a large variety of species, Becke introduced a Hartree-Fock admixture into his exchange functional, and applied a fit procedure in order to derive the ideal contribution of several exchange and correlation functionals. The result is by now the widely used B3LYP [71] functional:

$$E^{XC}_{B3LYP} = (1 - c_0)E^X_{LDA} + c_0 E^X_{HF} + c_X \Delta E^X_{B88} + (1 - c_C)E^C_{VWN3} + c_C E^C_{LYP} \tag{2.11}$$

The parameter c_0 allows any combination of LDA and Hartree-Fock local exchange, with the gradient correction part of the Becke88 functional, ΔE^X_{B88}, scaled by c_X. As correlation functional, a mixture of the local VWN3 and the gradient-corrected LYP functional are used, determined by the parameter c_C. The constants c_0, c_X, and c_C are those determined by Becke by fitting to the 56 atomization energies, 42 ionization potentials, 8 proton affinities, and 10 first-row atomic energies in the G1 molecule set, [71-73] obtaining values of $c_0 = 0.20$, c_X=0.72, and c_C=0.81. However, Becke used the PW91 functional instead of VWN3 and LYP. The applicability of the same fit parameters to different functionals illustrates that this approach is physically justified.

2.5.2 Basis Functions and Basis Sets

To calculate the energy $E[\rho(\vec{r})]$ of a given molecule, a self-consistent field approach is used. Starting with a reasonable guess for the electron density $\rho(\vec{r})$, the energy is calculated. According to the variation principle, the lowest energy is obtained from the physically correct function $\rho(\vec{r})$. In every iteration step, $\rho(\vec{r})$ is modified to lower the energy, until a stationary state is reached. This is determined by the convergence criterion, which is fulfilled when the energy difference between two subsequent iterations is smaller than a pre-chosen cutoff value. To make the formalism of electron density capable for computers, it is useful to express $\rho(\vec{r})$ by a set of molecular orbital wave functions $\phi_i(\vec{r})$, which are linear combinations of a set of N fixed functions $\chi_\mu(\vec{r})$, the *basis functions* [65]:

$$\phi_i(\vec{r}) = \sum_{\mu=1}^{N} c_{\mu i}\chi_\mu(\vec{r}) \tag{2.12}$$

In a closed-shell n electron system, the total wavefunction $\Psi(\vec{r})$ can be constructed from the n/2 molecular orbitals $\phi_i(\vec{r})$ and α and β spin functions. With $\rho(\vec{r}) = \left|\Psi(\vec{r})\right|^2$, the functional $E[\rho(\vec{r})]$ becomes a function of the (N×n/2) parameters $c_{\mu i}$, $E[\rho(\vec{r})] = E(c_{\mu i})$.

Introducing the functions $\chi_\mu(\vec{r})$ makes evaluation of the density functionals feasible. It introduces, however, constraints on the electron density $\rho(\vec{r})$, as the total wavefunction $\Psi(\vec{r})$ is composed of the fixed functions $\chi_\mu(\vec{r})$. This is a significant source of error in the calculated energies. It can, however, be minimized by choosing physically reasonable functions $\chi_\mu(\vec{r})$, and by providing a large enough number N of these functions, which gives back to the electron density $\rho(\vec{r})$ some of its initial flexibility.

Gaussian 98, as well as most other quantum chemical packages, employ atom-centered gaussian-type atomic functions $g(\alpha,\vec{r})$, the *primitive gaussians* [65]

$$g(\alpha,\vec{r}) = cx^n y^m z^l e^{-\alpha\vec{r}^2} \tag{2.13}$$

The radial extent of the function is determined by α, and the powers of x, y, z determine the spatial symmetry of g. The constant c ensures normalization.

An actual basis function is composed of several primitive gaussians, leading to *contracted gaussians* χ_μ:

$$\chi_\mu = \sum_p d_{\mu p} g_p \tag{2.14}$$

$d_{\mu p}$ are fixed constants within a given basis function. A set of basis functions that describes the orbitals of an atom is called basis set. Standard basis sets for most elements are available via the basis set library of *Gaussian 98*. Alternatively, the coefficients $d_{\mu p}$ and exponents α_p can be defined by the user.

2.5.3 Vibrational Frequency Calculation

Compared to conventional *ab initio* methods that include electron correlation (for instance MP2), the superior performance and cost-effectiveness of DFT are particularly desirable for larger molecules. The performance of five functional methods, SVWN, BLYP, BVWN, B3LYP, B3P86 used for calculations of vibrational frequencies and zero-point energies has been studied on large set, mainly carbon-containing molecules by *Wong* [74] and continued later by *Halls* and coworkers [75]. The hybrid DFT methods were concluded to be most reliable for the prediction of vibrational harmonic frequencies in agreement with experimental fundamentals. Scaling factors, compensating the anharmonicity of vibrational modes have also been found. In general, tests of this nature have confirmed that the methods employed can yield and predict not only frequencies but also their intensities with usable accuracy. Although computed intensities can not be taken too literally, their relative values may be reliably compared [65].

Studies of unsaturated hydrocarbons, their nitriles and similar species, being of particular interest in this work, were carried out by *Lee* [76,77]. This resulted in evaluation of scaling factors in the range of 0.96 – 0.98. The particular value depends on the vibrational mode of the molecule (e.g. stretching or bending vibration) to which certain factor is applied. These factors are consistent with data obtained recently by our group, for the B3LYP method applied to cyanoacetylene ion [78] and tetracyanoethylene cation and its cationic fragments [79]. These results show that scaling factor of ~ 0.96 is also valid for cationic species trapped in neon matrix.

For all infrared spectra calculated in this work, the *Gaussian 98* [43] suite of programs has been employed. All computations were carried out on a dual Pentium-III PC with 1 GB of RAM and Linux operating system.

References

[1] E. Whittle, D.A. Dows, G.C. Pimentel, *J. Chem. Phys.* **22**, 1943 (1954).

[2] V.E. Bondybey, T.A. Miller, Vibronic Spectroscopy and Photophysics of Molecular Ions in Low Temperature Matrices in T.A. Miller, V.E. Bondybey, eds. Molecular Ions: Spectroscopy, Structure and Chemistry; North Holland, Amsterdam, 1983.

[3] L. Andrews, M. Moskovits, ed., *Chemistry and Physics of Matrix-isolated Species*; North Holland: Amsterdam, 1989.

[4] V.E. Bondybey, A.M. Smith, J. Agreiter, *Chem. Rev.* **96**, 2113 (1996).

[5] V.E. Bondybey, M. Räsäanen, A. Lammers, *Ann. Rep. Prog. Chem., Sect. C* **95**, 331 (1999).

[6] M.E. Jacox, *Chem. Phys.*, **189**, 149 (1994).

[7] B. Meyer, *Low Temperature Spectroscopy*, American Elsevier Publishing Company, New York, 1971.

[8] V.E. Bondybey, A. Nitzan, *Phys. Rev. Lett.* **38**, 889 **(**1977).

[9] C. Crepin, A. Tramer, *Chem. Phys. Lett.* **170**, 446 (1990).

[10] H. J. Jodl in *Chemistry and Physics of Matrix-Isolated Species*; L. Andrews, M. Moskovits, eds., North Holland: Amsterdam, 1989.

[11] V.E Bondybey, L. E Brus, *Nonradiative Processes In Small Molecules In Low-Temperature Solids* in *Advances in Chemical Physics*, vol. 41, ed. R. Prigogine, S.A. Rice, John Wiley & Sons, New York, 1980.

[12] J.J. Linevsky, *J. Chem. Phys.* **38**, 658 (1963).

[13] M.L. Klein, J.A. Venables, eds. *Rare Gas Solids,* vol. 1, Academic Press, New York, 1976.

[14] K. Rebane, *Impurity Spectra of Solids*, Plenum, New York, 1970.

[15] K. Rebane, *Chem. Phys.*, **189**, 139 (1994).

[16] A. Gedanken, B. Raz, J. Jortner, *J. Chem. Phys.* **58**, 1178 (1973).

[17] G.W. Robinson, M.McCarthy, Jr., *J. Chem. Phys.* **30**, 999 (1959).

[18] R.L. Redington, D.E. Miligan, *J. Chem. Phys.* **39**, 1276 (1963).

[19] L. Andrews, *Annu. Rev. Phys. Chem.* **22**, 109 (1971).

[20] M.E. Jacox, D.E. Miligan, *J. Chem. Phys.* **54**, 3935 (1971).

[21] F.T. Prochaska, L. Andrews, *J. Am. Chem. Soc.* **100**, 2102 (1978).

[22] D.E. Miligan, M.E. Jacox, *J. Chem. Phys.* **48**, 2265 (1968).

[23] L. Andrews, *Annu. Rev. Phys. Chem.* **30**, 79 (1979).

[24] F. Legay, *Chemical and Biological Applications of Lasers*, Academic Press, New York, 1976.

[25] L. E. Brus and V. E. Bondybey, in *Radiationless Transitions*, ed. S. H. Lin, Academic Press, New York, 1980.

[26] H. Dubost and F. Legay in *Chemistry and Physics of Matrix-isolated Species*; L. Andrews, M. Moskovits, eds., North Holland: Amsterdam, 1989.

[27] H. Dubost, *J. Low Temp. Phys.* **111**, 615 (1998).

[28] K.S. Song and R.T. Williams, *Self-Trapped Excitons*, Springer Series in Solid State Science, vol. 105, ed. M. Cardona, Springer-Verlag, Berlin, 1996.

[29] J.A. Venables, B.L. Smith in *Rare Gas Solids,* ed. M.L. Klein, J.A. Venables, vol. 2, Academic, London, 1977.

[30] Chun-rong Fu and K.S. Song, *J. Phys.: Condens. Matter* **9**, 9785 (1997).

[31] E.V. Savchenko, A.N. Ogurtsov, O.N. Grigorashchenko, S.A. Gubin, *Chem.Phys.* **189**, 415 (1994).

[32] I.Ya. Fugol', *Advan. Phys.* **37** (1988) l.

[33] N. Schwentner, E.-E. Koch, J. Jortner, *Electronic Excitation In Condensed Rare Gases*, Springer, Berlin, 1985.

[34] G. Zimmerer, *Excited State Spectroscopy In Solids*, NorthHolland, Amsterdam, 1987.

[35] E.V. Savchenko, A.N. Ogurtsov, O.N. Grigorashchenko, *Phys. Solid State* **40**, 831 (1998).

[36] LYa. Fugol', A.N. Ogurtsov, O.N. Grigorashchenko and E.V. Savchenko, *Sov. J. Low Temp. Phys.* **18**, **27** (1992).

[37] M. Lannoo, J.C. Bourgoin, *Point Defects in Semiconductors II: Experimental Aspects*, Springer Series in Solid-State Sciences, vol. 35, Springer, Berlin 1983.

[38] D.R. Vij, in *Luminescence of Solids*, D.R. Vij, ed., Plenum Press, New York (1998).

[39] M. Kirm and H. Niedrais, *J. Luminesc.* **60-61**, 611 (1994).

[40] A.N. Ogurtsov, E.V. Savchenko, O.N. Grigorashchenko, S.A. Gubin, I.Ya. Fugol', *Low Temp. Phys.* **22**, 922 (1996).

[41] M. Kink, R. Kink, V. Kisand, J. Maksimov, and M. Selg, *Nucl. Instrum. Methods Phys. Res. B* **122**, 668 (1997).

[42] M.E. Fajardo and V.A. Apkarian, *J. Chem. Phys.* **89**, 4124 (1988).

[43] A.V. Danilychev and V. A. Apkarian, *J. Chem Phys.* **99**, 8617 (1993).

[44] R. Dersch, B. Herkert, M. Witt, H.-J. Stockmann, and H. Ackermann, *Z. Phys. B: Condens. Matter* **80**, **39** (1990).

[45] A. Schrimpf, C. Boekstiegel, H.-J. Stockman, T. Bornemann, K. Ibbeken, J. Kraft, and B. Herkert, *J. Phys.: Condens. Matter* **8**, 3677 (1996).

[46] J. Becker, O.N. Grigorashchenko, A.N. Ogurtsov, M. Runne, E.V. Savchenko, and G. Zimmerer, *J. Phys. D: Appl. Phys.* **31**, 749 (1998).

[47] L. Khriachtchev, M. Pettersson, S. Pehkonen, E. Isoniemi, and M. Räsänen, *J. Chem. Phys.* **111**, 1650 (1999).

[48] I.R. Dunkin, *Matrix-isolation techniques*, *A practical approach*, Oxford University Press, New York, 1998.

[49] A. Thoma, B.E. Wurfel,R. Schlachta, G.M. Lask and V.E. Bondybey, *J. Phys. Chem.* **96**, 7231 (1992).

[50] Ch. Dass, *Principles and practice of biological mass spectrometry,* A John Willey & Sons, Inc., 2001

[51] M.S.B. Munson, F.H. Field, *J. Am. Chem. Soc.* **88**, 2621 (1966).

[52] M. Lorenz, PhD's thesis, Technische Universität München, 2000.

[53] P.H. Dawson, *Quadrupole Mass Spectrometry and its Applications*, Elsevier, Amsterdam, 1976.

[54] H. J. Jodl, *Solid aspects of matrices* in L. Andrews and M. Moskovits *Chemistry and Physics of Matrix-Isolated Species* North-Holland, Amsterdam Oxford New York Tokyo, 1989.

[55] J. T. Godhout, T. M. Halasinski, G. E. Leroi, J. Allison, *J. Phys. Chem.* **100**, 2892 (1996).

[56] S. Fedrigo and W. Harbich and J. Buttet, *Phys. Rev. B: Condens. Matter Mater. Phys.* **58**, 7428 (1998).

[57] J. C. Rivoal, C. Grisolia, J. Lignieres, D. Kreisle, P. Fayet, L. Wöste, *Z. Phys. D* **12**, 481 (1989).

[58] V.E. Bondybey and M. Lorenz, *J. Low. Temp. Phys.* **122**, 509 (2001).

[59] V.E. Bondybey and T.A. Miller, J. Chem. Phys. **73**, 3035 (1980).

[60] W. Herres, J. Gronholz, Understanding FT-IR Data. Part 1: Data acquisition and Fourier transformation. Computer Applications in the Laboratory, 2, 216 (1984).

[61] W. Demtröder, *Laser Spectroscopy. Basic Concepts and Instrumentation.*, Springer Verlag, Berlin, 1988.

[62] W. Kohn, A.D.Becke, R.G. Parr, *J. Phys. Chem.* **100**, 12974 (1996).

[63] P. Hohenberg,; W. Kohn, *Phys. Rev. A* **136**, 864 (1964).

[64] T. Ziegler, *Chem. Rev.* **91**, 651 (1991).

[65] J. B. Foresman, A. Frisch, *Exploring Chemistry with Electronic Structure Methods*, Gaussian Inc.: Pittsburgh, 1996.

[66] *Gaussian 98*, *Revision A.11*, M. J. Frisch, G. W. Trucks, H. B. Schlegel, G. E. Scuseria, M. A. Robb, J. R. Cheeseman, V. G. Zakrzewski, J. A. Montgomery, Jr., R. E. Stratmann, J. C. Burant, S. Dapprich, J. M. Millam, A. D. Daniels, K. N. Kudin, M. C. Strain, O. Farkas, J. Tomasi, V. Barone, M. Cossi, R. Cammi, B. Mennucci, C. Pomelli, C. Adamo, S. Clifford, J. Ochterski, G. A. Petersson, P. Y. Ayala, Q. Cui, K. Morokuma, P. Salvador, J. J. Dannenberg, D. K. Malick, A. D. Rabuck, K. Raghavachari, J. B. Foresman, J. Cioslowski, J. V. Ortiz, A. G. Baboul, B. B. Stefanov, G. Liu, A. Liashenko, P. Piskorz, I. Komaromi, R. Gomperts, R. L. Martin, D. J. Fox, T. Keith, M. A. Al-Laham, C. Y. Peng, A. Nanayakkara, M. Challacombe, P. M. W. Gill, B. Johnson, W. Chen, M. W. Wong, J. L. Andres, C. Gonzalez, M. Head-Gordon, E. S. Replogle, and J. A. Pople, Gaussian, Inc., Pittsburgh PA, 2001.

[67] A.D. Becke, *Phys. Rev. A* **38**, 3098 (1988).

[68] S.H. Vosko, L. Wilk, M. Nusair, *Canadian J. Phys.* **58**, 1200 (1980).

[69] K. Burke, J.P. Perdew,; Y. Wang, *Electronic Density Functional Theory: Recent Progress and New Directions*, J.F. Dobson, G. Vignale and M.P. Das, eds., Plenum, 1998.

[70] C. Lee, W. Yang, R.G. Parr, *Phys. Rev. B* **37**, 785 (1988).

[71] A.D. Becke, *J. Chem. Phys.* **98**, 5648 (1993).

[72] J.A. Pople, M. Head-Gordon, D.J. Fox, K. Raghavachari, L.A. Curtiss, *J. Chem. Phys.* **90**, 5622 (1989).

[73] L.A. Curtiss, C. Jones, G.W. Trucks, K. Raghavachari, J.A. Pople, *J. Chem. Phys.* **93**, 2537 (1990).

[74] M.W. Wong, *Chem. Phys. Lett.* **256**, 353 (1996).

[75] M.D. Halls, J. Velkovski, H.B. Schlegel, *Theor. Chem. Acc.* **105**, 413(2001).

[76] S. Lee, *J. Phys. Chem.* **100**, 33, 13959 (1996).

[77] S. Lee, *Theo. Chem.* **427**, 267 (1998).

[78] A.M. Smith-Gicklhorn, M. Lorenz, R. Kołos and V.E. Bondybey, *J. Chem. Phys.* **115**, 7534 (2001).

[79] A.M. Smith-Gicklhorn, M. Frankowski and V.E. Bondybey, *Phys. Chem. Chem. Phys.* **4**, 1425 (2002).

PART II

Matrix-Isolation Studies of Neutral Molecules

This part consists of two chapters containing results on matrix-isolation spectroscopy of novel rare gas compounds and organic azides.

Deposition of acetylene rare gas discharge products in Xe, Ar and Kr matrices leads to formation of the XeC_2 molecule with the complete absence of C_2 in the xenon matrix. Experiments discussed in the first chapter indicate that ground state Xe and C_2 react uniquely and without a barrier to form the XeC_2 molecule. Its infrared-active C-C stretch is found to be close to the corresponding frequency of the C_2-anion, in excellent agreement with DFT calculations yielding a XeCC bent structure with substantial charge separation approaching $Xe^+C_2^-$. Numerous broad absorptions near 423 nm are clearly due to the XeC_2 molecule, however a NIR emission revealed by LIF studies is likely due to XeC_2 but not yet understood. The Xe–H and C–H stretches observed in xenon matrix reveal also less efficient formation of $HXeC_2H$ molecule.

In the second chapter infrared spectra of azidoacetonitrile, and azidoacetone were examined in different matrices, solid neon, argon and nitrogen as well as using the DFT method. Significant broadening of the observed azide bands indicates an awkward fit of these compounds into the solid environment. The strongest absorption is observed for both compounds in the regions of stretching vibrations of the N_3 group. Strong band splittings in the N_3 asymmetric stretch region suggests very strong Fermi resonances with the C–N stretch and combinations of the numerous lower frequency vibrational modes.

3 Rare gas compounds: XeC_2 and $HXeC_2H$ molecules

3.1 Introduction

Although stable noble gas compounds have already been predicted at the beginning of the 20th century the number of unsuccessful experiments on their synthesis established the rather widely held opinion that the rare gases are inert. This changed in 1962 after *Bartlett* published his results on $XePtF_6$ [1,2]. This discovery triggered a whole series of experiments which resulted in many new xenon, krypton and radon compounds. At present, after a less fruitful period in this area, rare gas chemistry seems to experience its renaissance [4,3]. In fact, most of the compounds known today contain either a Xe–F or Xe–O bond, while Xe–Cl, Xe–Br, Xe–I, Xe–S, Xe–N, Xe–C and Xe–B bonds have also been found by now. Although many of these may be regarded as metastable species, several, like XeF_2, salt-like compounds with a C–Xe bond in the cationic part, and recently a neutral C_6H_5XeF, are actually thermodynamically stable compounds used in preparative chemistry [4-6]. Matrix-isolation contributed significantly to this field through characterization of the first chlorides, $XeCl_2$ [7,8] and FXeCl [8], as well as of the first krypton compound, KrF_2 [8,9]. The matrix experiments around that time also led to the isolation and characterization by infrared spectrum of ground states of interesting HAr_2^+ and HKr_2^+ ions [10-12] isoelectronic with the well-known bihalide anions, HCl_2^- [12-14] and HBr_2^- [15,16].

Another breakthrough in this field was the discovery of a new family of compounds, rare-gas hydrides HRgY, (where Y is an electronegative fragment like F or other halogens, OH, SH, CN, etc.) prepared in xenon matrices using UV-laser photolysis of a HY precursor and subsequent mobilization of H atoms [3,17]. Since these Xe compounds were only observed in a Xe matrix, it was questionable whether these highly polar species could exist in a less stabilizing environment. *Lorenz*, *Räsänen* and *Bondybey* have recently shown that these species, in particular HXeCl and HXeBr, can be formed with similar efficiencies in a weakly interacting neon matrix, and this, together with the results of DFT calculations, suggest that they should exist as free molecules in the gas phase [18]. Recently, *Räsänen* and co-workers also provided experimental evidence for the first predominantly covalent, ground state Ar–heteroatom bond in H–Ar–F [3].

Due to the rapid development of quantum chemistry, nowadays the predictions of stable compounds precede the experiments. A recently predicted family of Xe compounds involves C–H and O–H bond insertion products. From the computational viewpoint, species like HXeCCH, $HXeC_6H_5$, $HXeOC_6H_5$, and even HXeCCXeH could exist [19]. HXeOH was found in 1999 by the *Räsänen* group [20] and quite recently, by the same group, and independently by *Feldman et al.*, HXeCCH and HXeCCXeH were found [21,22].

Another species of current interest is the C_2 molecule, observed as early as 1857 in the spectrum of flames [23]. Numerous studies of its rich electronic spectrum, with many low-lying electronic states, have contributed significantly to the development of molecular spectroscopy [24-26]. Investigations of C_2 in rare gas matrices have also made considerable contributions [27]. They provided useful information about nonradiative relaxation processes in the solid medium and led to the first observation of stimulated emission in matrices [28]. Up to recently, it was presumed that C_2 could be isolated and observed in all condensable rare gas matrices, but the literature shows that the spectrum of C_2, unlike that of the C_2^- anion [29-30], has only been observed in Ne, Ar, and Kr, but never in a Xe matrix. The reason is, as it is shown here, the facile formation of the XeC_2 molecule, whose bonding can be described as $Xe^+C_2^-$.

The XeC_2 molecule was first discovered by *Maier* and *Lautz* in 1998 through UV laser irradiation of C_2H_2/Xe matrices and identified via its infrared-active C=C stretch [31]. They found this species to be the sole contributor to the IR and VIS/UV spectrum and that the intensity of the signal was insensitive to annealing (30 min at 38, 46, or 50 K), but decreased upon VIS/UV irradiation ($\lambda \geq 254$ nm), with no new features appearing. In contrast to this, *Räsänen et al.* [21] found that subsequent annealing of such samples led to the formation of HXeCC, HXeCCH, and even HXeCCXeH molecules [21]. At the same time, *Feldman et al.* bombarded C_2H_2/Xe matrices with high energy electrons (1 MeV) and found after subsequent annealing to 40 – 45 K, infrared absorptions due to HXeCCH, with no mention of XeCC and the other related compounds [22].

This work on XeC_2 also started with attempts at making HXeCCH in our pulsed DC-discharge source of transients. In those experiments, a discharge of C_2H_2 diluted in the Xe matrix gas led to a very strong XeC_2 signal and a very weak HXeCCH signal, even after annealing at 50 K. The absorption spectra from 500 – 31 000 cm^{-1} and emission spectra from 4000 – 31 000 cm^{-1} spectra were recorded in an attempt to decipher the electronic spectra of this unusual molecule. By performing similar experiments with dilute mixtures of C_2H_2 and Xe with large excess of argon or krypton, it was possible to observe spectra of the XeC_2 species in Ar and Kr matrices, and thus to address the important question of solvent effects on this highly polar, charge-transfer molecule.

3.2 Experimental

The samples were generated by electric discharge through xenon doped with acetylene, as well as through gas mixtures with small amounts of acetylene and xenon diluted by Ar and Kr matrix gases. The products were deposited onto a KCl window cooled down to 12.5 K at the APD system. The gas samples (C_2H_2: 99%; $^{13}C_2H_2$: 99%; C_2D_2: 99%; Xe: 99.998%; Ar: 99.999%; Kr: 99.99%) were mixed in various ratios, typically C_2H_2/Xe(1/800-1100), C_2H_2/Xe/Ar(1/1-5/1000) and C_2H_2/Xe/Kr(1/5/1000). Usually 8 mmol of the gaseous mixture were deposited for 2 hours as estimated from the pressure drop and volume of the gas container. The self-igniting DC electric discharge source with the pulsed gas inlet system has been described before [*Chapter 2* [32,33].

All absorption and emission spectra of the deposited samples were recorded using a Fourier-transform Bruker IFS 120 HR spectrometer. Absorption spectra were measured in a wide spectral range from 500 – 31 000 cm^{-1} usually with a 0.06 cm^{-1} resolution in the IR and 1 cm^{-1} resolution in the VIS-UV region. Although samples were always cooled down to 12.5 K after deposition, use of the broadband light sources caused increase of the temperature up to 14 K at which all absorption measurements were performed.

Emission in the NIR region was obtained by exciting the matrix samples using cw lasers, including intensity stabilized tunable dye lasers (Coherent 899-01 ring laser operated with stilbene 3; Coherent 599 standing wave laser with rhodamine 6G). The dye lasers were optically pumped by Ar^+ ion lasers (Coherent) operating in multi-line UV (Innova-200) and multi-line visible (Innova-70) modes. In some experiments, the Ar ion lasers were also used directly for the sample excitation. The Innova-70 laser operating in single line mode allowed for selection of discrete emission wavelengths between 514 and 466 nm. In all cases the laser beams were transmitted via fiber optics and focused onto the matrix sample.

3.3 Results and Discussion

3.3.1 XeC_2: Density Functional Theory Calculations

The optimized geometry and vibrational frequencies of XeC_2 molecule were calculated using the hybrid DFT technique as implemented in the *Gaussian 98* suite of programs [34] at the B3LYP level of theory. All electrons on the carbon atoms were explicitly treated with the 6-311++G(3df,3pd) basis set. For the rare gas atom, the quasi-relativistic effective core potential SDD basis set was used [35]. The lowest electronic singlet and triplet states of C_2 are known experimentally to be very close in energy, with the triplet lying only 716 cm^{-1} above the ground state singlet. The theoretical results and experimental spectroscopic data for lowest singlet and triplet states of XeC_2 are summarized in Tables 3.1a and 3.1b, respectively, with the data for C_2 and C_2^- anion being also included for comparison. Corresponding geometries of the molecules are shown in Figure 3.1. The binding in the singlet and triplet XeC_2 molecules are predicted to be considerably different in character. The singlet molecule is found to have a relatively strong, 82.4 kJ/mol bond, and exhibit an appreciable (0.72 e^-) charge transfer from xenon to the C_2 unit. The triplet C_2, on the other hand, interacts with xenon more weakly (33 kJ/mol), with only 0.09 e^- being transferred. Particularly striking are the differences in geometry, with the linear (or nearly linear, see below) singlet XeC_2 molecule displaying a remarkably short, 2.107 Å Xe-C bond. The triangular triplet, on the other hand, exhibits much longer, 3.26 and 3.39 Å

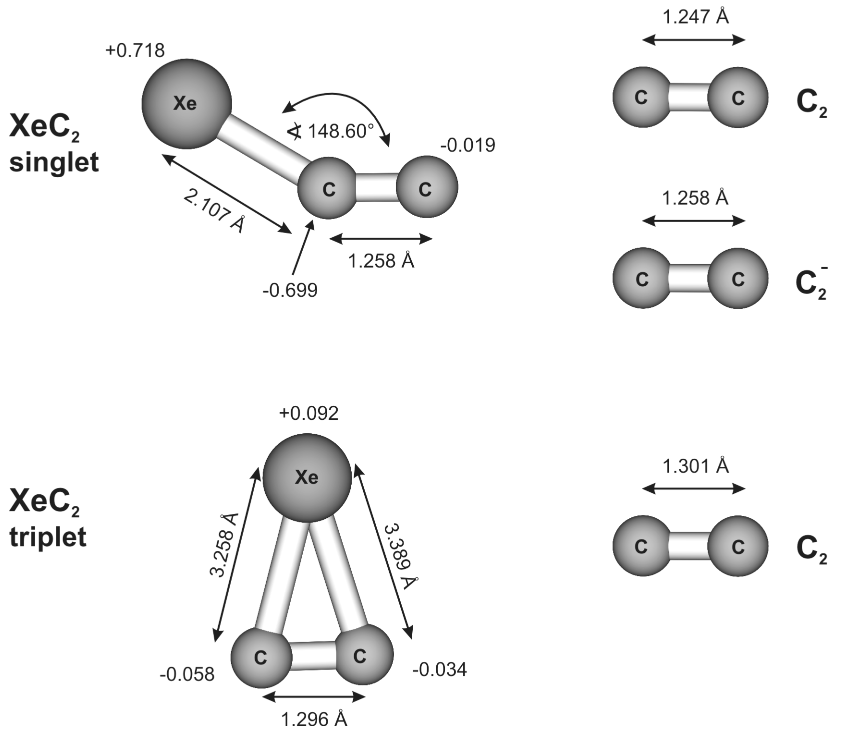

Figure 3.1. The computed geometries of XeC_2 in singlet and triplet state with charge distribution obtained from natural population analysis. C_2 is shown for comparison.

bonds to both the carbon atoms, and is probably best described as a weakly bound van der Waals complex.

This point of view is also confirmed by the computed vibrational frequencies. For the singlet, the computed C=C frequency decreases somewhat compared with free C_2 reflecting probably the fact that the corresponding mode in molecular XeC_2 involves also some motion of the heavy xenon atom. This is also consistent with the relatively high “skeletal” low frequency modes computed to be 325 and 87 cm^{-1}. On the other hand, in the triplet complex the C=C frequeny is found to display a smaller shift in the opposite direction, and the “skeletal” distortion modes decrease to 73 and 30 cm^{-1}, respectively. Again, the results are consistent with the novel singlet species being best described as a discrete ionic $Xe^+C_2^-$ molecule (see Table 3.1a, b), but the triplet as a weakly bound $Xe\cdots C_2$ complex.

Table 3.1a. Spectroscopic data for lowest singlet state of XeC_2 (in comparison to the ground states of C_2 and C_2^-).

Molecule, electronic state	Vibrational Frequencies in cm^{-1} {isotopic shifts}		
	DFT calculations (intensities in km/mol) B3LYP (6-311++G(3df,3pd) on C, SDD on Rg		Experiment
	unscaled	scaled with *f* = 0.96	
C_2 , $^1\Sigma_g^+$	1872.9 (0)	1798.0	1828.0 (gas) [a,c]
C_2^- , $^2\Sigma_g^+$	1841.9 (0)	1768.2	1779.7 (Ar) [a,d]
			1761.8 (Xe) [a,d]
			1757.9 (gas) [a,d]
XeC_2 , singlet	bend 87.4 (3)		
	Xe–C str. 325.1 (44)		
	C–C str.:		
	[132–12–12]*1858.5 (20)	1784.2	1767.4 (Xe) [b]
			1774.6 (Ar)
			1770.6 (Kr)
	[132–13–12] 1820.8 (20)	1748.0 {36.2}	1732.8 (Xe) {34.6}
	[132–12–13] 1823.8 (19)	1750.8 {33.4}	1734.1 (Xe) {33.3}
	[132–13–13] 1785.3 (18)	1713.9 {70.3}	1698.8 (Xe) [e] {68.6}
			1705.2 (Ar) {69.4}
	[129–12–12] 1858.5 (20)	1784.2	

[a] $\omega_e - 2\omega_e x_e$

[b] 1767.0 cm^{-1} as reported in [31]

[c] value from [37]

[d] value from [30]

[e] 1698.6 cm^{-1} as reported in [31]

* isotopes [Xe–C–C]

Table 3.1b. Spectroscopic data for lowest triplet state of XeC_2 (in comparison to the lowest triplet state of C_2).

Molecule, electronic state	Vibrational Frequencies in cm^{-1} {isotopic shifts}		
	DFT calculations (intensities in km/mol) B3LYP (6-311++G(3df,3pd) on C, SDD on Rg		Experiment
	unscaled	scaled with *f* = 0.96	
C_2 , $^3\Pi_u$	1694 (0)	1626	1618.0 (gas) [a]
XeC_2 , triplet	bend		
	29.6(0.2)		
	Xe–C str.		
	73.4(4.6)		
	C–C str.:		
	[132–12–12] 1708.8(19)	1640.4	
	[132–13–12] 1675.6(18)	1608.6 {31.8}	
	[132–12–13] 1675.5(18)	1608.5 {31.9}	
	[132–13–13] 1641.6(17)	1575.9 {64.5}	
	[129–12–12] 1708.8(19)	1640.4	

[a] $\omega_e - 2\omega_e x_e$ [37]

Returning to the structure of the singlet XeC_2 species, the optimizations converge smoothly to a linear Xe-C-C structure when the relatively primitive SDD basis set is used on all the atoms, including the carbons. On the other hand, with the larger 6-311++G(3df,3pd) basis set including diffuse and polarization functions on the carbon atoms, the computation yields for the linear geometry imaginary frequencies. Allowing the symmetry to be lowered, the optimization converges to a slightly bent structure with all real frequencies. The computed total energy of the singlet XeC_2 molecule as a function of Xe-C-C bending angle is shown in Figure 3.2. It can be seen that the bending potential is very flat with the linear and bent (140 – 180°) structures nearly isoenergetic, but the optimizations converge consistently to a bending angle around 148.6°. Some support for the bent structure can also be seen in the high intensity of the observed C=C stretching frequency observed for XeC_2. While for the linear arrangement the IR intensity predicted for this mode is extremely low (1 km/mol), the bent solutions give more than an order of magnitude higher infrared intensities (20 km/mol) of the C=C stretch, more consistent with the experimental results to be discussed below.

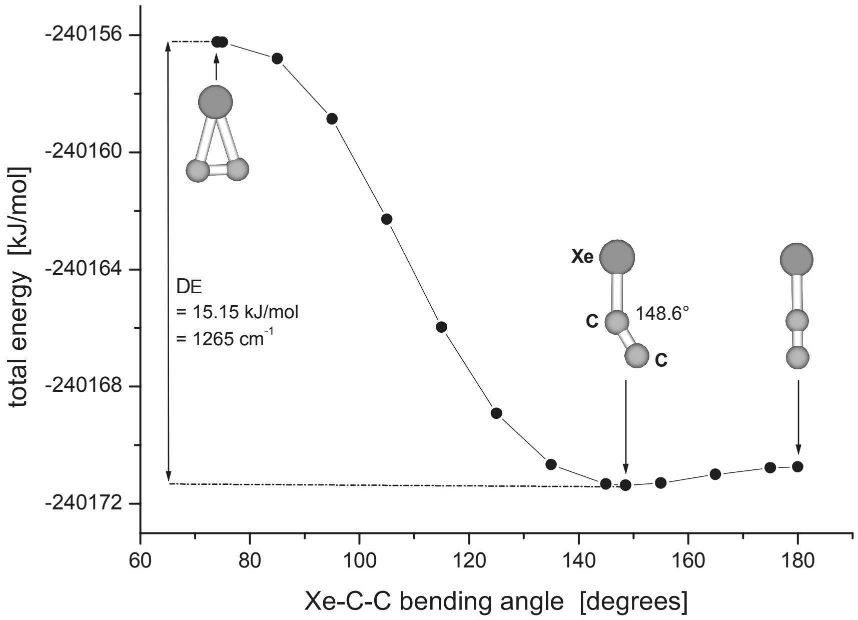

Figure 3.2. The total energy of XeC_2 molecule in function of Xe-C-C bending angle determined from density functional theory (B3LYP) calculations; basis set: (6-311++G(3df,3pd) on carbon atoms and SDD on rare gas atom.

Besides computations on XeC_2 the interaction of C_2 with more than one xenon atom has been also explored. Starting from a linear, centrosymmetric $D_{\infty h}$ XeCCXe structure, the optimization with the all SDD basis set results in two relatively long, 2.717 Å XeC bonds, and yields one rather high imaginary frequency. When the initial geometry is made slightly asymmetric, $C_{\infty h}$, the energy of the converged geometry drops substantially by nearly 22 kJ/mol, and the imaginary frequency disappears. The lengths of the two XeC bonds are now quite different, 2.139 and 4.063 Å, respectively. The converged structure is basically

XeC_2, with essential identical geometry and frequencies as in the three atom computations, very weakly bound to the additional Xe atom. A very similar result is obtained for a linear XeXeCC arrangement, where the optimized geometry again yields a Xe atom weakly interacting with the Xe end of the unperturbed triatomic XeC_2 , and with the Xe···Xe distance of 4.47 Å. Also other geometries where the C_2 is forced to interact simultaneously with more than one xenon atom yield high energy optimized structures. For instance a T-shaped C_{2v} Xe_2-CC geometry, where one of the carbon atoms interacts with two xenon atoms results in two long, 2.97 Å Xe-C bonds, and more than 45 kJ/mol above the asymmetric, linear global minimum.

Quite similar results are obtained with the larger, 6-311++G(3df,3pd) basis set on the carbon atoms. Again, trying to enforce symmetric configuration results in a high energy structure with large imaginary frequencies, but allowing symmetry lowering, optimization converges to an $XeC_2\cdots Xe$ structure, with a bent XeC_2 structure essentially identical to that obtained in the 3-atom computation, that is with C=C and C–Xe distances of 1.258 and 2.107 Å, respectively, and a CCXe bending angle of 146.8°, and with a weakly bound additional xenon atom at a large, 4.235 Å distance (see Figure 3.3).

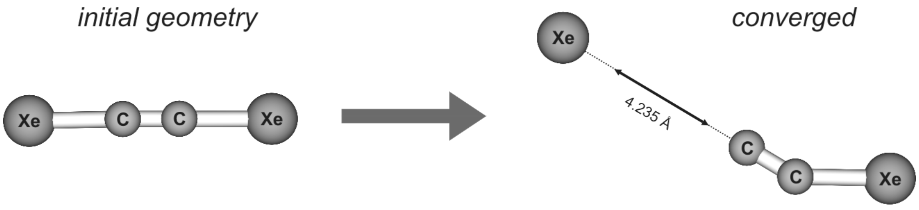

Figure 3.3. Geometry convergence for the four atomic Xe–C–C–Xe structure on the B3LYP/6-311++G(3df,3pd) level of theory.

The conclusions of these computations seem therefore inescapable: the XeC_2 is a well defined, strongly bound discrete molecule, and the C_2 dimer prefers to interact with one and only one xenon atom. The presence of any additional ligand atoms has very little influence upon the geometry and vibrational frequencies of the XeC_2 molecule. When the starting geometry involves two equivalent xenon ligands (and similar results were obtained for Kr and Ar as well), one of these is in the optimization process tightly bound, while the other is pushed away. In other words, independent of the number of ligands used, there is a strong interaction with one. These results contradict a previous prediction of a T-shaped equilibrium structure of Ar_2C_2 [36], which is clearly not the global minimum in calculations in our group, both with the SDD and the 6-311++ G(3df,3pd) basis sets.

3.3.2 XeC_2 in Xenon Matrix

The infrared spectra of a matrix obtained by discharging mixtures of acetylene and of its all ^{13}C isotopomer with xenon, are presented in Figure 3.4 a and b. Specific ratios of $^{12}C_2H_2$/Xe(1/870) in graph (a), and $^{12}C_2D_2$/Xe(1/807), $^{13}C_2H_2/^{12}C_2H_2$/Xe(1/1/1134) and $^{13}C_2H_2$/Xe(1/807) were used for the spectra in the top, middle and bottom panel of graph (b), respectively, and the measured vibrational frequencies are summarized in Table 3.1a. All curves were recorded at 14 K after deposition at a temperature of 30 K. Analysis of the spectra and of the observed isotopic shifts, combined with the theoretical calculations described above, clearly identify the 1767.4 cm^{-1} as the C=C stretch of the XeC_2 molecule, and confirm the previous assignment [31]. The lack of any shift with deuterated $^{12}C_2D_2$ (Figure 3.4 b) confirms the absence of hydrogen in the carrier, and the clearly resolved doublet of lines due to the mixed $Xe^{13}C^{12}C$ (1732.8 cm^{-1}) and $Xe^{12}C^{13}C$ (1734.1 cm^{-1}) species demonstrates the presence of two inequivalent carbon atoms. Unfortunately, the frequencies cannot be used to distinguish between the linear or 148.6^{o} bent configuration, since the effect of the angle is too small, and the agreement with the predicted isotopic shifts is good for both geometries.

3.3.3 XeC_2 in Argon and Krypton Matrices

Quite noteworthy is the absence of the so-called *Phillips bands* characteristic of C_2 in the VIS absorption region. These are always prominent in matrices other than xenon, whenever acetylene or another unsaturated hydrocarbon is discharged, as also exemplified by Figure 3.5, which compares the visible and near IR spectra of discharged acetylene in argon, krypton and xenon matrices. Apparently, C_2 produced in the discharge reacts in the xenon matrix with Xe atoms to produce *in situ* the XeC_2 molecules. This reaction must be

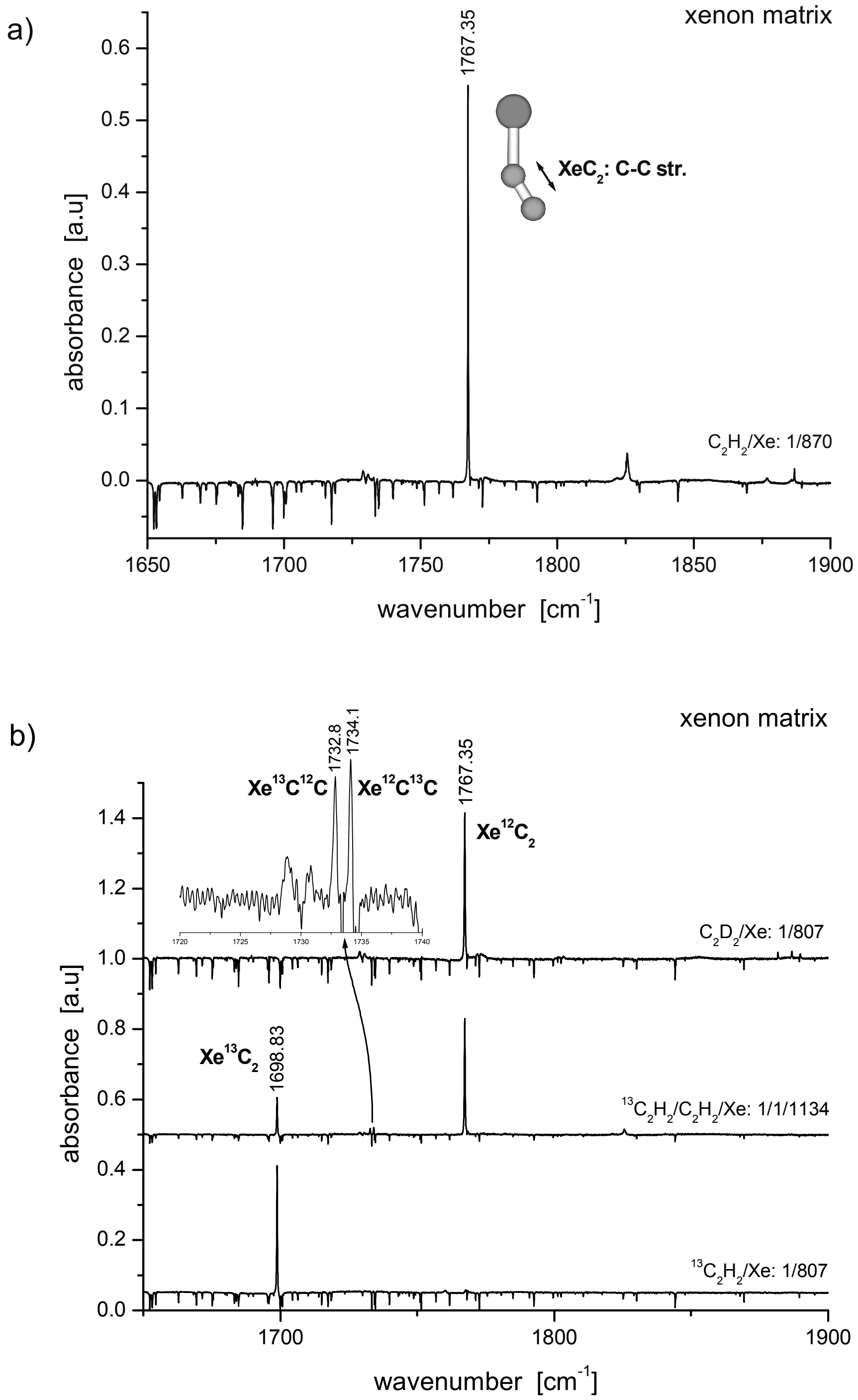

Figure 3.4. Infrared spectra of XeC_2 molecule and its isotopomers in Xe matrix at 14 K obtained using regular (a) and isotopically labeled acetylene (b).

nearly quantitative and proceed with essentially no activation barrier, since no trace of the *Phillips* bands is observed, and no further increase in the XeC_2 band absorption intensity can be detected when the xenon matrix is annealed at 40 K. It may be noted that the peak at 1852 cm^{-1} previously assigned to the ethynyl radical C_2H [22] is also not observed. A weak but unidentified feature appears at 1825.6 cm^{-1}.

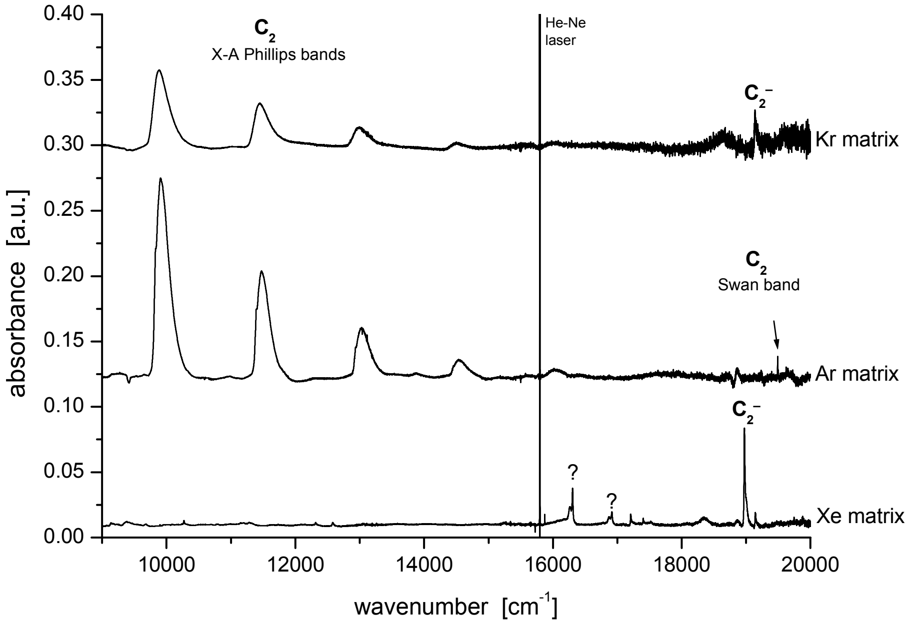

Figure 3.5. Comparison of the C_2 molecule NIR–VIS absorption region (*Phillips* bands: $X^1\Sigma_g^+ \rightarrow A^1\Pi_u$ and *Swan* band: $a^3\Pi_u \rightarrow d^3\Pi_g$) for Xe, Ar and Kr matrices.

Spectra obtained using argon and krypton matrix gases doubly doped by small amounts of Xe and acetylene are presented in Figures 3.5 and 3.6. The visible and near-IR spectra show, as noted above, a prominent progression of absorptions due to the A-X C_2 transition in solid argon and krypton, which is, however, quite absent in the xenon matrix (Figure 3.5). On the other hand, the strong band due to the origin of the Herzberg-Lagerqvist bands near 19 000 cm^{-1} [38] is present in all three matrices, indicating that C_2^-, unlike C_2 can be isolated in solid xenon also. Interestingly, the argon sample shows also a weak absorption due to the origin of the Swan bands of triplet neutral C_2.

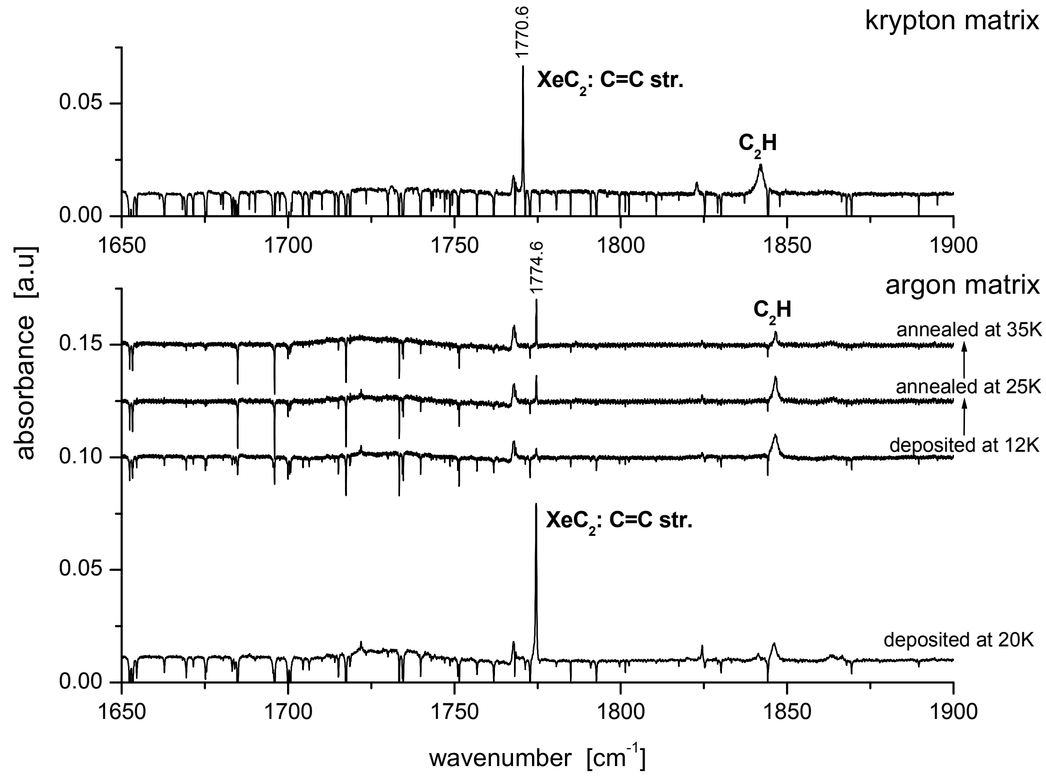

Figure 3.6. Infrared absorption spectra of XeC_2 molecule in Ar and Kr matrices. Spectra in Ar matrix show intensity changes upon two step annealing for sample deposited at 12 K (C_2H_2/Xe/Ar(1/1/1000) and for comparison at 20 K and higher Xe concentration (C_2H_2/Xe/Ar(1/5/1000)). Concentration for Kr matrix deposited at 30 K was C_2H_2/Xe/Kr(1/5/960).

Figure 3.6 shows the infrared spectra obtained with the doubly doped argon (C_2H_2/Xe/Ar=1/5/1000) and krypton (C_2H_2/Xe/Kr=1/5/960) samples. The presence of moderately intense, sharp bands at 1770.6 and 1774.6 cm^{-1} in solid krypton and argon, respectively, slightly blue shifted from the XeC_2 absorption at 1767.4 cm^{-1} in solid xenon show that the molecule can be isolated, alongside C_2, C_2^- and other carbon cluster molecules, in solid Ar and Kr environments. The assignment of these bands to XeC_2 is further confirmed by their strong dependence on the concentrations of both Xe and acetylene. Using isotopically labeled acetylene one obtains in solid argon a peak at 1705.2 cm^{-1}, which is clearly due to $Xe^{13}C_2$ (Table 3.1a). It may also be noted that the C=C stretching absorption band of this compound in solid Ar, 1774.6 cm^{-1} is just 5 cm^{-1} to the red from the vibrational frequency of the C_2^- anion, which is consistent with the appreciable charge separation predicted by the DFT calculations.

The three traces in the middle of Figure 3.6 show the results of an annealing experiment, where the sample was deposited at 12 K, and then progressively warmed up for 30 minutes to 25 and 35 K respectively, recooling each time to 12 K before recording the spectrum. It can clearly be seen, that the 1774.6 cm^{-1} band, which is rather weak in the original, at 12 K deposited sample (in the lowest trace), increases in intensity with each annealing step (the traces above it). The straightforward conclusion which can be drawn from this experiment is that during the annealing process and the resulting diffusion, the ground state Xe atoms and C_2 can react essentially without barrier to form the chemically bound XeC_2 molecule.

The results in the krypton and argon matrices are clearly in excellent agreement with the theoretical computations discussed in an earlier section. The diatomic C_2 prefers to react and interact strongly with a single xenon atom. Once this reaction occurs, and the molecular XeC_2 forms, its solvation by other atoms makes little difference. The vibrational frequencies, and presumably the structure of the molecule, are essentially independent of whether it is surrounded by additional xenon atoms, or whether it is isolated in krypton or argon matrices.

3.3.4 $HXeC_2H$ in Xenon Matrix

Besides the recent observation of XeC_2 [30], the motivation of the present work were calculations done by *Lundell et al.* [19] which suggested that HXeCCH should exist as a stable molecule (see Figure 3.7). Moreover, the results obtained by the latter group using perturbation MP2 and coupled cluster CCSD electronic structure algorithms, suggested that this species is one of the most stable xenon-containing rare gas hydride discovered so far. In contrast with the recently reported spectroscopic results on this molecule in a xenon matrix by *Khriachtchev et al.* [21] and *Feldman et al.* [22], experiments done in this work using discharge source produce it in very small yields. With the help of the previous assignments, these bands could however be identified in spectra measured in our laboratory, shown in Figures 3.8 and 3.9. Their analysis and the production of the molecule by a different technique provides some additional information and insights, complementary to the previous experimental work and above mentioned, earlier theoretical studies [19], and therefore are briefly discussed here.

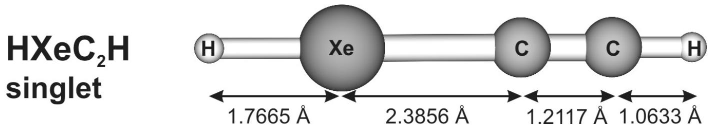

Figure 3.7. Equilibrium structure of Xe inserted in acetylene, computed at the B3LYP(6-311++G(3df,3pd/SDD) level of theory.

The experimental data, as well as the results of DFT computations done at the B3LYP level using 6-311++G(3df,3pd) basis set on C and H atoms, and SDD on rare gas atom are summarized in Table 3.2. For the ease of comparison, the measured intensities given in parentheses are scaled to the computed intensity of the strongest band. With the help of the previous assignments [21,22], the Xe–H and C–H stretching vibrations of HXeCCH at 1486.1 and 3273.5 cm^{-1} respectively, can be easily identified. In similar experiments using deuterated or ^{13}C substituted species, the corresponding vibrational modes of DXeCCD, as well as the previously unknown vibrations of the HXe^{13}C^{13}CH isotopomer could be established.

All the bands described above exhibit an interesting behavior upon photolysis and sample annealing which is useful in confirming their assignment to the same carrier. The very weak absorption bands present right after sample deposition almost completely disappear when the matrix is irradiated by the visible light of a tungsten lamp for 2 – 3 hours. When the sample is then annealed to 40 – 50 K, they reappear, and grow appreciably, undoubtedly due to reactions of the hydrogen atoms produced in the discharge. Unlike the photolysis experiments, however, which produces the H and C_2H pairs in close proximity, in our discharge setup the fragments are essentially randomly dis-

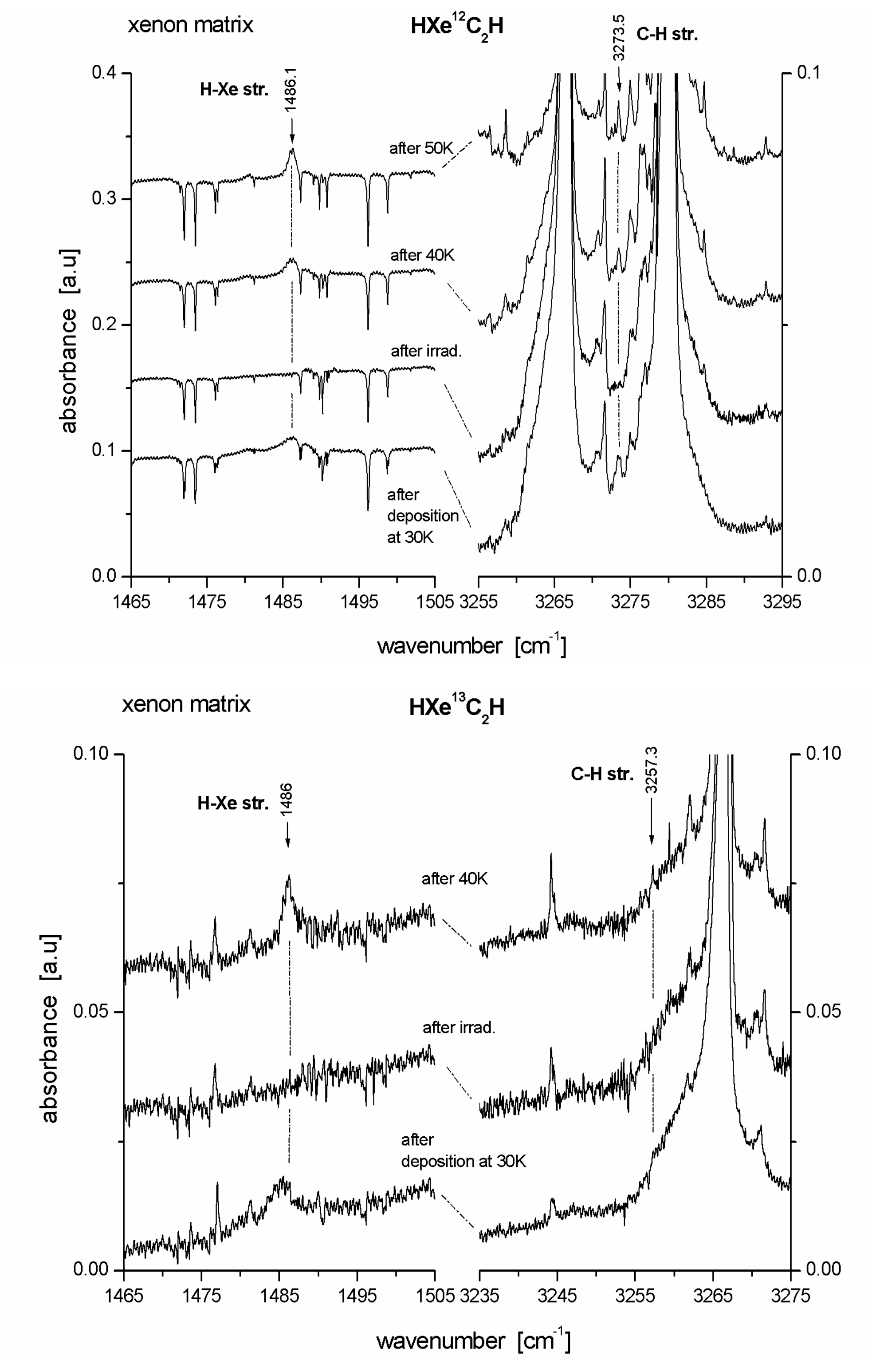

Figure 3.8. Regions of H–Xe and C–H stretching vibrations of HXeC$_2$H molecule and its ^{13}C-isotopomer (^{13}C–H is tentatively assigned).

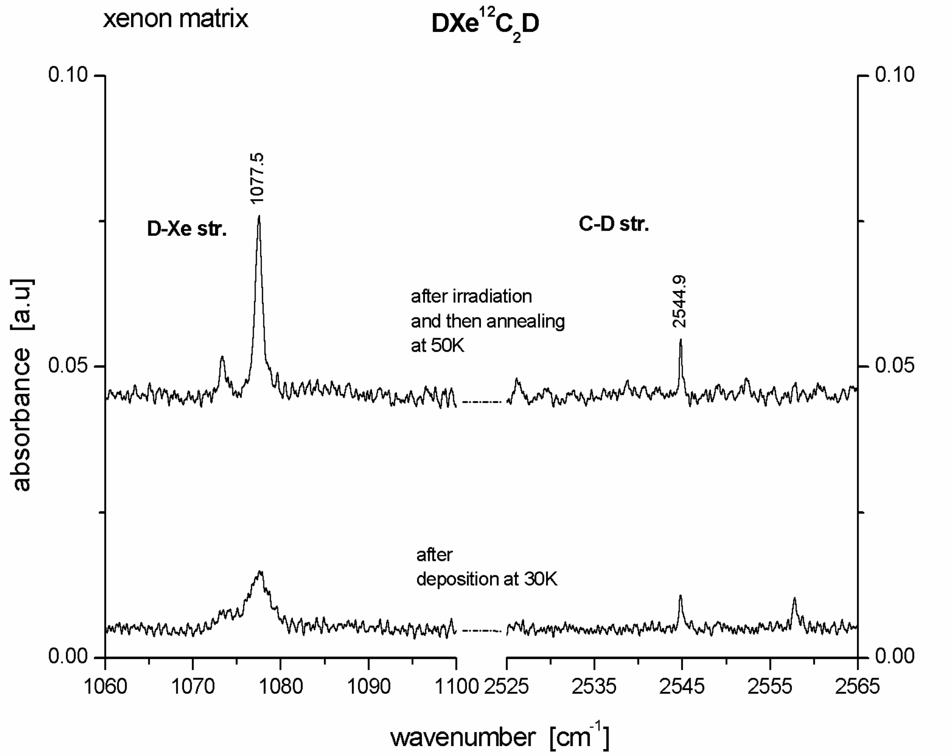

Figure 3.9. Regions of H–Xe and C–H stretching vibrations of the $DXeC_2D$ isotopomer.

tributed through the matrix. In the former experiments the two radical fragments have an appreciable probability of reacting with the same xenon atom to form the HXeCCH species, while in the random walk-like diffusion of the fragments in our discharge studies this probability is greatly reduced. One can suspect that a substantial fraction of the hydrogen atoms produced by the discharge in these experiments recombines, during either the sample deposition or the diffusion, to form molecular H_2, and are thus from the point of observable product formation irretrievably lost.

3.3.5 Electronic Spectra

While the interpretation of the XeC_2 infrared absorption is rather straightforward, the corresponding electronic spectra are more difficult to understand. The absorption spectra observed in the visible and near UV which are presented in Figure 3.10 exhibit a series of broad bands between 22 000 – 26 000 cm^{-1}, whose approximate frequencies are both for the $^{12}C_2H_2$/Xe and $^{13}C_2H_2$/Xe experiments summarized in Table 3.3. The excellent correlation between the intensity of these bands and that of the infrared spectrum strongly suggests that they are also due to the XeC_2 molecule, as proposed previously [31]. When

Table 3.2. DFT computed harmonic and experimental frequencies measured in Xe matrix for $HXe^{12}C^{12}CH$, $HXe^{13}C^{13}CH$ and $DXe^{12}C^{12}CD$ molecular vibrations.

assignments	vibrational frequencies in cm^{-1}		
	DFT calculations (intensities in km/mol) B3LYP (6-311++G(3df,3pd) on C and H atoms, SDD on Xe	Previous experiments	This work (relative intensities) *
$HXe^{12}C^{12}CH$			
C–C–H bend	677.7 (50)	626	626 v. weak
Xe–H str.	1627.4 (1131)	1486.0	1486.1 (1131)
C–H str.	3443.5 (43)	3273	3273.5 (199)
$HXe^{13}C^{13}CH$			
C–C–H bend	672.1 (49)		
Xe–H str.	1627.3 (1133)		1486
C–H str.	3425.6 (41)		3257.3 #
$DXe^{12}C^{12}CD$			
C–C–D bend	532.4 (18)	491.5	
Xe–D str.	1154.9 (571)	1077.5	1077.5 (571)
C–D str.	2663.1 (32)	2545	2544.9 (48)

* Experimental intensities were determined using *Levenberg-Marquardt* and *Local Least Squares* fitting algorithms (implemented in OPUS 4.0 Bruker software), then scaled to the maximal observed values and normalized to theoretical intensities for each experiment.

\# tentative assignment

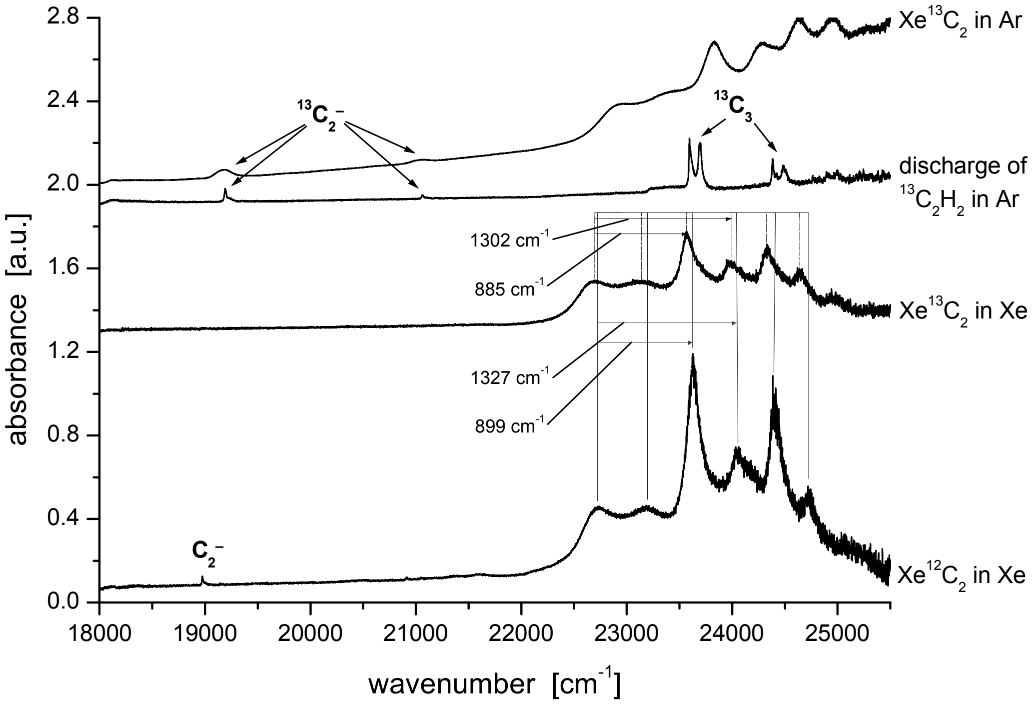

Figure 3.10. XeC_2 absorption region in VIS/UV spectral range in Xe and Ar matrices. For convenience the frequency intervals are sketched for $Xe^{12}C_2$ and $Xe^{13}C_2$ bands (for bands locations see Table 3.3). The spectrum recorded after $^{13}C_2H_2$/Ar discharge products deposition is shown for comparison.

pure argon or krypton with no xenon is used, the broad bands are absent, and much sharper bands due to a well-known transition of C_3 appear approximately in this region. C_3, however can be safely excluded as a carrier of the broad bands.

In view of the width of the bands, and lack of spectral details, a specific assignment or interpretation of these bands is difficult, in particular since no theoretical information on the excited electronic states of C_2Xe is available. The spacing of the bands decreases in the ^{13}C experiment, with the approximate isotopic frequency ratio of $\rho \approx 0.97$ being relatively close to that expected for pure carbon motion, 0.961. The spectrum appears relatively complex for a molecule as simple as XeC_2, and it is conceivable that overlapping progressions of two or more electronic states are present in this region.

Table 3.3. Measured VIS/UV absorption bands of $Xe^{12}C_2$ and $Xe^{13}C_2$ in Xe and Ar matrices and NIR emission observed from deposition of $^{12}C_2H_2$/Xe and $^{13}C_2H_2$/Xe discharge products.*

VIS/UV absorption $\tilde{\nu}$ [cm^{-1}]			NIR emission $\tilde{\nu}$ [cm^{-1}]	
$Xe^{12}C_2$/Xe	$Xe^{13}C_2$/Xe	$Xe^{13}C_2$/Ar	from $^{12}C_2H_2$/Xe discharge products	from $^{13}C_2H_2$/Xe discharge products
v. w. features in the region of 21200 – 21800		—	5883	5883
22735	22697	22969	6920	6872
23170	23124	23400	7095	7053
23634	23582	23826	8299	~8230
24062	23999	24283	8494	8403
24414	24341	24628	8703	8599
24711	24634	24967	~9862 v.w.	9740
w. features around 25000		~25300	~10104 v.w.	9947

* The location of band centers were determined using *Levenberg-Marquardt* fitting algorithm (v.w. – very weak)

If emission from the excited electronic state of the species of interest is observable, analysis of the fluorescence provides information complementary to the absorption spectrum, and often is of considerable help in untangling its structure. In the present case, however, even though an intense infrared fluorescence is observed, it only serves to further deepen the mystery. Unfortunately, there is no a light source in our laboratory which is capable of exciting the sample in the strongest absorption bands, and the two traces in Figure 3.11 result from excitation of matrices obtained in $^{12}C_2H_2$/Xe and $^{13}C_2H_2$/Xe experiments, in each case near the low energy end of the absorption, around 23 000 cm^{-1}. The emission bands are again relatively broad, and so the accuracy of their positions listed in Table 3.3 is probably not better than ±10 cm^{-1}. The bands exhibit distinct isotopic shifts, with their spacing reduced in the $^{13}C_2H_2$ experiment on average by about a factor $\rho \approx 0.965$, very close to what would be expected for instance for diatomic XeC or C_2. The band at 5883 cm^{-1} shows essentially no isotopic shift, and should therefore be the electronic origin. With this assignment, however, all the other observed bands occur at higher energies, suggesting that much of the emission would have to originate from vibrationally excited levels, which is rather unusual for polyatomic molecules. Furthermore, if this interpretation is accepted, the spectrum exhibits a strong negative anharmonicity, with the band spacing appearing to increase with increasing vibrational energy.

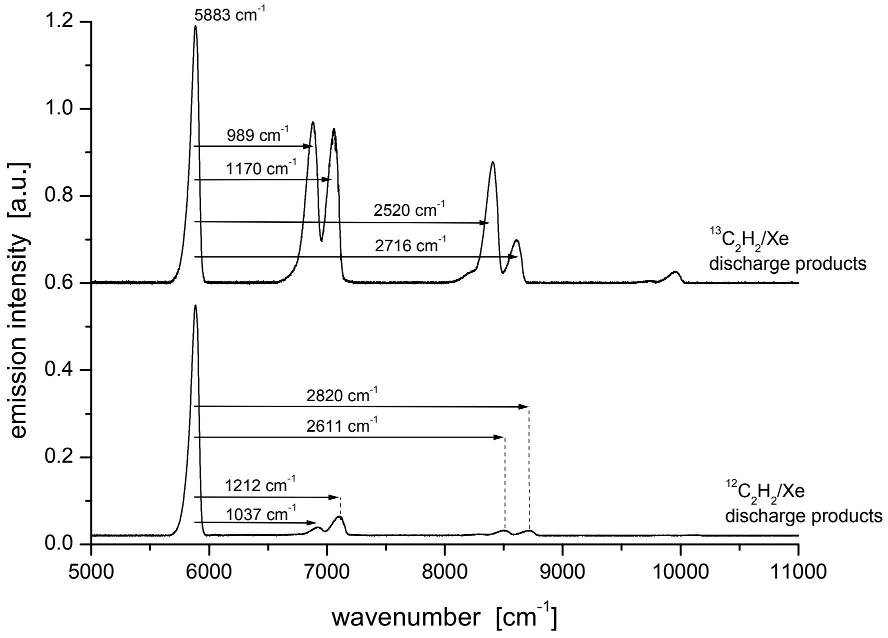

Figure 3.11. Near infrared emission under excitation at 431 nm by means of Stilbene 3 dye laser recorded after $^{12}C_2H_2$/Xe and $^{13}C_2H_2$/Xe discharge products deposition. The frequency intervals are shown with arrows and values; bands locations are given in Table 3.3.

Puzzling is also the absence of any emission at energies below the 5883 cm^{-1} origin, which could be assigned to excited levels of the ground state. While part of the reason may be the sensitivity of the detector, which cuts off around 4000 cm^{-1}, but certainly some emission to the low ground state levels would be expected (for example $\upsilon''(0) \rightarrow \upsilon'(1)$ band). In the absence of such emission, no information about the ground state is obtained.

The results must lead to conclusion that even though there appears to be a strong evidence for assigning the electronic spectrum to the XeC_2 molecule, at this point its structure is only little understood. Clearly additional experimental, and in particular theoretical work, would be desirable.

3.4 Conclusions

A self-igniting DC electric discharge of C_2H_2 in Xe (matrix gas) produces no C_2, little C_2^-, and mainly the XeC_2 molecule, as revealed by its infrared spectrum. The same molecule can be isolated in Ar and Kr matrices alongside diatomic C_2 and C_2^- and other carbon cluster molecules in discharges of C_2H_2/Xe diluted in Ar or Kr as matrix gas. The infrared-active C=C stretch of this compound is found just 5 cm^{-1} to the red (in Ar at 1774.6 cm^{-1}) from the C=C stretch of the C_2-anion, in excellent agreement with our density functional theoretical (DFT) calculations at the B3LYP level (basis sets 6-311++G(3df,3pd) on C, SDD on Xe). These yield a XeCC singlet species with substantial charge separation (natural charge populations of +0.72 e^- (Xe), -0.7 e^- (C) and -0.02 e^- (C)) and a remarkably short, 2.107 Å, Xe-C bond. The spectra of the Xe-^{13}C-^{12}C, Xe-^{12}C-^{13}C and Xe-^{13}C-^{13}C species are also obtained and the isotopic shifts are in excellent agreement with the DFT predictions, although not sufficient to distinguish a bent (a 148.6° structure is a shallow minimum) from a linear structure. More difficult to interpret is the broad electronic spectra of this species. Numerous broad absorptions centered near ~ 23 600 cm^{-1} (423 nm; in xenon matrix) are observed which are clearly due to the XeC_2 molecule. Laser-induced fluorescence studies reveal a near-infrared emission with origin at 5883 cm^{-1} likely due to XeC_2. The spectrum is rather unusual for a triatomic molecule and indicates a nonrelaxed vibrational emission.

The Xe matrix infrared spectra reveal Xe–H and C–H stretching vibrations of the HXeCCH molecule, observed also for its fully deuterated DXeCCD, or all-^{13}C isotopomers. However, deposition from a gas discharge leads to a random distribution of radical fragments through the matrix, and consequently formation of HXeCCH by diffusion is fairly inefficient.

4 FT-IR Spectroscopy of Organic Azides: Azidoacetonitrile and Azidoacetone

4.1 Introduction

Organic azides are compounds which are of great importance in chemistry as useful reagents in many fields [39-41]. Their strongly exothermic reactions make them useful as propellants [42]. Their ability to form highly reactive nitrene intermediates that are capable of inserting into otherwise stable chemical bonds makes them important synthetic reagents, with for instance a number of potential uses in semiconductor technology [43].

This work concentrates on two species: azidoacetonitrile (N_3CH_2CN, further abbreviated as AzN) and azidoacetone ($N_3CH_2COCH_3$, AzC). The AzN and AzC molecules were studied both in solution and in solid phase, but their relative volatility allows as well studies in the gas phase [44]. The thermal decomposition of these two compounds was recently studied using Ultraviolet Photoelectron Spectroscopy (UVPES) and matrix-isolation spectroscopy in solid nitrogen, as part of a general project on decomposition of aliphatic azides [45,46]. Theoretical calculations have been also carried out for conformers of AzC [47].

One can often obtain more insight and additional information about the interaction of isolated compounds with the solid medium by examining and comparing the spectra in several matrices. In the present work infrared spectra in solid neon, argon and nitrogen are reported. The experimental investigations in low temperature matrices are complemented by density functional theoretical (DFT) computations of their properties and structures. The obtained spectra are discussed with the help of computed vibrational frequencies and intensities.

4.2 Experimental

Sample preparation

Azidoacetonitrile was synthesized from chloroacetonitrile $ClCH_2CN$ and sodium azide (NaN_3) as given in [48]. Azidoacetone was prepared from chloroacetone $ClCH_2COCH_3$ and NaN_3, according to the procedure described in [45].

The organic azides vapors mixtures with matrix Ne, Ar and N_2 gases were prepared at room temperature with an estimated concentration of 1:700 for all experiments. Neon samples were continuously deposited onto the copper substrate (coated with silver and MgF_2) cooled to 6 K by a closed cycle helium cryostat, at the LEYBOLD system. Argon and nitrogen samples were deposited by means of a pulsed valve at 12 K onto the KCl substrate mounted on the cryotip of an APD system. To improve the optical quality of the N_2 matrix, deposition was started from 60 K and then the substrate was gradually cooled down to 12 K in 10 min. In all experiments the deposition rate was kept in the range of 2.5 – 3 mmol/h for a deposition time of 2 hours.

IR Spectroscopy

The infrared spectra of both compounds, N_3CH_2CN and $N_3CH_2COCH_3$, in solid Ne, Ar, and N_2 were recorded with a resolution of 0.06 cm^{-1} with a Bruker IFS 120 HR Fourier-transform spectrometer using a globar light source, a liquid nitrogen cooled HgCdTe (MCT) detector, and a KBr beam splitter. Typically at least 500 scans were averaged. The spectra were recorded immediately after deposition, then again after annealing of the samples, and after irradiation of the matrices with a tungsten lamp, a multi-line UV Ar^+ ion laser and the fourth harmonic of a Nd:YAG laser.

4.3 Results and Discussion

4.3.1 Computations

The optimized structures and vibrational frequencies of azidoacetonitrile and azidoacetone were calculated using the B3LYP/6-31+G(d,p) hybrid DFT technique as implemented in the *Gaussian 98* suite of programs [44]. To check for errors due to the incomplete basis set, calculations on the same level of theory but using the larger 6-311(3df,3pd) basis set were performed, which yielded no substantial changes from 6-31+G(d,p) results. Tables 4.1 and 4.2 summarize the results for the two most stable conformational minima, whose geometry is characterized by different values of the φ_{NNCC} dihedral angle. In the case of AzC the two local minima at 64° (gauche) and 180° (anti) are nearly isoenergetic, in AzN the 67° gauche conformer is found to be considerably lower in energy than the 180° anti isomer. The tables list the computed, unscaled vibrational frequencies of both molecules. The equilibrium geometries of AzN and AzC conformers are illustrated in Figure 4.1.

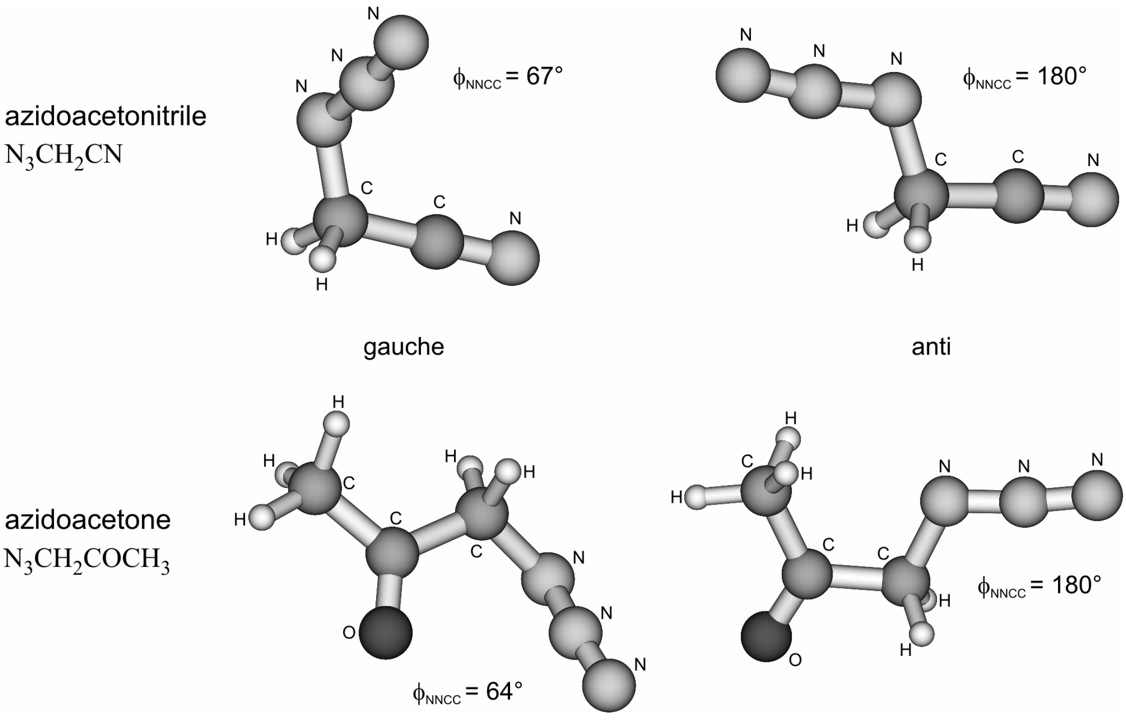

Figure 4.1. Equilibrium structures of the *gauche* and *anti* conformers of azidoacetonitrile and azidoacetone predicted at the B3LYP/6-31+G(d,p) level of theory.

Table 4.1. Calculated frequencies of vibrational modes of azidoacetonitrile conformers (method: B3LYP/6-31+G(d,p))

anti: *dihedral angle* $\varphi_{NNCC} = 180°$		gauche: *dihedral angle* $\varphi_{NNCC} = 67°$		approximate assignment
frequency [cm^{-1}]	intensity [km/mol]	frequency [cm^{-1}]	intensity [km/mol]	
34.9	1.3	55.7	5.5	
145.2	9.2	193.1	7.7	
260.2	1.6	258.6	9.6	
358.6	0.6	351	0.1	C–C≡N bend
519.4	2.7	523	0.1	C–C≡N bend
544.9	6.9	556.3	8.7	NNN bend
628.1	5	687.3	15.7	NNN bend
945	20.7	884.4	13.4	C–C/C–N sym. str.
973.6	0.9	937.6	26	CH_2 rock + C–C/C–N asym. str.
979	15.7	1006.2	9	CH_2 rock + C–C/C–N asym. str.
1241.5	0.6	1253.9	1	CH_2 twist
1332.6	145.2	1314.1	163.1	NNN sym. str.
1373.7	10.9	1372	10.9	CH_2 wag
1479.1	7.4	1476.5	8.4	CH_2 bend
2255.1	517.8	2254.3	450.9	NNN asym. str.
2376.7	0.9	2358	0.6	C≡N
3021.4	15.4	3043.9	14.3	CH_2 sym. str.
3062.3	4.3	3135.7	0.4	. CH_2 asym. str.

The infrared absorption spectra calculated using the B3LYP/6-31+G(d,p) hybrid DFT method revealed that due to relatively high intensities (451 – 518 km/mol for N_3CH_2CN, Table 4.1; 602 – 522 km/mol for $N_3CH_2COCH_3$, Table 4.2) the N–N–N asymmetric stretching vibration is the most useful “fingerprint” in spectrosopic characterization of both azide compounds.

Table 4.2. Calculated frequencies of vibrational modes of azidoacetone conformers (method: B3LYP/6-31+G(d,p))

anti: *dihedral angle* φ_{NNCC} *= 180°*		gauche: *dihedral angle* φ_{NNCC} *= 64°*		approximate assignment
frequency [cm^{-1}]	intensity [km/mol]	frequency [cm^{-1}]	intensity [km/mol]	
35.4	15.3	61.1	1.9	
46.9	1.3	81	2.5	
137.8	3.8	98.6	0.3	CH_3 torsion
140.9	0	216.5	4.5	CH_3 torsion
262	10.5	274	4.9	
449	1.1	381.1	5.2	
473.8	0.8	461.3	2.5	
499	18.4	556	6	NNN bend
556.1	8.1	573.4	20.9	NNN bend
644.2	11.7	694.3	8.2	
799.9	2.3	794.6	2.2	
839.1	0.5	858.6	17.1	
969.6	19.5	949	23.5	
1012.3	2.1	994.7	4.5	
1069.5	0.5	1077.9	1.6	
1232.5	2.2	1181.8	95.9	CH_2 twist
1240.6	132.4	1251	2.9	CH_2 twist
1342.8	5.8	1340.3	105.4	NNN sym. str. + CH_2 wag
1348.9	147.5	1368.1	32.1	NNN sym. str. + CH_2 wag
1394.6	45.2	1393.5	32	CH_3 umbrella mode
1454.5	8.3	1463.4	2.3	CH_2 bend + CH_3 umbrella
1461.4	52.3	1469.6	22.5	CH_2 bend + CH_3 umbrella
1468.3	12.8	1482.5	10.7	CH_3 str. + torsion

Table 4.2 …*continued*

anti: *dihedral angle* φ_{NNCC} *= 180°*		gauche: *dihedral angle* φ_{NNCC} *= 64°*		approximate assignment
frequency [cm^{-1}]	intensity [km/mol]	frequency [cm^{-1}]	intensity [km/mol]	
1794.3	207.7	1807.4	109.7	CO str. + ?
2255.3	601.8	2255.9	522.3	NNN asym. str.
3024.1	21.8	2990.8	31.9	CH_2 sym. str.
3050.2	0.3	3041.7	3.4	CH_3 sym. str.
3069.8	7.5	3104.6	8	CH_2 asym. str. + ?
3110.9	3.3	3112.3	7.8	CH_2 str. + CH_3 str.
3167.2	10	3161.2	5	CH_3 asym. str.

4.3.2 Experimental Results

The infrared absorption spectra of both compounds in solid neon, argon and nitrogen were recorded in the range from 500 cm^{-1} to 4000 cm^{-1}, with selected regions being shown in Figures 4.1 – 4.5. A comprehensive listing of the bands observed in our experiments, and their tentative interpretation, as well as the previous assignments for AzN by *Klaeboe et al.* [44] are collected in Tables 4.3(AzN data) and 4.4(AzC) at the end of this subchapter.

Very often matrix isolation yields excellent quality spectra with sharp absorption bands, which exhibit little perturbation when compared with the gas phase. In fact, one way to judge the extent of the medium effect is to compare spectra using several different matrix materials — negligible changes from matrix to matrix usually imply also a small medium shift from gas phase to matrix, and this was one of the reasons for performing our current study.

However, in the present case, most of the observed spectral bands are relatively broad, and they also exhibit appreciable, matrix dependent changes in terms of band width, band shape, and band intensity from matrix to matrix. Also somewhat surprisingly, the observed bands are broadest in solid neon, which usually yields the best quality spectra. One usually gets excellent quality sharp spectra when the guest fits well into the crystalline structure of

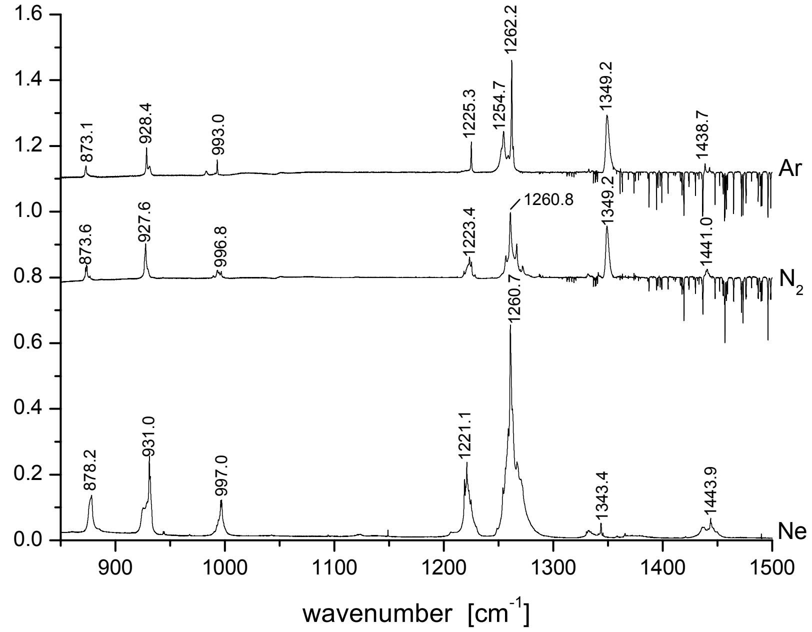

Figure 4.2. Infrared spectra of azidoacetonitrile in neon, nitrogen and argon matrices (“negative” lines in CH_2 bend region originate from gas phase water subtraction).

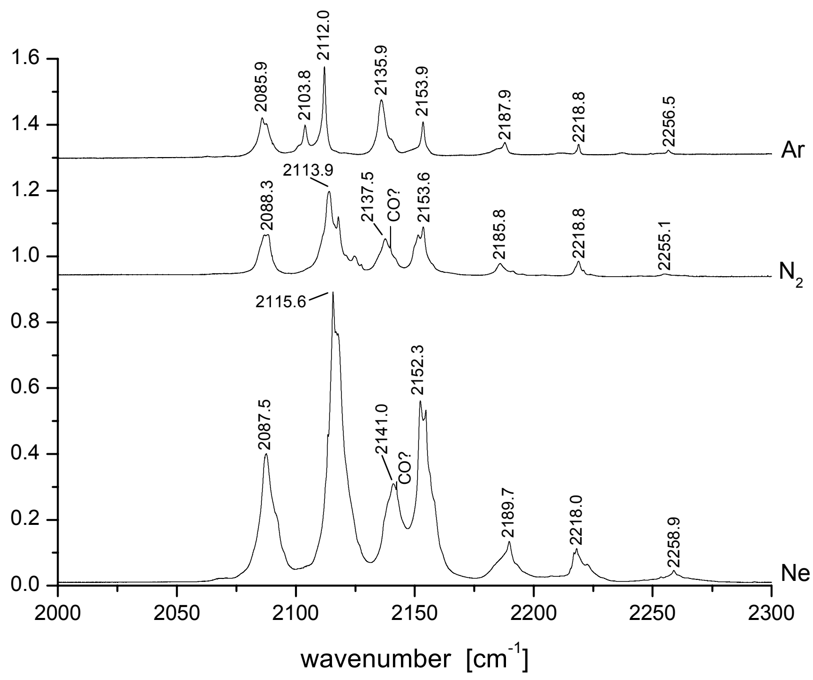

Figure 4.3. Infrared spectra of azidoacetonitrile in neon, nitrogen and argon matrices.

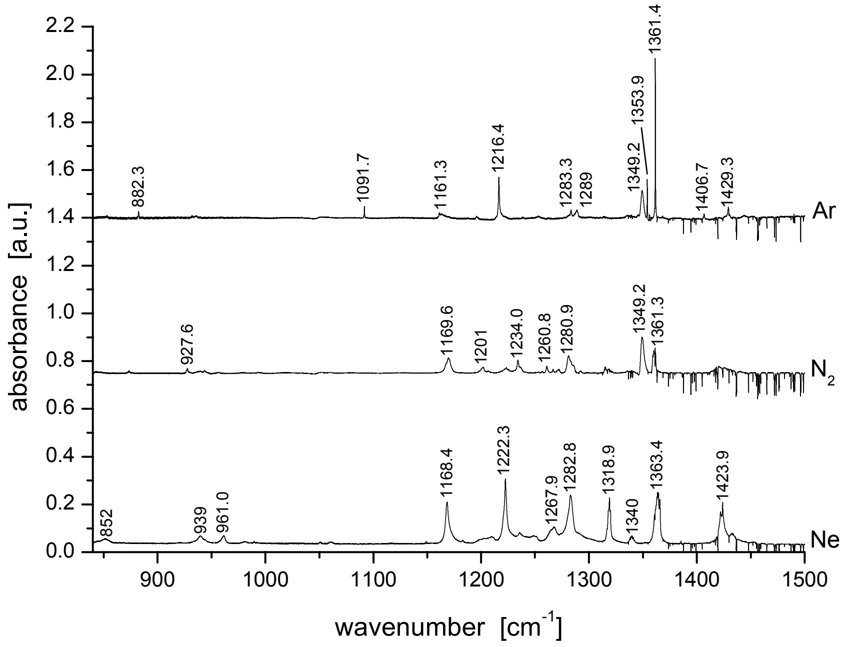

Figure 4.4. Infrared spectra of azidoacetone in neon, nitrogen and argon matrices.

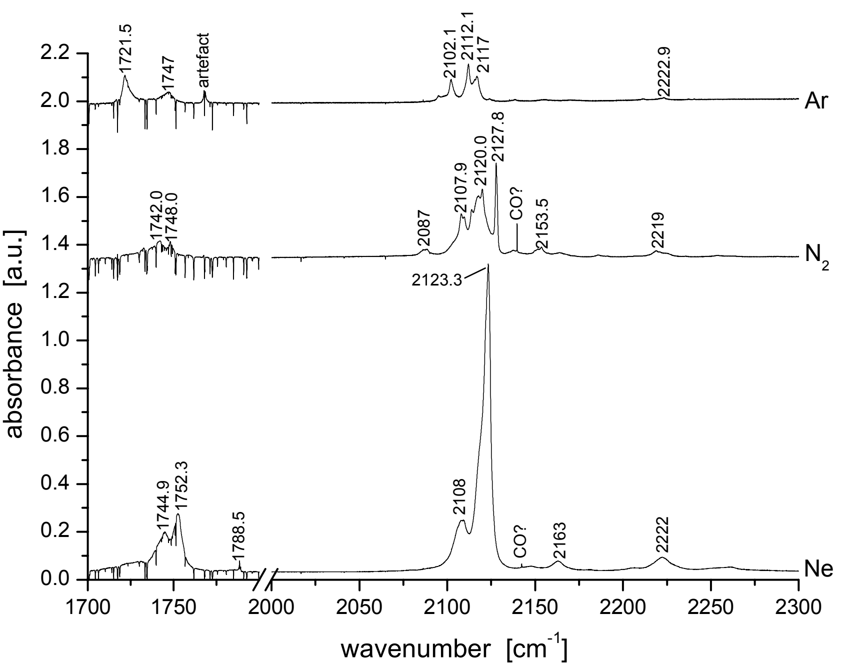

Figure 4.5. Infrared spectra of azidoacetone in neon, nitrogen and argon matrices (“negative” lines in CO stretch region originate from subtraction of gas phase water). No spectral features in 1800 – 2000 cm^{-1} have been observed.

the host. Thus linear compounds and cations of the type $X–(C_2)_n–Y$, or for instance fluorinated benzene cations, yield very sharp, unperturbed spectra [49-51]. In fact, in both cases two spectrally shifted sites are observed, which were attributed to species isolated in relatively unperturbed closely packed crystalline fcc or hcp environment, respectively. The former, linear compounds replace a row in a plane of neon atoms, while the latter, benzenes, fit well into a site replacing seven atoms in a crystallographic plane. One interpretation of broad bands is an awkward fit of the relatively bulky, low symmetry guest into the solid host, preventing formation of a well-developed local crystalline structure, and resulting in poorly-defined sites, with a wide range of local geometries.

Also the theoretical computations are of less help than is often the case. Thus, as shown in Table 4.1, by far the strongest band computed for AzN is the asymmetric stretching frequency of the N_3 group, predicted to lie in both conformers at about 2254 cm^{-1} (unscaled) with the only other fundamental frequency in this region being the almost three orders of magnitude weaker C–N stretching frequency expected at 2358 cm^{-1} (2377 cm^{-1} in the anti compound). The experimental spectrum reveals at least seven bands, several of them quite strong, extending from 2085 to 2259 cm^{-1} (Figure 4.3). Some of these bands exhibit asymmetric line shapes and additional splitting, and appreciable changes in their shapes, frequencies, and relative intensities from matrix to matrix. The corresponding N_3 symmetric stretch is computed to be the second strongest absorption band. It is predicted to be in the anti and gauche conformers at 1333 and 1314 cm^{-1}, respectively, with the latter value scaled by a factor of 0.96 coming very close to the observed band appearing in all three matrices between 1260 – 1262 cm^{-1} (Figure 4.2).

The three weak to moderately intense bands appearing in all three matrices in the relatively narrow regions around 1221 – 1225, 1343 – 1349 and 1438 – 1444 cm^{-1} (Figure 4.2) are with all probability due to the motions of the CH_2 group, twist, wagging and bending, respectively, in acceptable agreement with the predicted values of 1254, 1372 and 1476 cm^{-1}, unscaled (gauche, Table 4.1). These modes are computed at similar frequencies and intensities in the gauche and anti species, and therefore do not provide a useful basis for distinguishing between the two.

Most useful for discriminating between the two conformers appears to be the 700 – 1100 cm^{-1} region. The three moderately intense bands observed in the experimental spectrum of AzN near 993 – 997, 928 – 931, and 873 – 878 cm^{-1}, respectively (Figure 4.2), are in a distinctly better agreement with the comparably intense 1006, 938, and 884 cm^{-1} bands predicted for the gauche conformer, than with the two strong and one very much weaker anti species bands, computed to lie near 979, 974 and 945 cm^{-1}.

The previously noted, complex structure in the region of the asymmetric N_3 stretch, which is insensitive to the sample deposition rate and conditions, and which does not change upon sample annealing or photolysis is unlikely to be due to the presence of multiple conformers. The more than 150 cm^{-1} range of the observed bands is way too large to be attributed to matrix sites, and suggests that the appearance of the spectrum is due to an intrinsic property of AzN. The molecule has a low, C_1 symmetry, and the most likely explanation of the observed multiple strong bands seems to lie in very strong Fermi resonances between the N_3 asymmetric frequency, the CN stretching frequency, and combinations and overtones of the numerous lower frequency vibrational modes expected in this region. It should be mentioned that also a previous study [44] suggested a similar complexity in this region even in the gas phase spectrum. A rather weak band observed in all three matrices around 2255 – 2259 cm^{-1}, but absent from the spectra of azidoacetone to be discussed below is undoubtedly due to the C–N stretching vibration (Figures 4.3, 4.5).

For the more complex azidoacetone molecule (AzC), with its twelve atoms and thirty vibrational modes, more complex infrared spectra should be expected, making their interpretation correspondingly more difficult. Similar to AzN, also in the AzC by far the most intense infrared fundamental is predicted to be the asymmetric N_3 vibration, computed to lie in both conformers near 2255 cm^{-1} (unscaled). Also here several structured bands are found in this region, whose appearance, width and splitting changes substantially from matrix to matrix (Figure 4.5). In neon a dominant band appears at 2123.3 cm^{-1} with a much weaker shoulder at 2108 cm^{-1} and two much weaker ones at 2163 and 2222 cm^{-1}. All these bands are relatively symmetric, and have widths in excess of 10 cm^{-1}. In argon and nitrogen matrices there is not one dominant band, but a more complex structure, with the strong band appearing to have split into several components with differing widths and intensities, as can be seen in Figure 4.5.

Three other bands of the AzC gauche conformer are predicted to have appreciable intensities: the C–O stretch at 1807 cm^{-1}, and bands at 1340 and 1182 cm^{-1}, presumably the symmetric N_3 stretch and a CH_2 twist. These two latter modes are possibly strongly mixed, and they are computed to be somewhat shifted to 1349 and 1241 cm^{-1} in the higher energy anti conformer. Experimentally, in all three matrices, two bands are found in the carbonyl region, at 1752.3 and 1744.9 cm^{-1} in neon, 1747 and 1721.5 cm^{-1} in argon, and 1748 and 1742 cm^{-1} in nitrogen (Figure 4.5). Besides significant changes in their frequencies from matrix to matrix, also their relative intensities are found to change, with the higher frequency band being more intense in neon, but the lowest, 1721.5 cm^{-1} band having the highest intensity in the argon matrix.

The assignment of the numerous lower frequency modes, which are probably in view of the low molecular symmetry strongly mixed, becomes more difficult. Comparison with the AzN would seem to dictate assigning in solid neon the rather strong band at 1282.8 cm^{-1} to the N_3 symmetric stretch, and the absorptions near 1222, 1363, and 1424 cm^{-1} to the twisting, wagging, and bending motions of the CH_2 group (Figure 4.4).

As it was already commented above, many of the spectral lines of the matrix isolated molecules investigated here are unusually broad, and it was suggested that one explanation might be an awkward fit into the matrix site, preventing the formation of a well-developed crystalline structure of the host matrix in the neighborhood of the guest dopant. Another remarkable observation involves the significant shifts of individual bands from matrix to matrix, and in particular the large changes in the band widths and relative intensities. A possible interpretation of this may lie in the polar nature of the azide group. In general, matrices tend to stabilize strongly ionic or polar structures, and this stabilization will be a strong function of the polarizability of the host atoms or molecules.

One should also notice that in a series of annealing experiments, and photolysis of the matrices at various wavelengths, for both AzN and AzC compounds, no appreciable spectral changes were detected. No new bands appeared following irradiation of the matrices, there were also no substantial changes in relative band intensities, and for a given matrix the relative intensities remained consistent from experiment to experiment. Overall, the observed spectra can be interpreted in terms of the azides being isolated in the lowest energy, gauche conformation, and no clear evidence of the simultaneous presence of several conformers was found.

Table 4.3. Experimental data for azidoacetonitrile isolated in Ne, N_2 and Ar solids.[*]

Ne matrix	N_2 matrix	Ar matrix	assignment	
			previous (N_2) [#]	
561.8	560.0 [#]	560.1	NNN bop	
563.3	~561.3			
689.1	~684	686.1	NNN bend	NNN bend
691.5	~691	698.1		
	872.8			C-C/C-N
878.2 m	873.6 m	873.1 m	C-C/C-N	sym. str.
	874.1		bend	
~925.5	927.6 s	928.4 s	CH_2 rock	CH_2 rock
~929.2	929.7	931.2		+
931.0 s				C–C/C–N asym
931.8				str
943.7				
944.6				
990.0	~989.4	982.8 b		CH_2 rock
992.6	~993	993.0 m		+
993.9	994.7			C–C/C–N asym
962.2	996.8			str
997.0 m				
~1123				
1149.1				
~1206				
1218.9				
1220.0	1218.5			
1221.1	1223.4 m	1225.3 s		CH_2 twist
1222.1 s	1225.5			
1223.1	1228.7		CH_2	
1224.9			tors.	
1248.6		~1252.5		
1254.0		1254.7 m		
~1256.3	1256.6			
~1258.9	1258.6	~1258.9		
1260.7 vs	1260.8 vs		CH_2 wag	NNN
1262.7	~1266.7	1262.2 vs		sym. str.
~1266.8	~1272.3	1263.5		
~1270.7				
~1272.2				

Table 4.3 *…continued*

Ne matrix	N_2 matrix	Ar matrix	assignment	
			previous (N_2) [#]	
1330.3 1332.6 1334.5	~1331.6	1332.5	N=N str.	
1343.4 1343.8	1349.2 vs	1349.2 vs		CH_2 wag
1345.5				
1365.5		1361.4		
1437.4 b 1443.9 1449.7	~1440 1440.5 1441.0	1438.7 1442.7 1442.8	CH_2 bend	CH_2 bend
2087.5 s ~2092.2	2085.8 2088.3 s	2085.9 s 2087.8 2103.8 s		
2113.4 2115.6 vs 2116.9 2117.7	2113.9 vs 2117.7 2124.8 2127.6	2112.0 vs	N≡N str.	bands due to anharmonic resonance involving mainly NNN asymmetric stretching
2141.0	2137.5 s	2135.9 s ~2140.3		
2152.3 vs 2154.6	2151.4 2153.6 s	2153.5 s		
2189.7 m	2185.8 m 2191.4	2187.9 m		
2216.9 2218.0 m 2222.6	2218.8 m 2221.4	2218.8		
~2253.6 2258.9	~2254.7 b	2256.5	C≡N str.	C≡N str.

---

[*] i) Weak bands around 2500 cm^{-1} and in the range of 2900 – 4500 cm^{-1} as well as matrix isolated water and CO_2 bands regions have been omitted.

ii) Frequencies grouped in braces show fine structure of the bands; m–medium, s–strong, vs–very strong, the others are weak or very weak ; b–broad.

[#] Underlined frequencies correspond to previous assignment [44].

Table 4.4. Experimental data for azidoacetone isolated in Ne, N_2 and Ar solids.*

Ne matrix	N_2 matrix	Ar matrix	assignment
~573.7	~573.9	~575	NNN bend
~643.3	~641.1		
~695.5	~700.2		
852.2		882.3	
931.0	927.6	932.4	
		~935.1	
~939 m,b	~939		
959.7	943.8		
~961.0 m,b	~956.6 b		
~980 b			
1050.8			
1061.0		1091.7	
1149.1			
		1161.3	
1168.4 s	1169.6 m	~1163 b	
~1208 b	~1201	~1195.9	
~1210 b	~1223.3	1216.4 s	
	1225.4		
1222.3 s			CH_2 twist
	1234.0 m		
1235.4	~1236.0		
~1249 b			
	1260.8		
	1266.7		
1264	1271.8		
1267.8 m			
	1280.9 m		
1282.8 s	1285.7		NNN
		1283.3	sym. str.
	1292.3	~1289 b	
1316.5	~1315.0		
1317.8	~1318		
1318.9 m			
1319.9			
~1339.5 b			

* i) Weak bands around 2500 cm^{-1} and in the range of 2900 – 4500 cm^{-1} as well as matrix isolated water and CO_2 bands regions have been omitted.

ii) Frequencies grouped in braces show fine structure of the bands; m–medium, s–strong, vs–very strong, the others are weak or very weak ; b–broad.

Table 4.4 …*continued*

Ne matrix	N_2 matrix	Ar matrix	assignment
1349.2 s	1349.2 s	1353.9 s	
1363.4 s	1359.2	1354.8	CH_2 wag
1364.4	1360.0 m	1356.2	
1365.6	1361.3	1357.6	
		1358.1	
		1361.4 vs	
		1362.6	
		1363.1	
		1363.2 m	
1421.9	~1422 b	1406.7	
1423.9 s		1429.3	CH_2 bend
1432.9 m,b			
~1729	~1732.4 m	1721.5 s	CO str. + ?
~1744.9 s	1742.0	~1747 m,b	
1752.3 s	1748.0		
1788.5			
	~2087		
~2108 s	2107.9 s	~2095.1	
	2109.7	2102.1 s	
		2112.1 s	
	2113.9	2115.6	bands
	~2117	2116.8 s	due to
2123.3 vs	2120.0 vs		anharmonic
	2127.8 vs		resonance
			involving
	2151.4		mainly
	2153.6		NNN
2163 b			asym. str.
	~2219.0 m,b	2211.3	
~2222 m,b	2224.9	2222.9	

4.4 Conclusions

The infrared spectra of organic azides, azidoacetonitrile (N_3CH_2CN) and azidoacetone ($N_3CH_2COCH_3$), isolated in low temperature solids have been measured by means of Fourier-transform technique in the range from 500 to 4000 cm^{-1}. A comparative study in neon, argon and nitrogen matrices has shown that most of the observed spectral bands are relatively broad, exhibiting appreciable changes in terms of band width, band shape, and band intensity from host to host. Significant broadening of the recorded azide bands indicate an awkward fit of the low symmetry molecules into the solid host, resulting in a wide range of local environments. Based on the DFT calculations of IR spectra for optimized structures, the strongest absorption bands observed for both compounds were assigned to asymmetric and symmetric stretches of the N_3 azide group. Strong Fermi resonances involving N_3 asymmetric stretch, CN stretch and combinations and overtones of the numerous lower frequency vibrational modes are the most probable reason for the strong band splittings occuring in the asymmetric stretch region of the N_3 group.

References

[1] N. Bartlett, *Proc. Chem. Soc.* **218** (1962).

[2] F.O. Sladky, P.A. Bulliner, N. Bartlett, *J. Chem. Soc. A* 2179 (1969).

[3] L. Khriachtchev, M. Pettersson, N. Runeberg, J. Lundell, M. Räsänen, *Nature* **406**, 864 (2000).

[4] K.O. Christe, *Angew. Chem. Int. Ed.* **40**, 1419 (2001).

[5] H-J. Frohn, N. LeBlond, K. Lutar, B. Zemva, *Angew. Chem. Int. Ed*. **39**, 391 (2000).

[6] W. Tyrra and D. Naumann, *Inorganic Chemistry Highlights*, *Organoxenon Compounds*, ed. G. Meyer, D. Naumann, L. Wesemann, John Wiley & Sons, New York, 2002.

[7] L.Y. Nelson and G.C. Pimentel, *Inorg. Chem.* **6**, 1758 (1967).

[8] W.F. Howard, Jr. and L. Andrews, *J. Am. Chem. Soc.* **96**, 7864 (1974).

[9] J.J. Turner and G.C. Pimentel, *Science* **140**, 974 (1963).

[10] V.E. Bondybey and G.C. Pimentel, *J. Chem. Phys.* **56**, 3832 (1972).

[11] D.E. Milligan and M.E. Jacox, *J. Mol. Spectrosc.* **46**, 460 (1973).

[12] C.A. Wight, B.S. Ault and L. Andrews, *J. Chem. Phys.* **65**, 1244 (1976).

[13] P.N. Noble and G.C. Pimentel, *J. Chem. Phys.* **49**, 3165 (1968).

[14] D.E. Milligan and M.E. Jacox, *J. Chem. Phys.* **53**, 2034 (1970).

[15] V. Bondybey, G.C. Pimentel and P.N. Noble, *J. Chem. Phys.* **55**, 540 (1971).

[16] D.E. Milligan and M.E. Jacox, *J. Chem. Phys.*,**55**, 2550 (1971).

[17] M. Pettersson, J. Lundell, M. Räsänen, *Euro. J. Inorg. Chem*. 729 (1999).

[18] M. Lorenz, M. Räsänen, V.E. Bondybey, *J. Phys. Chem. A* **104**, 3770 (2000).

[19] J. Lundell, A. Cohen, R.B. Gerber, *J. Phys. Chem. A* **106**, 11950 (2002).

[20] M. Pettersson, L. Khriachtchev, J. Lundell, M. Räsänen, *J. Am. Chem. Soc.* **121**, 11904 (1999).

[21] L. Khriachtchev, H. Tanskanen, J. Lundell, M. Pettersson, H. Kiljunen, M. Räsänen, *J. Am. Chem. Soc.* **125**, 4696 (2003).

[22] V.I. Feldman, F.F. Sukhov, A.Yu. Orlov, I.V. Tyulpina, *J. Am. Chem. Soc.* **125**, 4698 (2003).

[23] W. Swan, *Ann. Physik. Chemie* **100**, 306 (1857).

[24] S.R. Langhof, M.L. Sink, R.H. Pritchard, C.W. Kern, S.J. Strickler, M.J. Boyd, *J. Chem. Phys.* **67**, 1051 (1977).

[25] J.E. Bourlot, E. Roueff, *J. Mol. Spectrosc.* **120**, 157 (1986).

[26] E.F. van Dishoeck, J.H. Black, *Astrophys. J.* **258**, 583 (1982).

[27] G.M. Lask, J. Agreiter, R. Schlachta, V.E. Bondybey, *Chem. Phys. Lett.* **205**, 31 (1993).

[28] V.E. Bondybey, *J. Chem. Phys.* **65**, 2296 (1976).

[29] V.E. Bondybey, L.E. Brus, *J. Chem. Phys.* **63**, 2223 (1975).

[30] L.E. Brus, V.E. Bondybey, *J. Chem. Phys.* **63**, 3123 (1975).

[31] G. Maier, Ch. Lautz, *Eur. J. Org. Chem.* **769** (1998).

[32] A. Thoma, B.E. Wurfel,R. Schlachta, G.M. Lask, V.E. Bondybey, *J. Phys. Chem.* **96**, 7231 (1992).

[33] A.M. Smith, J. Agreiter, M. Härtle, C.Engel, V.E. Bondybey, Chem. Phys. 189, 315 (1994).

[34] *Gaussian 98*, *Revision A.11*, M. J. Frisch, G. W. Trucks, H. B. Schlegel, G. E. Scuseria, M. A. Robb, J. R. Cheeseman, V. G. Zakrzewski, J. A. Montgomery, Jr., R. E. Stratmann, J. C. Burant, S. Dapprich, J. M. Millam, A. D. Daniels, K. N. Kudin, M. C. Strain, O. Farkas, J. Tomasi, V. Barone, M. Cossi, R. Cammi, B. Mennucci, C. Pomelli, C. Adamo, S. Clifford, J. Ochterski, G. A. Petersson, P. Y. Ayala, Q.

Cui, K. Morokuma, P. Salvador, J. J. Dannenberg, D. K. Malick, A. D. Rabuck, K. Raghavachari, J. B. Foresman, J. Cioslowski, J. V. Ortiz, A. G. Baboul, B. B. Stefanov, G. Liu, A. Liashenko, P. Piskorz, I. Komaromi, R. Gomperts, R. L. Martin, D. J. Fox, T. Keith, M. A. Al-Laham, C. Y. Peng, A. Nanayakkara, M. Challacombe, P. M. W. Gill, B. Johnson, W. Chen, M. W. Wong, J. L. Andres, C. Gonzalez, M. Head-Gordon, E. S. Replogle, and J. A. Pople, Gaussian, Inc., Pittsburgh PA, 2001.

[35] A. Nicklass, M. Dolg, H. Stoll, H. Preuss, *J. Chem. Phys.* **102**, 8942 (1995).

[36] F.Y. Naumkin, R.W. McCourt, *J. Chem. Phys.* **107**, 1185 (1997).

[37] K.P. Huber, G. Herzberg, *Molecular Spectra and Molecular Structure, Band IV: Constants of Diatomic Molecules*, Van Nostrand Reinhold, New York (1979).

[38] G. Herzberg, A. Lagerqvist, Can. J. Phys. **46**, 2363 (1968).

[39] M A Bohn, *Thermochimica Acta* **33**, 121 (1999).

[40] C. Gauthier , Y. Ramodenec, *Tetrahedron* **57**, 7513 (2001).

[41] A.E. Taubl , K. Langhans, T. Kappe, W. Stadbauer, *J. Heter. Chem.* **39**, 1259 (2002).

[42] O.P. Korobeinichev, L.V. Kuibeida, E.N. Volkov, A.G. Shmakov, *Comb. Flame* **129**, 136 (2002).

[43] G. Williams, C. Dsilva, *Sensors and Actuators B-Chem.* **30**, 151 (1996).

[44] P. Klaeboe, K. Kosa, C. J. Nielsen, H. Priebe, S. H. Schei, *J. Mol. Struct.* **160**, 245 (1987).

[45] J. M. Dyke, A.P. Groves, A. Morris, J. S. Ogden, M.I. Catarino, A. A. Dias, A. M. S. Oliveira, M. L. Costa, M. T. Barros, M. H. Cabral, A. M. C. Moutinho, *J. Chem. Phys. A* **103**, 8239 (1999).

[46] M. Algarra, A. A. Dias, M. L. Costa, P. Rodrigues, M. T. Barros, V. H. C. Lopes, M.N.D.S. Cordeiro, G. Levita, J. M. Dyke, A. Morris, J. S. Ogden *(to be submitted).*

[47] M. I. Catarino, B. J. Costa Cabral, M. L. Costa, *J. Mol. Struct. (Theochem)* **397**, 223 (1997).

[48] K. Freudenberg, H. Eichel, F. Leutert, *Ber. Dtsh. Chem. Ges.* **65**, 1183 (1932).

[49] J. Agreiter, A.M. Smith, V.E. Bondybey, *Chem. Phys. Lett.* **241**, 317 (1995).

[50] A.M. Smith, J. Agreiter, V.E. Bondybey, *Chem. Phys. Lett.* **244**, 379 (1995).

[51] V.E. Bondybey, M. Lorenz, *J. Low Temp. Phys.* **122**, 509 (2001).

PART III

Matrix-Isolation Infrared Spectroscopy of Mass-Selected Ions

Selectively deposited positive molecular ions in neon matrices are characterized spectroscopically by means of the FT-IR method. Ionic species are generated by electron impact ionization with parallel fragmentation and ion-molecule reactions of a precursor substance in an electron impact (EI) source. The ions are deposited together with an excess of electrons to prevent a buildup of space charge. Infrared assignments are supported by density functional (DFT) calculations. This part includes three chapters dealing with the tetracyanoethylene cation and its ionic fragments, protonated and fragment ions of acetonitrile and the acetylene cation.

The first two chapters show results on the molecular ions containing cyano (CN) groups, which are of special interest for processes occurring in interstellar space. The first chapter concentrates on the tetracyanoethylene cation, $C_6N_4^+$, and its fragment ions C_2N^+, $C_4N_2^+$, $C_3N_2^+$, $C_5N_3^+$, $C_6N_3^+$.

An interesting photochemical effect was observed in all IR spectra in neon matrices: a detrapping or photomobilization of electrons resulted in formation of a $C_6N_4^-$ anion.

Use of the acetonitrile precursor resulted in the infrared spectra of protonated acetonitrile CH_3CNH^+. The N–H(D) and $CH(D)_3$ stretching vibrations observed in neon matrix are attributed to the CH_3CNH^+ and its deuterated analogue CD_3CND^+. Deposition of cyanomethyl radical cations $C_2H(D)_2N^+$ allowed for identification of the unknown $HCCNH^+$ ($DCCND^+$) isomer. Tentative spectral assignments are also made for two other isomers, $H(D)_2CCN^+$, $H(D)_2CNC^+$.

The results of investigation of acetylene cation, $C_2H_2^+$ are presented in the last chapter.

General Overview

Molecular and atomic ions are ubiquitous species in terrestrial and extraterrestrial environments. On our home planet one can distinguish plasmas and flames as two prominent gas-phase media where ions occur. Although ions represent only a minute fraction of the total mass of the Earth's atmosphere they play a crucial role in many geophysical phenomena [1-3]. Interest in the behavior of the electrons and ions in the Earth's atmosphere has provided major impetus to atomic physics for many years. In outer space, interstellar clouds and tails of comets are of special interest for occurring ionic processes. The observed species are mainly organic and reflect a high abundance of elemental carbon [4]. However, their examination reveals that species containing linear carbon atom chains are quite disproportionately represented. Polyacetylenic chain molecules, being rather unstable and reactive are quite ubiquitous in dense interstellar clouds or carbon stars as formed efficiently by numerous radical and ionic reactions. On the other hand, besides the atmospheric and interstellar space environment one should consider the phenomena of life. In this case, most of the chemical and biochemical processes involve ions in liquid solutions [5].

Indeed, the reason for which a field of molecular ion spectroscopy and high sensitive mass spectrometry methods have developed into a very active subject, become very obvious. Nowadays one can still observe an explosive growth in this research field. While mass spectrometry and related methods can provide very useful data about the existence and stability of molecular ions, they give little information about their structures and usually can not even differentiate between isomeric species. Fortunately the recent progress in experimental methods significantly extended this area making it also available to spectroscopists. This contributed a wealth of new information about the geometry of ionic species, their vibrational and electronic structures, and their chemistry [6]. The studies of molecular ions in the gas phase are complemented by infrared and optical absorption techniques applied to ions isolated in rare gas matrices. Ions trapped and accumulated in such cryogenic solids are also examined using extremely sensitive emission techniques employing laser sources.

The first ionic species observed in matrices, and classified as isolated, were $B_2H_6^-$ and C_2^- anions separated by an undetermined number of host atoms from their counterions (in 1969 by *Kasai* and *McLeod*, *Miligan* and *Jacox* [7,8]). These ionic systems have been characterized as Coulomb ion pairs existing because of essentially zero overlap between the wavefunctions of the electrons of the recipient molecule and the cation formed after providing the electron [9]. Formation of such an ion in the solid host requires that the ionization energy of the embedded precursor atom or molecule is supplied by an external source producing electron and cation. Electrons can be trapped somewhere in the matrix or by another species to form anions. Another class of ions examined in matrices are ions described as chemically bound with respect to the counterion, i.e. charge-transfer complexes, with the first one, $Li^+O_2^-$, studied by *Andrews* [10]. Later results obtained by *Bondybey et al.* for $C_6F_6^+$ in solid Ne provided unambiguous information on trapped cations fully demonstrating the usefulness of this technique for future spectroscopic studies [11].

Although many successful experiments have been reported, one of the problems in exploring complex polyatomic ions as well as radicals is that they are rarely produced selectively by ion sources. Often deposited matrices result in complex mixtures of the target species characterized by different elemental composition and different charge. This situation has obviously an influence on the interpretation of obtained spectra which for polyatomic species become extremely difficult, and tedious, if possible at all. The combination of the two applied experimental techniques presented in this work, mass spectrometry and high resolution FT-spectroscopy of mass-selected species isolated in rare gas matrices, makes this method unsurpassable in its effectiveness in obtaining new spectroscopic information. In such a case the assignments of the observed peaks are based on the comparison of the spectra obtained from the samples prepared by deposition of ions of different masses.

Studies of Mass-Selected Species in Rare Gas Matrices

In spite of considerable difficulties, one can observe a dynamic progress since the first successful experiments were reported by several research groups some fifteen years ago. The attempts with radical H_2O^+ and CO^+ cations in Ne matrix generated in an electron impact source and selectively deposited using a quadrupole mass filter were very briefly commented by *Knight* [12] as rather inefficient. *Rivoal et al.* adapted a triple quadrupole system for mass-selected studies of metal clusters to a matrix-isolation setup starting from experiments with Ag_3^+ and Ni_3^+ produced with a sputter source [13,14]. Ions were deposited with Kr matrix gas and neutralized by electrons emanating from a tungsten filament. In spite of the attempts to decelerate incoming ions and "soft land" the ions on the matrix surface in the early experiments, considerable fragmentation apparently took place. Fortunately, further refinements permitted depositing observable (UV range) amounts of neutral Ag_n clusters with n up to 39 [15,16]. A series of interesting studies of absorption and resonance Raman spectra on small metal clusters, including dimers like V_2 [17], W_2 [18], Ta_2 [19], Hf_2 [20], Re_2 [21], Co_2 [22], Rh_2 [23], Ru_2 [24] and Pt_2 [25], trimers Zr_3 [26], Ni_3 [27], Nb_3 [28] Hf_3 [29] as well as Ta_4 [30] were performed by *Lindsay, Lombardi* and their coworkers. Successful experiments done by *Moskovits* and coworkers [31] started from the direct synthesis of metal cluster complexes by deposition of mass-selected Fe clusters with excess CO as ligand. In the next step, using resonance Raman method they were able to characterize Ag_3, Ag_5 and Fe_3 [32,33] in Ar matrices.

Leroi and *Allison* were able to reproduce the LIF spectrum of the CS_2^+ ion in solid Ar, but only the parent CS_2 and diatomic CS could be detected in the IR region [34]. The explanation of this observation has been found in neutralization of the ion accompanied by fragmentation to CS + S [35]. Later the same research group reported that the ion yield could be significantly enhanced by adding small quantities (0.1 %) of CO_2 to the matrix gas, which then traps the electrons and suppresses the ion-electron recombination [36]. In consequence the CS_2^+ ion was finally detected in the IR [37]. Later, experiments in Ar and Ne matrices resulted in infrared spectra of several ions, including the CF_3^+ and CO_2^+ [36,38]. The IR and the electronic spectra of CS_2^+ cation generated by microwave discharge were also recorded in our laboratory [39].

A series of very successful experiments on numerous carbon chain species has been carried out by the group of *Maier* [40]. Using typically acetylene or its derivatives diluted by helium or Ar as a precursor gas, the carbon chain molecules were produced in a hot-cathode discharge source [41]. The deposited mass selected species were examined in solid Ne matrices in the VIS/UV range, using a wave-guide absorption technique. The spectra obtained in this way for the HC_nH^+ (with $n = 4 – 16$), $HC_{2n+1}H$ ($n = 2 –7$) neutrals, $H–(C \equiv C)_n–CN^+$ ($n = 2 –6$) and $NC–(C \equiv C)_n–CN^+$ ($n = 1 –5$) [42-44] cations provided complementary information to LIF studies [45,47]. The same researchers used recently an electron impact ion source based on a hot-cathode Penning discharge to produce linear carbon chain anions [47,48]. Neutralization of anionic species through a photo-detachment of electrons allowed as well for characterization of the corresponding neutral species. Electronic absorption spectra of neutral and anionic carbon clusters, obtained by sputtering of a graphite target, seem to be particularly interesting since some of the spectral lines assigned to anions closely coincide with frequencies of the so-called diffuse interstellar bands [49,50].

A series of successful experiments have been demonstrated using the apparatus recently constructed in our laboratory in combination with homebuilt microwave discharge or electron impact ion sources. These studies involve a variety of species, like CS_2^+ and isotopic $^{34}S^{12}C^{32}S^+$, $C_6F_6^+$ [39] and more recently the EI ionization products of cyanoacetylene [51]. With the later precursor, besides a dicyanoacetylene cation $C_4N_2^+$ and known from the gas phase CNC^+ species, a HC_3N^+ and deuterated DC_3N^+ ions were observed. Tentative assignments were also possible for the C_3N^+ cation.

This work concentrates on Ne-matrix studies of several molecular ions containing a nitrile, CN group, like C_2N^+, $C_4N_2^+$, $C_3N_2^+$, $C_5N_3^+$ and $C_6N_3^+$ upon EI ionization of a tetracyanoethylene precursor. The same method allowed for observation of a protonated acetonitrile as well as some cationic $C_2H_2N^+$ isomers of a cyanomethyl radical using acetonitrile as precursor. In this case, spectral assignments are supported by deuterium isotopic study. The known acetylene $C_2H_2^+$ ion was also studied in Ne matrix. Density functional theory (DFT) with the hybrid B3LYP technique turned out to be an invaluable help in interpretation of infrared spectra for this type of compounds.

5 Tetracyanoethylene Ion and Its Ionic Fragments

5.1 Introduction

An apparatus for the deposition of mass-selected ions was recently applied to the FT-IR study of cyanoacetylene and dicyanoacetylene cations in neon matrices [51]. These successful experiments were motivation to continue the investigations of this family of compounds using tetracyanoethylene C_6N_4 as a precursor, commercially known as TCNE.

The choice of tetracyanoethylene is a result of searching for a suitable, stable, and readily available cyanocarbon precursor. Besides these properties, the C_6N_4 compound is sufficiently volatile and can be successfully used in our electron impact source. One of the goals of this experimental task was the detection and characterization of the C_5N_2 molecule found in the course of experiments designed to generate various cyano-carbon radicals and ions in low temperature matrices using a DC-discharge source [52]. As a result, although the EI source allowed producing the $C_5N_2^+$ ions using precursor, their yield was relatively minor. However, more than a dozen other ions, their majority being C_nN_m species, appeared in the mass spectrum with at least comparable intensities. C_2N^+, $C_4N_2^+$ and the parent ion $C_6N_4^+$, were more intense by more than an order of magnitude. Literature studies of those compounds revealed that many of these ions or corresponding neutrals were not known or very incompletely known, although their structures and properties appeared, in view of their abundance and easy formation in the electron impact source, to be of considerable interest. This situation was an inspiration to use the mass-selection apparatus to deposit and investigate some of these species. Like in previous studies on cyanoacetylene cations [51] recently done in our laboratory, the experimental observation of infrared spectra of the TCNE ion and its ionic fragments as well as neutral

C_5N_2 molecule, have been complemented with the support of density functional theoretical studies employing the *Gaussian 98* suite of programs [53].

Besides the various fragmentation products, there is also a considerable interest in the parent TCNE and its ions. It has been known for a number of years that compounds containing the $=C(CN)_2$, i.e. dicyanomethylene group, are highly electron deficient. In consequence they readily form charge transfer complexes, and are frequent components of conducting "organic metals" [54]. Particularly interesting and potentially important are complexes of TCNE with various organometallic compounds, which were shown to be molecular ferromagnets [55]. In these materials, unlike metals where the active spins are located in the atomic d or f orbitals, one active spin site is a molecular orbital made of atomic s and p orbitals, for instance the lowest unoccupied orbital (LUMO) of TCNE. While many of these species are ferromagnets only at extremely low temperatures of a few kelvins, recently a TCNE complex with bis(benzene)vanadium was found to retain its magnetic properties well above room temperature, with $T_c = 400$ K [56].

In view of the considerable interest in the charge transfer compounds, the structure of both TCNE and of its anions in various complexes have been extensively investigated. Depending on the composition of the complex and nature of the cation, formally either one or two electrons could be transferred to the TCNE. Both infrared and Raman spectra have in fact been reported not only for the neutral parent [57] and the radical anion, $TCNE^-$, but also for the doubly charged anion, $TCNE^{2-}$ [58]. Although the anion is readily formed and studied, at least as a complex, the electron impact source provided high yield of the $TCNE^+$ cations, with currents more than an order of magnitude higher than that of the $C_5N_2^+$.

In the present chapter the studies of mass-selected TCNE ions, as well as of several of its ionic fragments, deposited in solid neon matrices at a temperature of 7 K, are summarized. The infrared spectra for the parent molecule cation $C_6N_4^+$ (TCNE, mass 128 amu) and fragment cations: $C_4N_2^+$ (76 amu), C_2N^+ (38 amu), $C_3N_2^+$ (64 amu), $C_5N_3^+$ (102 amu), $C_6N_3^+$ (114 amu) isolated in Ne matrix are reported. Revisited examination of electronic transitions of the neutral C_5N_2 molecule — from mass 88 amu cation deposition — using the laser excitation method (VIS region) confirms the previous assignment to a linear NC_5N structure. The mass-selective cation deposition allows to identify and assign observed vibrational or electronic transitions for examined species. A comparison of spectra of samples obtained for different masses of deposited ions in combination with the results of density functional (DFT) computations facilitate the data interpretation.

Some interesting aspects related to the deposition and presence of positive ions and electrons in solid neon matrices, like neutralization and photochemical effects observed in all IR spectra are discussed on examples. Regarding the latter one, the formation of the well-known tetracyanoethylene anion $C_6N_4^-$ by means of a detrapping or photomobilization of electrons can be observed.

5.2 Experimental

Commercially available tetracyanoethylene (TCNE, Aldrich, 98 %) was used as precursor. To achieve a sufficient pressure the sample had to be heated during the deposition to 60 – 80° C, resulting in a pressure at 1×10^{-5} mbar pressure in the source chamber. In a typical experiment, the EI source was optimized for the ion of interest and the deposition was started after cooling down the cryostat to 7 K (LEYBOLD). Depending on the ion current the deposition times varied from 2 to over 20 hours. The Table 5.1 summarizes the deposition parameters for individual ions from the TCNE precursor.

Infrared, visible, or UV absorption spectra of the samples were then obtained with the BRUKER IFS 120 HR spectrometer, using the glowbar and tungsten sources, respectively. Spectra in the IR were usually measured with 0.06 cm^{-1} resolution, in the visible and UV range 1 cm^{-1} was in most cases adequate. Depending on the spectral range, liquid nitrogen cooled MCT and InSb (infrared) or Si or GaP (VIS, UV) detectors were used. Reference spectra containing the multiplied frequency responses of light source, detector and optical elements like windows and mirrors were obtained prior to deposition, and then at various times during the experiment, with digital spectral subtraction permitting to follow sensitively changes resulting from photolysis or annealing of the samples.

In order to record laser excitation spectra in the region of 440 nm of the C_5N_2 absorption, the samples were irradiated by a tunable ring dye laser operating with stilbene 3 dye and pumped by a multiline-UV Ar^+ ion laser. The fluorescence signal after pass through suitable filter eliminating or reducing scattered laser light was detected by a photomultiplier via a lock-in amplifier (see Figure 2.9 in *Chapter 2*).

Table 5.1. Ion current and total deposition time for examined cations selectively deposited in Ne matrix upon EI ionization of C_6N_4 precursor.

Cation	mass [amu]	average ion current [pA]	total deposition time [hrs.]
C_2N^+	38	175	15¾
$C_3N_2^+$	64	100	17.5
$C_4N_2^+$	76	1000	1.5
$C_5N_2^+$	88	40	16
$C_5N_3^+$	102	85	23
$C_6N_3^+$	114	175	17
$C_6N_4^+$	128	600	17.5

5.3 Results and Discussion

5.3.1 Computations

Computations were carried out by means of *Gaussian 98* using the hybrid B3LYP technique, and made first with the relatively modest 3-21+G** basis set. For some of the investigated compounds very little about their geometry was known, and in some cases the existence of several isomeric species was possible. The optimization with the small basis sets usually proceeded smoothly, yielding the approximate geometry and spectral information of the ion or molecule of interest. Subsequently, a new optimization was started departing from the converged geometry of the less sophisticated computation, this time using a larger 6-311++G(3d,3pd) basis set with two diffuse and four polarization functions on each atom.

Density functional computations seem to perform well for unsaturated hydrocarbons, their nitriles and similar species [59,60]. A useful approach for checking the accuracy and reliability of the methods used is naturally to carry out a similar computation for molecules for which well-established experimental data are available. Thus in the present case where many of the species investigated were unknown, computations were carried out for related known compounds, for instance the neutral tetracyanoethylene molecule, C_6N_4, or the C_2N^+ and $C_4N_2^+$ ions. In general, tests of this nature have confirmed that the methods employed can yield and predict not only molecular vibrational frequencies but also their intensities with usable accuracy and reliability. The computed frequencies in this work have all been scaled with a factor of 0.96, as used in previous work done in our group on the cyanoacetylene ions [51].

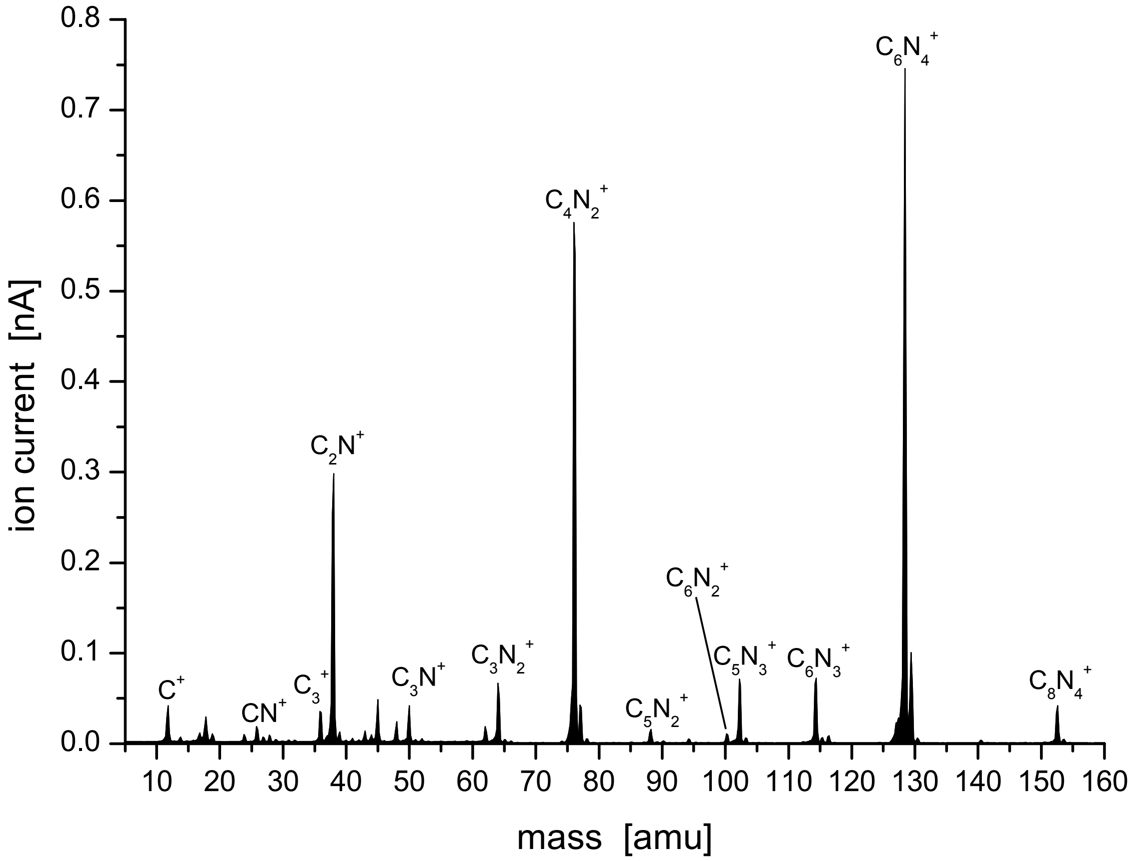

Figure 5.1. The quadrupole mass spectrum produced from the electron-impact ionization of tetracyanoethylene (TCNE) heated to 80 °C.

5.3.2 Mass Spectrum

The typical quadrupole mass spectrum of tetracyanoethylene (C_6N_4) heated to 80 °C and ionized in an electron impact ion source (EI) is shown in Figure 5.1. One can immediately notice that the spectrum is dominated to a large extent by C_nN_m compounds. The most intense ion peaks correspond to the tetracyanoethylene parent ion $C_6N_4^+$ and the fragments formed via loss of two CN groups, leading to $C_4N_2^+$ followed probably by breakage of the ethylene bond, leading to C_2N^+. With about an order of magnitude weaker currents appear the fragment ions $C_6N_3^+$, $C_5N_3^+$, $C_3N_2^+$, C_3N^+ and C_3^+. Secondary ion–molecule reactions in the source are evidenced by the appearance of ions with masses higher than the parent, for instance $C_8N_4^+$, which appears with an intensity similar to these fragment ions.

5.3.3 Matrix-Isolated Neutral TCNE

Previous studies carried out on mass-selected ions revealed that in view of the tortuous path from the source to the cryostat, with a right angle bend and several narrow apertures, there was in most cases relatively little evidence of the neutral parent reaching the matrix. In the present study, one could after deposition always identify in the spectrum besides absorptions due to the usual impurities, CO_2 and H_2O, also several bands of TCNE, tetracyanoethylene, used in the ion source. This is probably due to several factors. In the first place, the deposition times in the range from 10 to over 20 hours in the present work were considerably longer than those used in most previous studies with more volatile precursors. In the second place, the low volatility of TCNE, as well as the presence of the polar nitrile groups and multiple bonds in the molecules makes them apparently adhere strongly to the metal surfaces of the apparatus, making it difficult to completely free the apparatus of the compound after each experiment. This effect was very clearly seen after few experiments where pre-mixed tetracyanoethylene vapors and neon matrix gas were directly deposited onto the cold substrate. In this case even few of the later deposited samples of nominally pure neon contained TCNE neutral molecules which could easily be detected by infrared spectroscopy.

The set of vibrational frequencies derived from experiments and DFT calculations, together with the vibrational symmetry of the transitions, are listed in Table 5.2. For ease of comparison with theoretical results the intensity of the strongest experimentally observed peak is scaled to 100. Figure 5.2 shows the computed geometries for species presented in Table 5.2. The vibrations of TCNE are easily identifiable and exhibit accidental overlaps with the bands of the product ions. However, they did not disturb the experiment. Bands clearly associated with TCNE were the CN stretching modes at 2258.6, 2253.1 and 2222.8 cm^{-1}, as well as bands assigned to C–C stretches at 1153.5 and 955.6 cm^{-1}, all of them only slightly shifted from the known spectra of the solid [57]. As will be explained later, the assignment of all these bands to the same carrier, C_6N_4, is also confirmed by its photochemical behavior upon irradiation of the sample.

As already noted above, the vibrational spectrum of TCNE provides a convenient test of the computational methods used. As shown in Table 5.2, the B3LYP results suggest four relatively weak bands in the 600 – 4000 cm^{-1} infrared region investigated in the present work. The predicted frequencies (in cm^{-1}; intensities in km/mol) of 2252 (7), 2233 (31), 1105 (33) and 939 (19), scaled with the factor of 0.96 are in good agreement with the recorded bands. The experimental observation of three absorptions in the CN stretching region is probably due to a Fermi resonance involving IR-inactive vibrational modes.

It should be noted that the bands due to the neutral C_6N_4 were certainly not stronger in experiments where the parent $C_6N_4^+$ ions (nominal mass 128 amu) were deposited, than in those involving its ionic fragments. The presence of most of the neutral TCNE observed could therefore not be due to the neutralization of its cation. This is consistent with previous results and conclusions that charge recombination in the matrix during deposition is quite inefficient in experiments performed on our setup, in spite of the simultaneous spraying of the substrate with electrons from the hot filament during cation deposition.

5.3.4 Matrix-Isolated TCNE Cation

When the parent $C_6N_4^+$ cation is deposited (0.6 nA, 17.5 hours), besides the neutral C_6N_4 bands and the obvious impurities two new absorptions appear in the spectrum. As

Table 5.2. Infrared transitions frequencies [cm^{-1}] and intensities [km/mol]

Theory: DFT (B3LYP/6-311++G(3d,3pd)), scaled with *f* = 0.96			Experiment
ion, ground state	vibrational symmetry	DFT frequencies	Neon matrix[a]
neutral C_6N_4	b_{1u}	2252(7)	2258.6(100),2253.1(39)
$^1A'$	b_{2u}	2233(31)	2222.8(57)
D_{2h}	b_{2u}	1105(33)	1153.5(74)
	b_{1u}	939(19)	955.6(29)
$C_6N_4^+$	b_{1u}	2174(300)	2163.9(27)
$^2B_{3u}$	b_{2u}	2116(1395)	2108.4(100)
D_{2h}	b_{2u}	1158(91)	
	b_{1u}	958(20)	
$C_6N_4^-$	b_{1u}	2170(167)	2099(12)
$^2B_{3g}$	b_{2u}	2125(386)	2076(100)
D_{2h}	b_{1u}	957(9)	
$C_6N_3^+$	a’	2205(783)	?
$^1A'$	a’	2143(1088)	2158.4(100)
$C_{2\upsilon}$	a’	2133(481)	
	a’	1356(183)	
$C_6N_3^+$		2212(188)	
		2200(198)	
C_S		2181(408)	2158.4(100)
		1396(580)	?
$C_5N_3^+$		2221(179)	2248(100)
$^1?$		2212(210)	2219(67)
$C_{2\upsilon}$		2067(178)	
$C_3N_2^+$	σ_u	1908(1141)	1920.14(100)
$^2\Pi_g$	σ_u	1522(1)	
$D_{\infty h}$	π_u	365(7)	
CNC^+			
$^1\Sigma_g^+$	σ_u	1937(1363)	1972.9(100)[b]
$D_{\infty h}$	π_u	42(1)	65[c]

[a] Intensity of strongest IR peak in experiment is scaled to 100 to ease comparison.

[b] Gas phase at 1974.07 cm^{-1}, see Ref. [61]

[c] Observed as $\nu_3 + 2\nu_2$

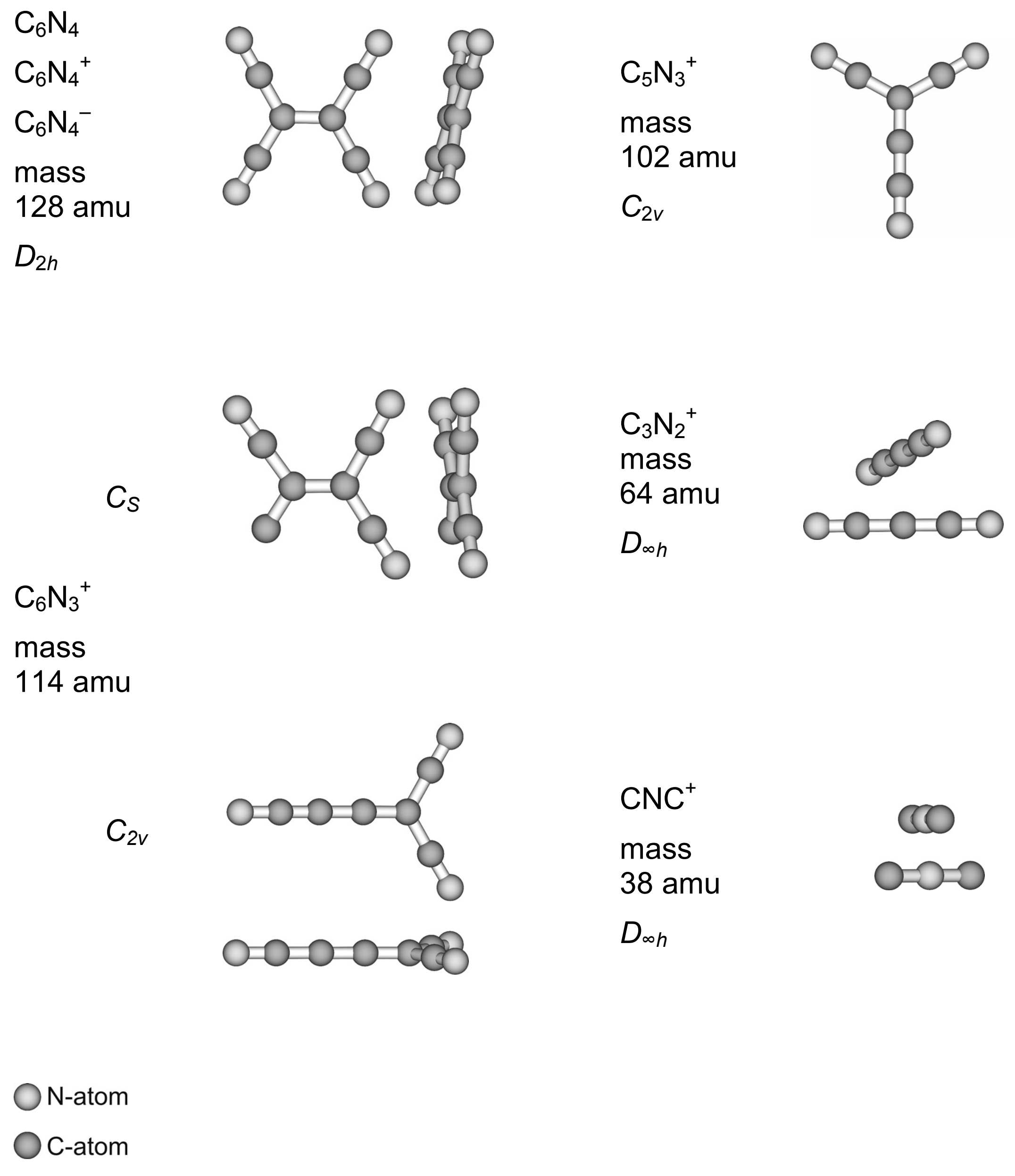

Figure 5.2 The computed geometries of TCNE molecule (angles for CN groups differ slightly for neutral, cationic and anionic form) and some of the observed ionic fragments.

can be seen in the relevant section of the spectrum in the top trace of Figure 5.3, one group of new, closely spaced sharp bands appears centered around 2108.4 cm^{-1}, with a similar group some 55 cm^{-1} higher in energy. This is in excellent agreement with the B3LYP calculation on $C_6N_4^+$ (D_{2h}), which predicts an extremely strong absorption band at 2116 cm^{-1} (1395), with a somewhat weaker one at 2174 cm^{-1} (300), and otherwise much weaker lower frequency infrared transitions, as listed in Table 5.2.

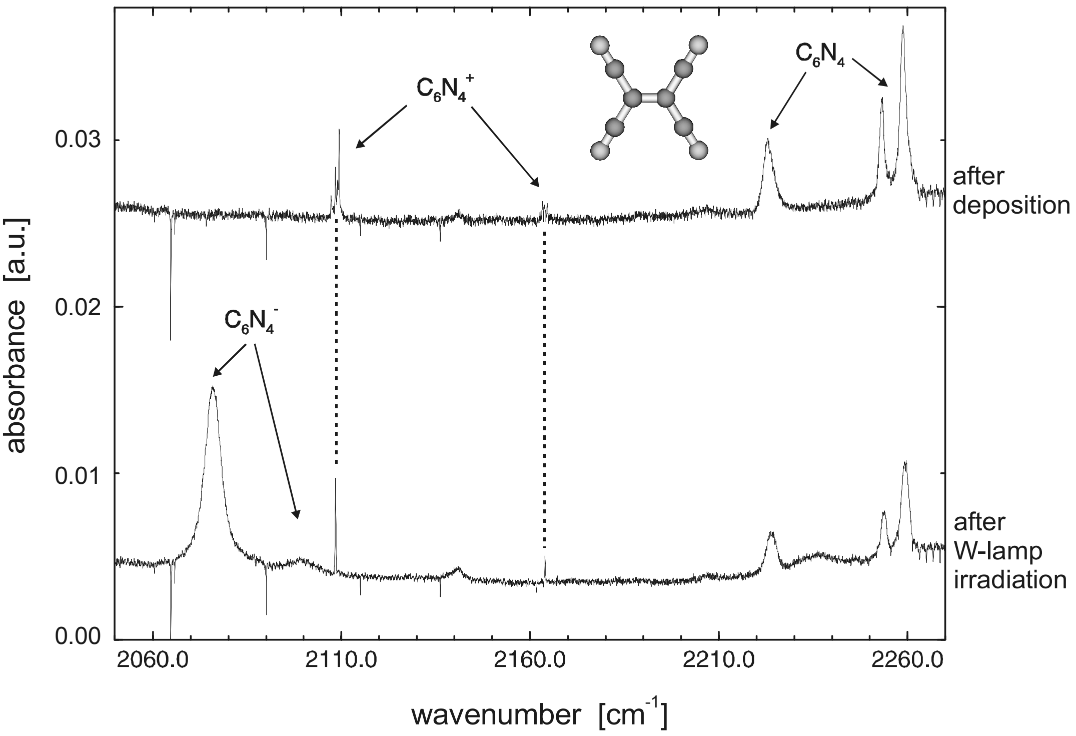

Figure 5.3. The triple bond stretch region of the FT-IR spectra of a neon matrix formed after deposition of mass 128 amu ($C_6N_4^+$). The upper trace was recorded after matrix deposition, lower – after the matrix had been subjected to several hours of tungsten lamp (W-lamp) radiation.

Matrix-isolated ions usually exhibit sensitivity to matrix annealing or irradiation or both. The effect of exposing the matrix to the visible light of a tungsten lamp can be seen in the bottom trace of Figure 5.3. Each of the groups of bands attributed above to the cation collapses to a single band, at 2108.4 and 2163.9 cm^{-1}, with an overall decrease of the integrated intensity. A further effect clearly visible in the spectrum is a significant decrease in the bands due to the neutral parent. Finally, a very strong and rather broad band centered at 2076 cm^{-1} grows in following the irradiation, with similarly broad, but much weaker bands appearing near 2099 and 2238 cm^{-1}. Few other weaker bands can be identified in other spectral regions.

The output of the lamp is too weak to lead to a significant bulk heating, and so the effects produced are simply due to absorption of individual photons — a photochemical process. Tungsten lamps have insignificant output beyond 25 000 cm^{-1}, so that the photons usually can not break chemical bonds. There also are no species present in the matrix that could be isomerized with such a low activation barrier. One effect which one often observes is that following a photon absorption a trapped molecule can relax nonradiatively. Redistribution of the photon energy leads then to relaxation of the lattice in the neighbourhood of the guest, and changes in the nature and geometry of the trapping site. The observed narrowing of the $C_6N_4^+$ absorptions and conversion of the initial multiple structure into a single sharp line is surely due to such relaxation of the ions isolated initially in metastable local environments into the more stable neon lattice site.

If a matrix contains charged species, then a second process, shown schematically in Figure 5.4, which can be induced by low energy photons, is detachment of electrons from

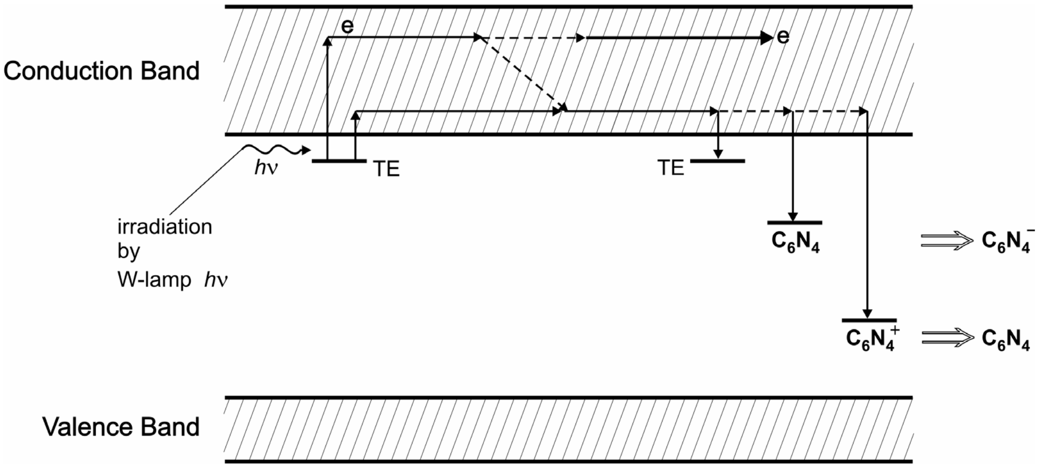

Figure 5.4. Photo-induced detrapping and promotion of trapped electrons (TE) and their propagation through the conduction band of the Ne matrix. The electrons are retrapped by the C_6N_4 cations or neutrals (forming $C_6N_4^-$) present in the matrix.

weakly bound anions, or in general detrapping of electrons. Such electrons, promoted into the conduction band can then propagate through the lattice. Under some circumstances they can actually leave the solid sample (exoelectron emission), but most of them will eventually lose their energy and be trapped again, in most cases being reattached to one of the species present in the matrix. The slight decrease in the intensity of the $C_6N_4^+$ integrated absorption, which is visible in Figure 5.3 is probably the consequence of such a charge recombination, and one might consequently expect the neutral C_6N_4 intensity to increase. Actually, however a substantial decrease of all bands assigned to TCNE following tungsten lamp irradiation is observed.

5.3.5 Matrix-Isolated TCNE Anion

Besides neutralizing a positively charged ion, the electrons freed by the irradiation can also attach to neutral species, in particular if these have an appreciable electron affinity. Based on the observed infrared absorption spectrum, by far the dominant guest species in the sample is neutral C_6N_4. The computations we have carried out for the $C_6N_4^-$ anion predict a moderately strong (intensity 386 km/mol) band at 2125 cm^{-1}, with a weaker one at 2170 cm^{-1} (167 km/mol), in acceptable agreement with the observed bands growing in upon irradiation, as listed in Table 5.2. Thus the bands growing in after tungsten lamp irradiation can be attributed to the $C_6N_4^-$ anion, as labeled in the bottom trace of Figure 5.3 and Figure 5.5. It should be mentioned, that these anion bands appear following tungsten lamp irradiation, whenever TCNE was used in the ion source and the neutral bands were initially present. Conversely, they were completely absent in all experiments where different ion precursor compounds were employed. Besides the two CN stretches, the theory computes three other infrared bands for the anion at 1131 (10), 959 (4), and 720 cm^{-1} (1) within the range studied, but these are all predicted to be more than an order of magnitude weaker.

As can also be clearly seen in Figures 5.3 and 5.5, the bands of neutral C_6N_4 are reduced by about one half upon the visible irradiation by the tungsten lamp. While it would be difficult to explain this disappearance of tetracyanoethylene by any other process, it can reasonably be attributed to conversion of the neutral into an anion by electron attachment.

Naturally, besides the bands, which can be seen in Figures 5.3, 5.5 and 5.6, also all other absorptions due to the neutral parent compounds decrease in intensity by a similar factor, which in turn confirms their assignment to the same molecule, tetracyanoethylene.

5.3.6 Matrix-Isolated Fragment Cations

As already described in preceding paragraphs, besides the parent cation, a large number of different fragments and products appear in the mass spectrum of the ions emanating

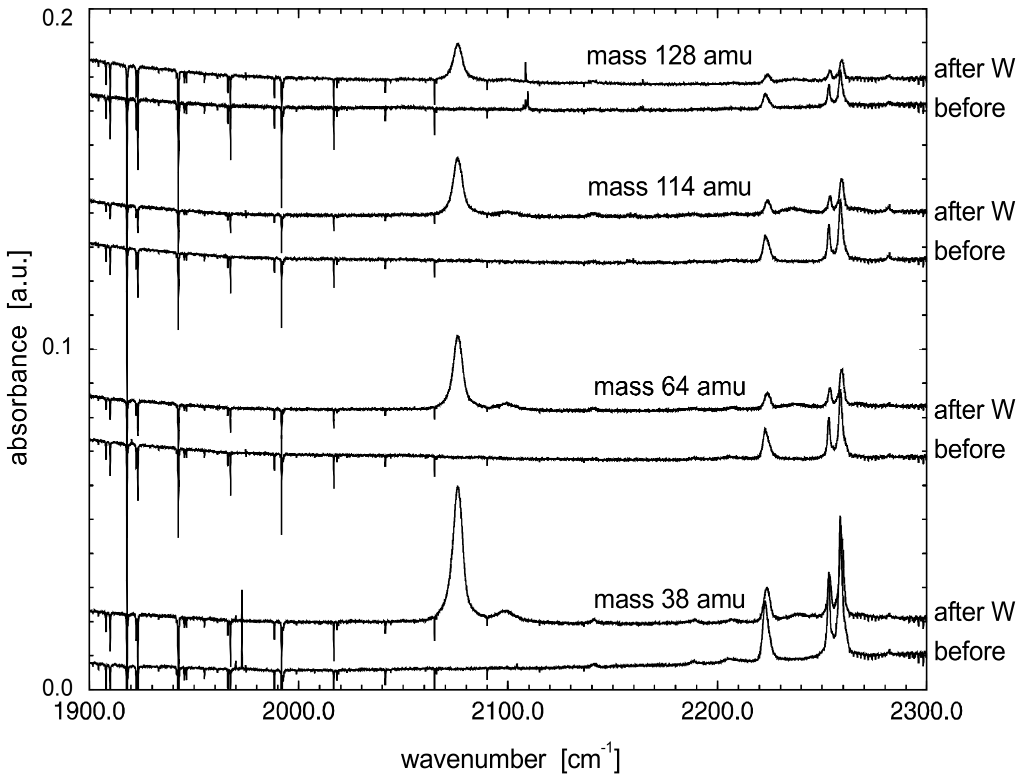

Figure 5.5. The triple bond stretch region of several FT-IR spectra from neon matrices formed from the mass-selective deposition of varying ion masses. For each mass, the spectrum is shown after deposition (or before W-lamp irradiation) and after W-lamp irradiation to show the changes in the spectrum which are independent of the deposited mass.

from the electron impact source (Figure 5.1). A series of experiments depositing several of these fragments have been carried out, and in each case new, ion specific infrared absorptions were observed. As noted above, regardless of the deposited ion, also absorptions due to the neutral tetracyanoethylene C_6N_4 were observed in each case after sample deposition, confirming that their presence in the experiments where the $C_6N_4^+$ cation is deposited is not due to the ion neutralization, but rather predominantly to leakage of the parent compound from the source region.

A common feature of these experiments was that during subsequent irradiation of the sample by the tungsten lamp, absorptions due to both the deposited ion, and to the neutral C_6N_4 compound decreased, while the strong bands attributed to the TCNE anion ($C_6N_4^-$) grew in. This similarity between all the IR spectra from deposited ions of various masses is demonstrated in Figure 5.5. It should again be emphasized, that no such 2076 cm^{-1} band was observed in numerous previous experiments done in our laboratory where precursors other than TCNE were employed. Besides features common to all the spectra, as already mentioned, one observes in each spectrum also unique absorptions, specific to the mass of the selected and deposited ion. The results obtained on: $C_4N_2^+$ (mass 76 amu), C_2N^+ (38 amu), $C_3N_2^+$ (64 amu), $C_5N_3^+$ (102 amu) and $C_6N_3^+$ (114 amu) ions are discussed in the following sections.

$C_4N_2^+$ Ion – Mass 76 amu

Besides the parent, the strongest fragment ion is at nominal mass 76 amu, corresponding to a cation of $C_4N_2^+$ elemental composition. Several isomers corresponding to this formula are possible, of which the linear, centrosymmetric dicyanoacetylene was previously extensively studied both in our laboratory [62] and by *J.P. Maier's* group [63,64]. Deposition of the ions of mass 76 amu (1 nA, 1.5 hour), results in both the known electronic absorption of this linear cation, as well as its CN asymmetric stretching infrared absorption, previously detected in this apparatus using dicyanoacetylene as precursor [51]. No evidence for any other absorptions attributable to other isomers were detected, suggesting that the $C_4N_2^+$ fragment is indeed at least predominantly dicyanoacetylene. A Y-shaped vinylidene type isomer is also predicted to have strong infrared bands, in particular in the triple bond region at 2036 cm^{-1} (1047) and 2088 cm^{-1} (317), and thus should be observable if produced in quantities comparable to the linear isomer. In view of the source molecule used, this is chemically surely reasonable, since the linear isomer can easily be formed by the symmetrical loss of two CN groups from the C_6N_4 parent.

C_2N^+ *Ion – Mass 38 amu*

An ion of mass 38 amu, corresponding to C_2N^+, seems to be quite abundant in discharges through compounds containing nitrogen and carbon, and is also the third most abundant ion generated in our electron impact source when TCNE is used. A part of the spectra obtained in an experiment where mass-selected C_2N^+ ions were deposited is presented in Figure 5.6. In the upper trace obtained right after sample deposition, one can see besides the C_6N_4 parent and known impurity bands also a new strong, sharp band at 1972.9 cm^{-1}, with a much weaker satellite at 1969.9 cm^{-1}. Another similarly sharp but considerably weaker band appears at 2104.2 cm^{-1}, i.e. 134.3 cm^{-1} higher in energy. The lower trace shows the effect of irradiation of the sample by the visible tungsten lamp radiation. One can again observe a considerable decrease in the intensities of the bands of the parent, neutral C_6N_4, and an even larger decrease of the new sharp bands. At the same time there appears again a very strong band at 2076 cm^{-1}, which as argued above we attributed to the $C_6N_4^-$ anion.

Clearly, diffusion of electrons through the sample results in their attachment to the neutral parent compound, and in neutralization of the positive ions. The strongest sharp band is in good agreement with the calculated ν_3 asymmetric stretching vibration of CNC^+, 1937 cm^{-1} (intensity 1363 km/mol), as well as with its known gas phase value of 1974.07 cm^{-1} [61]. The weaker sharp band is likely due to a combination of this stretch with the overtone of the low frequency bend, estimated here to be about 65 cm^{-1}, as discussed recently in [51]. The neutral C_2N species have been extensively studied, and both the symmetric CNC as well as the CCN isomer are known in the gas phase (CCN – [65-70] and others CNC – [71]), as well as in low temperature matrices (CNC [72], CCN [73]). Even though both of them have strong electronic transitions in the visible, and also their infrared transitions in the matrix are well-known, none are observed in our experiments. This again confirms that under conditions of our deposition, ion neutralization is relatively inefficient.

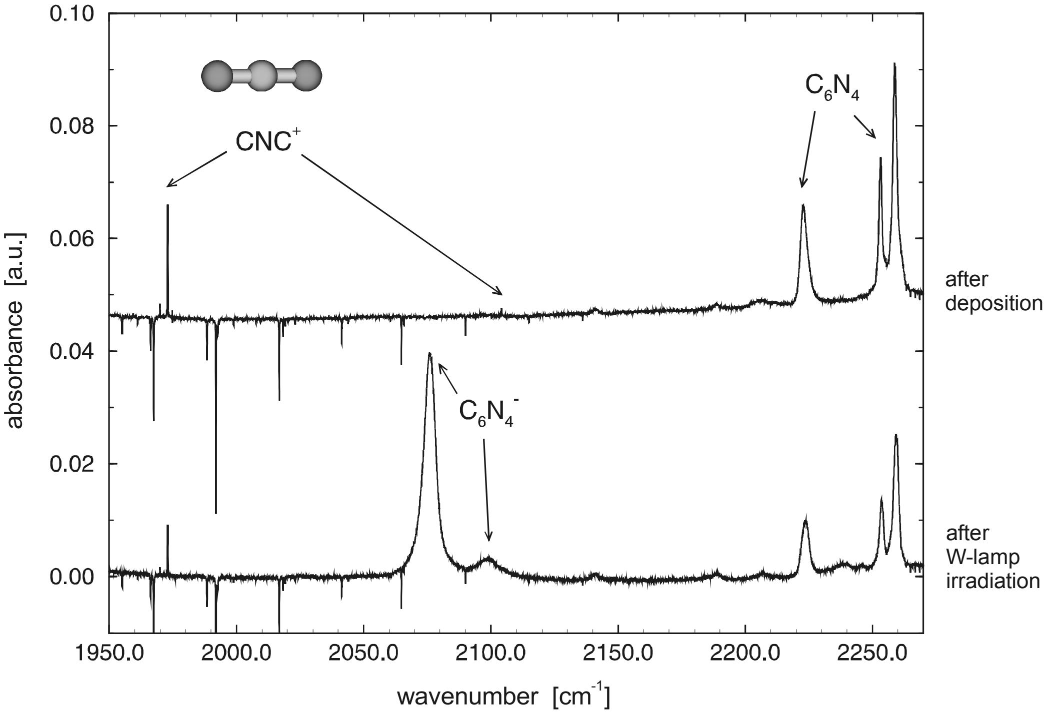

Figure 5.6. The triple bond stretch region of the FT-IR spectra of a neon matrix formed after deposition of mass 38 amu (C_2N^+). The upper trace was recorded after matrix deposition. The lower trace was recorded after the matrix had been subjected to several hours of W-lamp radiation.

$C_3N_2^+$ *Ion – Mass 64 amu*

$C_3N_2^+$ ion, corresponding to a mass of 64 amu, could, for instance, be produced by cleaving the ethylene bond in the parent C_6N_4, and essentially splitting it in half, resulting in an NCCCN chain species. We have carried out a series of computations for the corresponding ion, which is predicted to be linear and possess a single, extremely strong infrared absorption at 1908 cm^{-1} (1141), seen in Table 5.2. This is in good agreement with a sharp band appearing at 1920.1 cm^{-1} when the mass of 64 amu is deposited. This band which can be seen in the top left trace of Figure 5.7 completely disappears following tungsten lamp irradiation, as shown in the bottom left trace. A careful comparison of the IR spectra resulting from deposition of various other masses from the same precursor as shown in Figure 5.7 at the right showed no trace of this 1920.1 cm^{-1} absorption, confirming its unique assignment to mass 64 amu. Like in the case of all the other ions, the tungsten irradiation is also accompanied with loss in the intensity of the parent C_6N_4, and a concurrent growth of the $C_6N_4^-$ anion band.

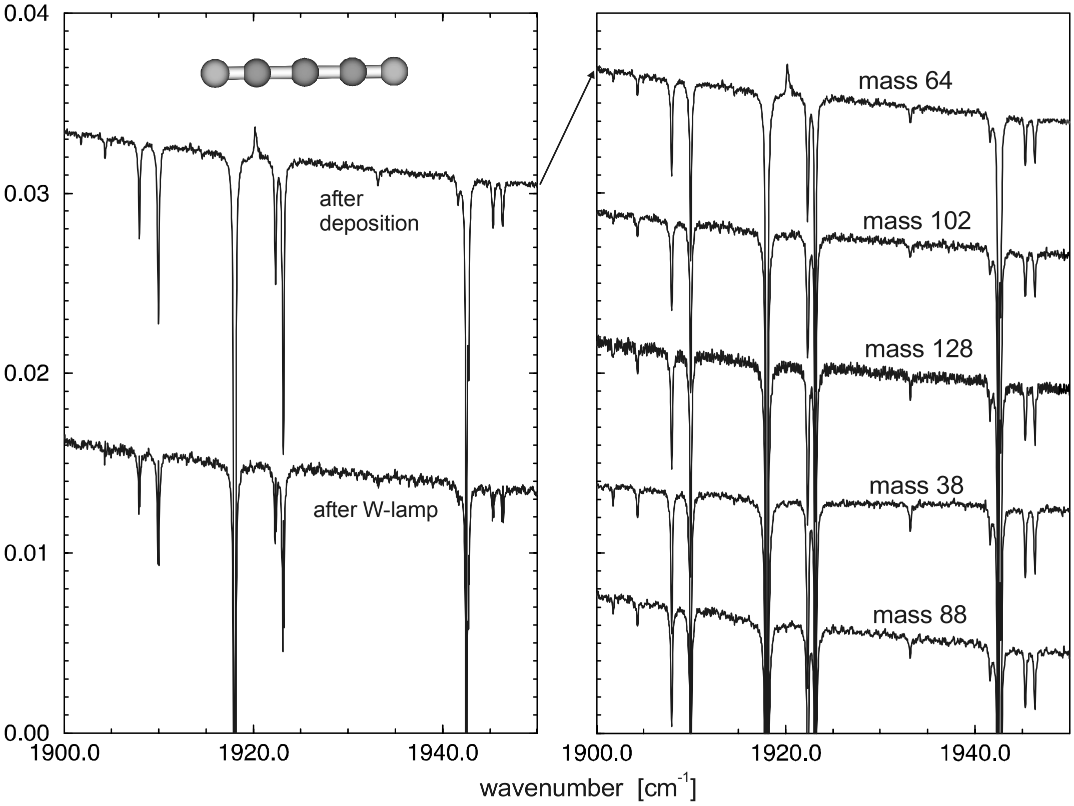

Figure 5.7. The two left-hand traces show sections of the FT-IR spectra of a neon matrix formed after a deposition of mass 64 amu ($C_3N_2^+$). Absorption at 1920.1 cm^{-1}, assigned here to the CN stretch of $C_3N_2^+$, is completely bleached by the W-lamp radiation. The traces in the right diagram show the same section of the FT-IR spectra taken after the deposition of varying ion masses. The 1920.1 cm^{-1} absorption appears only after the deposition of mass 64 amu, confirming its assignment to $C_3N_2^+$.

$C_5N_3^+$ *Ion – Mass 102 amu*

An ion of a nominal mass 102 amu corresponds to $C_5N_3^+$, and one could expect it to be easily produced from the C_6N_4 precursor by the loss of a single nitrile group. In spite of this, the ion appears relatively weakly in the source mass spectrum. This probably suggests that when one CN is lost, the remaining tricyanoethylene entity is destabilized and easily loses a second CN, resulting in the most abundant $C_4N_2^+$ ion fragment discussed above. Computations for the $C_5N_3^+$ ion were carried out, starting with the geometry of the $C_6N_4^+$ cation with one CN group removed. A geometry optimization converged smoothly to a symmetric, planar C_{2v} conformation, NCCC(CN)$_2$, with a linear NCCC chain. Theoretical computations predicted for this ion two moderately strong absorptions, slightly red shifted

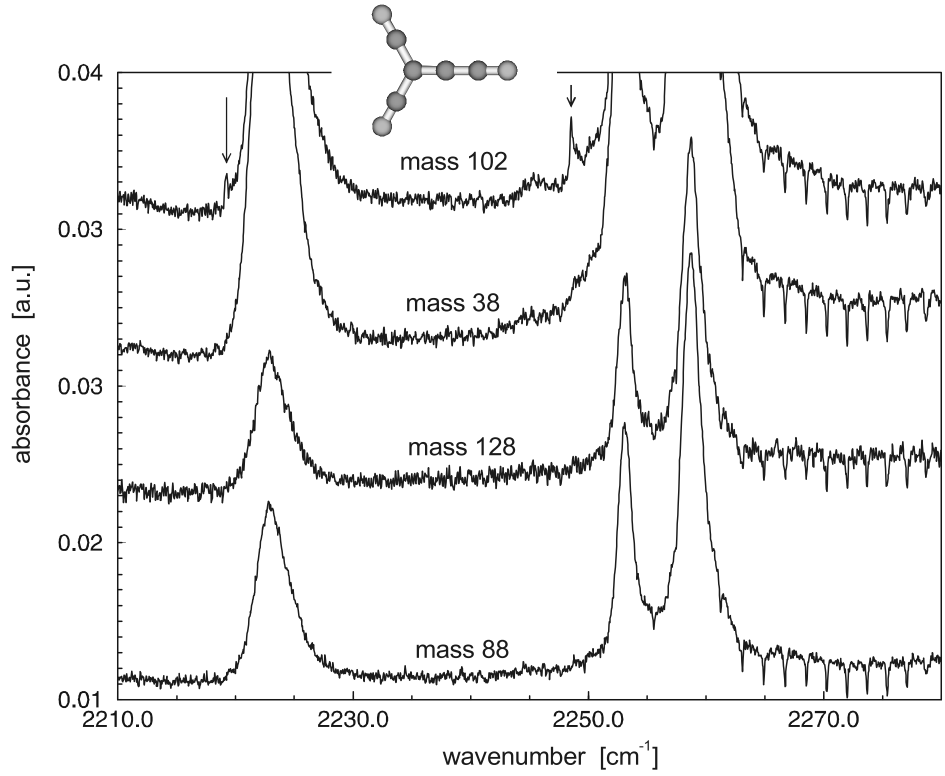

Figure 5.8. The upper trace shows a section of the FT-IR spectrum of a neon matrix formed after a deposition of mass 102 amu ($C_5N_3^+$). The two new absorptions at 2248 and 2219 cm^{-1} indicated by arrows, appear in wings of the strong neutral C_6N_4 peaks in this region, but are absent when fragments ions of various other masses are deposited, confirming their assignment to $C_5N_3^+$.

in frequency from the two strong CN stretching absorptions of the parent neutral C_6N_4. Examination of the spectrum of a sample resulting from deposition of the mass 102 amu indeed reveals two weak, sharp new bands just below the broad 2253.1 and 2222.8 cm^{-1} C_6N_4 absorptions. In spite of a careful search, no trace of these new, 2248 and 2219 cm^{-1}, bands could be detected in any of the spectra resulting from deposition of ions of other masses, as demonstrated for several masses in Figure 5.8.

$C_6N_3^+$ *Ion – Mass 114 amu*

Mass 114 amu corresponds to $C_6N_3^+$, that is a loss of nitrogen atom from the C_6N_4 parent. Deposition of this ion produced a group of very weak, closely spaced sharp bands near 2158.2 cm^{-1}. Again, numerous isomers are possible, and we have carried out DFT calculations for several of them. The observed frequency is in good agreement with a fairly intense 2181 cm^{-1} infrared band computed for an C_S isomer formed simply by the loss of a nitrogen atom from one of the four CN groups. This would, of course require breakage of the CN triple bond, which on the other hand might be consistent with the relatively low intensity of the ion. A problem with the assignment is also that the computation predicts a comparably strong absorption at 1396 cm^{-1}, which is not observed. The presence of a group of at least five closely spaced lines in the case of $C_6N_3^+$ would be consistent with the relatively low symmetry of the molecule, and the possibility of a number of different site geometries. Like in the case of all the other ionic species studied here, the new absorptions decrease upon tungsten lamp irradiation, and the relative intensities of the multiplet components change, supporting their assignment to several sites exhibiting different degree of stability. Either are some of the sites more effectively neutralized during the optical detrapping and diffusion of electrons, or the ions absorb the radiation, and their nonradiative relaxation results in their conversion into presumably more stable sites.

The intensity of the mass 114 amu peak however, comparable to the mass 102 amu peak of $C_5N_3^+$ (Figure 5.1), seems to point to a different formation mechanism than discussed above. As we have observed in previous mass spectra from this source, ion-molecule reactions between the most abundant fragments are quite common [51]. Thus it seems more reasonable here to attribute the formation of $C_6N_3^+$ to secondary ion-molecular reactions, as for example:

$$C_6N_4^+ + C_2N \rightarrow C_6N_3^+ + C_2N_2^+,$$

which could lead to a Y-shaped or C_{2v} $C_6N_3^+$. A C_{2v} $C_6N_3^+$ ionic species is predicted to have also two strong IR peaks at 2143 and 2205 cm^{-1} with intensities 1088 and 2205 km/mol, respectively. The former is also in reasonable agreement with the observed 2158.4 cm^{-1} but again no candidate for the 2205 cm^{-1} predicted peak was observed. In conclusion, it is not possible from the observations to decide on the C_S or C_{2v} geometry for this ion; its intensity in the mass spectrum seems to point to a C_{2v} geometry whereas the appearance of several sites may point to a lower symmetry of the molecule.

5.3.7 C_5N_2 Molecule

A matrix resulting from deposition of $C_5N_2^+$ (mass 88 amu) resulted in an infrared absorption spectrum exhibiting very weak origin bands of 440 nm spectrum, which has been previously assigned [74] to the C_5N_2. The presence of the spectrum is, however, clearly confirmed in this work by the much more sensitive laser excitation method using the tunable ring dye laser (see Figure 2.9 in *Chapter 2*). A laser scan shown in Figure 5.9 reveals two rather strong lines at 22762.5 and 22784.8 cm^{-1}, exactly the previously observed frequencies for the two sites of the 440 nm carrier in a neon matrix [74]. Their intensity is not changed dramatically upon annealing or bombardment with electrons, in contrast to the peaks of the related ionic species observed recently in the infrared [51], which provides some support for assignment to the neutral C_5N_2. As it is seen in Figure 5.9, the spectra obtained in the same frequency range from the matrices after deposition of mass 38 amu as well as TCNE parent ion of mass 128 amu reveal the absence of the 22762.5 and 22784.8 cm^{-1} bands.

The relative weakness of the 22762.5 and 22784.8 cm^{-1} fluorescence peaks was expected since, as already shown in [39,51], charge recombination in matrices continuously sprayed with electrons do not effectively produce the neutrals. It is therefore very likely that the matrix contains large quantities of the $C_5N_2^+$ cations, but only very few of them were neutralized. The lack of the ionic absorption can be explained by the fact that in all the cases where the infrared spectra were recorded with an acceptable signal to noise ratio, the deposited integrated current was considerably higher than in the $C_5N_2^+$ case.

Subsequent cavity-ring-down measurements by *Linnartz et al.* [75] confirmed previous assignments to a linear NC_5N molecule. However, considering the structure of the TCNE molecule, one has to notice that a linear C_5N_2 molecule is not expected to form readily in the course of its fragmentation, since the longest carbon atom chain present within its molecule contains only four carbon atoms. Figure 5.1 shows that upon EI ionization the most abundant fragment is the well-known and very stable $C_4N_2^+$ cation, and one possibility would be that the C_5N_2 species are formed by its reactions. Such reactions, however, would seem to be likelier to produce branched or even cyclic species, rather than the linear centrosymmetric attributed to the absorption in the 440 nm region. It is possible that majority of deposited mass 88 amu ions are not the linear species, but its structural isomers. Obviously, the presence of several isomers would redistribute or “dilute” the signal, and make experimental observation of their spectra considerably more difficult.

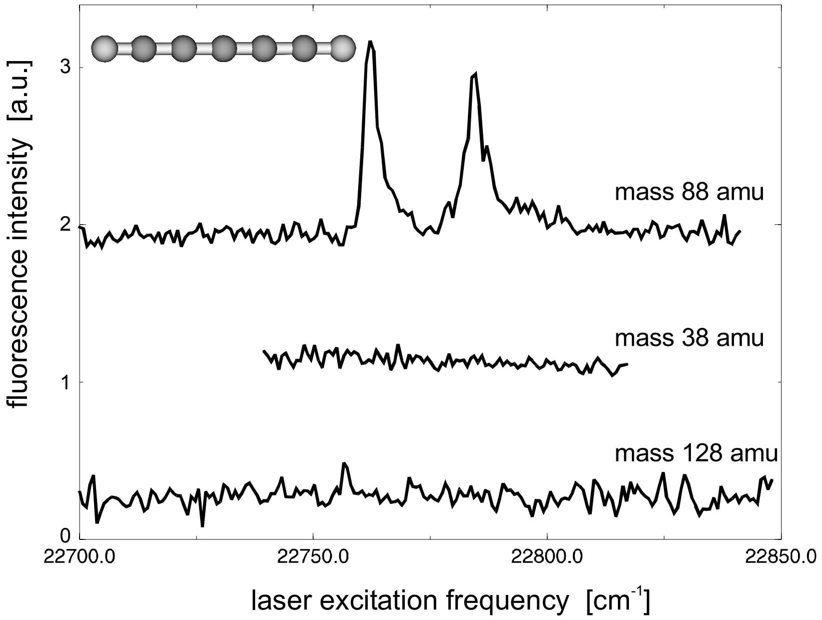

Figure 5.9. Laser excitation scans of the C_5N_2 origin region from various Ne matrices. The two characteristic sites centered at 22784.8 and 22762.5 cm^{-1} in solid Ne, appear only in the spectra of mass 88 amu and the signal is not changed dramatically after annealing with electron bombardment, pointing to a neutral species as the carrier.

5.4 Conclusions

Selectively deposited positive ions from a heated tetracyanoethylene (C_6N_4, TCNE) precursor were examined in neon matrices. Investigated species are of astrophysical interest. The heated tetracyanoethylene used as a precursor substance were ionised and fragmented in an electron impact ion source. After mass selection of the ion of interest by means of a quadrupole mass filter, they were deposited simultaneously with Ne matrix gas onto the substrate at a temperature of 7 K. The parent cation $C_6N_4^+$ of mass 128 amu as well as the following ions produced by its fragmentation: $C_4N_2^+$ (76 amu), C_2N^+ (38 amu), $C_3N_2^+$ (64 amu), $C_5N_3^+$ (102 amu), $C_6N_3^+$ (114 amu) were studied using Fourier-transform spectroscopy technique. Infrared absorption spectra were recorded in the range of 600 – 4000 cm^{-1} using with the 0.06 cm^{-1} resolution.

The mass-selective deposition allowed for identification and assignments for vibrational transitions observed correspondingly to isolated molecular ions. The interpretations of obtained spectra are based on correlation study and fundamental frequencies predicted by means of density functional B3LYP calculations. This resulted in first observations of the infrared vibrational spectra of the parent cation $C_6N_4^+$ and its fragmentation products $C_3N_2^+$, $C_5N_3^+$ and $C_6N_3^+$. The $C_4N_2^+$ and C_2N^+ ions were also identified. Deposition of $C_5N_2^+$ cation allowed as well for re-examination of electronic transitions of neutral C_5N_2 molecule in the visible 440 nm region by means of laser excitation spectra. The results have confirmed the previous assignment to C_5N_2. In all cases, independent of the deposited mass the intense neutral C_6N_4 bands were observed.

An interesting photochemical effect was also observed in all IR spectra in neon matrix: a detrapping or photomobilization of electrons resulted in subsequent recombination with the residual, and highly electronegative C_6N_4 precursor and formation of the well-known tetracyanoethylene anion $C_6N_4^-$.

6 Protonated and Fragment Ions of Acetonitrile

6.1 Introduction

An investigation of reactive cyano-compounds and particularly their molecular ions is of special interest for physical and chemical processes occurring in interstellar space [4,76,77]. Listings of neutral and ionic molecular species (published by National Radio Astronomy Observatory NRAO, and The Department of Millimeter and Submillimeter Radioastronomy (DEMIRM) of the Observatoire de Paris) detected in spectral regions which span from radiofrequency to the far-infrared, reveal that nitriles and their metastable isomers are prevailing species in this environment. This includes the largest observed interstellar molecule, a linear chain $HC_{11}N$ [78] and other cyanopolyynes, $HC_{2n}N$, as well as some of their methyl cyanoacetylene derivatives. The acetonitrile molecule, CH_3CN, and its CH_3NC isomer [79-81] and cyanomethyl CH_2CN radical were also detected [82].

Radioastronomical observations resulted, so far, in identification of only two molecular ions containing nitrile group: $HCNH^+$ and HC_3NH^+ [83,84]. These protonated species are considered as precursors of HCN, HNC, HC_3N and HNC_3 molecules produced via dissociative recombination of the ions with electrons [84]. Searches for the protonated molecules seem to be of considerable importance for ion-molecule chemical reactions in the interstellar medium [83]. Although the protonated acetonitrile, CH_3CNH^+ has not been unambiguously identified in space, it is thought to be formed from CH_3^+ and HCN, and in turn, to be involved in formation of the acetonitrile molecule, CH_3CN [85-89].

The first spectroscopic identification of protonated acetonitrile, CH_3CNH^+, was made by *Amano* using a frequency difference laser system [87,88]. The N–H stretching fundamental has been observed at 3527.288 cm^{-1}. *Gottlieb et al.* [90] applied the Fourier-transform microwave technique to a supersonic molecular beam that resulted in observation of its pure rotational spectrum. These authors precisely determined values of rotational and centrifugal distortion constants for CH_3CNH^+. At the same time *Botschwina* [91] reported its accurate equilibrium structure and dipole moment using various *ab initio* methods. However, as mentioned above, earlier radioatronomical observations done by *Turner et al.* [83] have brought only very tentative results on the CH_3CNH^+ species.

Also quite recently intensive studies have been carried out on the C_2H_2N family of cations and radicals. Research on these compounds involves activities in many different fields, such as microwave spectroscopy [92], photoionization efficiency (PIE) spectroscopy [93], mass spectrometry and thermochemistry [94]. Anionic species examined by means of photoelectron spectroscopy were widely reported by *Moran et al.* [95,96]. Experimental efforts were accompanied by theoretical study carried out by *Horn et al.* [97] and later by *Lau et al.* [98] and gave some insight into the structure and fundamental vibrational modes of CH_2CN and CH_2NC radicals and their cations. The latter group revealed up to seven kinetically stable $C_2H_2N^+$ isomers. However, besides theoretical data, no infrared spectra of $C_2H_2N^+$ has been reported to date.

As demonstrated here, Ne-matrix study supported by DFT/B3LYP computations, partially fills this gap. The matrix-isolation technique employing mass-selective deposition of target ions can be a valuable tool in the spectroscopic characterization of such elusive species. In the current work, the compounds are generated upon electron impact ionization of acetonitrile CH_3CN, and its deuterated CD_3CN analogue. In spite of the fact that the spectra recorded after mass-selective deposition do not show clear evidence of the parent cation, $CH(D)_3CN^+$, acetonitrile turned out to be a suitable precursor for other molecular ions with apparently greater IR activity. The experiments resulted in the spectral characterization of protonated acetonitrile CH_3CNH^+, as well as the identification of three cationic cyanomethyl $C_2H_2N^+$ isomers: H_2CCN^+, H_2CNC^+ and $HCCNH^+$. Although the spectral assignments for two H_2CCN^+ and H_2CNC^+ ionic isomers can be only tentative, experimental results give rather strong evidence for the occurrence of the linear $HCCNH^+$ ion.

6.2 Experimental

Acetonitrile (99.93, HPLC grade, Aldrich Chem. Co.), and its deuterated analogue (acetonitrile-d_3 99.8 % atom D) have sufficient vapor pressure (of above 100 mbar at ~ 294 K), to be used without heating in our electron impact ion source. Typically, the pressure in the source chamber was about $5 – 8 \times 10^{-5}$ mbar. Target species were deposited at temperature of 6 K (LEYBOLD system) after optimization of the EI source and ion-optics potentials. 6 – 7 mmol of the neon matrix gas (99.999 % Messer Griesheim) was deposited under the pressure (cryostat chamber) ranging from 2 to 3×10^{-6} mbar. Optimized, average ion current and deposition time for the particular ions are summarized in Table 6.1.

Table 6.1. Ion current and total deposition time for ions selectively deposited in neon matrix from EI source using CH_3CN and CD_3CN precursors.

Species	mass [amu]	average ion current [nA]	total deposition time [hrs.]
CH_4CN^+	42	3	7.5
CH_3CN^+	41	2	4
$C_2H_2N^+$	40	0.4	7.5
CD_4CN^+	46	5.2	6
CD_3CN^+	44	0.35	4
$C_2D_2N^+$	42	1.1	8
C_2DN^+	40	0.3	7.5

The absorption measurements in the infrared range as well as in VIS and UV were carried out using a BRUKER IFS 120 HR spectrometer and broadband light sources: glowbar and tungsten lamp. Spectra in the range of 400 – 4000 cm^{-1} were recorded with 0.06 cm^{-1} resolution and with 1 cm^{-1} in the VIS/UV range. Infrared measurements were repeated subsequently after irradiation of the sample with the tungsten source (or VIS/UV measurements) or/and annealing (at 10 K) in order to monitor changes in the spectra. No spectral features in the VIS/UV region were observed.

6.3 Results and Discussion

6.3.1 Mass Spectra

The quadrupole mass spectra of CH_3CN and CD_3CN precursors ionized in electron impact ion source (EI) are shown in the diagrams a) and b) of the Figure 6.1, respectively. The weak peaks can be attributed to ionized carbon and nitrogen atoms as well as carbon-hydrogen compounds CH_n ($n = 1, 2, 3$) and their deuterated analogues. Some of the peaks at higher masses observed for both precursors suggest an occurrence of the molecular nitrogen ion and CN^+. Besides the parent cations CH_3CN^+ (mass 41 amu) and CD_3CN^+ (44 amu), seen in the group of stronger peaks, one can observe several species formed in fragmentation or ion–molecule reactions. Thus, the prominent peak corresponding to $CH(D)_4CN^+$ ion of mass 42 amu (46 amu) can be assigned to the protonated acetonitrile CH_3CNH^+ and CD_3CND^+. The spectrum in Figure 6.1b shows rather high isotopic purity i.e. almost no scrambling of H and D atoms is observed. The peaks at mass 40 and 42 amu, seen in spectrum a) and b), respectively, corresponds to ions with $C_2H_2N^+$ and $C_2D_2N^+$ stochiometry. The much weaker peak observed at mass 39 amu (40 amu for deuterated ion), corresponds to ion with $C_2H(D)N^+$ stochiometry. The 38 amu peak resulted from both precursors originates in the well-known C_2N^+ cation. Ions detected at mass 54 and 58 amu seem to differ by one carbon atom from both protonated CH_3CNH^+ and CD_3CND^+ species.

6.3.2 Computational Methods

Density Functional computations (DFT) have been applied for selected ions of interest at B3LYP level in order to predict infrared spectra. As before all computations were carried out using the *Gaussian 98* software package [99]. Analogous to former experiments (e.g. TCNE ion), for unknown or little known species, the relatively modest 6-31+G(d,p) basis set was initially used. Optimization was then subsequently continued with the larger 6-311++G(3df,3pd) basis set. Data previously obtained in our group using this method as well as results reported in the literature confirmed its usefulness not only for fundamental frequencies but also their relative intensities [59,100,101]. The calculations include proto-

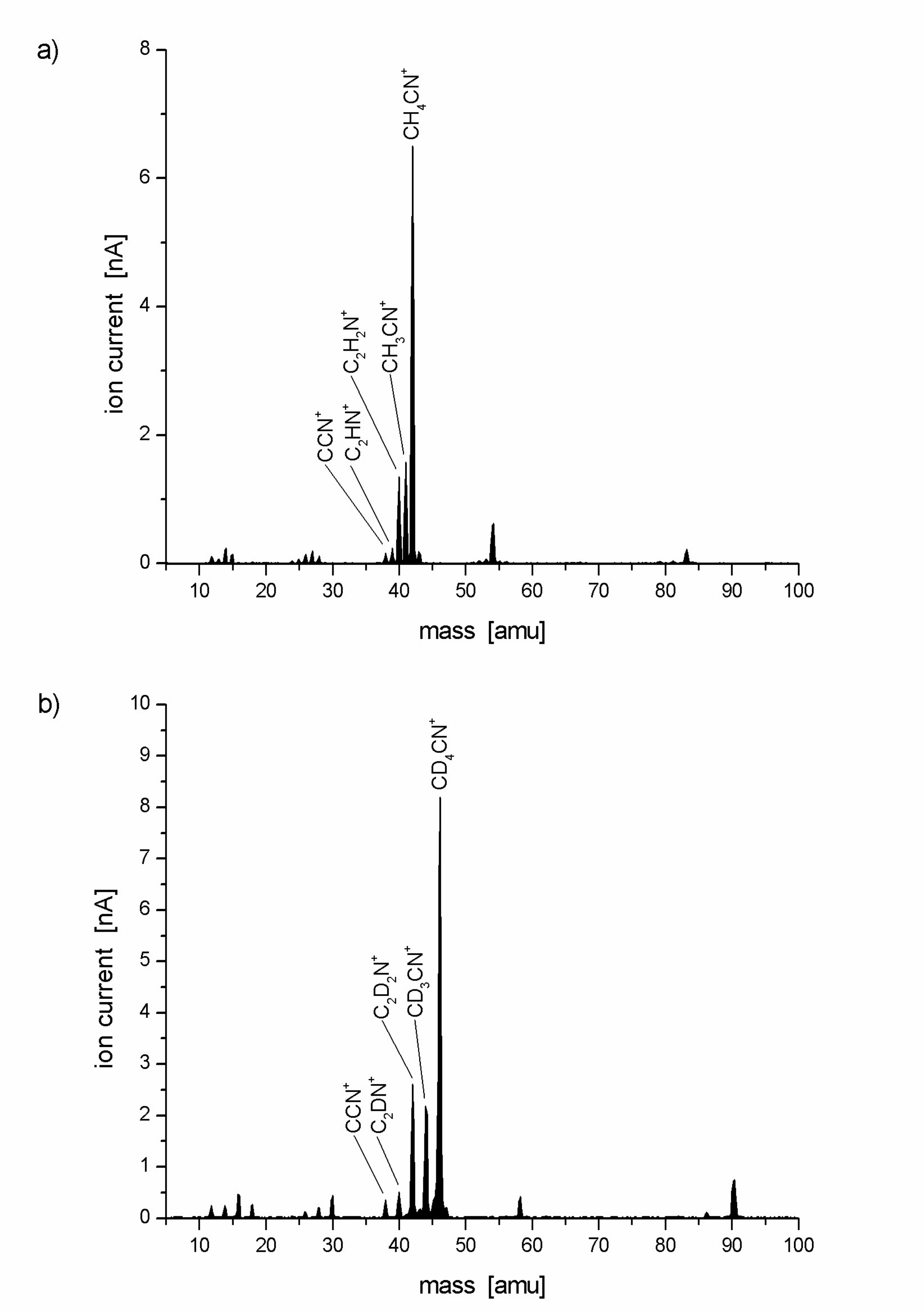

Figure 6.1. The quadrupole mass spectra produced from the electron impact ionization of acetonitrile CH_3CN (spectrum a) and its deuterated analogue CD_3CN (b).

nated acetonitrile CH_3CNH^+, isomers of the cyanomethyl cations H_2CCN^+ and H_2CNC^+ and protonated $HCCNH^+$, selected based on observed data. The infrared spectra were also calculated for isotopically substituted (all H atoms with D) ions.

An important point in the discussion of assignments of new spectral features is a scaling factor used for computed frequencies. Often, the empirical knowledge about scaling factors applied to the number of molecules, usually in the gas phase, significantly facilitates interpretation of obtained results. In view of the fact that most of the infrared frequencies for the species observed in solid neon are only slightly shifted with respect to the gas phase [102], the factors are fully applicable in matrix-isolation vibrational spectroscopy.

6.3.3 *Protonated Acetonitrile: CH_3CNH^+*

As mentioned above, protonated acetonitrile CH_3CNH^+ has been extensively studied theoretically by *Amano* [87] and *Botschwina* [91] as well as experimentally by rotational spectroscopy [90]. This resulted in structure, spectroscopic constants and rotational transition frequencies. However, the only information on its IR spectroscopy concerns the N–H stretching band observed at 3527.288 cm^{-1} [87]. In order to obtain more data on fundamental vibrational modes and support an interpretation of obtained neon matrix spectra DFT computations have been carried out. Optimization of the structure on the B3LYP/6-311++G(3df,3pd) level of theory resulted in C_{3v} symmetry, in agreement with data from [91]. The geometry, bond lengths and C–C–H angle are shown in Figure 6.2. Calculated harmonic frequencies of fundamental vibrational modes for CH_3CNH^+ and deuterated CD_3CND^+ are summarized in Table 6.2. It is seen that the strongest absorption (intensity of 738 km/mol) corresponds to the N–H stretching vibration predicted to occur at 3667.7 cm^{-1} (unscaled). The intensity of N–D stretching at 2853.3 cm^{-1} is lower, 545 km/mol. The second strongest absorption computed for both isotopomers is associated with C–N–H(D) bending mode near 566(446) cm^{-1} (unscaled).

Selected regions of the infrared spectra measured in the wavenumber range of 500 – 4000 cm^{-1} are shown in Figures 6.3 and 6.4. Apart from typically observed impurities, mainly water and carbon dioxide, the infrared spectra contain characteristic, usually much

Table 6.2. Spectroscopic data for CH_3CNH^+, CD_3CND^+ cations.

		DFT calculations B3LYP/6-311++G(3df,3pd)		Experiment	
vibrational symmetry and mode		vibrational frequencies in cm^{-1} (calc. intensities in km/mol)			
		unscaled	scaled*	Ne matrix$^\#$	literature
CH_3CNH^+, C_{3v}, $^1A_1$ ground state					
A_1	N–H str.	3677.7 (738)	3519.6	3500.6 (677) 3508.2 (61)	3527.29 ^{G}
E	CH_3 asym. str.	3108.3 (58)	2974.6	2946.5 (53) 2940.2 (29)	
A_1	CH_3 sym. str.	3027.8 (61)	2897.6		
A_1	C–N–H str.	2379.5 (97)	2277.2		
E	CH_3	1426.8 (40)	1365.4		
A_1	CH_3 umbrella	1392.1 (25)	1332.2		
E	CH_3	1040.1 (18)	995.4		
A_1	C–C str.	916.3 (6)	876.9		
E	C–N–H bend	565.6 (269)	541.3		
E	C–C–N–H bend	398.3 (13)	381.2		
CD_3CND^+					
A_1	N–D str.	2853.4 (545)	2730.7	2745.7 (483) 2749.8 (61)	
E	CD_3 asym. str	2302.4 (30)	2203.4	2156.7 (6) ^{T}	
A_1	C–N–D str.	2219.8 (4)	2124.3		
A_1	CD_3 sym. str.	2170.9 (40)	2077.6	2105.6 (7) ^{T}	
A_1	CD_3 umbrella	1103.8 (17)	1056.3		
E	CD_3	1023.6 (14)	979.6		
E	CD_3	858.5 (10)	821.6		
A_1	C–C + CD_3 umbrella	825.1 (2)	789.6		
E	C–N–D bend	445.7 (106)	426.5		
E	C–C–N–D bend	338.9 (28)	324.3		

*scaling factor of 0.957 is taken as average value from experimental N–H and N–D frequencies

$^\#$ intensities (in a.u.) are scaled to the strongest IR peak and normalized to the calculated ones

^{G} gas phase, from [87]

^{T} tentative assignment

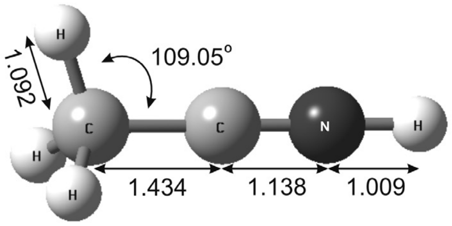

Figure 6.2. Computed equilibrium geometry (C_{3v} symmetry) for protonated acetonitrile (DFT method at the B3LYP/6-311++G(3df,3pd) level of theory). Bond lengths are given in Å.

weaker bands, which appear only if a certain, selected ion mass is deposited. The plots show spectral regions of N–H (N–D) and CH_3(CD_3) stretching vibrations corresponding to different ion masses, deposited upon EI ionization of CH_3CN (Figure 6.3) and CD_3CN (Figure 6.4), respectively. Thus, the Figure 6.3 shows IR spectra obtained after deposition of ionic species of masses 40, 41 and 42 amu with respect to the mass spectrum shown in Figure 6.1a. Figure 6.4 shows spectra recorded for deposition of ions of 40, 42, 44 and 46 amu (see mass spectrum in Figure 6.1b).

Deposition of ion of mass 42 amu revealed the occurrence of a relatively strong absorption at 3500.6 cm^{-1} with much weaker satellite at 3508.2 cm^{-1} (Figure 6.3). One can notice, that a much weaker peak is also present at 3500.6 cm^{-1} after deposition of mass 41 amu ions. Since there is a trade-off between ion throughput and mass resolution, increase of the ion current causes some “mass leakage” and ion of another mass, characterized by higher intensity, could interfere with the selected one. In fact, this is only relevant to the ionic species separated by one mass unit, in this case products of ionization of CH_3CN precursor and does not concern its deuterated analogue, CD_3CN. However, changes in observed band intensities upon shifting of the filter in the mass scale allow for facile distinction of their origin. This is the case for 3500.6 cm^{-1} absorption and also the peak associated with mass 40 amu, localized at 3480.6 cm^{-1}. The latter one will be discussed in the next section. Deposition of ion of mass 42 amu revealed also two closely localized peaks at 2940.2 and 2946.5 cm^{-1}, which are not observed in the spectra taken for mass 40 and 41 amu ion deposition. Both groups of peaks exhibit the same behavior upon 4 hours of irradiation with the tungsten lamp, which causes considerable decrease in their intensities. As extensively discussed in the previous chapter dealing with C_nN_m

cyanocarbon ions, such a process can involve positive ions which are neutralized by electrons freed from their traps and mobilized after interaction with photons.

Thus, the observation of the set of peaks at 3500.6, 3508.2, 2940.2 and 2946.5 cm^{-1} suggests their origin in positively charged ionic species. The strongest predicted band at 3667.7 cm^{-1} (unscaled) with an intensity over 700 km/mol (Table 6.2) indicates that the 3500.6 cm^{-1} absorption corresponds to the N–H stretching vibration of the CH_3CNH^+ ion. The weaker satellite peak shifted by 7.6 cm^{-1} is very likely due to a matrix site effect and

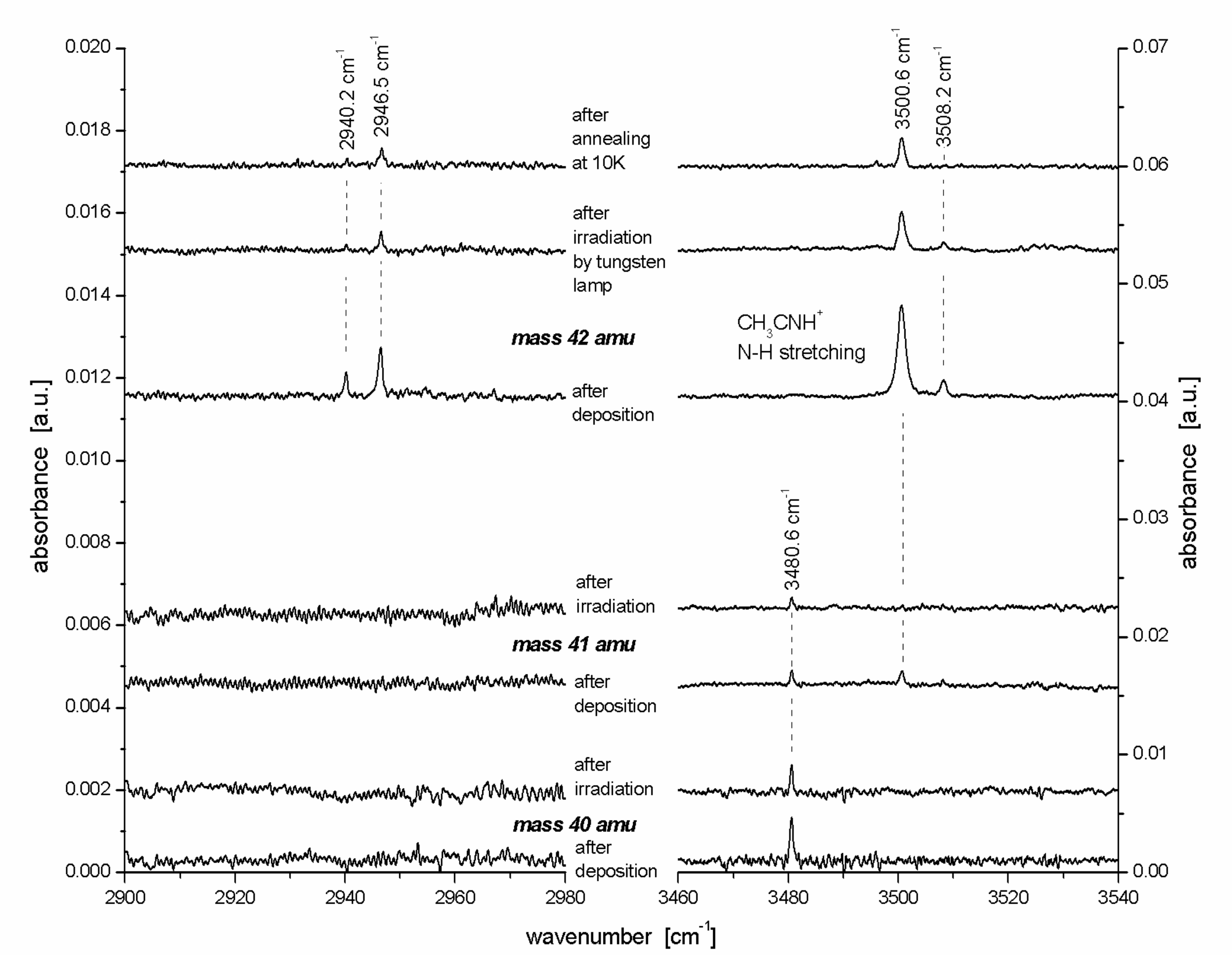

Figure 6.3. Infrared absorption spectra in the region of N–H stretching and CH_3 group stretching vibrations. For each ion mass, spectrum right after deposition at 6 K and after irradiation (~ 4 hrs for mass 40 and 42 amu samples and only 15 min. for 41 amu) with tungsten lamp is presented. Additionally for mass 42 amu sample the annealing effect (at 10 K for 15 min.) is shown.

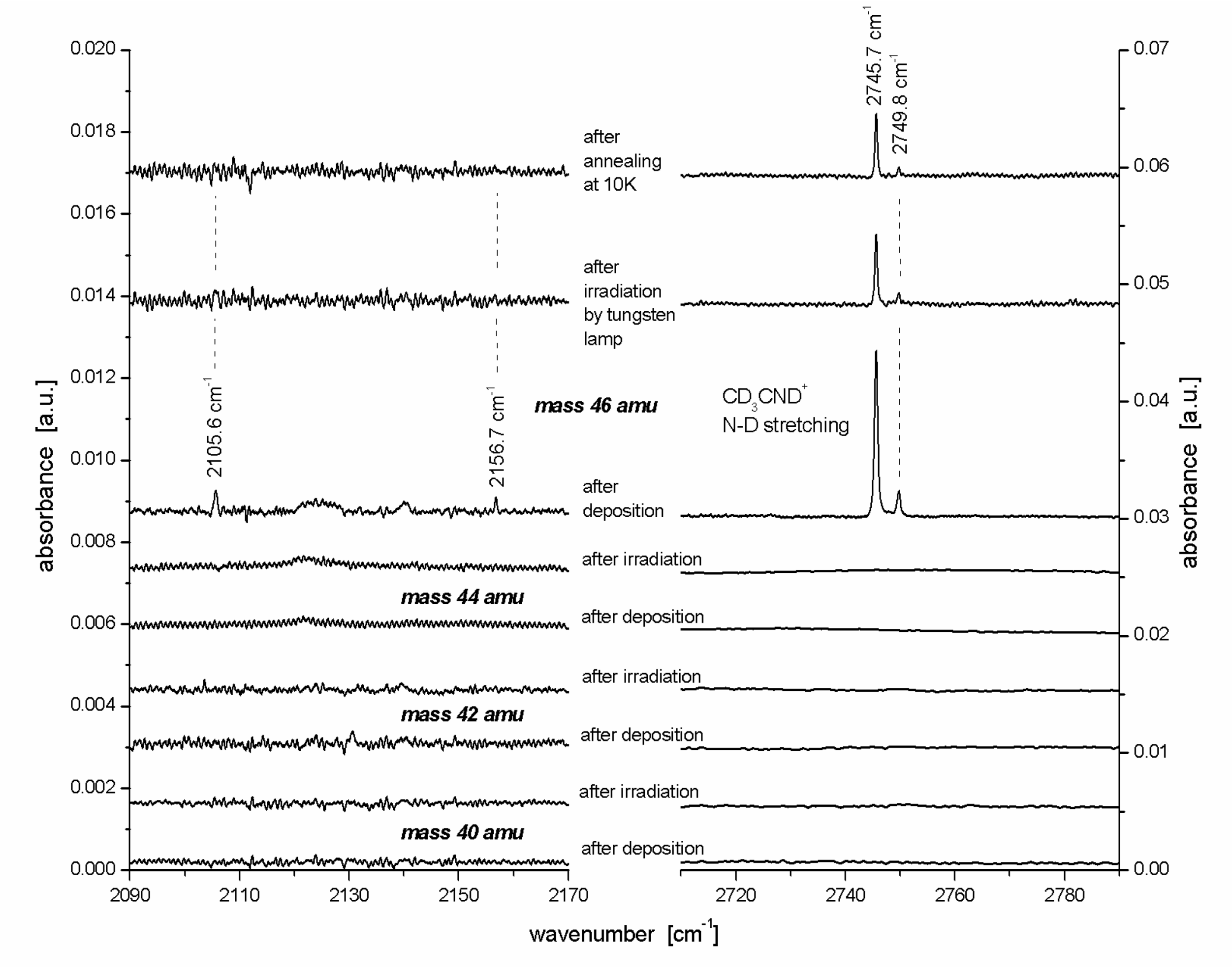

Figure 6.4. Infrared absorption spectra in the region of N–D stretching and CD_3 group stretching vibrations. For each ion mass, spectrum right after deposition at 6 K and after irradiation with tungsten lamp (~ 4 hrs) is presented. Additionally for mass 46 amu sample the annealing effect (at 10 K for 15 min.) is shown.

corresponds to the same vibrational mode. A number of matrix-isolation data [42,43,103] reveal that large linear compounds, in particular $X–(C_2)_n–Y$ type cations, result in two spectrally shifted sites in a Ne matrix. Observed sites were correspondingly attributed to species isolated in relatively unperturbed crystalline fcc (face cubic centered) or hcp (hexagonal close packed) structures. The frequency difference for the pair of peaks at 2940.2 and 2946.5 cm^{-1}, a 6.3 cm^{-1}, is similar to the one above and those two peaks seem to originate in the same molecular vibration. DFT frequency (2974.6 cm^{-1}, scaled,

Table 6.2) predicted for the asymmetric stretch of the CH_3 group of CH_3CNH^+ clearly suggests their assignment to this vibrational mode. Although the predicted intensity of the symmetric stretch is almost equal to the asymmetric one, its frequency is appreciably shifted, by ~ 80 cm^{-1} towards the red. The second strongest band (269 km/mol) of CH_3CNH^+ predicted by theory to be at 566 cm^{-1} (unscaled) belongs to the doubly degenerate C–N–H bending mode. Unfortunately, the sensitivity of the detector in this region is much lower and the spectrum shows no evidence of its occurrence. Its detection can be more difficult if the matrix lifts the degeneracy resulting in two weaker bands. Especially, if they would be further weakened by redistribution in two matrix sites.

A pair of sharp absorption peaks separated by 4.1 cm^{-1} at 2745.7 and 2749.8 cm^{-1} are also observed in spectra recorded after deposition of ions of mass 46 amu using deuterated acetonitrile, CD_3CN, as precursor (Figure 6.4). These two peaks are not observed if ions of masses of 44, 42 and 40 amu are deposited. CD_3 stretching vibrational region reveals two much weaker absorption bands, first at 2156.7 cm^{-1} and second shifted by ~ 51 cm^{-1} toward lower frequencies, at 2105.6 cm^{-1}. By analogy to the CH_3CNH^+ ion the peak localized at 2745.7 cm^{-1} with its blue-shifted satellite at 2749.8 cm^{-1} can be assigned to N–D stretching vibration of isotopically labeled CD_3CND^+ species. The computed frequency (2730.7 cm^{-1}, scaled, Table 6.2) is again in good agreement with experimental one. The relatively high intensity of the N–D mode is an effect of the higher ion current obtained during optimization that resulted in ~ 1.4 times higher number of deposited ions (see Table 6.1).

The assignment of the 3500.6 and 3508.2 cm^{-1} bands to the N–H stretch, and those at 2853.4 and 2749.8 cm^{-1} to the N–D mode is supported by the good agreement between theoretical and experimental values of isotopic shifts. The obtained frequency ratios expressed by $\rho = \nu_{\text{N–H}}/\nu_{\text{N–D}}$ are of $\rho_{calc.} = 1.289$ from DFT results, and of $\rho_{Ne} = 1.275$ (1.276 for blue-shifted peaks) from absorptions measured in Ne matrix.

The interpretation of the two weak absorptions at 2156.7 and 2105.6 cm^{-1}, also observed only for mass 46 amu, appears to be rather difficult and for these two peaks, assignments can be only tentative (Table 6.2). The large separation between the peaks suggests their different origin. Although the 2156.7 cm^{-1} frequency lies closer to the computed value for the C–N–D stretch, its low intensity (predicted as 4 km/mol) together with data obtained for CH_3CNH^+ indicate the assignment of the 2156.7 cm^{-1} absorption to the CD_3 asymmetric stretching of CD_3CND^+. Similarly the band at 2105.6 cm^{-1} seems to be attributed to the symmetric stretching vibration of the same CD_3 group, predicted to be 10 times stronger than the C–N–D mode. The isotopic shift for CH_3 and CD_3 asymmetric vibrations estimated for the theoretical frequencies of $\rho_{calc.} = 1.350$ corresponds approximately to the experimental value $\rho_{Ne} = 1.366$ (1.363 for red-shifted peak).

An experiment on CH_3CNH^+ in Ne matrix reveals a red-shift over 26 cm^{-1} of the N–H stretching frequency with respect to the reported gas-phase value [87]. In this case estimated percent shift ($\nu_{gas} - \nu_{Ne}/\nu_{gas}$ ratio) of ~ 0.8 % is relatively small and close to that observed for NH_3^+ [104] ion. The correlation between proton affinity and the extent of the shift in stretching fundamental involving H^+ in matrix-isolated, protonated species, has been investigated by *Jacox et al.* [104]. These authors concluded that the Ne-matrix shift may be anomalously large for protonated molecules which are derived from protonated species with proton affinities close to or below 550 kJ/mol. Even if the proton affinity of a neon atom is considerably smaller (198.8 kJ/mol [105]), the competition between protonated species and surrounding neon atoms, in trapping site, may lead to an appreciable shift of the stretching vibration involving H^+. Taking into account the proton affinity of acetonitrile of 779.2 kJ/mol [105], which is well above the determined 550 kJ/mol value, one can expect a relatively small shift, like the one observed in the present experiment. For comparison, percent shift values reported in [104] for ClH^+, BrH^+, IH^+, NH_3^+, H_2O^+ and acetylene cation are ≤ 1.2 %.

6.3.4 $C_2H(D)_2N^+$ Cations

Figure 6.5 illustrates calculated equilibrium structures of the four most stable cyanomethyl cationic isomers. The geometries of all $C_2H_2N^+$ cations were obtained using the same relatively large B3LYP/6-311++G(3df,3pd) basis set allowing for the comparison of total energies of all molecules. In agreement with a previous *ab initio* (at MP2(Full)/6-31G(d) level of theory) study done by *Lau et al.* [98] the DFT/B3LYP method indicates a cyclic, C_{2v} structure as a most stable isomer and yields approximately the same bond lengths and N–C–N angle. A disagreement with MP2 data was found for the $HCCNH^+$ isomer, for which B3LYP predicts a linear geometry instead of a bent C_s structure. The

$HCCNH^+$ calculated here, is slightly more (6.3 kJ/mol lower in energy) stable than H_2CNC^+.

Although both DFT and MP2 [98] predict cyclic structure as a most stable among $C_2H_2N^+$ isomers, the fragmentation path in EI ion source favors production of H_2CCN^+ species. Furthermore, the IR intensities of cyclic ion are predicted to be weak (with the strongest one about 170 km/mol). The infrared spectra, discussed below, also do not reveal any evidence of occurrence of cyclic species in Ne matrix.

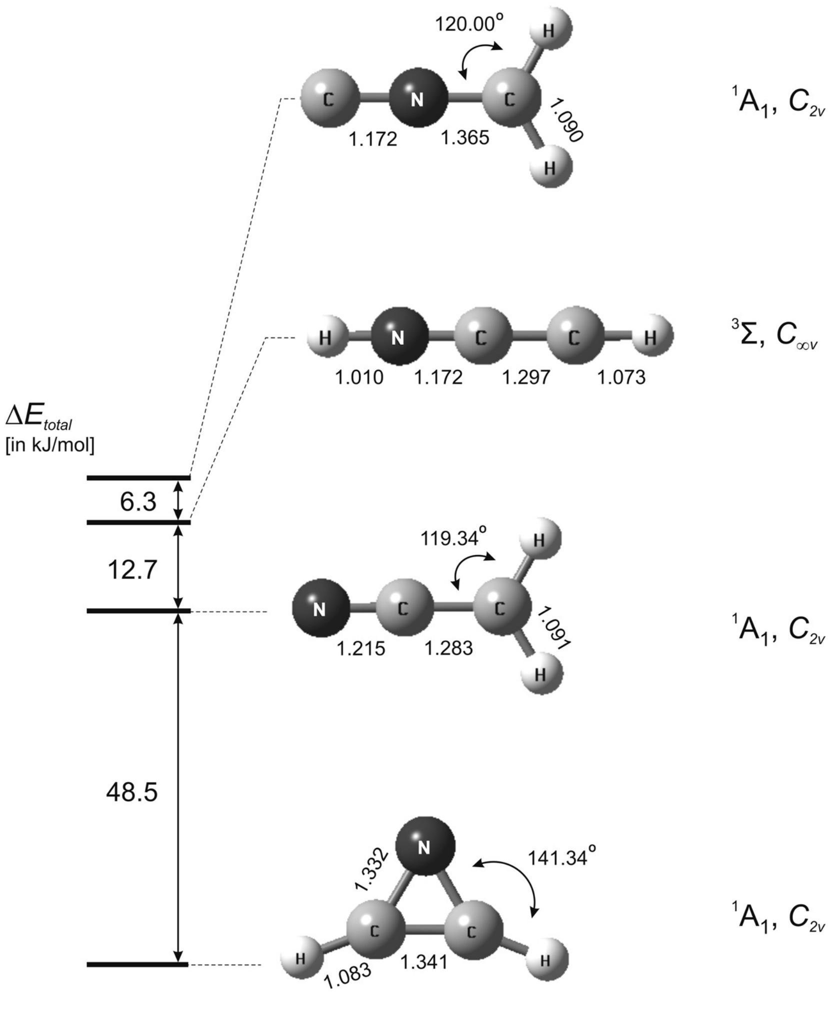

Figure 6.5 Calculated structures of the four most stable $C_2H_2N^+$ cations using the DFT method at the B3LYP/6-311++G(3df,3pd) level of theory. Relative total energies (in kJ/mol) with respect to the most stable isomer are shown schematically. Bond lengths are given in Å.

$HCCNH^+$ and $DCCND^+$

As shown above the DFT computations indicate that $^3\Sigma$ linear $HCCNH^+$ is a possible isomer, and slightly more stable than the isonitrile. The mass spectra obtained from EI ionization of acetonitrile CH_3CN, shown in Figure 6.1, suggest that $HCCNH^+$ and $DCCND^+$ can be possibly produced in ion-molecule reaction involving a C_2HN^+ (C_2DN^+) fragment ion with the CH_3CN (CD_3CN) precursor. The DFT results obtained for the $HCCNH^+$ ion using relatively large (B3LYP/6-311++G(3df,3pd)) basis set clearly indicate a linear, $C_{\infty v}$ point group symmetry, with a triplet $^3\Sigma$ electronic ground state (as illustrated in Figure 6.6). It must be noted that calculations for the singlet electronic state with linear geometry resulted in 121.4 kJ/mol higher energy giving as well imaginary values for the two lowest frequency vibrational modes. Those results were also reproduced for different initial atomic distances in the data input and the same for smaller basis set (B3LYP/6-31+G(d,p)), suggesting that the calculated potential did not reach the global minimum, resulting in a saddle point on the potential energy surface. On the other hand, calculations for singlet state, starting from a planar bent geometry resulted again in a higher potential minimum than for linear $^3\Sigma$ state. A non-planar structure did not converge, but approached a planar one. Additionally, comparison of two different geometries of singlet states favors

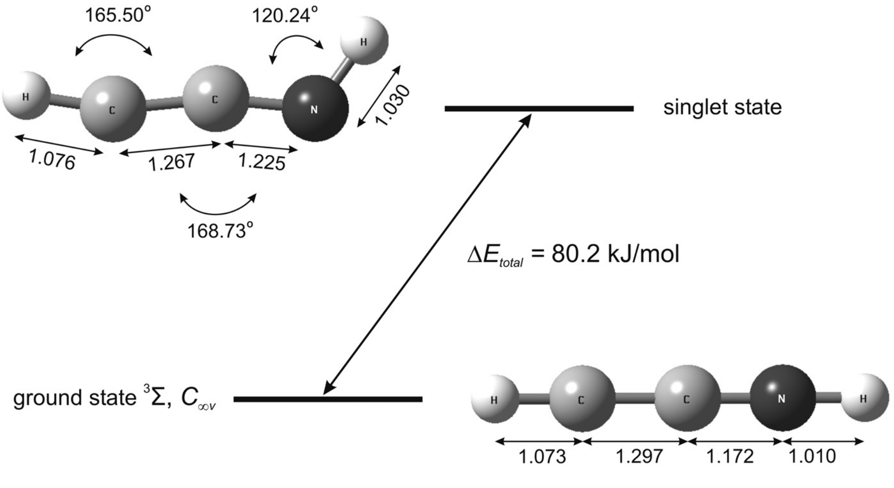

Figure 6.6. Equilibrium geometries of $HCCNH^+$ cation for ground $^3\Sigma$ state and higher singlet state (planar) predicted by DFT calculations using B3LYP/6-311++G(3df,3pd) level of theory. Bond lengths are given in Å.

Table 6.3 Spectroscopic data for $HCCNH^+$, $DCCND^+$ cations.

DFT calculations, B3LYP/6-311++G(3df,3pd)				Experiment
vibrational symmetry and mode	vibrational frequencies in cm^{-1} (calculated intensities in km/mol)			
	unscaled		scaled*	Ne matrix
$HCCNH^+$, $^3\Sigma$, $C_{\infty v}$				
π	270.0	(146)	257.8	
π	270.1	(146)	257.9	
π	287.8	(2)	274.8	
π	288.0	(2)	275.0	
π	443.2	(22)	423.3	
π	443.2	(22)	423.3	
σ	1263.1	(6)	1206.3	
σ	2011.3	(0)	1920.8	
σ C–H str.	3337.0	(255)	3186.8	~ 3178 ^{T}
σ N–H str.	3657.2	(700)	3492.6	3480.6
$DCCND^+$				
π	207.5	(78)	198.2	
π	207.6	(78)	198.3	
π	223.9	(2)	213.8	
π	224.0	(2)	213.9	
π	418.2	(0)	399.4	
π	418.3	(0)	399.5	
σ	1196.4	(5)	1142.6	
σ	1931.2	(12)	1844.3	
σ C–D str.	2499.8	(104)	2387.3	
σ N–D str.	2752.2	(383)	2628.4	2636.6

*scaling factor of 0.955 is taken as average value from experimental N-H and N-D frequencies

^{T} tentative assignment

bent (planar) over the linear one due to much lower energy of 81.2 kJ/mol with respect to the predicted ground linear $^3\Sigma$ state (Figure 6.6). One should note that the bent geometry did not converge in case of the triplet state, for which the optimization was approaching linear geometry resulting in change of the symmetry.

The infrared frequencies computed for the $^3\Sigma$ ground state of the $HCCNH^+$ ion and isotopically labeled $DCCND^+$ ion are summarized in Table 6.3. These results reveal that the strongest absorptions belong to N–H and N–D stretching vibrations at 3657.2(700) cm^{-1} (unscaled frequency; intensity in parentheses in km/mol) and 2752.2(383) cm^{-1}, respectively. Weaker absorptions are attributed to C–H(C–D) stretching 3337.0(255) cm^{-1} (2499.8(104) cm^{-1}) and doubly degenerated, lowest frequency modes. As it is seen, predicted intensities are a factor of 1.8 for N–H and 2.5 for C–H higher than those of the deuterated species.

Spectral regions of N–H and N–D stretching vibrations of the $HCCNH^+$ ion and its deuterated analogue are shown in Figure 6.7. Diagram a) shows spectra recorded after deposition of three different ionic species (masses: 40 amu – $C_2H_2N^+$, 41 amu – parent ion, and 42 amu – CH_4CN^+) obtained from EI ionization of a CH_3CN precursor. Besides the two bands at 3500.6 and 3508.2 cm^{-1} attributed to protonated acetonitrile, one can see a weaker band localized at 3480.6 cm^{-1}. As mentioned above the mass resolution during ion deposition was significantly reduced and exceeded one mass unit. This allowed for "leakage" of ions corresponding to one amu lower and higher masses. Thus one can observe both stronger peaks at 3480.6, 3500.6 cm^{-1} after ions of mass 41 amu were deposited, which are, otherwise, well separated if the mass filter was set, respectively at mass 40 and 42 amu. The peak at 3480.6 cm^{-1} does not occur in the spectra recorded for mass 42 amu and thus it is unambiguously attributed to deposition of ions of mass 40 amu.

The absorption intensity at 3480.6 cm^{-1} appreciably decreases upon tungsten lamp irradiation, exhibiting a similar behavior to the majority of other positive ions observed in the whole series of experiments. Figure 6.7a allows for direct comparison of intensity changes recorded for protonated acetonitrile. As one can notice, thermal treatment of the sample, i.e. annealing at 10 K for 15 minutes caused again only slightly discernible decrease of the intensity, similarly to the 3500.6 and 3508.2 cm^{-1} bands (Figure 6.3).

The set of spectra recorded after deposition of ionic species of four different masses (40 amu – C_2DN^+, 42 amu – $C_2D_2N^+$, 44 amu – parent ion, and 46 amu – CD_4CN^+) upon

EI ionization of the CD_3CN precursor exhibits an occurrence of only one weak band localized at 2636.6 cm^{-1} (Figure 6.7b) and seen only for 42 amu deposition. The 2636.6 cm^{-1} peak which appeared as relatively broad right after deposition at 6 K, becomes narrower upon tungsten lamp irradiation and almost unchanged after annealing at 10 K (during 15 min.). Although, in the first view, its behavior upon irradiation seems to be dif-

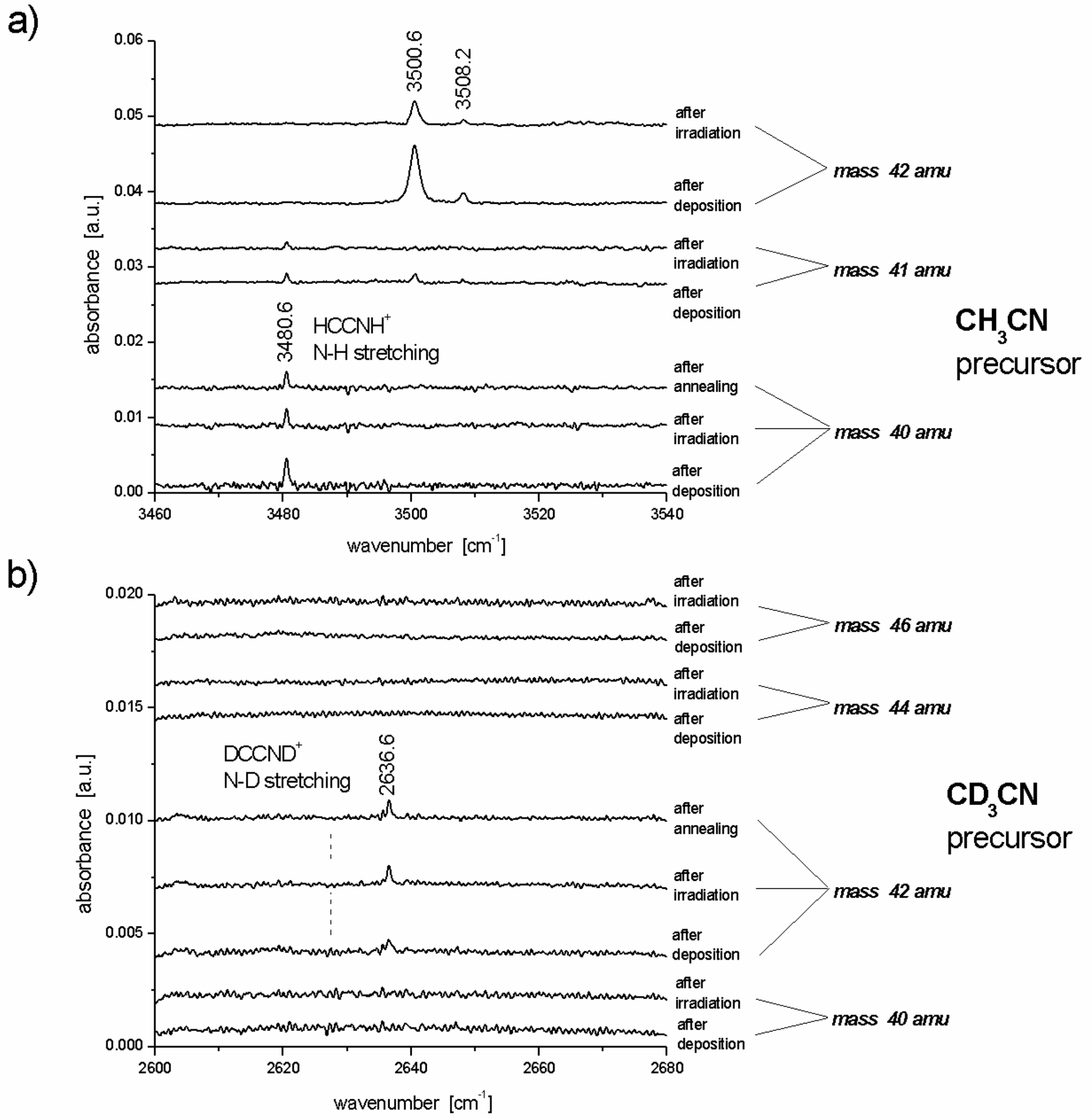

Figure 6.7. Infrared spectra of N–H (a) and N–D (b) stretching vibration recorded after deposition of different ionic species. Additionally, spectra measured after annealing at 10 K (15 min.) for mass 40 amu (a) and 42 amu (b) are shown.

ferent from those observed previously, it can be an effect of two competitive processes. Thus, the decrease of the intensity is compensated by simultaneous sharpening of the peak via relaxation of the metastable matrix sites. However, the low value of signal to noise ratio does not allow for accurate quantitative analysis of the changes in band intensity.

Analysis of the experimental results obtained for both CH_3CN and CD_3CN precursors (Figure 6.7) with calculated infrared spectra (Table 6.3) allows for spectral assignment of 3480.6 and 2636.6 cm^{-1} bands to $HCCNH^+$ and $DCCND^+$ species, respectively (Table 6.3). The 3480.6 cm^{-1} absorption, associated with deposition of ion mass of 40 amu, the $C_2H_2N^+$, appears to be in very good agreement with the strongest vibrational mode predicted by the calculations and attributed to the N–H stretching of the $HCCNH^+$ cation. Similarly, the deposition of ion of mass 42 amu, the $C_2D_2N^+$, results in the 2636.6 cm^{-1} absorption which cannot be obtained if ions of another mass are deposited. Thus the latter peak can be assigned to the N–D stretch of the $DCCND^+$ cation. The computed frequencies given in Table 6.3 were scaled using a factor of $f = 0.955$. The f value results from averaging of two scaling factors obtained for experimental frequencies for N–H and N–D stretching vibrations giving 3492.6 and 2628.4 cm^{-1} values, respectively.

Another argument supporting the 3480.6 and 2636.6 cm^{-1} bands' assignment arises from the excellent agreement of theoretical and experimental values of the isotopic shift between the N–H and N–D vibrational frequencies. The obtained frequency ratios of $\rho = \nu_{\mathrm{N-H}}/\nu_{\mathrm{N-D}}$ are of $\rho_{calc.} = 1.33$ from DFT results and of $\rho_{Ne} = 1.32$ from absorptions in neon matrix.

As noted above predicted absorption intensities of C–H (3186.8 cm^{-1}, scaled) and C–D (2387.3 cm^{-1}) stretching bands (Table 6.3) are, respectively, about 2.7 and 3.7 times lower than those of N–H(D) vibrations. Possibly, a very weak absorption could be seen in the corresponding spectral region after deposition of the 40 amu ion. Indeed a very weak band occurring at ~ 3178 cm^{-1} (not shown) could be considered as possible candidate for the C–H vibration of the $HCCNH^+$ ion. As it is seen in Figure 6.7b the N–D absorption is very weak and as could be expected from comparison of DFT intensities, there is no evidence of C–D absorption after 42 amu ion deposition from the CD_3CN precursor.

$H(D)_2CCN^+$ and $H(D)_2CNC^+$ Cations

Use of acetonitrile as a precursor substance suggests that the most abundant fragments product of the EI source must be those resulting from breaking the C–H bond. On the other hand, earlier matrix-isolation experiments (on the CNC^+ ion [51,106]) revealed that the C–C–N chain can easily isomerize into C–N–C, and H_2CNC^+ is also expected. DFT computations for H_2CCN^+ and H_2CNC^+ cations revealed singlet electronic ground states of both isomers (Figure 6.5). Both molecules have planar geometry with C_{2v} symmetry. The potential energy minimum for the more stable isomer, H_2CCN^+ is 19 kJ/mol lower than that of H_2CNC^+. On the other hand, as shown in Table 6.4, the intensity of the C–C–N asymmetric stretch at 2214.7 cm^{-1} (unscaled) of the H_2CCN^+ ion are about a factor of 2 lower than for the C–N–C asymmetric stretch at 2039.3 cm^{-1} of less stable H_2CNC^+ isomer. The difference between corresponding vibrational intensities in D_2CCN^+ and D_2CNC^+ species is only slightly higher. In general, the intensities of the strongest vibrational modes of deuterated species are only a little lower than those with hydrogen atoms. Transition intensities associated with CH_2 stretching motions are predicted to be relatively stronger in H_2CCN^+ than for H_2CNC^+ and comparable with the C–C–N symmetric stretch of the former isomer.

It must be noted that the DFT IR frequencies presented in Table 6.4 differ from values calculated for vibrational structure of PE (photo-electron) spectra by *Botschwina et al.* [97]. In this case to be consistent with the results reported above, only the DFT results presented here are taken into consideration in the analysis of the experimental data.

Deposition of ions of mass 40 amu resulted in a very weak absorption at 2119.8 cm^{-1}, which cannot be observed if ions of other masses are selected (Figure 6.8a). The diagrams b) and c) show two absorptions associated with deposition of ion mass of 42 amu, using the deuterated precursor. The weaker peak localized at 2130.5 cm^{-1} and much stronger one at 1965.9 cm^{-1} did not appear for deposition of other ionic masses. All three bands exhibit sensitivity to the tungsten lamp and disappear or diminish upon a few hours of irradiation depending on the initial absorption intensity. The ion current for deuterated species was about a factor of 3 higher than for the non-deuterated ones (Table 6.1).

These data indicate that all spectral features seen in Figure 6.8 originate from ionic species. The frequency of the 2119.8 cm^{-1} peak corresponds to the spectral region of the asymmetric C–C–N stretching of H_2CCN^+ ion and in view of the DFT calculation results

Table 6.4 Spectroscopic data for H_2CCN^+, D_2CCN^+, H_2CNC^+ and D_2CNC^+ cations. DFT computations on B3LYP/6-311++G(3df,3pd) level of theory.

vibrational symmetry and mode		vibrational frequencies in cm^{-1} (calculated intensities in km/mol)			
		DFT unscaled	Ne matrix	DFT unscaled	Ne matrix
		H_2CCN^+, C_{2v}, singlet state		**D_2CCN^+**	
B_1	N–C–C bend	248.8 (0)		239.3 (1)	
B_2	N–C–C bend	339.5 (0)		307.8 (0)	
B_2	$CH(D)_2$ rock	1029.1 (0)		840.1 (1)	
A_1	C–C–N sym. str.	1100.0 (65)		937.9 (37)	
B_1	$CH(D)_2$ wag	1154.9 (8)		925.4 (1)	
A_1	$CH(D)_2$ bend	1449.8 (8)		1201.7 (14)	
A_1	C–C–N asym. str.	2214.7 (339)	2119.8^T {0.957}*	2179.3 (281)	2130.5^T {0.978}*
A_1	$CH(D)_2$ sym. str.	3081.1 (55)		2272.1 (61)	
B_2	$CH(D)_2$ asym. str.	3190.5 (84)		2381.8 (30)	
		H_2CNC^+, C_{2v}, singlet state		**D_2CNC^+**	
B_1	C–N–C bend	195.2 (2)		189.0 (1)	
B_2	C–N–C bend	230.1 (9)		215.7 (4)	
B_2	$CH(D)_2$ rock	1146.0 (8)		903.8 (13)	
B_1	$CH(D)_2$ wag	1198.8 (7)		953.4 (0)	
A_1	C–N–C sym. str.	1218.8 (7)		1295.3 (0)	
A_1	$CH(D)_2$ bend	1506.7 (9)		1004.1 (6)	
A_1	C–N–C asym. str.	2039.3 (723)		2017.3 (685)	1965.9 {0.975}*
A_1	$CH(D)_2$ sym. str.	3066.9 (21)		2245.0 (28)	
B_2	$CH(D)_2$ asym. str.	3187.1 (51)		2384.7 (14)	

*scaling factors estimated for individual DFT frequencies
^{T}tentative assignment

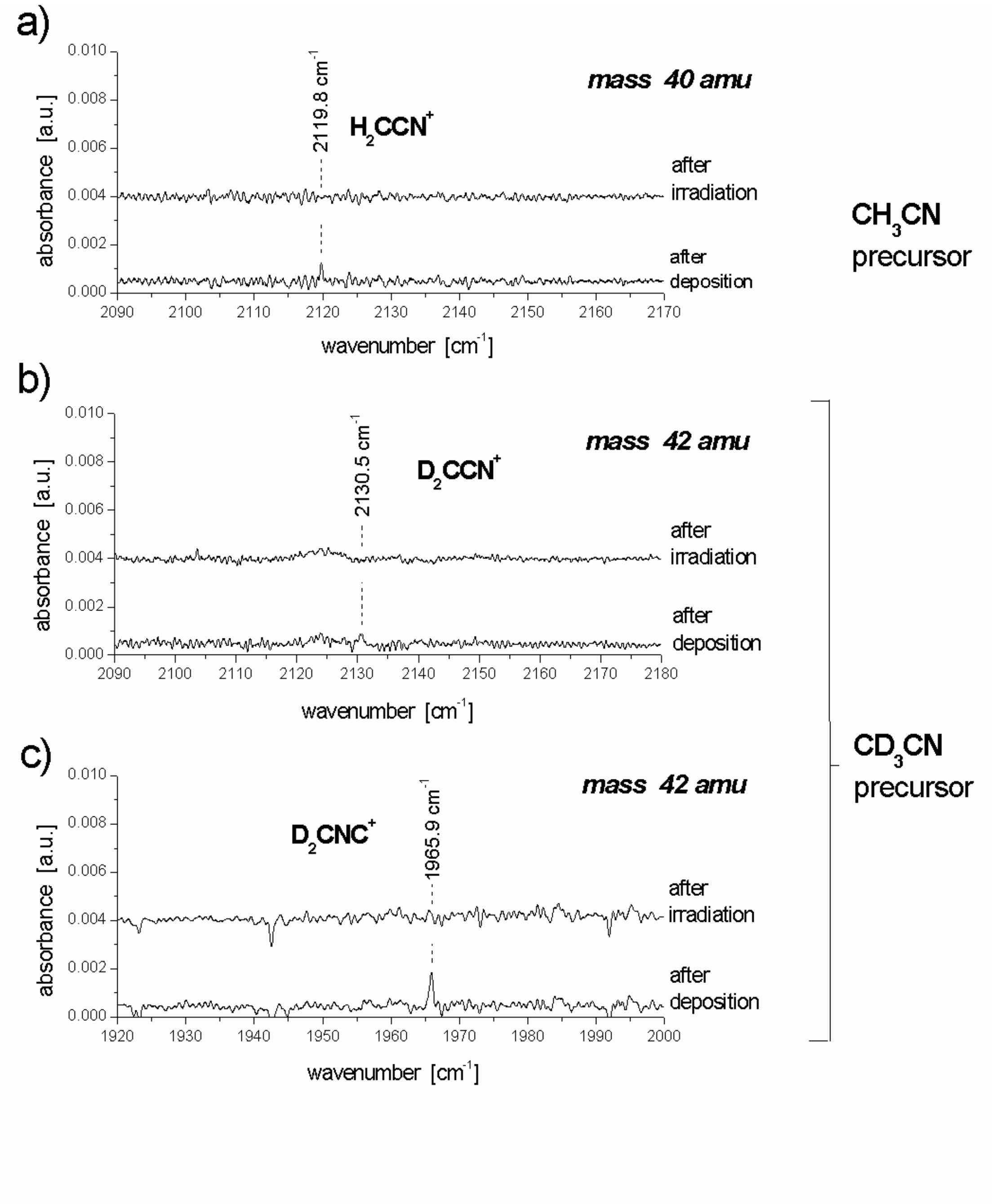

Figure 6.8. Infrared spectra recorded after deposition of ionic species of masses 40 and 42 amu, upon EI ionization of CH_3CN and CD_3CN precursors, respectively. The effect of ~ 4 hrs tungsten lamp irradiation is demonstrated on upper spectrum of each diagram. Plots (a) and (b) show absorptions in C–C–N stretching region of H_2CCN^+ and D_2CCN^+ species, respectively. Plot (c) shows an absorption band in the C–N–C stretching region of the D_2CNC^+ isomer.

can be tentatively assigned to this vibrational mode. The assignment is supported by the value of the scaling factor of 0.957 found for the respective theoretical frequency from Table 6.4. Poor signal to noise ratio allows as well only for tentative assignment of very weak and broader band at 2130.5 cm^{-1}. In this case the scaling factor used for the computed frequency of the C–C–N stretching vibration of the D_2CCN^+ ion is 0.978. On the other hand, while about three times more deuterated than hydrogenated ions were deposited (see Table 6.1), absorption of the former ones is expected to be even higher (especially since the difference between predicted intensities is only 20 %). Considering the stronger absorption band centered at 1965.9 cm^{-1}, additional experiments revealed that the intensity of this peak increases with the number of deposited ions and its assignment is rather clear. Its frequency corresponds to that of the C–N–C asymmetric stretching of D_2CNC^+ predicted as the most intense band at 2017.3 cm^{-1} (unscaled, Table 6.4). The estimated scaling factor is 0.975. Evidence for occurrence of C–N–C of H_2CNC^+ has unfortunately not been found in the recorded spectra, which in view of the low intensity of 2119.8 cm^{-1} band is not surprising.

Experiments show that among all ions of mass 40 amu, produced upon EI ionization of CH_3CN, and selectively deposited in neon matrix at 6 K, the band attributed to the $HCCNH^+$ ion clearly dominates in the IR spectra. Assuming that predicted IR intensities of observed bands (Tables 6.3 and 6.4) of all three $C_2H_2N^+$ isomers (H_2CCN^+, H_2CNC^+, $HCCNH^+$) can be compared, the deposition clearly indicate that the mostly abundant ion in neon matrix is $HCCNH^+$. As mentioned in the previous section, the formation of $HCCNH^+$ could possibly proceed via ion–molecule reaction of C_2HN^+ fragment ion with the acetonitrile precursor.

Another question is related to the origin of the H_2CNC^+ isomer. Indeed, the experiment does not allow to determine if this ion is generated in the EI source or rather produced *in situ* during the deposition process. The latter way would include isomerization by means of electron irradiation used for neutralization of the neon matrix, which seems to be, however fairly inefficient.

6.4 Conclusions

This chapter deals with the results of matrix-isolation FT-IR study of selectively deposited positive ions from an acetonitrile CH_3CN precursor. The ions are generated by electron impact (EI) ionization. The products of ionization, fragmentation and ion-molecule reactions are deposited in neon matrix at a temperature of 6 K. Isotopically labeled species are also examined using the deuterated CD_3CN precursor.

Mass-selective deposition of ions using CH_3CN and CD_3CN precursors, result in infrared bands attributed to CH_3CNH^+, H_2CCN^+, H_2CNC^+ and $HCCNH^+$ cations. The interpretation of the IR spectra is supported by predicted harmonic fundamentals using density functional (DFT/B3LYP) computations. Correlated changes in intensities (decrease) upon irradiation of the samples with a tungsten lamp, which involves the photochemical effect leading to photomobilization of electrons and neutralization of the cations, allow to distinguish cationic species from impurities.

Protonated acetonitrile, CH_3CNH^+ (mass 42 amu) is well characterized by its strong N–H stretching vibration observed in Ne matrix. The N–H frequency is shifted by about 27 cm^{-1} to the red with respect to the gas phase value. An absorption attributed to the CH_3 symmetric stretch is also observed. The spectral assignments are based on correlation and isotopic study (CD_3CND^+, mass 46 amu) and are in very good agreement with calculated frequencies.

Although it appears at first glance that the IR signal from mass 40 amu (from CH_3CN) and 42 amu (from CD_3CN) must be due to CH_2CN^+ and CH_2NC^+, several isomers are possible. Experimental and theoretical data allowed for spectral identification of cationic $HCCNH^+$ isomer (mass 40 amu) via its N–H stretching vibration. The assignment for this ion and its deuterated analogue is confirmed by the agreement between the predicted and observed isotopic shift. Tentative assignments are also made for two other isomers, H_2CCN^+ and H_2CNC^+, obtained from the same deposition. In this case the observed absorptions are fairly weak, but indicate an ion abundance of H_2CCN^+ and H_2CNC^+ in the ion ensemble of mass 40 amu.

7 Acetylene Cation

7.1 Introduction

Molecular ions composed of carbon and hydrogen atoms, so-called carbo-ions have been extensively investigated by mass spectrometry but their spectroscopic data were considerably limited until a series of direct observations done some twenty years ago. A series of experiments on the most fundamental polyatomic CH_n^+ ($n \geq 2$) and $C_2H_n^+$ ($n \geq 1$) ions was initiated by recording the infrared spectrum of the CH_3^+ cation by *Crofton et al.* [107,108]. The acetylene ion $C_2H_2^+$ is one among those species, playing an important role in nature, e.g. processes in the atmospheres of outer planets of the Solar System as well as in combustion and plasmas. It is generated as primary ion from stable neutral acetylene compound, which is known as an ubiquitous product of the degradation of carbon and hydrogen containing compound in high-energy systems. Most data have been obtained for $C_2H_2^+$ from the spectroscopy of Rydberg states — first results were reported already in 1935 by *Price* [109], and from photoionization and photoelectron spectroscopy of its neutral parent. This research was continued later by many investigators including *Herzberg* [110] and some data gained from a high resolution infrared study in a discharge cell have been reported quite recently [111].

Gas phase studies of carbo-ions were accompanied by relevant experimental efforts using matrix-isolation [112,113]. The asymmetric C–H stretching mode of $HCCH^+$ embedded in solid neon has been identified by *Jacox* and coworkers at 3137.6 cm^{-1} [114,115] i.e. close to that known from the gas phase at 3135.98 cm^{-1} [108], and shifted by 32.1 cm^{-1} from the same vibration band observed in an argon matrix [113,114,116]. In this experiment the C_2H_2/Ne sample was codeposited with pure neon gas that had been passed through a microwave discharge. The same spectra for isotopically substituted species (^{13}C and deuterium) have also been recorded.

Our experimental efforts using an acetylene precursor gas in the electron impact ion source were aimed at the C_2^+ radical cation. Unfortunately, its well-known electronic transitions could not be observed in this experiment after mass-selective deposition of C_2^+ in a neon matrix. However, deposition of the parent cation $C_2H_2^+$, in spite of its relatively weak infrared transition, resulted in detection of this ion. These results are discussed in the following sections. The visible and UV spectra also showed no evidence of C_2 or C_2^-

7.2 Experimental

The acetylene precursor gas (Messer Griesheim, 99 %) was introduced to the electron impact ion source under a pressure of about 3×10^{-5} mbar (source chamber). As usually, the EI source and ion-guiding optics were optimized for the ion of interest, and the deposition was then started after cooling down the cryostat to 6 K (LEYBOLD system). The flow rate of the matrix neon gas, deposited in an amount of 7 mmol, was monitored by the pressure growth in the cryostat chamber, about $3 - 5 \times 10^{-6}$ mbar, and its drop in the gas container. The pressure in the source chamber was kept constant during deposition, typically for 4 – 6 hours, and the ion current was monitored in order to check its stability and to estimate its average value, which for $C_2H_2^+$ (mass 26 amu) cation was between 2.9 – 3.6 nA. Average ion current of the C_2^+ radical was substantially lower, less than 1 nA.

The measurements of infrared, visible, or UV absorption spectra were performed with the BRUKER IFS 120 HR spectrometer, using the glowbar and tungsten sources. Infrared spectra in the range of 400 – 4000 cm^{-1} were recorded with 0.06 cm^{-1} resolution, and 1 cm^{-1} in the visible and UV range. Additionally, the samples were irradiated by tungsten lamp, and annealed at temperature of 10 K to follow changes resulting from photochemical effects or thermal treatment of the matrix.

7.3 Results and Discussion

7.3.1 Computations

Extensive experimental and theoretical studies indicate that $C_2H_2^+$ is a linear molecule in its ground electronic state of $^2\Pi_u$ symmetry, formed upon ionization of the neutral acetylene by removal of the one from the four π_u electrons [111,117,118]. Nevertheless, the infrared spectra were independently calculated in this work in order to check the accuracy of the theoretical method used complementary to other studies. Computations were carried out by means of *Gaussian 98* using the hybrid B3LYP technique, and made with the large 6-311++G(3df,3pd) basis set. Optimization started from linear geometry resulted in equilibrium H–C and C–C distances of 1.04 and 1.24 Å, respectively, with the latter one close to the 1.23 Å obtained experimentally [111]. The frequencies of infrared-active vibrational transitions are shown in Table 7.1. The scaling factor obtained for the C–H frequency of ~ 0.96, the same as usually applied for this type of compounds [59,60,100,101], indicates very good agreement between theory and experiment.

Table 7.1. $C_2H_2^+$ cation: infrared-active transition frequencies

Theory: DFT (B3LYP/6-311++G(3df,3pd))			Experiment
unscaled	scaled [a]	vibrational symmetry	Ne matrix
714.2 (32)	688.1	π_u	
752.2 (111)	724.7	π_u	
3253.7 (444)	3135.98	σ_u	3134.8 [b]

[a] scaling factor f = 0.9638 estimated from frequency for C–H stretching in the gas phase 3135.98 cm^{-1} [108]

[b] reported at 3137.6 cm^{-1} in [114]

7.3.2 Mass Spectrum

The quadrupole mass spectrum of C_2H_2 ionized in the electron impact ion source (EI) is shown in Figure 7.1. Apart from the most intense peak of the $C_2H_2^+$ parent cation, fragmentation results in a relatively strong C_2H^+ ion peak, weaker fragments like C^+, C_2^+, CH^+, protonated acetylene $C_2H_3^+$, and much weaker ethylene radical $C_2H_4^+$ ion (though, with available resolution one cannot estimate the contribution of residual N_2^+ ion (mass 28 amu) to this peak). In the higher mass region one can notice the presence of $C_4H_2^+$ as well as acetylene and C_2H ionic complexes.

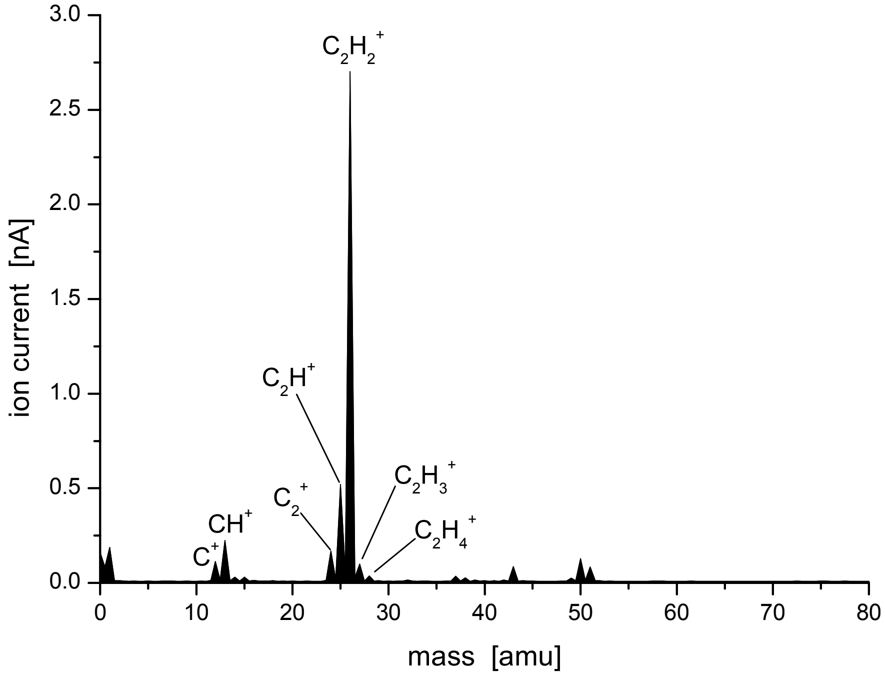

Figure 7.1. The quadrupole mass spectrum produced from the electron impact ionization of acetylene, C_2H_2.

7.3.3 Matrix-Isolated $C_2H_2^+$ Cation

The infrared spectrum, recorded in the frequency range of 500 – 4000 cm^{-1} reveals, besides a few known impurity absorptions including water and CO_2, two relatively strong groups of bands in the regions of bending, about 732 cm^{-1}, and C–H asymmetric stretching vibrations around 3279 cm^{-1}, attributed to neutral C_2H_2 species. It should be noted that these absorptions exhibit a rather complex structure in contrast to those observed in a xenon matrix. However, spectra of neutral acetylene, their origin and appearance, are outside the scope of this work and will not be discussed here. Apart from broad feature of parent molecule at 3279 cm^{-1}, a recorded spectrum indicates an occurrence of sharp and relatively weak band shifted about 144 cm^{-1} toward lower frequencies, centered at 3134.8 cm^{-1} — see Figure 7.2. The bottom trace in the graph shows a spectrum recorded directly after $C_2H_2^+$ ion beam deposition (in neon matrix at 6 K). After the first

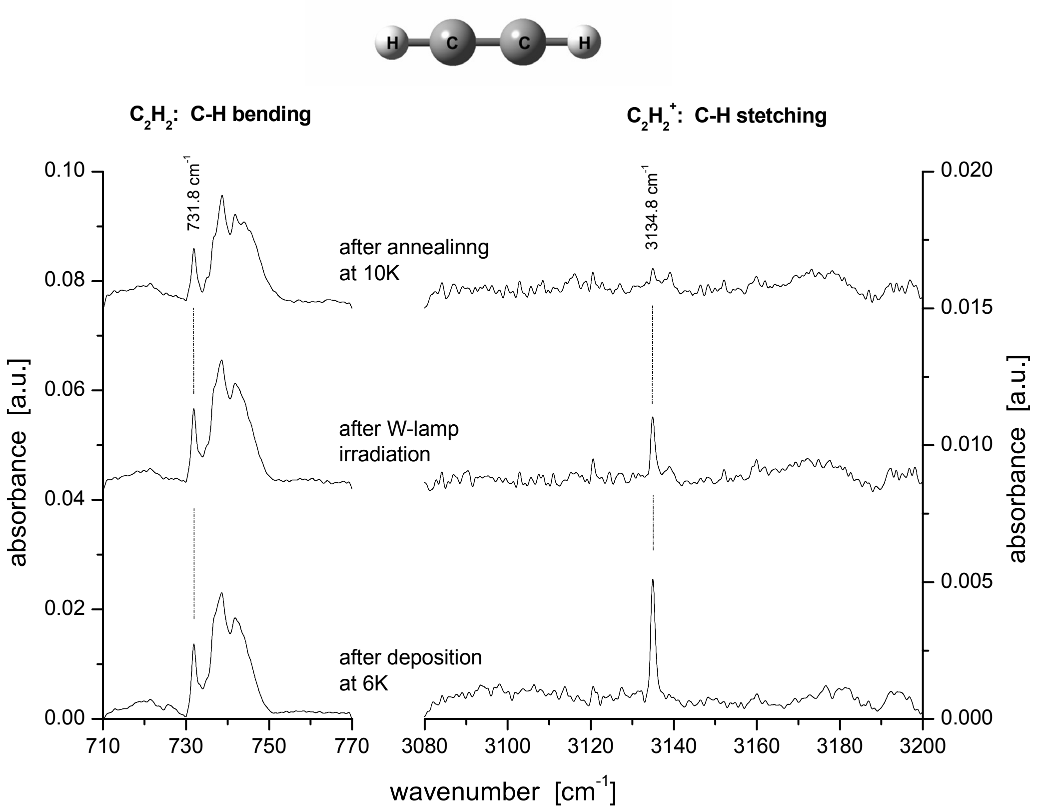

Figure 7.2. Infrared absorption spectra in the region of C–H bending of neutral C_2H_2 (right panel) and C–H stretching vibration after $C_2H_2^+$ cation (on left) deposition in Ne matrix. Bottom trace shows spectrum recorded directly after sample deposition at 6 K; middle — after irradiation of the matrix for 5 hours with tungsten source; top — after 15 minute annealing at 10 K.

measurement was completed, the matrix sample was subjected to about 5 hours irradiation using tungsten broadband light source. As it can be seen in the middle spectrum in Figure 7.2, the irradiation results in a considerable drop in the 3134.8 cm^{-1} peak intensity. In the third step, the sample was annealed for 15 minutes at a temperature of 10 K. As shown in the upper spectrum, the thermal treatment causes further, dramatic reduction of the intensity of the observed peak.

Comparison of the 3134.8 cm^{-1} band intensity obtained for different values of average ion current during deposition indicates its proportional growth with the number of deposited $C_2H_2^+$ ions. This absorption has also not been observed when a C_2H_2/Ne mixture was deposited or the EI was switched off. These results, together with data obtained in previous experiment in Ne matrix by *Jacox et al.* [114], allows to assign the 3134.8 cm^{-1} frequency to the C–H vibration of $C_2H_2^+$ cation (Table 7.1). In fact, the experimental value obtained in our laboratory is shifted by 2.8 cm^{-1} toward lower frequency from the previously reported value [114], and no satellite peak in neighborhood is seen. However, direct comparison of spectra obtained in these two experiments are rather difficult and the results suggest that the different ways used in introducing the ions into the neon matrix are responsible for this shift.

As it is seen in middle and upper traces in Figure 7.2, the observed absorption is sensitive to matrix irradiation and annealing. The first effect has been already discussed in the previous chapters as a consequence of retrapping of photo-mobilized electrons by positive ions embedded in the neon matrix. Significant decrease in the signal upon annealing can be explained by recombination with other guest species or impurities due to their diffusion through neon at 10 K

As mentioned above, besides the ion line, much stronger parent molecule absorptions are observed in all spectra (Figure 7.2). In order to test once again the question of efficiency of ion neutralization in the deposition process, an additional control experiment was performed. By comparison of the C_2H_2 spectra obtained from deposition of acetylene — under exactly the same conditions — with or without ionization of the gas passing through the EI source, one could estimate the amount of the neutral acetylene compound reaching the neon matrix directly from the source chamber during ion deposition. Indeed, measurements revealed that C_2H_2 absorption intensities, around 732 and 3279 cm^{-1}, are very close for both deposits. Clearly, the trapping of neutral molecules gives the main contribution to the observed neutral bands.

7.4 Conclusions

Mass selected deposition of acetylene cation $C_2H_2^+$ in neon matrix at temperature of 6 K resulted in observation of single, sharp absorption peak localized at frequency of 3134.8 cm^{-1}, which exhibits sensitivity to tungsten lamp photolysis and matrix annealing. Recorded absorption has been attributed to C–H stretching vibration of $C_2H_2^+$ ion and found to be shifted of about ~ 1.2 cm^{-1} toward the lower frequencies from corresponding gas phase value. Density functional computational results reveal very good agreement of predicted C–H frequency (scaled by ~ 0.96) with the experiment.

References

[1] E.E. Ferguson, F.C. Fehsenfeld, D.L. Albritton, in *Gas Phase Ion Chemistry*, vol.1, ed. M.T. Bowers, Academic Press, New York, San Fracisco, London, 1979.

[2] R.P. Wayne, *Chemistry of Atmospheres*, Claredon Press, Oxford,1991.

[3] J.P. Maier, *Mass Spectrom. Rev.***11**, 119 (1992).

[4] E.Herbst, *Ann. Rev. Phys. Chem.* **46**, 27 (1995).

[5] R.B. Cole, *Electrospray Ionization Mass Spectrometry. Fundamentals, Instrumentation and Applications*, John Wiley and Sons, Inc., New York, 1997.

[6] L. Andrews in *Molecular Ions: Spectroscopy, Structure and Chemistry*, ed. T.A. Miller and V.E. Bondybey, North Holland, Amsterdam, 1983.

[7] P.H. Kasai, D. Mcleod, Jr., *J. Chem. Phys.* **51**, 1250 (1969).

[8] D.E. Milligan, M.E. Jacox, *J. Chem. Phys.* **51**, 1952 (1969).

[9] L.E. Brus, V.E. Bondybey, *J. Chem. Phys.* **63**, 3123 (1975).

[10] L. Andrews, *J. Am. Chem. Soc.* **90**, 7368 (1968).

[11] V.E. Bondybey, T.A. Miller, J.H. English, *J. Chem. Phys.* **72**, 2193 (1980).

[12] L.B. Knight, Jr., in *Molecular Ions: Spectroscopy, Structure and Chemistry*, ed. T.A. Miller and V.E. Bondybey, North Holland, Amsterdam, 1983.

[13] S. Fedrigo, F. Meyer, D.M. Lindsay, I. Ligniers, J.C. Rivoal, D. Kreisle, *J. Chem. Phys.* **93**, 8535 (1990).

[14] S. Fedrigo, W. Harbich, J. Buttet, *J. Chem. Phys.* **99**, 5712 (1993).

[15] W. Harbich, S. Fedrigo, J. Buttet, *Z. Phys. D* **26**, 138 (1993).

[16] W. Harbich, Y. Belyaev, R. Kleiber, J. Buttet, *Surf. Rev. Lett.* **3**, 1147 (1996).

[17] Z. Hu, B. Shen, Q. Zhou, S. Deosaran, J. R. Lombardi, D. M. Lindsay, W. Harbich, *J. Chem. Phys.* **95**, 2206 (1991).

[18] Z. Hu, J.-G. Dong, J. R. Lombardi, D.M. Lindsay, *J. Chem. Phys.* **97**, 8811 (1992).

[19] Z. Hu, B. Shen, J.R. Lombardi, D.M. Lindsay, *J. Chem. Phys.* **96**, 8757 (1992).

[20] Z. Hu, J.-G. Dong.. J.R. Lombardi, D.M. Lindsay, *J. Phys. Chem.* **97**, 9263 (1993).

[21] Z. Hu, G. Jian, J.R. Lombardi, D.M. Lindsay, *J. Chem. Phys.* **101**, 95 (1994).

[22] J.-G. Dong, Z. Hu, R. Craig, J.R. Lombardi, D. M. Lindsay, *J. Chem. Phys.* **101**, 9280 (1994).

[23] H. Wang, H. Haouari, R. Craig, Y. Liu, J. R. Lombardi, D.M. Lindsay, *J. Chem. Phys.* **106**, 2101 (1997).

[24] H. Wang, Y. Liu, H. Haouari, R. Craig, J. R. Lombardi, D.M. Lindsay, *J. Chem. Phys.* **106**, 6534 (1997).

[25] H. Wang, Y. Liu, H. Haouari, R. Craig, J. R. Lombardi, D.M. Lindsay, *J. Phys. Chem. A* **101**, 7036 (1997).

[26] H. Haouari, H. Wang, R. Craig, J. R. Lombardi, D.M. Lindsay, *J. Chem. Phys.* **103**, 9527 (1995).

[27] H. Wang. H. Haouari, R. Craig, J. R. Lombardi, D.M. Lindsay, *J. Chem. Phys.* **104**, 3420 (1996).

[28] H. Wang, R. Craig, H. Haouari, Y. Liu, J.R. Lombardi, D. M. Lindsay, *J. Chem. Phys.* **105**, 5355 (1996).

[29] H. Wang, Z. Hu, H. Haouari, R. Craig, Y. Liu, J. R. Lombardi, D.M. Lindsay, *J. Chem. Phys.* **106**, 8339 (1997).

[30] H. Wang, R. Craig, H. Haouari, J.-G. Dong, Z. Hu, A. Vivoni, J.R. Lombardi, D. M. Lindsay, *J. Chem. Phys.* **103**, 3289 (1995).

[31] S. Fedrigo, T.L. Haslett, M. Moskovits, *J. Am. Chem. Soc.* **118**, 5083 (1996).

[32] T.L. Haslett, K. . Bosnick, M. Moskovits, *J. Chem. Phys.* **108**, 3453 (1998).

[33] T.L. Haslett, K.A. Bosnick, S. Fredrigo, M. Moskovits, *J. Chem. Phys.* **111**, 6456 (1999).

[34] J.R. Gilbert, G.E. Leroi, J. Allison, *Int. J. Mass Spectrom. Ion Processes* **107**, 247 (1991).

[35] M.S. Sabo, J. Allison, J.R. Gilbert, G.E. Leroi, *Appl. Spectr.* **45**, 535 (1991).

[36] J.T. Godhout. T.M. Halasinski, G.E. Leroi, J. Allison. *J. Phys. Chem.* **100**, 2892 (1996).

[37] T.M. Halasinski, J.T. Godbout, J. Allison, G.E. Leroi, *J. Phys. Chem.* **100**, 14865 (1996).

[38] T.M. Halasinski, J.T. Godbout, J. Allison, G.E. Leroi, *J. Phys. Chem.* **98**, 3930 (1994).

[39] M. Lorenz, V.E. Bondybey, *Low. Temp. Phys.* **26**, 1044 (2000).

[40] J. P. Maier, *Mass Spectrom. Rev.* **11**, 119 (1992).

[41] J.P. Maier, *Chem. Soc. Rev.* **26**, 21 (1997).

[42] P. Freivogel. J. Fulara. D. Lessen. D. Forney, J. P. Maier, *Chem. Phys.* **189**, 335 (1994).

[43] J. Fulara, P. Freivogel, D. Forney, J. P. Maier, *J. Chem. Phys.* **103**, 8805 (1995).

[44] D. Forney. P. Freivogel, J. Fulara., J. P. Maier, *J. Chem. Phys.* **102**, 1510 (1995).

[45] J. Agreiter. A.M. Smith, V.E. Bondybey, *Chem. Phys. Lett.* **241**, 317 (1995).

[46] A.M. Smith, J. Agreiter, and V.E. Bondybey, *Chem. Phys. Lett.* **244**, 379 (1995).

[47] M. Grutter, M. Wyss, J. Fulara, and J.P. Maier, *J. Phys. Chem. A* **102**, 9785 (1998).

[48] M. Grutter, M. Wyss, J. P. Maier, *J. Chem. Phys.* **110**, 1492 (1999).

[49] P. Freivogel. M. Gutter. D. Forney, J.P. Maier, *J. Chem. Phys.* **107**. 4468 (1997).

[50] D.A. Kirkwood. H. Linnartz. M. Grutter. O. Dopfer, C. Motylewski, M. Pachkov, M. Tulej, M. Wyss, J.P. Maier. *Faraday Discuss.* **109**, 109 (1998).

[51] A.M. Smith-Gicklhorn, M. Lorenz, R. Kołos V.E. Bondybey, *J. Chem. Phys.* **115**, 7534 (2001).

[52] A.M. Smith, C. Engel, A. Thoma, G. Schallmoser, B.E. Wurfel, and V.E. Bondybey, *Chem. Phys.* **184**, 233 (1994).

[53] *Gaussian 98, Revision A.7*, M.J. Frisch, G.W. Trucks, H.B. Schlegel, G.E. Scuseria, M.A. Robb, J.R. Cheeseman, V.G. Zakrzewski, J.A. Montgomery, Jr., R.E. Stratmann, J.C. Burant, S. Dapprich, J.M. Millam, A.D. Daniels, K.N. Kudin, M.C. Strain, O. Farkas, J. Tomasi, V. Barone, M. Cossi, R. Cammi, B. Mennucci, C. Pomelli, C. Adamo, S. Clifford, J. Ochterski, G.A. Petersson, P.Y. Ayala, Q. Cui, K. Morokuma, D.K. Malick, A.D. Rabuck, K. Raghavachari, J. B. Foresman, J. Cioslowski, J.V. Ortiz, A.G. Baboul, B.B. Stefanov, G. Liu, A. Liashenko, P. Piskorz, I. Komaromi, R. Gomperts, R.L. Martin, D.J. Fox, T. Keith, M. A. Al-Laham, C.Y. Peng, A. Nanayakkara, C. Gonzalez, M. Challacombe, P.M. W. Gill, B. Johnson, W. Chen, M.W. Wong, J.L. Andres, C. Gonzalez, M. Head-Gordon, E.S. Replogle, J.A. Pople, Gaussian Inc., Pittsburgh PA, 1998.

[54] P. Cassoux and J.S. Miller, *Electron Transfer Salt-Based Conductors, Superconductors and Magnets, Chemistry of Advanced Materials: A New Discipline*, VCH, New York, 1997.

[55] J.S. Miller, A.J. Epstein, W.M. Reiff, *Science* **240**, 40 (1988).

[56] J.M. Manriquez, G.T. Yee, R.S. McLean, A.J. Epstein, J.S. Miller, *Science* **252**, 1415 (1991).

[57] F.A. Miller, O. Sala, P. Devlin, J. Overend, E. Lippert, W. Lüder, H. Moser J. Varchin, *Spectrochim. Acta* **20**, 1233 (1964).

[58] D.A. Dixon, J.S. Miller, *J. Am. Chem. Soc.* **109**, 3656 (1987).

[59] S. Lee, *J. Phys. Chem.* **100**, 33, 13959 (1996).

[60] S. Lee, *Theo. Chem.* **427**, 267 (1998).

[61] M. Fehér, C. Salud and J.P. Maier, *J. Chem. Phys.* **94**, 5377 (1991).

[62] J. Agreiter, A.M. Smith, M. Härtle and V.E. Bondybey, *Chem. Phys. Lett.* **225**, 87 (1994).

[63] J.P. Maier, O. Marthaler and F. Thommen, *Chem. Phys. Lett.* 60, 193 (1979).

[64] J.P. Maier, L. Misev and F. Thommen, *J. Phys. Chem.* **86**, 514 (1982).

[65] M. Kakimoto and T. Kasuya, *J. Mol. Spectrosc.* **94**, 380 (1982).

[66] A.J. Merer and D.N. Travis, *Can. J. Phys.* **43**, 1795 (1965).

[67] N. Oliphant, A. Lee, P.F. Bernath and C.R. Brazier, *J. Chem. Phys.* **92**, 2244 (1990).

[68] R. Brazier, L.C. O'Brien and P.F. Bernath, *J. Chem. Phys.* **86**, 3078 (1987).

[69] M. Fehér, C. Salud and J.P. Maier, *J. Mol. Spectrosc.* **145**, 246 (1991).

[70] M. Fehér, C. Salud, J.P. Maier and A.J. Merer, *J. Mol. Spectrosc.* **150**, 280 (1991).

[71] A.J. Merer and D. N. Travis, *Can. J. Phys.* **44**, 353 (1966).

[72] M. E. Jacox, *J. Mol. Spectrosc.* **71** , 369 (1978).

[73] V. E. Bondybey and J. H. English, *J. Mol. Spectrosc.* **70**, 236 (1978).

[74] M. Smith, C. Engel, A. Thoma, G. Schallmoser, B.E. Wurfel and V. E. Bondybey, *Chem. Phys.* **184**, 233 (1994).

[75] H. Linnartz, O. Vaizert, P. Cias, L. Gruter, J.P. Maier, *Chem. Phys. Lett.* **345**, 89 (2001).

[76] E. Herbst, C.M. Leung, *Astrophys. J. Supl. Series* **69**, 271 (1989).

[77] D. Smith, *Chem. Rev.* **92**, 1473 (1992).

[78] M.B. Bell, P.A. Feldmann, M.J. Travers, M.C. McCarthy, C.A. Gottlieb, P. Thaddeus, *Astrophys. J.* **483**, L61 (1997).

[79] H.E. Matthews, T.J. Sears, , *Astrophys. J. Lett.* **267**, L53 (1983).

[80] B.E. Turner,P. Friberg, W.M. Irvine, S. Saito, S. Yamamoto, *Astrophys. J.* **355**, 546 (1990).

[81] L. Olmi, R. Cesaroni, R. Neri, C.M. Walmsley, *Astron. and Astrophys.* **315**, 565 (1996).

[82] W.M. Irvine, P. Friberg, A. Hjalmarson, S. Ishikawa, N. Kaifu, K. Kawaguchi, S.C. Madden, H.E. Matthews, M. Ohishi, et al., *Astrophys. J.* **334**, L107 (1988).

[83] B.E. Turner, T. Amano, P.A. Feldman, *Astrophys. J.* **349**, 376 (1990).

[84] P. Botschwina, *Phys. Chem. Chem. Phys.* **5**, 3337 (2003).

[85] M.J. McEvan, V.G. Anicich, W.T. Huntress, P.R. Kemperer, M.T. Bowers, *Chem. Phys. Lett.* 75, 278 (1980).

[86] D.R. Bates, *Astrophys. J.* **270**, 564 (1983).

[87] T. Amano, *Astrophys. J. Lett.* **330**, L137 (1988).

[88] T. Amano, *J. Mol. Spectr.* **153**, 654 (1992).

[89] W.T. Huntress, G.F. Mitchell, *Astrophys. J.* **231**, 456 (1979).

[90] C.A. Gottlieb, A.J. Apponi, M.C. McCarthy, P. Thaddeus, H. Linnartz, *J. Chem. Phys.* **113** , 1910 (2000).

[91] P. Botschwina, *J. Mol. Spectr.* **203**, 203 (2000).

[92] S. Saito, S. Yamamoto, W.M. Irvine, L.M. Ziurys, H. Suzuki, M. Ohishi, N. Kaifu, *Astrophys. J.* **334**, L113 (1988).

[93] R.P. Thorn, Jr., P.S. Monks, L.J. Stief, S.-C. Kuo, Z. Zhang, S.K. Ross, R.B. Klemm, *J. Phys. Chem. A* **102**, 846 (1998).

[94] J.L. Holmes, P. M. Mayer, *J. Phys. Chem.* **99**, 1366 (1995).

[95] S. Moran, H. B. Ellis, , Jr. D. J. DeFrees, A. D. McLean, G. B. Ellison, *J. Am. Chem. Soc.* **109**, 5996 (1987).

[96] S. Moran, H. B. Ellis, , Jr. D. J. DeFrees, A. D. McLean, S. E. Paulson, G. B. Ellison, *J. Am. Chem. Soc.* **109**, 6004 (1987).

[97] M. Horn, M. Oswald, R. Oswald, P. Botschwina, *Ber. Bunsenges. Phys. Chem.* **99**, 323 (1995).

[98] Kai-Chung Lau, Wai-Kee Li, C.Y. Ng, S.-W. Chiu, *J. Phys. Chem. A* **103**, 3330 (1999).

[99] *Gaussian 98*, *Revision A.11*, M. J. Frisch, G. W. Trucks, H. B. Schlegel, G. E. Scuseria, M. A. Robb, J. R. Cheeseman, V. G. Zakrzewski, J. A. Montgomery, Jr., R. E. Stratmann, J. C. Burant, S. Dapprich, J. M. Millam, A. D. Daniels, K. N. Kudin, M. C. Strain, O. Farkas, J. Tomasi, V. Barone, M. Cossi, R. Cammi, B. Mennucci, C. Pomelli, C. Adamo, S. Clifford, J. Ochterski, G. A. Petersson, P. Y. Ayala, Q. Cui, K. Morokuma, P. Salvador, J. J. Dannenberg, D. K. Malick, A. D. Rabuck, K. Raghavachari, J. B. Foresman, J. Cioslowski, J. V. Ortiz, A. G. Baboul, B. B. Stefanov, G. Liu, A. Liashenko, P. Piskorz, I. Komaromi, R. Gomperts, R. L. Martin, D. J. Fox, T. Keith, M. A. Al-Laham, C. Y. Peng, A. Nanayakkara, M. Challacombe, P. M. W. Gill, B. Johnson, W. Chen, M. W. Wong, J. L. Andres, C. Gonzalez, M. Head-Gordon, E. S. Replogle, and J. A. Pople, Gaussian, Inc., Pittsburgh PA, 2001.

[100]M.W. Wong, *Chem. Phys. Lett.* **256**, 353 (1996).

[101]S. Lee, *Theo. Chem.* **427**, 267 (1998).

[102]M.E. Jacox, *Chem. Phys.*, **189**, 149 (1994).

[103]V.E. Bondybey and M. Lorenz, *J. Low Temp. Phys.* **122**, 509 (2001)

[104]C.L. Lugez, M.E. Jacox, Johnson, D. Russell III, *J. Chem. Phys.* **110**, 5037 (1999).

[105]E.P. Hunter, S.G.Lias, *J. Phys. Chem. Ref. Data* **27**, 413 (1998).

[106]A.M. Smith-Gicklhorn, M. Frankowski and V.E. Bondybey, *Phys. Chem. Chem. Phys.* **4**, 1425 (2002).

[107]M.W. Crofton, W.A. Kreiner, M.-F. Jagod, B.D. Rehfuss, T. Oka, *J. Chem. Phys.* **83**, 3702 (1985).

[108]M.W. Crofton, M.-F. Jagod, B.D. Rehfuss, T. Oka, *J. Chem. Phys.* **86**, 3755 (1987).

[109]W.C. Price, *Phys. Rev.* **47**, 444 (1935).

[110]G. Herzberg, *Molecular Spectra and Molecular Structure III, Electronic Spectra and Electronic Structure of Polyatomic Molecules*, Van Nostrand, New York, 1966.

[111]M.-F. Jagod, M. Rösslein, C.M. Gabrys, B.D. Rehfuss, F. Scappini, M.W. Crofton, T. Oka, *J. Chem. Phys.* 97 (10), 7111 (1992).

[112]M.E. Jacox, *Chem. Phys.* **7**, 424 (1975).

[113]M.E. Jacox, W.B. Olson, *J. Chem. Phys.* **86**, 3134 (1987).

[114]D. Forney, M.E. Jacox, W.E. Thompson, *J. Mol. Spec.* **153**, 680 (1992).

[115]D. Forney, M.E. Jacox, W.E. Thompson, *J. Mol. Spec.* **170**, 178 (1995).

[116]L. Andrews, G.P. Kushto, M. Zhou, S.P. Willson, ; P.F. Souter, *J. Chem. Phys.* **110**, 4457 (1999).

[117]T.J. Lee, J.E. Rice, H.F. Schaefer III, *J. Chem. Phys.* **86**, 3051 (1987).

[118]L.A. Curtiss, J.A. Pople, *J. Chem. Phys.* **91**, 2420 (1989).

PART IV

Activation Spectroscopy of Rare Gas Solids

This part deals with characterization of thermally- and photon-activated electrons emitted from neon and argon matrices upon heating or laser irradiation, respectively. In spite of the negative electron affinity of Ne and Ar atoms, appreciable concentrations of electrons can be trapped in the corresponding solids. Solid Ne and Ar films are deposited on a cold substrate under electron irradiation, or are irradiated after deposition is completed. Electrons are trapped at defect sites or by impurities, and can be promoted into the conduction band in an annealing process or by interaction with photons. Subsequently they can recombine with positive centers producing VUV Thermally Stimulated Luminescence (TSL, thermoluminescence), but can also be extracted from the solid, and detected as an “exoelectron” current — TSEE (Thermally Stimulated Exoelectron Emission) or PSEE (Photon-Stimulated Exoelectron Emission).

The TSEE profiles of the electron current versus temperature reveal two broad features near 7.5 and 10 K in solid Ne, which are shown to correspond to two distributions of electron trapping sites with slightly different activation energies.

TSEE measurements in solid Ar reveal a prominent maximum around 12 K, a broad band between 14 and 16 K and a much weaker near 22 K coinciding with those observed in TSL. This indicates an occurrence of electron traps contributing to recombination of charged species and emission of electrons from the solid.

PSEE and TSEE results obtained from nominally pure and doped Ar samples suggest an occurrence of cascade relaxation processes in which electrons are activated by photons generated in thermally induced radiative recombination.

8 Exoelectron Emission from Neon and Argon Solids

8.1 Introduction

Solidified rare gases constitute the simplest solids — atomic cryocrystals — which are ordered cubic arrays of closed shell atoms barely interacting via *van der Waals* attraction [1]. Rare Gas Solids (RGS) are the widest band gap insulating materials [2]. Through their simplicity, RGS provide an attractive and fundamental model framework for exploring the interconnection between electronic and atomic processes, studying the stability and dynamics of charged centers and intermediates as well as electronic relaxation processes. Charge carriers formed in RGS subjected to ionizing radiation are of considerable interest for fundamental solid-state physics as well as for molecular processes in condensed hosts, particularly for matrix-isolated spectroscopy of ionic species. Research conducted in this field find a number of important applications in material science, photochemistry, and radiation physics.

While rare gas atoms have a closed electronic shell, and their anions are not stable in the gas phase, electrons are bound in the condensed, heavier solids of more polarizable rare gases. Table 8.1 shows selected parameters of electronic band structure of Ne, Ar, Kr and Xe solids [2]. Electron affinities, or in other words electron solvation energies are positive, $E_a = 0.3$ eV for krypton and 0.5 eV for xenon, so that an electron in the conduction band has to overcome a considerable barrier in order to leave the solid, and at least this amount of energy needs to be supplied to dislodge it from the surface [2,3]. On the other hand for the lightest gases, like neon and argon, repulsive forces prevail and electron affinities are negative (Table 8.1). In this case, energy has to be expended to bring an electron from vacuum into a neon or argon lattice, and conversely, when an electron exits such solid and leaves its surface, this excess energy may be converted into its kinetic energy. Due to the negative electron affinities conduction electrons in solid Ne and Ar repel surrounding rare gas atoms creating a lattice expansion or "bubble" around it [2,4].

Table 8.1 Selected parameters of the electronic band structure of rare-gas solids: I_p – ionization energy of atoms, E_g – energy band gap at the point Γ, E_{VB} – valence band width, and E_a – electron affinity; from [2]

RGS solid	I_p [eV]	E_g [eV]	E_{VB} [eV]	E_a [eV]
Neon	21.559	21.58	1.3	- 1.3
Argon	15.755	14.16	1.7	- 0.4
Krypton	13.996	11.01	2.3	0.3
Xenon	12.127	9.33	3.0	0.5

In spite of the negative electron affinities of the light atoms, numerous experiments show that appreciable concentrations of electrons can be stabilized in solid argon and even in neon. When, for instance, a rare gas solid is exposed to an ionizing, vacuum UV, or energetic electron beam, annealing of the sample even an appreciable time after completed irradiation results in "thermoluminescence", usually attributed to electron – positive charge center recombination. This is also observed when samples are grown by condensing products of an electric discharge [5].

A simple calculation shows that an approximate overall neutrality of the sample has to be maintained, since already for an extremely low excess of electrons (or positive charges) the Coulombic repulsion exceeds the binding energy of the rare gas [6]. The simultaneous presence of electrons and positively charged rare gas centers is evidenced in the annealing experiment, where as temperature is slowly raised the trapped electrons are thermally mobilized, and light emission from the solid is invariably observed [7-9]. Obviously, also reactions of neutral species can result in photon emission, and there is a considerable volume of literature available involving studies of the so-called thermoluminescence in matrices [10-18]. In this case an emission is observed from solids prepared under conditions where no charged species can be generated.

The luminescence associated with electron – positive charge recombination usually occurs in the annealing experiments at lower temperatures than that due to neutral reactions, and much of it typically occurs in the VUV, close to the energy range characteristic of rare gas cation – electron recombination processes [7,8]. Since, as mentioned above, a considerable energy has to be expended to insert an electron into solid neon or argon, the observed luminescence can clearly not be due to completely free conduction band electrons. Thus, such electrons must be localized in lower energy trapping sites, perhaps by Coulombic interaction with nearby positive charges. The most common counter-ions in nominally pure rare gases are intrinsic, positively charged centers, which can be viewed, as shown both theoretically [2] and experimentally [19-21], as Rg_2^+ dimers (or so-called self-trapped holes) formed during sample irradiation. Electrons can be stabilized in the proximity of lattice defects, vacancies, vacancy clusters or pores, and some may be attached to impurities invariably present in the samples, which thus act as "electron scavengers".

The emission attributable to the electron – ion recombination usually occurs first during sample heating, and may as the temperature is raised be successively followed by chemiluminescence due to reactions of neutral hydrogen atoms and then also to heavier species. The strong recombination luminescence thus provides an experimental tool for studying localized electrons or other reactive species, and information about the nature and depth of the corresponding trapping sites. Since a quite modest, few Kelvin increase in the sample temperature results in luminescence, at least some of the traps must be relatively shallow, and electrons easily mobilized. With the increase in temperature, they are promoted into the conduction band, diffuse through the solid, and recombine with the positively charged counter-ions.

Very recently, experimental work done in our laboratory in cooperation with the group of *E.V. Savchenko* from *Verkin Institute of Low Temperature Physics and Engineering of National Academy of Sciences* in Ukraine, have shown that the trapped electrons can also be observed directly. With the help of a small extraction potential, they can be freed from the solid and detected as an electric current. Since the first demonstration, a few years ago, when TSEE was detected from nominally pure solid argon [9], research in this area was extended to doped argon samples and recently also to solid neon [22]. The latter experiments are presented in this part of the thesis. The **T**hermally **S**timulated **L**uminescence (TSL, thermoluminescence) **T**hermally **S**timulated **E**xoelectron **E**mission (TSEE) and recently also **P**hoton-**S**timulated **E**xoelectron **E**mission (PSEE) are useful complementary methods for investigating high energy intermediates and their trapping in rare gas solids,

The following sections deal with the spectroscopy of thermally activated exoelectrons from nominally pure neon and argon samples deposited as thin films on a metal substrate. In case of condensed argon the TSL, TSEE and PSEE techniques have also been implemented to examine the influence of O_2, N_2 and CO guest species on the observed spectra.

8.2 Experimental

The samples on nominally pure Ne and Ar, as well as Ar doped with O_2 , CO and N_2 were grown from the gas phase by pulsed deposition on a metal substrate cooled by the closed-cycle helium refrigerator — LEYBOLD system. The neon samples were deposited continuously at 6 K. For argon, continuous deposition started at a relatively high temperature of 60 K and then gradually decreased within ~10 minutes to 6 K. This resulted in good optical quality, transparent Ar films. High purity matrix gases Ne (99.999 %), Ar (99.999 %), and doping gases O_2 (99.98 %), CO (99.997%) and N_2 (99.999 %) were used.

Charged centers were generated using electron irradiation in two ways: (i) by deposition of the gas under electron bombardment, and (ii) by irradiation of the neutral sample after deposition. In the latter case the thickness of the subsurface layer containing charged centers depends on the electros energy and can be easily varied. By using the first way it is possible to generate charged centers across the whole sample. For the sample grown under irradiation, the kinetic energy of the electrons was determined by the potential applied to filament kept in the range of -120 – -130 eV. A higher potential, up to -600 V was used for irradiation of neutral sample. In general, the kinetic energy of electrons used in the irradiation was lower than the threshold energy for defects formation via elastic collisions with lattice atoms — the so-called “knock-on” mechanism. The reported threshold energy for Ar is 4.8 keV [8].

8.3 Results and Discussion

Thermoluminescence due to charge recombination, and exoelectron emission are two closely related phenomena [23]. The recombination of an electron with a positively charged intrinsic center results in population of electronically excited states of the rare gas dimers Rg_2^*, whose relaxation into the ground state is accompanied by VUV radiation. There are several mechanisms, which may contribute to exoelectron emission. The most straightforward mechanism is thermal promotion of the trapped electron into the conduction band, which of course is, in view of the low temperatures involved in the annealing process [24], only possible for electrons in very shallow trapping sites. There are several processes which can result in promotion and detrapping of electrons in deeper trapping sites. A photon resulting from thermoluminescence due to chemical reaction or charge recombination can be subsequently absorbed, resulting in the promotion of a second electron into the conduction band. Another suggestion to interpret exoelectron emission invoked an Auger type process [25], in which the energy set free upon recombination of one trapped electron with a positive charge center is nonradiatively transferred to another, nearby trapped electron. Similarly, an electron could be freed from its potential trap by energy resulting from a nearby chemical reaction, which again would then allow it to move through the solid. Clearly, the latter three processes are the product of two consecutive events, and they should exhibit a pronounced, quadratic dependence upon the concentration of the electrons and defects, which is not observed here.

8.3.1 Solid Neon

To establish the optimum potential for extracting the thermally stimulated exoelectrons, a series of almost identical experiments have been carried out, changing only the potential applied to the Faraday plate. The set of curves representing total yields of TSEE current is shown in Figure 8.1 including also the integrated intensities of two distinct features, a broader and weaker one centered near 8 K, and a sharper one located around 10.6 K. The change in potential did not substantially affect the shape of the exoelectron current curves, but as might be expected the integrated signal grew with increasing voltage reaching a plateau around +9 V. This potential was then used in most experiments. Interestingly, weak signals are observed even for small negative voltages. As noted above, the electrons could actually gain kinetic energy while leaving the conduction band and exiting into vacuum. However, the main reason is probably that due to accumulation of charged species, the surface of the nonconducting rare gas layer may be at a different potential than the metal substrate.

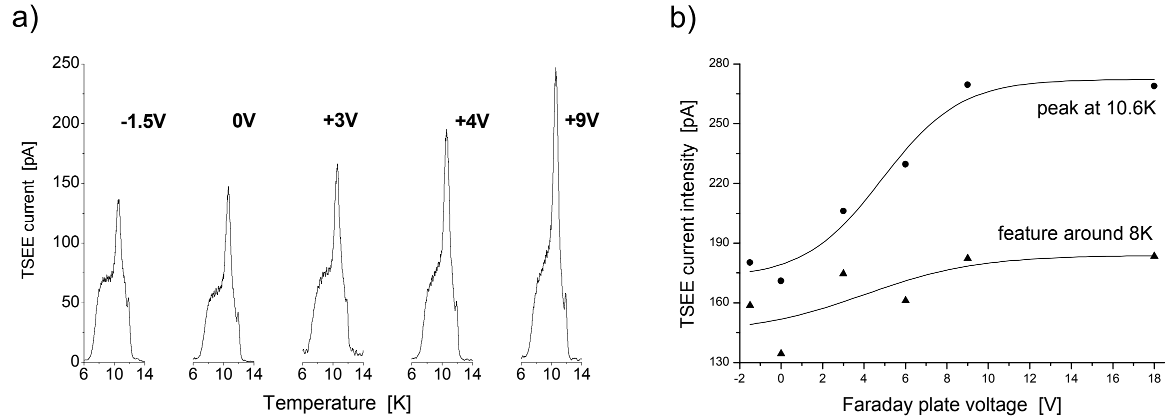

Figure 8.1. a) TSEE from solid Ne recorded with various extraction voltages applied to the Faraday plate. b) shows integrated intensities estimated for features centered around 8 K and 10.6 K. In all experiments 1.7 mmol of Ne was deposited under electron irradiation ($I_e = 3$ μA, $V_{fil} = -130$V) over 30 min.; estimated layer thickness $d \approx 110$ μm.

Typical profiles of the thermally stimulated exoelectron (TSEE) current as a function of temperature are shown in Figure 8.2. The shape of the yield curves is dependent on the rate of temperature increase, as can be seen in the graph which shows three profiles recorded with heating rates of 0.5, 1.0, and 2.0 K/minute. The signal for the 0.5 K curve was multiplied, and that of 2.0 K/min divided by a factor of 2 to show that the time-integrated current, given by the area below the curve, remains approximately constant. The signals suggest two broad maxima, located roughly between 7 and 9 K, and between 9.5 and 11 K, which, as one might expect, shift slightly, by about 1 K, to higher temperatures with increasing heating rate. This trend can be expected since under slow heating most electrons will be released close to the temperature threshold for any given process, while one can "overshoot" this threshold when the rate of temperature rise is increased. The sharp spike, appearing on the high temperature side of the latter, 9.5 – 11 K maximum coincides with a rapid increase in pressure in the cryostat chamber, and probably corresponds to the loss of the sample.

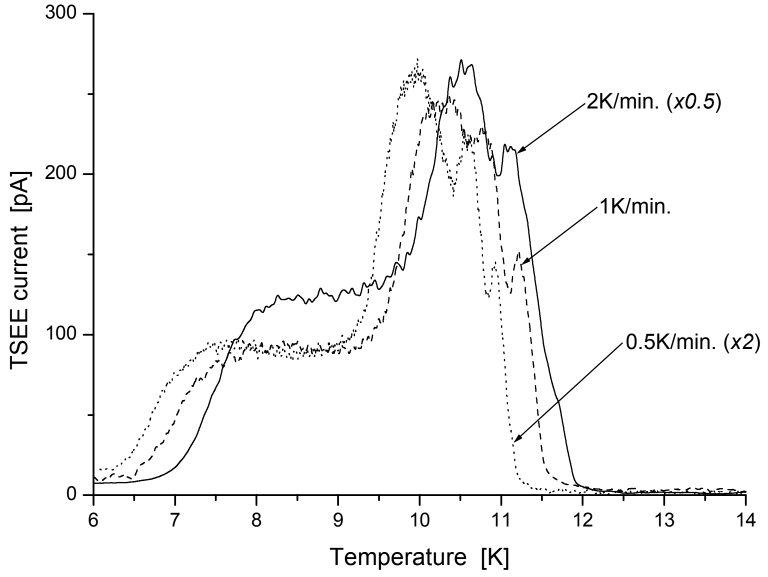

Figure 8.2. TSEE emission from solid Ne measured with different heating rates: 2.0, 1.0 and 0.5 K/minute. The currents for the 2.0 and 0.5 K/min. rates were multiplied by factors of 0.5 and 2.0, respectively, so that the areas under the curves represent the time-integrated exoelectron currents. In each experiment, 0.6 mmol of Ne was deposited during 10 minutes under electron irradiation with electron current of $I_e = 5$ μA, potential $V_{fil} = -130$V, resulting in a layer thickness $d \approx 36$ μm.

Some additional insights can be gained from an experiment whose results are presented in Figure 8.3, where the sample was not heated at a steady rate, but in a series of discrete, 1 K steps. As shown in the middle — curve b, even immediately after deposition, that is while the sample was at the lowest 6 K temperature, there was an observable, approximately exponentially decreasing exoelectron current. After about 10 minutes, when the signal dropped nearly (but not quite) to zero, the temperature was rapidly increased to 7 K, and this stepwise heating was repeated until the matrix was lost. Each temperature step up to 11 K resulted in a rapid increase of TSEE signal, followed by a gradual decay. As can be seen in the figure, the largest current burst occurred at 7 and 10 K, respectively,

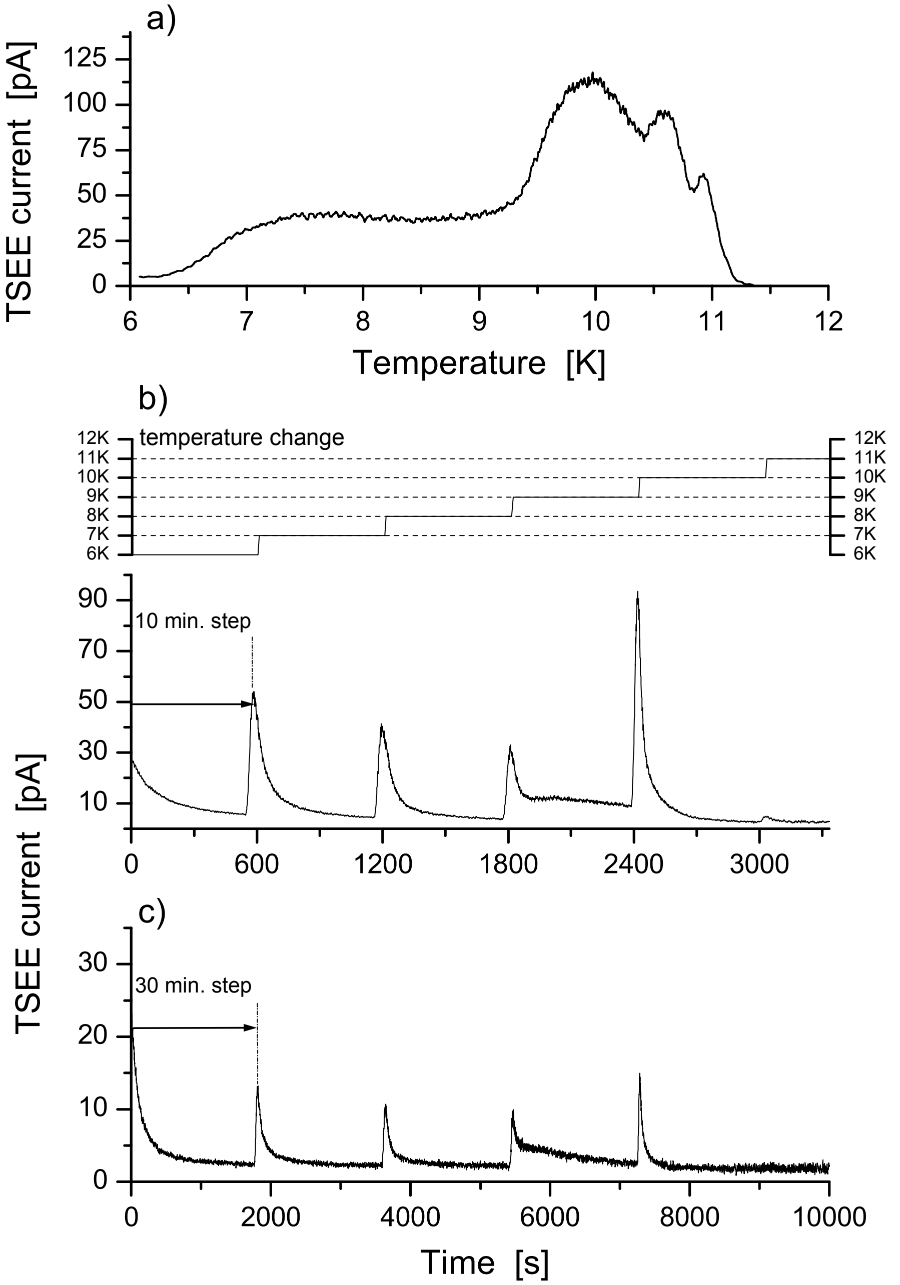

Figure 8.3. The TSEE curve obtained in the uniform rate heating experiment (0.5 K/min.), trace a), compared with the isothermal decay curves for stepwise heating — b,c). The sample was heated in 1 K steps from 6 to 12 K. In the trace b) the interval between steps was 10 minutes, in trace c) — 30 minutes. The upper sketch shows the temperature change during the current measurement in 1 K steps. Electron current during deposition was $I_e = 4$ μA.

coinciding approximately with the broad maxima obtained in the uniform heating experiments reproduced in Figure 8.3a. Repeating the measurement, but with 30 minutes delay between individual steps gave, as shown in curve 3c, very similar results.

This experiment suggests that each increase in temperature is followed by thermal mobilization of the electrons trapped in shallow traps in the lattice. The current disappears after all the electrons which can be activated at a given temperature are lost, but reappears when the temperature is increased, and electrons in slightly deeper traps become accessible. This view is supported by the fact that the profile shows little dependence on the spacing of the temperature steps, and has similar appearance in the 10 minute and 30 minute step experiments.

The two distinct features seen in the exoelectron current plots, suggest that there might be at least two different "sites" or kinds of electron traps in the solid. One way used to explain why electrons can be trapped, in spite of the negative electron affinities, even in the light rare gases, is to propose that they are located at various lattice defects. As the temperature is raised, the defects are annealed away, and the electrons released. To probe this, several additional measurements were carried out with the so-called “cleaning curve technique” [23]. Here the sample grown under irradiation at 6 K was carefully annealed up to 8 K with the TSEE yield measured at a 0 V extraction potential (curve A in Figure 8.4a). After that the sample was cooled back to 6 K. The following repeated heating to the same, 8 K temperature, resulted in essentially no current, even when higher extraction potentials of +6 and +9 V was used (curve B and C), confirming that all the traps which can be depopulated at this temperature were emptied by the previous annealing cycle. However, when the annealing was extended to higher temperature, a strong exoelectron current was detected, but with onset above 8 K, when more stable defects could be annealed, and deeper trapped electrons mobilized. In an alternative experiment (Figure 8.4b) the sample of solid neon grown under irradiation was heated first up to 9 K, and then after re-cooling down to 6 K irradiated with electrons for 20 minutes. After this irradiation, the TSEE current curve over the entire range of 6 – 14 K was recorded. The curve exhibits no current right up to the 9 K annealing temperature of the previous heating cycle, demonstrating the close relation between annealing of defects and depopulation of the electron traps. Contrary to the 8.4a, the TSEE spectra in the 8.4b graph were recorded with the Faraday plate at a fixed +9 V potential. Although the low temperature defects could not be regenerated by electrons accelerated using V_{fil} = -130V, an additional experiment — which will be discussed later in this chapter — has shown that it is possible by increase of the intensity and energy of the beam.

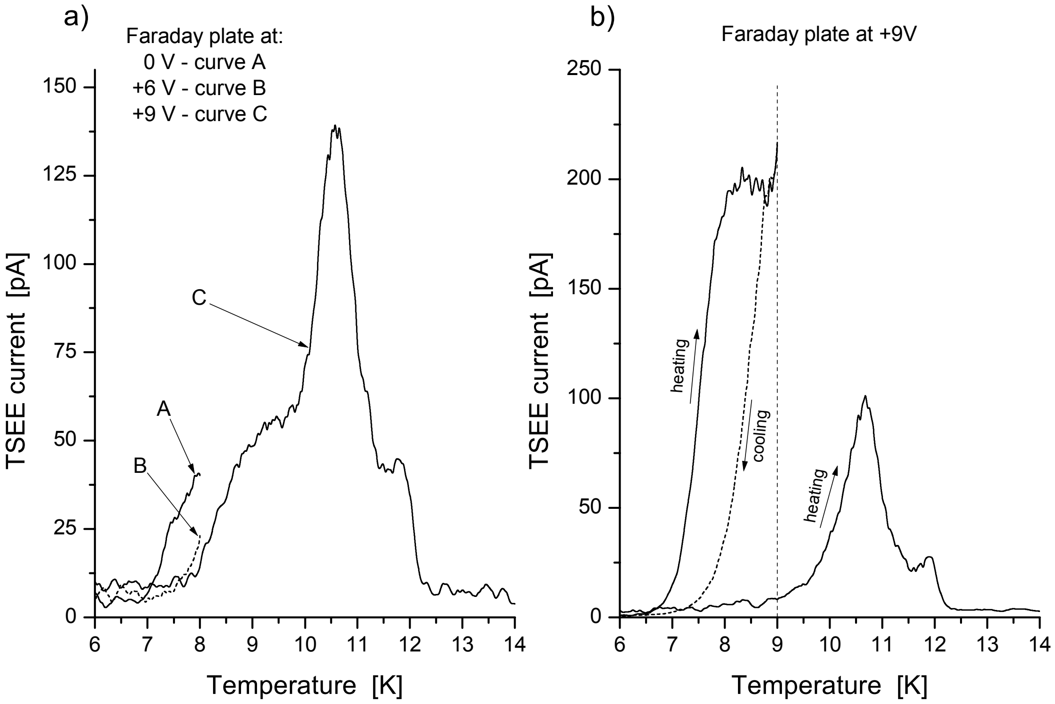

Figure 8.4. a) TSEE current measured from the same Ne sample in three steps with different extraction potentials (at Faraday plate) – sample was cooled down to 6 K after A and then after B measurements. b) TSEE was measured during heating–cooling–heating cycle (using +9 V). The sample cooled down to 6 K was irradiated by electrons under V_{fil} = -130V for 20 min. and current was measured again upon heating to 14 K. Heating rate for both experiments was 2 K/min.

These results suggest that the electrons are not localized in well-defined traps of uniform depth, and with identical activation energy, but that there is a nearly continuous distribution of traps with varying depths, which, however, exhibits the two broad maxima which are apparent in Figures 8.1 – 8.4. The stepwise heating experiment demonstrated in Figure 8.3(b,c) show that current decays after each step are slightly non-exponential, but at least the first decay can in most cases be reasonably fitted to a single lifetime, which is basically identical for the 10 min. and 30 min. experiments. Interestingly, specifically for the 9 K step, the fall-off of the current is quite clearly nonexponential, and suggestive of two appreciably different time constants. Actually, after an initial fast decay to slightly less than half of the initial value, there appears to be a plateau, or even a slight rise in the exoelectron current, with a subsequent, much slower decay. It suggests that at this temperature some other, slower process, possibly involving atomic reactions or recombination, may contribute to the TSEE phenomenon.

The lifetimes obtained by fitting of the initial, 6 K electron current decay curves are 94 and 98 seconds in the 10 minutes/step (Figure 8.3b) and 30 minutes/step (Figure 8.3c) experiments, respectively. The average lifetimes for the initial decay gradually decrease with increasing temperature, and are about 60 ± 5 seconds for the 7 K step, 45 ± 5 seconds at 8 K, 30 ± 5 seconds at 9 K, and finally 20 ± 5 seconds for the 10 K temperature step. As already noted, while at the other temperatures the initial decays are reasonably well fitted by a single exponential, for the 9 K temperature increase step the decay is very clearly multi-exponential, and fitting the latter portion of the current decay curve yields a much longer lifetime of more than 10 minutes.

To test whether the observed electrons are extracted from the entire volume of the sample or only from the surface layers, a series of experiments were performed. In this case the samples were deposited under otherwise identical conditions for 10, 20, 30, 40, and 60 minutes (corresponding to sample thickness of about 36 to 180 μm), and then an-

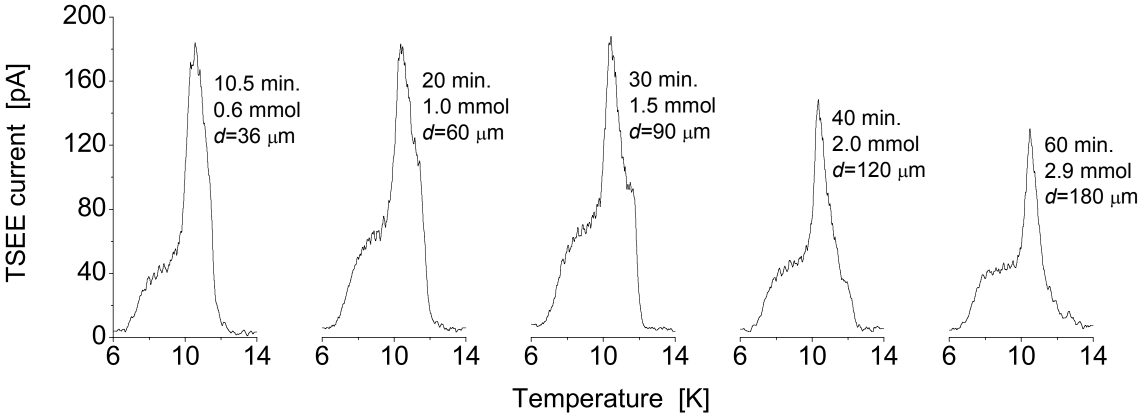

Figure 8.5. TSEE current recorded for different thickness of deposited Ne layer. The electron current during deposition was $I_e = 3$ μA for all experiments.

nealed in continuous heating with a rate of 2 K/minute. The resulting currents are shown in the Figure 8.5. One should point out that there is only a little change in the integrated current between the 10, 20, and 30 min. experiments, with a slight decrease in signal at the still longer times. The fact that increasing the length of deposition beyond 10 minutes has little effect on the integrated current implies that the electrons are extracted mainly from the top layer of less than 30 μm (corresponding to some 10^5 monolayers). The reduced signal at longer deposition times is probably a result of the poor thermal conductivity of solid rare gases. During the sample deposition process, the heat deposited on the sample surface will, when the underlying layer is already thick, result in heating and annealing of the surface, so that part of the charged species may already have recombined and been removed, before the actual measurement started.

Another set of measurements were carried out in order to test from what depth the thermalized electrons in solid neon can be extracted. In this case samples were grown with irradiation under otherwise identical conditions, and subsequently covered by layers of neutral, non-irradiated neon "spacers" of variable thickness. Figure 8.6 shows the depen-

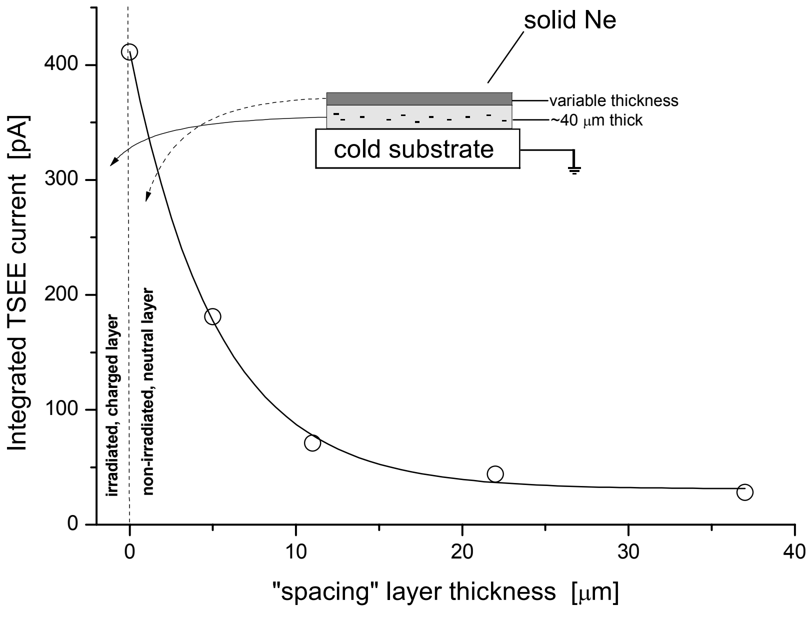

Figure 8.6. Experiment with non-irradiated neutral ("spacer") Ne film deposited on top of irradiated (charged) one. The trace shows integrated TSEE current intensities for 10.6 K peak as a function of the thickness of the "spacing" Ne layer.

dence of the integrated TSEE current on the thickness of the non-irradiated neon layer on top of the sample (geometry is schematically shown in the inset). This results in signals which decrease approximately exponentially with the thickness spacer, and is decreased by about a factor of 4 by a 10 µm layer. This again suggests that most of the observed exoelectron current originates from the top 10 – 20 µm of the sample.

Some control experiments done in order to check the effect of the delay between the end of deposition and the TSEE measurement have shown that already 10 minutes time causes a considerable decrease in the recorded current. This can be most likely attributed to trace amount of impurities in the vacuum chamber, which by condensation on the sample surface build up the addition spacing layer suppressing exoelectrons escaping from neon. The effect is obviously stronger in case of efficient electron scavengers as for instance, oxygen. On the other hand, it is negligible during the deposition process and significantly diminished during sample annealing.

Besides generating the solid layers by electron irradiation during sample deposition, in several other experiments samples were first deposited without electrons, and then subsequently irradiated by electrons (Figure 8.7). When the same conditions as in the concurrent irradiation experiments, that is the beam energy corresponding to V_{fil} = 130 eV

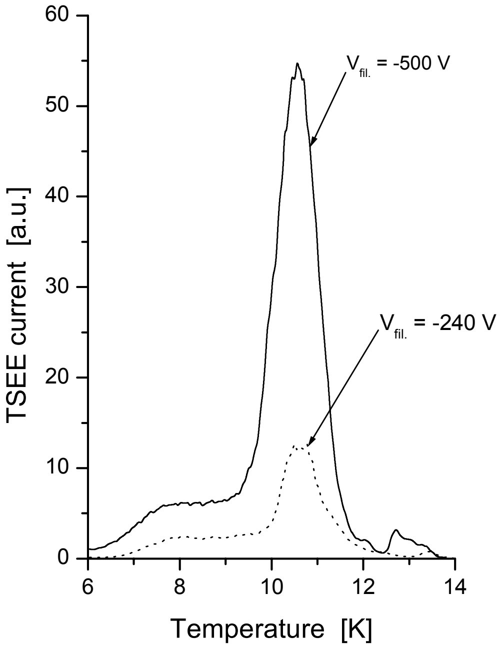

Figure 8.7 Relative intensities of recorded TSEE current curves from Ne samples deposited without electron irradiation and then irradiated for 20 minutes with different electrons energy (filament voltage V_{fil} of -240 V and -500 V). The curves were obtained with a heating rate of 2 K/min.

was used, only marginal exoelectron signals were detected. If the electron energy was roughly doubled to 240 eV, a well-observable signal was detected. Further doubling of the energy to 500 eV resulted in signal increase by about a factor of 5. Both of these energies are well above 50 eV, a value above which the gas phase ionization cross-section decreases. In the solid, however, the fast electron will undergo multiple collisions with individual atoms, gradually losing energy, and can therefore ionize many atoms and produce a number of charge centers in the rare gas lattice. The considerable increase in the TSEE yield associated with the approximate doubling of the beam accelerating potential reflects the higher energy available for ionization, as well as the larger penetration depth and consequently increased thickness and volume of the surface layer accessible for ionization.

The two features in the TSEE spectrum, including the narrower one centered near 10.6 K clearly themselves do not represent a single, well-defined trapping site, but rather a distribution of trapping sites. Several methods are available for estimating the activation energy E_d for the process involved in the detrapping, either from the isothermal decay data, or using the method of different heating rates [23]. The E_d values obtained in this way are ~28 and 18 meV (estimated error for the second value does not exceed 20 %), respectively, which are in reasonable agreement with our previous estimate of 20 meV based on the descending part of the TSEE curve [22]. All these numbers are also close to the E_d value predicted by theory for electronically induced defects and the formation of Frenkel pairs in solid neon [4]. Taking into account that the release of electrons correlates with the defect annealing, the agreement of the experimental and theoretical E_d values seems to support the predicted configuration of stable electronically induced defects — the second neighbor Frenkel pairs (vacancy–interstitial pairs). Recombination of the interstitials with their counterparts results in release of electrons from the vacancy sites.

8.3.2 Solid Argon

In contrast to neon, for which the temperature range available for investigations of thermally activated processes is relatively narrow, solid argon, pure and doped, has been extensively studied using various experimental techniques, including spectrally resolved thermoluminescence, thermally stimulated conductivity and also the TSEE method as recently demonstrated by *Savchenko et al.* [6,8,9].

Nominally Pure Ar Solids

The typical TSEE characteristics measured upon uniform heating for a sample grown from nominally pure Ar gas and then irradiated with electrons is shown in the upper part of the Figure 8.8. The middle trace shows the total yield of TSL obtained previously from a sample [9,27,28] prepared under approximately the same conditions. Measurements were done in the temperature range from 8 to 44 K with a heating rate of 3.2 K/minute. One can easily distinguish the intense pronounced peak around 11 – 12 K and a broad feature centered in the region of 14 – 16 K. Both of them are characteristic for the undoped Ar matrix and can be suppressed by the presence of some impurities in the sample. Some preliminary data obtained for Ar samples deposited at 6 K also revealed TSEE features already around 8 K, which likely stem from lattice defects.

Similarly to the neon case, an additional experiment was carried out for Ar sample deposited under electron irradiation at $T = 6$ K and heated in a series of discrete steps for which the isothermal decay of exoelectron current was observed (lower part of Figure 8.8). During the TSEE current measurement, from 8 – 44 K, the temperature was held constant for 10 minutes, and then quickly raised by 2 K in 6 seconds. Upon completion of deposition, the sample was kept at 6 K for one minute and heated to 8 K before the first decay curve was registered. After 10 minutes the temperature was quickly raised to 10 K and after next 10 minutes to 12 K that resulted in intense maxima observed for both temperature values. As one can note, the signal for the first three peaks at 8, 10 and 12 K does not reach noise level, which is likely due to the relatively short time chosen for the decay curves measurements. On the other hand, a long measurement causes significant loss of the argon layer and appreciably extends a drop of the signal while the sample approaches sublimation temperature. In the present case the time needed to perform the scan exceeded 3 hours. Stepwise temperature increase was repeated until the temperature of 44 K was reached. A considerable change in intensity in agreement with the uniform he-

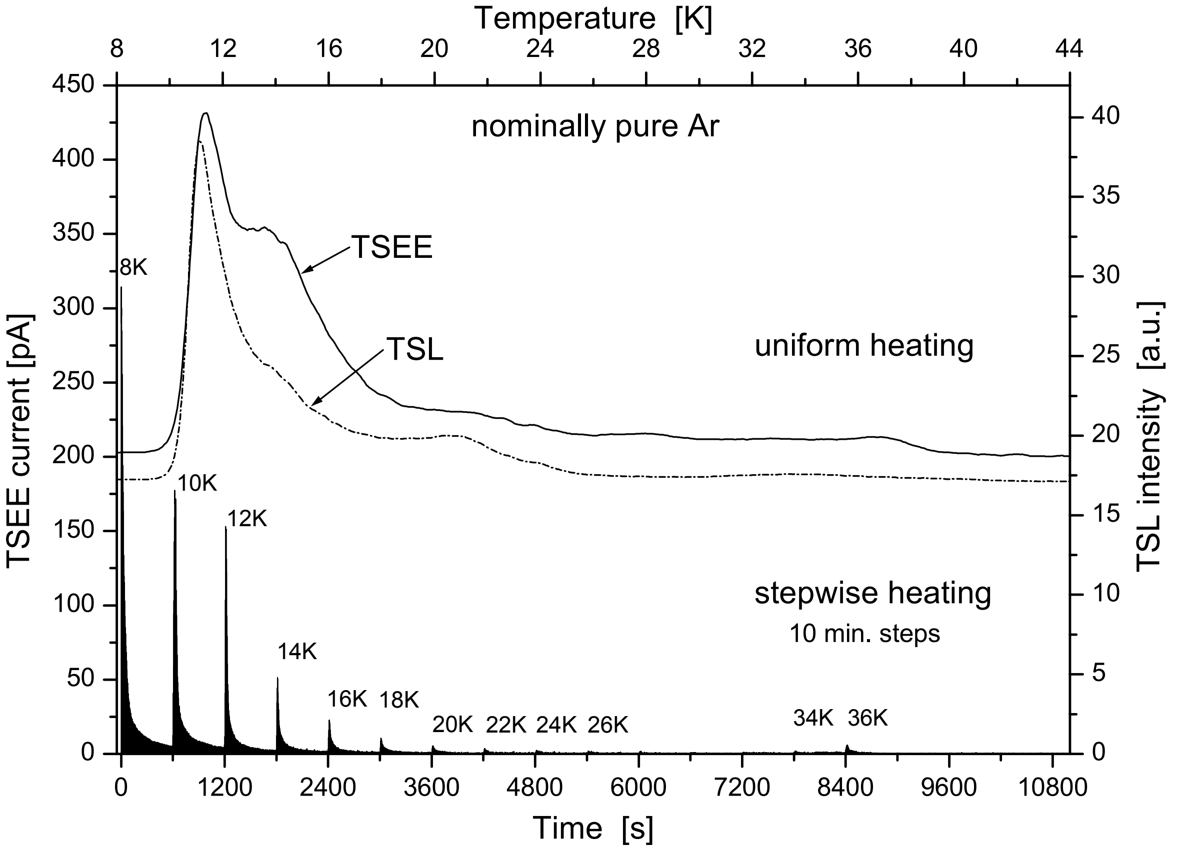

Figure 8.8. TSL intensity and TSEE current (upper traces) for the nominally pure Ar solid deposited at temperature of 7 K and heated from 8 to 44 K with the rate of 3.2 K/min. Lower part — isothermal decay of TSEE current from sample deposited at 6 K and heated in 2 K steps with 10 minute time intervals, in a temperature range from 8 to 44 K.

ating experiments is observed for peaks above 14 K, with current practically fading away at 30 K to grow up again at 34 and 36 K.

In general, the bursts of the current recorded in steps approximately coincide with broad features observed for uniform heating. However, the 2 K steps taken as a consequence of the large temperature range for the measurement do not provide direct information on maximal current value for 11 K, which is expected to be higher than that seen for 10 K. The exact interpretation of the origin of the 8 K peak needs further experiments. Obtained trace clearly shows that the electron current can be reactivated in each temperature step as it was also observed for solid neon, and suggests again the lack of well-defined shallow traps for electrons and their very dense, possibly continuous distribution in energy.

A correlation between TSEE and TSL features around 11 – 12 K, 14 – 16 K and 21 – 22 K indicates the occurrence of electron traps contributing both to recombination of charged species and to emission of electrons from the solid. As it is clearly seen in Figure 8.8 the low temperature peak located between 11 and 12 K dominates in both the TSEE and the TSL spectra. Previous analysis [9] of changes in the TSL characteristics upon the second cycle of irradiation and annealing have shown that this feature can be attributed to the release of electrons from traps localized at the surface or at inner interfaces of the sample. Spectrally resolved TSL measurements in the VUV range identified the origin of 11 – 12 K feature as intrinsic recombination, corresponding to the well-known M-band of the excited molecular Ar_2^* centers, i.e. self-trapped excitons, at 9.7 eV (127.8 nm) [8]. The second TSEE feature of about 14 – 16 K correlates as well with the peak observed in the total yield of TSL. One can also observe the correlation of TSEE with spectrally resolved TSL that stems from recombination luminescence of intrinsic [8,9] and extrinsic [29] centers with electrons. Previously done experiments [29-31] show that the TSL feature at 14 K exhibits a pronounced dose dependence and thus can be interpreted as related to radiation induced defects. Thus, these defects contribute to the emission from the bulk of the Ar layer.

The electrons released from traps by heating and promoted to the conduction band can escape the sample (exoelectrons) or can reach positively charged intrinsic centers and recombine with them yielding TSL. The latter process can be represented by the reaction:

$$Ar_2^+ + e \rightarrow Ar_2^* \rightarrow Ar + Ar + \Delta E_k + h\nu \text{ (9.7 eV)} \qquad (8.1)$$

The energy absorbed during the irradiation and stored by localized charge carriers and reactive neutral species is released in the form of light as recombination emission from the Ar_2^* excimer ${}^{1,3}\Sigma_u^+ \rightarrow {}^1\Sigma_g^+$ transition (M-band) [2,8]. The excess energy ΔE_k of about 1 eV becomes available as kinetic energy of lattice atoms. This can lead to electronically induced desorption of the matrix [5,32,33].

Ar Doped with O_2

A series of experiments provide clear evidence that also oxygen is involved in the relaxation processes. The broad, very weak maximum, localized around $T = 22$ K appears in addition to the much stronger low temperature peaks in the total yield of TSL emission from nominally pure Ar solids. It is also seen in the same range as a hump in TSEE characteristics. Figure 8.9 shows the TSL curves obtained from deposition of an Ar/O_2 gas mixture ($1/10^{-4}$), and the one obtained from nominally pure Ar.

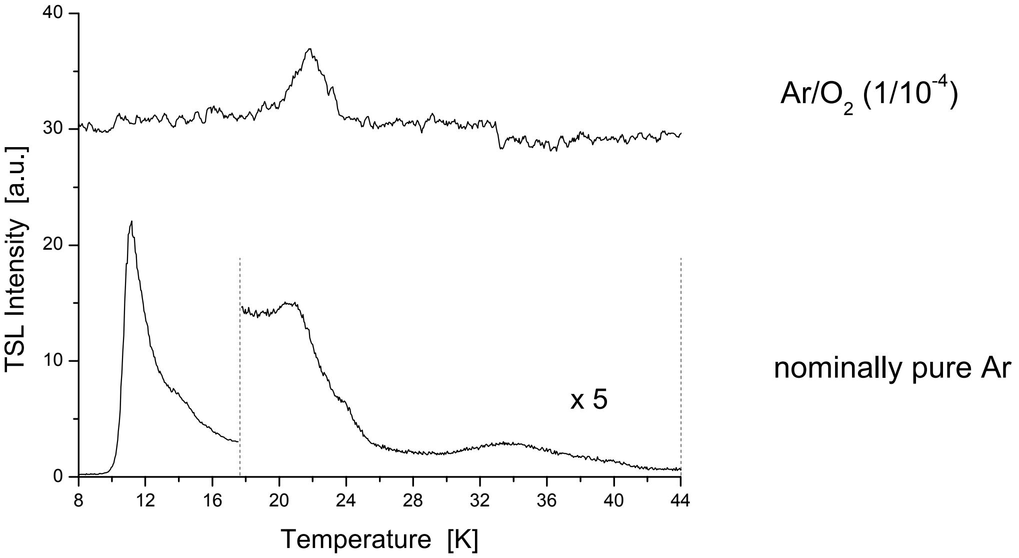

Figure 8.9. Total yield of TSL measured from nominally pure Ar sample (at the bottom) and O_2 doped Ar (matrix ratio 10^{-4}) — top curve. In order to emphasize the weak signal near 22 K data were multiplied by factor of 5.

The second curve was recorded for an Ar/O_2 sample deposited under electron irradiation. Doping with O_2 yields one sharp feature near 22 K (upper trace in Figure 8.9). It is clearly seen that low temperature features typically observed from undoped Ar are completely suppressed by the oxygen content. A strong band around 22 K has been also recorded in one of the previous experiments done in our laboratory, where the matrix was grown from discharge of Ar/O_2 [5].

Schrimpf et al. performed a series of experiments [31] with different dopants, recording spectrally resolved TSL. A TSL measurements at the frequency corresponding to the emission of O_2 (*Herzberg* bands) revealed only one peak at $T = 22$ K. This was explained by recombination of oxygen anions O^- with neutral O atoms followed by detachment of electron from O^-. Indeed, it was found that O atoms start to diffuse at about $T = 20$ K to form molecular O_2 centers and this process of thermally stimulated atom diffusion leads to recombination of neutral atoms resulting in chemiluminescence. This TSL feature also coincided with the maximum of thermally stimulated conductivity (TSC) located around 22 K as observed in Ar/O_2 solids [31].

Oxygen atoms are inevitably formed via ionization of O_2 during electron irradiation of the sample. In their ground state ^3P, O atoms are effective deep traps for electrons because of the high electron affinity $E_a = 1.46$ eV [34]. The activation energy estimated for the 22 K peak is $E_t = 60$ meV [29]. The binding energy E_b of an electron to O^- is defined by electron affinity E_a of oxygen atom and the polarization energy E_p of the Ar matrix $E_p = -1.15$ eV [35]: $E_b = E_a - E_p = 2.61$ eV. Since the E_t differs by two orders of magnitude from the E_b value, the peak at 22 K clearly cannot be attributed to a direct process of thermally activated electron detachment. A similar conclusion can be drawn for the molecular O_2^- anion, for which $E_b = 1.6$ eV. An interpretation involving thermal diffusion of O atoms and O^- anions and their radiative recombination is more probable; however, as it was demonstrated in the experiments on transmission of ions through rare gas crystals, ions are characterized by short-range mobility [36]. Contrary, neutral oxygen atoms in cryogenic solids are characterized by long-range mobility reaching up to 30 nm [15,37]. Recombination of O atoms results in the bound excited state $A^3\Sigma_u$ and can be illustrated by the reaction (8.2). Relaxation to the lowest vibrational state proceeds nonradiatively via a phonon mechanism.

$$O\,(^3P) + O\,(^3P) \rightarrow O_2^*\,(A^3\Sigma_u) \rightarrow O_2\,(X^3\Sigma_g) + h\nu\,(2.1 - 3.6\ \text{eV}) \qquad (8.2)$$

In view of these data, one can conclude that feature observed at 22 K observed in TSEE is an effect of radiative detrapping and mobilization of the electrons by means of photons generated in the reaction 8.2. The energy released into the Ar crystal lattice does not exceed the Debye energy of 12 meV, which is much less than the binding energy of the electron in deep (thermally disconnected) O^-, O_2^- traps (see above) while the energy released via radiative transition $A^3\Sigma_u \rightarrow X^3\Sigma_g$ exceeds E_b for both kind of deep traps. One must consider the kinetic energy of freed electrons in relation to the width of the conduction band of an Ar crystal which is several eV. Following this, such a radiation can produce both so-called "cold" electrons at the bottom of the conduction band from deeper traps and "hot" electrons at the top of the conduction band released from shallower traps. In fact, there are two possible ways of the further fate of mobilized electrons: they can escape from the surface or recombine with positively charged intrinsic and extrinsic centers (guests).

PSEE experiment

In order to verify the suggested scenario of radiative electron-detrapping, special experiments on PSEE (photo stimulated exoelectron emission) were performed. As a light source a stilbene 3 dye laser (pumped by Ar^+ laser) was applied. The laser frequency was tuned to 2.7 eV i.e. in the region of the O_2 *Herzberg* progression. The photo-activated electron characteristics are shown in Figure 8.10 and 8.11 with current-time transient curves obtained from nominally pure Ar solid and that from an O_2 doped Ar sample. The laser power did not exceed 20 mW in both experiments.

The experiment with the undoped sample consists of two steps (Figure 8.10). In the first one the emission of electrons was recorded at $T = 8$ K immediately after sample preparation — the so-called "afteremission" — step I. On completion of its decay, i.e. when the signal dropped to the noise level, the laser beam was focused on the sample. In the same time the PSEE current was monitored as a function of time (diagram on right) — step II. During the measurement, temperature of $T = 8$ K was held constant to exclude all temperature assisted (thermally stimulated) processes. The decay of the current curve characterizes the decrease of the density of electrons mobilized in the detrapping process. Test experiments have shown, as expected, that no current is observed from the substrate and from a non-irradiated Ar sample. Even if one takes into account uncoated spots or micro-scratches on the substrate (with removed thin MgF_2 coating layer), the energy of photons used in the PSEE experiments is considerably lower than the threshold energy of photoemission from the Ag surface (work function of 4.74 eV), and no photoelectron current was detected.

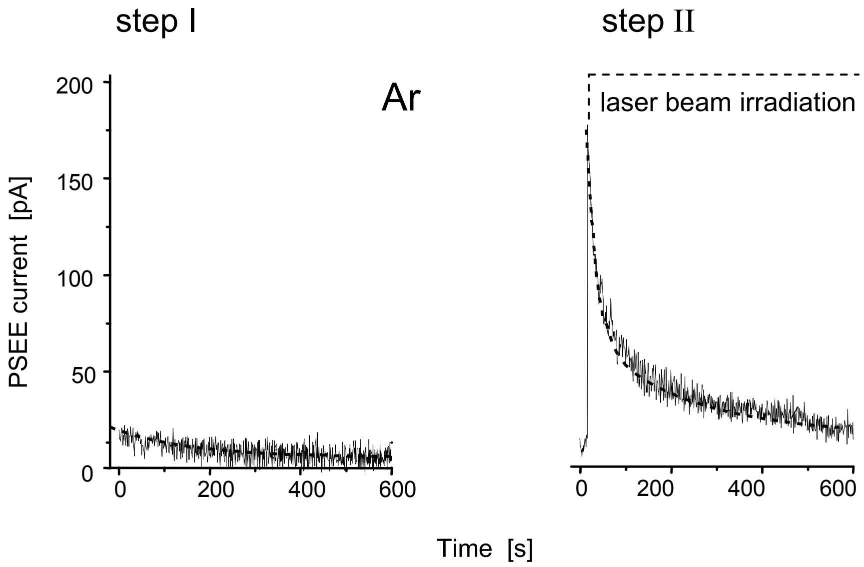

Figure 8.10. Temporal variation of PSEE from preirradiated solid Ar at 8 K. step I shows “afteremission” recorded immediately after deposition, step II – exoelectron current under laser excitation at 2.76 eV.

Another PSEE experiment has been carried out using an O_2 doped Ar sample ($1/10^{-4}$) (Figure 8.11). The temperature during measurement was constant, $T = 7$ K. Initially no electron emission was observed from the sample. Upon exposition to the laser beam a sharp rise of exoelectron current was observed followed by a slow decay. Blocking of the laser light resulted in immediate disappearance of the signal, but the decay of the emission continued from the same signal level after the sample was exposed again to laser light.

The kinetics of the PSEE current decay measured from nominally pure Ar solid (Figure 8.10) can be described by a double exponential expression with $\tau_1 = 21$ s and $\tau_2 = 190$ s, with the latter value coinciding within the fitting accuracy, of about 30 %, with the characteristic “afteremission” decay time for this sample.

Both experiments demonstrate an intensive emission of electrons under laser excitation. Photons for which the energy is sufficient to excite the trapped electrons into the conduction band generate mobile electrons capable of escaping from the solid. The decay of the free-carrier density N_c can be represented for the case of no-retrapping — i.e. assuming first order kinetics — by a simple exponential expression [38]:

$$N_c = g\, \tau_{CB}\, N_0 \exp(-gt) \tag{8.3}$$

where g is the product of the density of photons irradiating the sample and the effective interaction cross-section of the photons and the electrons in the traps, τ_{CB} is the effective lifetime of the electrons in the conduction band. For insulators containing space charge τ_{CB} is a complex function of the mobility of charge carriers, the applied voltage, and the electrode spacing, and its evaluation requires special experiments. The exponential function in the current-time transient curve describes the decrease in mobile electron densi-

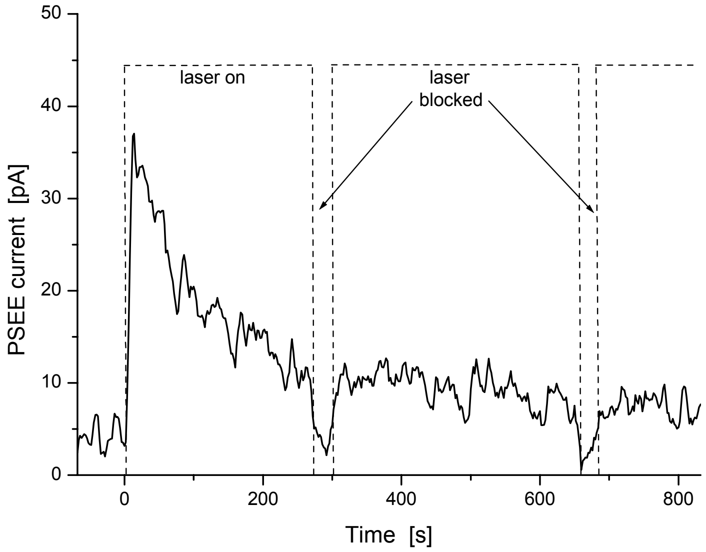

Figure 8.11. Yield of PSEE current from O_2 doped Ar sample at 7 K, measured under irradiation of laser beam at 2.71 eV.

ty during trap emptying. $\tau = g^{-1}$ can be estimated from the curve. The fact that the PSEE curve is best fitted by a double exponential law indicates contributions of two different kinds of traps with different τ_1 and τ_2 parameters.

Again, neglecting retrapping the decay of the current-time transient curve recorded from Ar/O_2 (Figure 8.11) can also be represented by Equation (8.3). The first part of the decay curve, about 30 % of the height at maximum can be fitted by a single exponent resulting in $\tau = g^{-1} = 60 \pm 10$ s. Apparently, the accuracy in this case is even lower than above due to the smaller signal to noise ratio, caused by a low value of the PSEE signal (below 40 pA at maximum). The deviation observed in the curve on a long time scale can be caused by retrapping mechanisms.

The data obtained from both PSEE experiments seem to confirm the suggested radiative mechanism of electron-detrapping. Photons of energy of 2.7 eV — corresponding to the energy of photons emitted in O–O chemiluminescence — are able to release electrons from shallow lattice traps, and also from those which are thermally disconnected, like deep O^- and O_2^- traps.

While the above data indicate that the radiative recombination of neutral O atoms gives the main contribution to the TSL at 22 K, this feature was also detected in spectrally resolved VUV TSL from recombination of Ar_2^+ ionic centers with electrons (reaction 8.1) [28]. However, when an Ar solid was doped with CO, a TSL at 22 K occurred at frequency corresponding to 5.65 eV, i.e. (0 → 1) vibronic transition of well-known *Cameron* band ($a^3\Pi \rightarrow X^1\Sigma^+$) of matrix-isolated CO [39]. The ionization potential of the CO molecule is lower than that of argon atoms and CO^+ ions can be generated in Ar matrix, and then subsequently neutralized via recombination with electrons released from the traps. Radiative relaxation of the excited CO^* molecule gives rise to the observed TSL. A correlation with weak TSEE feature around 22 K indicates common relaxation processes underlying those phenomena.

Analysis of the whole set of data on TSEE, PSEE and TSL allows to propose a sequence of atomic and electronic elementary processes of relaxation in the temperature region around $T = 22$ K. O atoms generated in the matrix under irradiation and trapped in substitutional and perhaps in interstitial octahedral sites [40] start to diffuse upon heating most likely by a vacancy annealing mechanism. The estimated energy of vacancy formation near a guest O atom in solid Ar is 90 ± 30 meV, and this value is relatively close to the activation energy for the 22 K peak of $E_t = 60$ meV given above. Recombination of O atoms results in formation of an excited O_2^* molecule in the bound state $A^3\Sigma_u$. Radiative relaxation of excited O_2^* molecule, producing photons in the range of 2.1 – 3.6 eV, can be the key process in a cascade of elementary relaxation processes illustrated in reaction (8.4). The released electron can escape the sample contributing to PSEE process or can be retrapped by either recombination with a guest ion or an intrinsic ionic center Rg_2^+ (rare gas ionic dimer or self-trapped hole). The latter two processes contribute to TSL emission in the UV or VUV wavelength range.

$$\begin{tikzcd}
 & & & & \text{PSEE} \\
O + O \rightarrow O_2^* \rightarrow O_2 + h\nu \arrow[r] & e^- \arrow[urrr, phantom] \arrow[ur] \arrow[r] \arrow[dr] & Rg_2^+ + e^- \rightarrow Rg + Rg + h\nu_1 + \Delta E \\
 & & \text{guest}^+ + e^- \rightarrow \text{guest}^* \rightarrow \text{guest} + h\nu_2
\end{tikzcd} \tag{8.4}$$

Ar Doped with N_2

A series of TSEE measurements reveal that doping with N_2 causes an enhancement of high-temperature peaks above 30 K. However, registration of the electron current in this region as well as interpretation of data is significantly hindered by extensive evaporation of the Ar sample. On other hand, the nitrogen containing argon solids represent especially attractive systems for the investigation of radiative transitions involved in cascades of relaxation processes. Under the electron bombardment N atoms are efficiently formed in rare-gas matrices, evidenced by the well-known forbidden transition $^2D \rightarrow {}^4S$ (523 nm). This transition is characterized by a radiative life-time of more than 40 seconds [41]. Consequently, one can also expect an appearance of chemiluminescence originating from the reformation of N_2 molecules due to diffusion of N atoms upon heating of the matrix. Measurement of exoelectron current right after sample deposition (with matrix ratio of 10^{-3}, grown under electron irradiation) at $T = 7$ K results in a weak signal exhibiting double-exponential decay — see Figure 8.12. Similar curves were also obtained for N_2

concentrations of 5×10^{-3} and 10^{-2}. Decay rates determined from second order exponential fitting are $\tau_1 = 33 \pm 7$ s and $\tau_2 = 170 \pm 25$ s.

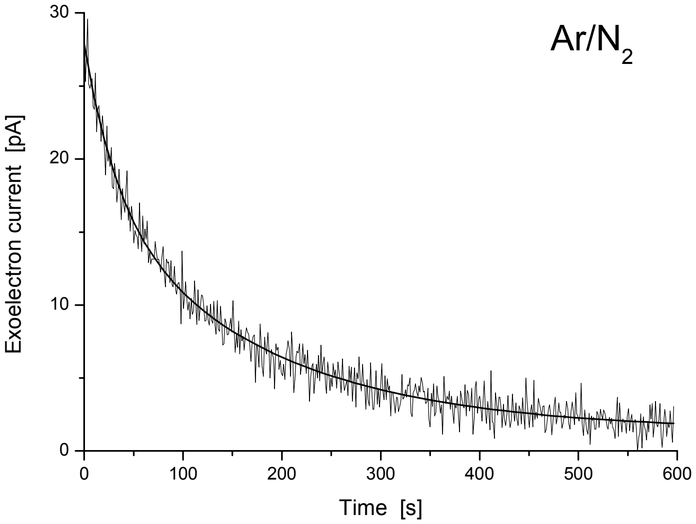

Figure 8.12.Yield of electron ”afteremision” from N_2 doped Ar solid (with matrix ratio of 10^{-3}).

The recorded curve is a typical characteristic of the so-called “afteremission” observed simultaneously with discernible green fluorescence (“afterglow”) from Ar/N_2 solid. A possible mechanism responsible for exoelectron afteremission is the photo-detrapping of electrons caused by “glowing” N atoms. Although the N atom has negative electron affinity $E_a = -0.1$ eV [42] taking into account the polarization energy of Ar matrix of -1.15 eV [35] gives binding energy of about 1 eV and N atoms can be considered as deep, thermally disconnected traps. Thus, the energy of a photon emitted by $^2D \rightarrow {}^4S$ transition of N atoms is sufficient to excite trapped electrons into the conduction band, thus stimulating electron transport followed by exoelectron emission. $\tau_1 = 33 \pm 7$ s extracted from the current decay curve compares favorably with the radiative lifetime of the metastable ^2D state of the N atom $\tau_{rad} = 43 \pm 1$ s [39]. The slower decay component about 170 s is probably an effect of an electron retrapping process. A PSEE experiment with the laser tuned close to $^2D \rightarrow {}^4S$ transition, demonstrated that the signal can be still recorded from a sample annealed at 16 K [32]. This allowed to distinguish between the contribution of electrons stemming from shallow lattice traps, and those from thermally disconnected deep traps indicating guest species.

The discussed photon-assisted processes can be illustrated using an energy-band model. It is shown schematically in Figure 8.13. The left part of the drawing shows trapping of charge carriers. Electrons can be released from two different kinds of traps: 1) shallow traps (s-t) as vacancies, vacancy clusters or pores; 2) deep or thermally-disconnected traps (d-t) as impurities or dopants (guests) characterized by positive electron affinity in the matrix (O, O_2, N species). Besides the defect annealing process in which a low barrier (several tens of meV) can be overcome and electrons can be freed from (s-t) kind of traps, the electrons can be released from both (s-t) and (d-t) traps by absorption of photon. Photons of appropriate energy — lower than conduction band-witdh plus electron trap-depth — can be generated in chemiluminescence (via recombination of for instance O and N atom resulting in excited molecular centers O_2^*, N_2^*) or by external light source (e.g. laser).

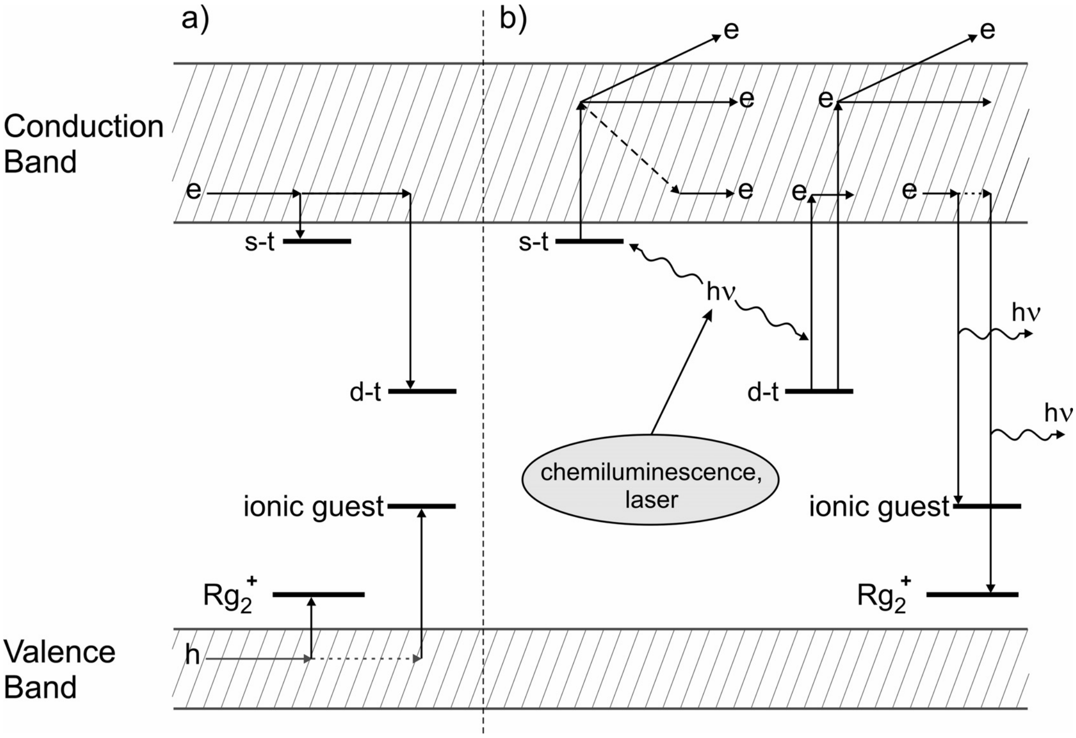

Figure 8.13. Schematic representation of charge carriers trapping mechanism — a), and photon-induced relaxation processes — b) using energy-band model.

Those electrons which gain kinetic energy sufficient to escape the sample contribute to PSEE. The energy of photons originating in recombination of electrons with positive charge centers (Rg_2^+ or guest ion, e.g. CO^+) is usually too high and those photons do not contribute to PSEE phenomenon, being, however observed in TSL emission.

8.4 Conclusions

The present studies explore electronically-induced processes in neon and argon solids by means of activation spectroscopy methods: Thermally Stimulated Luminescence (TSL, “thermoluminescence”) Thermally Stimulated Exoelectron Emission (TSEE) and Photon Stimulated Exoelectron Emission (PSEE).

In spite of their negative electron affinities, considerable concentrations of electrons can be trapped in solid argon and even in solid neon matrices. In an annealing experiment, these electrons are promoted into the conduction band and can recombine with positive counterions, resulting in thermoluminescence, but they can also be extracted from the sample surface, and detected as exoelectron current.

The TSEE current curves obtained from Ne samples as a function of temperature resemble the thermoluminescence curves over the same temperature range, and exhibit two broad maxima near 7.5 and 10 K. These are shown to be due to distributions of electron trapping sites. For the narrower, higher temperature maximum, an average activation energy of about 23 meV is deduced, in good agreement with predictions based on the theory of electronic defect formation.

A correlation between TSEE and TSL features observed in solid argon with a dominant maximum around 12 K, a broad band between 14 – 16 K and a much weaker near 22 K, indicates the occurrence of electron traps contributing to the recombination of charged species and emission of electrons from the solid. It was found that the 22 K feature stems mainly from a cascade relaxation process in which an exoelectron is activated by photon generated in thermally induced radiative recombination of O atoms.

Analysis of thermally stimulated currents (TSEE) and photons (TSL) in comparison with yields of photon-stimulated exoelectrons (PSEE) made possible to discriminate between reactions of neutral species and charge carriers in argon matrices allowing to some extent to elucidate their interconnection. These results support the suggested mechanism of the conversion of energy released in a chemical reaction into kinetic energy of electrons, which can be followed by its escape from solid. However, in some cases, complete understanding of those processes requires further experimental examination involving spectroscopic methods. Primarily, an experimental approach should concentrate on simultaneous registration of electrons and spectrally resolved photons emitted from solids upon thermal treatment.

References

[1] M.L. Klein, J.A. Venables, eds. *Rare Gas Solids,* vol. 1, Academic, New York, 1976.

[2] K.S. Song and R.T. Williams, *Self-Trapped Excitons*, Springer Series in Solid State Science, vol. 105, ed. M. Cardona, Springer-Verlag, Berlin, 1996.

[5] E.V. Savchenko, A.N. Ogurtsov, Grigorashchenko, *Phys. Solid State* **40**, 831 (1998).

[4] Chun-rong Fu and K.S. Song, *J. Phys.: Condens. Matter* **9**, 9785 (1997).

[5] E.V. Savchenko, O.N. Grigorashchenko, A.N. Ogurtsov, V.V. Rudenkov, G.B. Gumenchuk, M. Lorenz, M. Frankowski, A.M. Smith-Gicklhorn, V.E. Bondybey, *Surf. Sci.* **507-510**, 754 (2002).

[6] H. J. Jodl, *Solid Aspects Of Matrices* in L. Andrews, M. Moskovits *Chemistry and Physics of Matrix-Isolated Species* North-Holland, Amsterdam, 1989.

[7] M. Kink, R. Kink, V. Kisand, J. Maksimov, M. Selg, *Nucl. Instrum. Methods Phys. Res. B* **122**, 668 (1997).

[8] E.V. Savchenko, A.N. Ogurtsov, O.N. Grigorashchenko, S.A. Gubin, *Low Temp. Phys*. **22**, 926 (1996).

[9] E.V. Savchenko, O.N. Grigorashchenko, A.N. Ogurtsov, V.V. Rudenkov, G.B. Gumenchuk, M. Lorenz, A. Lammers, V.E. Bondybey, *J. Low Temp. Phys*. **122**, 379 (2001).

[10] L.J. Schoen, H.P. Broida, *J. Chem. Phys.* **32**, 1184 (1959).

[11] J. Fournier, C. Lalo, J. Deson, C. Vermeil, *J. Chem. Phys.* **66**, 2656 (1977).

[12] J.P. Lee, G.C. Pimentel, *J. Chem. Phys.* **69**, 3063 (1978).

[13] J. Fournier, J. Deson, C. Vermeil, G.C. Pimentel, *J. Chem. Phys.* **70**, 5726 (1979).

[14] M.E. Fajardo, V.A. Apkarian, *J. Chem. Phys.* **89**, 4124 (1988).

[15] A.V. Danilychev, V. A. Apkarian, *J. Chem Phys.* **99**, 8617 (1993).

[16] L. Khriachtchev, M. Pettersson, S. Pehkonen, E. Isoniemi, M. Räsänen, *J. Chem. Phys.* **111**, 1650 (1999).

[17] V.E. Bondybey, M. Räsänen, A. Lammers, *Ann Rep. Prog. Chem. C* **95**, 331(1999).

[18] V. A Apkarian, N. Schwentner, *Chem. Rev.* (Washington D.C.) **99**, 1481 (1999).

[19] E.V. Savchenko, N. Caspary, A. Lammers, V.E. Bondybey, *J. Low Temp. Phys*. **111**, 693 (1998).

[20] O.N. Grigorashchenko, O.M. Sokolov, E.V. Savchenko, J. Agreiter, N. Caspary, A. Lammers, V.E. Bondybey, *Rad. Effects & Defects in Solids* **149**, 197 (1999).

[21] E.V. Savchenko, O.N Grigorashchenko, O.M Sokolov, J. Agreiter, N. Caspary, A. Lammers, and V.E. Bondybey, *J. Electron Spectrosc. Relat. Phenom*. **101-103**, 377 (1999).

[22] O.N. Grigorashchenko, V.V. Rudenkov, I.V. Khizhnyi, E.V. Savchenko, M. Frankowski, A.M. Smith-Gicklhorn, M.K. Beyer, V.E. Bondybey, *Low Temp. Phys.* **29**, 876 (2003).

[23] D.R. Vij, in: *Luminescence of Solids*, D.R. Vij (ed.), Plenum Press, New York, 1998.

[24] M. Lannoo, J.C. Bourgoin, *Point Defects in Semiconductors II, Experimental Aspects*, Springer Series in Solid-State Sciences, vol. 122, Springer, Berlin 1981.

[25] G. Herzberg, The Spectra and Structures of Simple Free Radicals, An Introduction to Molecular Spectroscopy, Cornell University Press, Ithaca and London, 1971.

[26] E.V. Savchenko, A.N. Ogurtsov, S.A. Gubin, O.N. Grigorashchenko, *Excitonic Processes In Condensed Matter,* ed. M. Schreiber, Dresden, Dresden University Press, 1996.

[27] E.V. Savchenko, O.N. Grigorashchenko, A.N. Ogurtsov, V.V. Rudenkov, M. Lorenz, M. Frankowski, A.M. Smith-Gicklhorn, V.E. Bondybey, *J. Lumin*. **94-95**, 475 (2001).

[28] E.V. Savchenko, O.N. Grigorashchenko, A.N. Ogurtsov, V.V. Rudenkov, M. Lorenz, A.M. Smith-Gicklhorn, M. Frankowski, V.E. Bondybey, *Surf. Rev. Lett.* **9**, 353 (2002).

[29] J. Becker, O.N. Grigorashchenko, A.N. Ogurtsov, M. Runne, E.V. Savchenko, and G. Zimmerer, *J. Phys. D: Appl. Phys.* **31**, 749 (1998).

[30] A.N. Ogurtsov, E.V. Savchenko, O.N. Grigorashchenko, S.A. Gubin, I.Ya. Fugol', *Low Temp. Phys.* **22**, 922 (1996).

[31] A. Schrimpf, C. Boekstiegel, H.-J. Stockman, T. Bornemann, K. Ibbeken, J. Kraft, and B. Herkert, *J. Phys.: Condens. Matter* **8**, 3677 (1996).

[32] E.V. Savchenko, O.N. Grigorashchenko, G.B. Gumenchuk, A.N. Ogurtsov, M. Frankowski, A.M. Smith-Gicklhorn, V.E. Bondybey, *Radiation Effects & Defects in Solids* **157**, 729 (2002).

[33] E.V. Savchenko, O.N. Grigorashchenko, G.B. Gumenchuk, A.G. Belov, E.M. Yurtaeva, M. Frankowski, A.M. Smith-Gicklhorn, V.E. Bondybey, *Surf. Sci.* **528**, 266 (2003).

[34] D.R. Lide, ed., *Handbook of Chemistry and Physics*, CRC Press, Boca Raton (FL) USA, London, Tokyo, 1993.

[35] L.E. Lyons, M.G. Sceats, *Chem. Phys. Lett.* **6**, 217 (1970).

[36] M. Akbulut, N.J. Sack, T. Madey, *Surf. Sci. Rep.* **28**, 177 (1997).

[37] C. Bressler, M. Dickgiesser, N. Schwentner, *J. Chem. Phys.* **107**, 10268 (1997).

[38] J.D. Brodribb, D. O'Colmain, D.M Hughes, *J. Phys. D: Appl. Phys.* **8**, 856 (1975).

[39] E.V. Savchenko, A.N. Ogurtsov, and G. Zimmerer, *Low Temp. Phys*. **29**, 270 (2003).

[40] E.V. Savchenko, A.N. Ogurtsov, O.N. Grigorashchenko, S.A. Gubin, *Chem. Phys.* **189**, (1994) 415.

[41] J. Eloranta, K. Vaskonen, H. Häkkänen, T. Kiljunen, H. Kunttu, *J. Chem. Phys.* **109**, 7784 (1998).

[42] L.D. Thomas, R.K. Nesbet, *Phys. Rev.* **12**, 2369 (1975).

Summary and Outlook

Spectroscopic studies of mass-selected molecular ions, unstable molecules and electrons trapped in cryogenic matrices have been presented in this thesis:

- Studies of neutral molecules in various matrices brought new results on the XeC_2 molecule as well as $HXeC_2H$. The XeC_2 molecule was formed via the deposition of acetylene rare gas discharge products in Xe, Ar and Kr matrices. This results in the complete absence of C_2 in the xenon matrix. Experiments indicate that ground state Xe and C_2 react without a barrier to form chemically bound XeC_2 molecule. Its infrared-active C-C stretch is found to be close to the corresponding frequency of the C_2-anion, and in excellent agreement with predictions from B3LYP density functional theory (DFT) calculations. The computations yield a Xe–C–C bent structure with substantial charge separation approaching $Xe^+C_2^-$. Numerous broad absorptions near 423 nm are clearly due to the XeC_2 molecule. A near-infrared emission observed in laser-induced fluorescence studies is likely due to XeC_2 but not yet understood. The Xe–H and C–H stretches observed in xenon matrix indicate the presence of the $HXeC_2H$ compound. Corresponding absorptions are also observed for its fully deuterated DXeCCD, or all-^{13}C isotopomers. However, deposition from a gas discharge leads to a random distribution of radical fragments through the matrix, and consequently formation of HXeCCH by diffusion is fairly inefficient.

  Future Studies…

  Future research on XeC_2 should mainly involve theoretical study, which would lead to an understanding of its electronic spectra. Experiments in neon matrix will likely result in less perturbed spectra. Advanced computational methods applied to the ground state of XeC_2, like multi-reference methods will provide complementary information on its geometry and electronic symmetry.

- Investigation of organic azides, azidoacetonitrile (N_3CH_2CN) and azidoacetone ($N_3CH_2COCH_3$) in neon, argon and nitrogen matrices, supported by B3LYP/DFT calculations, provided new information on their vibrational spectra. Significant broadening of the observed azide bands indicates an awkward fit of these compounds into the solid environment. The strongest absorption is observed for both compounds in the regions of the stretching vibrations of the N_3 group. Strong band splittings in the N_3 asymmetric stretch region suggests very strong Fermi resonances with the C–N stretch and combinations of the numerous lower frequency vibrational modes.

  Future Studies…

  Gas phase rotational spectroscopy studies could verify computational data on the most stable conformers. On the other hand, additional theoretical efforts could give some insight in the anharmonicity of the observed vibrations, which in turn would help to understand the Fermi resonances in these systems.

- A series of successful experiments were carried out on positive molecular ions deposited selectively in neon matrices. Ions were deposited with an excess of electrons to prevent a buildup of space charge. In these studies several previously unknown molecular ions of astrophysical importance, containing CN (cyano) groups, have been identified by means of Fourier-transform infrared spectroscopy. Complementary DFT calculations provided fundamental frequencies which were usefull in assignments. The ionic species were produced by ionization, fragmentation and ion-molecule reactions in electron impact (EI) source using cyano-precursors like tetracyanoethylene (TCNE) and acetonitrile.

  A mass-selective matrix-isolation study using the tetracyanoethylene precursor resulted in the first observations of the infrared vibrational spectra of the parent cation $C_6N_4^+$ (TCNE) and its fragmentation products: $C_3N_2^+$, $C_5N_3^+$ and $C_6N_3^+$. The previously known $C_4N_2^+$ and C_2N^+ ions were also identified. Deposition of $C_5N_2^+$ cation allowed for the re-examination of the electronic transitions of neutral C_5N_2 molecule using highly sensitive laser excitation technique. These results have confirmed the previous assignment to C_5N_2. Interesting photochemical effects were also observed in all infrared spectra of TCNE in neon matrix: a detrapping or photomobilization of electrons resulted in subsequent recombination with the residual (and highly electronegative) neutral precursor and formation of the well-known tetracyanoethylene anion $C_6N_4^-$.

Using acetonitrile CH_3CN and CD_3CN precursors resulted in infrared bands attributed to CH_3CNH^+, H_2CCN^+, H_2CNC^+ and $HCCNH^+$ cations and their isotopes. Correlated changes in absorption intensities upon irradiation of the samples with a tungsten lamp allowed to distinguish cationic species from impurities. Protonated acetonitrile, CH_3CNH^+, has been identified through its strong N–H stretching vibration and absorption attributed to the CH_3 symmetric stretch. The spectral assignments are based on correlation and isotopic study with CD_3CND^+ and are in very good agreement with the predicted frequencies. B3LYP density functional calculations and the obtained infrared spectra suggest an occurrence of several stable isomers of the cyanomethyl cationic radical, $C_2H_2N^+$. Indeed, new data allowed for spectral identification of the $HCCNH^+$ isomer via its N–H stretching vibration. The spectral assignment for this ion and its deuterated analogue is confirmed by the agreement between predicted and observed isotopic shifts. Two other isomers, H_2CCN^+ and H_2CNC^+, have been assigned tentatively.

Although using an acetylene precursor did not allow for the detection of the well-known C_2^+ electronic transitions after mass-selective deposition of this ion, the acetylene parent cation was observed in the IR. The $C_2H_2^+$ was identified via an absorption attributed to the C–H stretching vibration.

Future Studies…

The neon-matrix vibrational frequencies will definitely contribute to high resolution gas-phase spectroscopic studies. Gas-phase data could be used in astronomical searches, which in turn would provide a better understanding of the physical and chemical processes occurring in interstellar space. Tentative spectral assignments made for some of $C_2H_2N^+$ isomers require further study, e.g. using more efficient precursors (like iodoacetonitrile or chloroacetonitrile).

In general, further progress in experimental studies of mass-selected ions will obviously depend to a large extent on progress in development of more efficient ion sources, high transmission mass filters and ion-transfer methods.

- Activation spectroscopy of condensed neon and argon has shown that in spite of the negative electron affinity of Ne and Ar atoms, appreciable concentrations of electrons can be trapped in the corresponding solids. Charge centers in solid Ne and Ar were generated upon or after deposition of the samples by electron irradiation. Such pre-irradiated solids were characterized by thermally- and photon-activated electron emission upon heating or laser irradiation as well as by thermally stimulated luminescence (TSL). For both Ne and Ar solids, characteristic features have been revealed by TSEE (thermally stimulated exoelectron emission) profiles measured as electron current versus temperature. Observed maxima are shown to correspond to distributions of electron trapping sites with slightly different activation energies. A correlation between TSEE and TSL features observed in solid argon indicates the occurrence of electron traps contributing to the recombination of charged species and emission of electrons from the solid. PSEE (photon-stimulated exoelectron emission) and TSEE results obtained from nominally pure and doped Ar samples suggest cascade relaxation processes in which electrons are activated by photons generated in thermally induced radiative recombination.

  Analysis of the whole set of TSEE and TSL data compared with yields of photon-stimulated exoelectrons (PSEE) made it possible to discriminate between reactions of neutral and charge-carriers in argon solids and allowed, to some extent, to elucidate their interconnection. The results support the suggested mechanism of the conversion of energy released in a chemical reaction into kinetic energy of electrons, which can be followed by its escape from solid.

  Future Studies…

  Further experiments are planed involving spectroscopic methods. Future efforts will concentrate on the correlation study of TSEE and spectrally resolved TSL. Using tunable lasers in PSEE could determine threshold conditions for this phenomenon.

Some earlier results obtained in the group of *Prof. Gerard Śliwiński* in the *Department of Photophysics and Laser Technique, The Szewalski Institute of Fluid-Flow Machinery of Polish Academy of Sciences*, and other data which are beyond the scope of this thesis, can be found in the following list of publications.

Appendix

List of Publications

1. M. Frankowski, A.M. Smith-Gicklhorn, Z. Sun and V.E. Bondybey
   Protonated and fragment ions of acetonitrile; Mass-selective matrix-isolation study
   in preparation
2. A.M. Smith-Gicklhorn, M. Frankowski and V.E. Bondybey
   Predictions of novel Xe compounds with BN; Xenon insertion into iminoborane and borazine
   Molecular Physics, accepted for publication (June 2004)
3. M. Frankowski, E. V. Savchenko, A.M. Smith-Gicklhorn, O.N. Grigorashchenko, G. B. Gumenchuk and V.E. Bondybey
   Thermally stimulated exoelectron emission from solid neon
   Journal of Chemical Physics **121***,* 1474-1479 (2004)
4. M. Frankowski, A.M. Smith-Gicklhorn and V.E. Bondybey
   Spectroscopy of the XeC_2 molecule in xenon, argon and krypton matrices
   Canadian Journal of Chemistry (*G. Herzberg memorial issue*) **82**(6), (2004)
5. O.N. Grigorashchenko, V.V. Rudenkov, I.V. Khizhnyi, E. V. Savchenko,
   M. Frankowski, A.M. Smith-Gicklhorn, M. K. Beyer and V.E. Bondybey
   Activation spectroscopy of electronically induced defects in solid Ne
   Low Temperature Physics **29**, 876-879 (2003)
6. M. Frankowski, M. Algarra, P. Rodrigues, M.T. Barros, M.N.D.S. Cordeiro, B.S. Fox,
   A.M. Smith-Gicklhorn, M.K. Beyer, M.L. Costa and V.E. Bondybey
   Matrix-isolation FT-IR study of azidoacetone and azidoacetonitrile
   Low Temperature Physics **29**, 870-875 (2003)

7. G. Śliwiński, M. Frankowski and N. Schwentner
   Luminescence and formation of alkalihalide ionic excimers in solid Ne and Ar
   Low Temperature Physics **29**, 848-851 (2003) 848-851

8. E.V. Savchenko, O.N. Grigorashchenko, G.B. Gumenchuk, A.G. Belov, E.M. Yurtaeva, M. Frankowski, A.M. Smith-Gicklhorn and V.E. Bondybey
   Relaxation processes induced by radiative electronic transitions in preirradiated rare gas solids
   Surface Science **528**, 266-272 (2003)

9. E.V. Savchenko, O.N. Grigorashchenko, G.B. Gumenchuk, A.N. Ogurtsov, M. Frankowski, A.M. Smith-Gicklhorn and V.E. Bondybey
   Defect-related relaxation processes in irradiated rare gas solids
   Radiation Effects and Defects in Solids **157**, 729-735 (2002)

10. A.M. Smith-Gicklhorn, M. Frankowski and V.E. Bondybey
    Tetracyanoethylene, its ions and ionic fragments
    Physical Chemistry Chemical Physics **4**, 1425-1431 (2002)

11. E.V. Savchenko, O.N. Grigorashchenko, A.N. Ogurtsov, V.V. Rudenkov, G.B. Gumenchuk, M. Lorenz, M. Frankowski, A.M. Smith-Gicklhorn and V.E. Bondybey
    Photo- and thermally assisted emission of electrons from rare gas solids
    Surface Science **507-510**, 754-761 (2002)

12. E.V. Savchenko, O.N. Grigorashchenko, A.N. Ogurtsov, V.V. Rudenkov, M. Lorenz, A.M. Smith-Gicklhorn, M. Frankowski and V.E. Bondybey
    Thermally assisted emission of electrons and VUV photons from irradiated rare gas solids
    Surface Review and Letters **9**, 353-358 (2002)

13. E.V. Savchenko, O.N. Grigorashchenko, A.N. Ogurtsov, V.V. Rudenkov, M. Lorenz, M. Frankowski, A.M. Smith-Gicklhorn and V.E. Bondybey
    Thermally stimulated exoelectron emission from rare gas solids in weak external electric fields
    Journal of Luminescence **94**, 475-481 (2001)

14. A.M. Smith-Gicklhorn, M. Lorenz, M. Frankowski, R. Kołos and V.E. Bondybey
    C_5N_2 revisited: mass-selective matrix isolation and DFT studies
    Chemical Physics Letters **351**, 85-91 (2002)

15. J. Agreiter, M. Frankowski and V.E. Bondybey
    Ionization and hydrolysis of dinitrogen pentoxide in low temperature solids
    Low Temperature Physics, **27**, 890-894 (2001)

16. M. Frankowski, G. Śliwiński and N. Schwentner
    Investigation of the luminescence and lasing potential of Mo in solid Ar films
    Proceedings of SPIE–The international Society for Optical Engineering **4397** (Laser Physics and Applications), 104-108 (2001)

17. M. Frankowski, G. Śliwiński and N. Schwentner
    Investigation of doped inert gas solids for cryogenic lasers
    Journal of Low Temperature Physics **122**, 443-449 (2001)

18. M. Frankowski, G. Śliwiński and N. Schwentner
    Investigation of the lasing potential of solidified gas mixtures
    Proceedings of SPIE–The international Society for Optical Engineering **4237** (Laser Technology VI: Progress in Lasers), 39-44 (2000)

19. M. Frankowski, G. Śliwiński, N Schwentner
    Doped inert gas crystalline media for cryogenic lasers
    Proc. of SPIE–The international Society for Optical Engineering **3724** (Single Crystal Growth, Characterization and Applications), 362-367 (1999)

Presentations at Scientific Meetings and Conferences

1. **Fourth International Conference on Cryocrystals and Quantum Crystals**
   Freising, Germany, 27-31.10.2002 – member of the Organizing Committee

   M. Frankowski, M. Algarra, P. Rodrigues, M.T. Barros, M.N.D.S. Cordeiro, B.S. Fox, A.M. Smith-Gicklhorn, M.K. Beyer, M.L. Costa and V.E. Bondybey
   Matrix-isolation FT-IR study of azidoacetone and azidoacetonitrile – poster

   O.N. Grigorashchenko, V.V. Rudenkov, E.V. Savchenko, M. Frankowski, A.M. Smith-Gicklhorn, and V.E. Bondybey
   Activation spectroscopy of solid Ne – poster

2. **EuroConference:**
   Matrix 2001, The Chemistry and Physics of Matrix Isolated Species
   Szklarska Poręba, Poland 7-13.06.2001

   A.M. Smith-Gicklhorn, M. Lorenz, R. Kołos, M. Frankowski and V.E. Bondybey
   Mass-selective matrix-isolation spectroscopy: FT-IR spectra of $H(D)C_3N^+$, $C_4N_2^+$, CNC^+, $C_3N_2^+$, $C_5N_3^+$, $C_6N_3^+$, $C_6N_4^+$; C_5N_2***’s identification***
   – poster

   E.V. Savchenko, V.V. Rudenkov, A.M. Smith-Gicklhorn, M. Lorenz, M. Frankowski and V.E. Bondybey
   Thermally and photostimulated exoelectron emission from doped rare-gas matrices
   – poster

3. **11-th International School of Quantum Electronics,**
   Laser Physics and Applications
   Varna, Bulgaria, 18-22.09.2000

   M. Frankowski, G. Śliwiński and N Schwentner
   Investigation of the luminescence and lasing potential of Mo in solid Ar films
   – poster

4. **Third International Conference on Cryocrystals and Quantum Crystals**
   Szklarska Poręba, Poland, 28.07-4.08.2000

   M. Frankowski, G. Śliwiński and N Schwentner
   Investigation of doped inert gas solids for cryogenic lasers – poster

5. **VI Symposium of Laser Technique** – national meeting
   Szczecin-Świnoujście, Poland 27.09-1.10.1999

   M. Frankowski, G. Śliwiński and N Schwentner
   Investigation of laser properties of solidified gas mixtures – poster

6. **International Conference on Solid State Crystals,**
   Material Science and Applications
   Zakopane, Poland, 12-16.10.1998

   M. Frankowski, G. Śliwiński and N Schwentner
   Doped inert gas crystalline media for cryogenic lasers – poster

7. **The Jabłoński Centennial International Conference**
   on Luminescence and Photophysics
   Toruń, Poland, 23-27.07.1998

   G. Śliwiński, M. Frankowski and N. Schwentner
   Luminescence and formation of alkalihalide ionic excimers in solid Ne and Ar
   – poster

Presentations at
Meetings of the RTN Network on "Reactive Intermediates"

Lisbon, Portugal, 18-22 April 2001
Matrix isolation studies of reactive intermediates – talk

Garching, Germany, 11-14 October 2001
Matrix isolation spectroscopy of mass-selected tetracyanoethylene ions and ionic fragments – talk

Heraklion, Crete from 18-23 April 2002
Matrix isolation spectroscopy of mass-selected ions generated by electrospray ionization – talk

Southampton, Great Britain, from 8-11 September 2002
Matrix isolation FT-IR study of azidoacetonitrile and azidoacetone
– short talk & poster

Bremen, Germany, from 26-30 March 2003 – talk
Spectroscopy of rare gas molecules: XeC_2 in solid Xe, Ar and Kr – talk

Lyndhurst, Great Britain, 6-8 April 2004
Protonated and Fragment Ions of Acetonitrile, Mass-Selective Matrix-Isolation Study – talk

Acknowledgments

This work is dedicated to *my Parents* who took care of my education and helped me at each step on the way to it. There are neither any words to express my gratitude to my dear wife *Anna* for her support, persistence and patience.

I would like to express my deep "thank you" to all the people I had an opportunity to learn from and to work with. Doing research under supervision of *Professor Vladimir E. Bondybey* is a real scientific adventure. His fruitful ideas, overwhelming knowledge, and critical advice are the sound foundation of this work. An open minded and cooperative attitude together with the relaxed atmosphere in the PCII team makes it an ideal environment for development and creative thinking. This turned most of the efforts into pleasure.

This thesis could not have been written without the work of my three co-supervisors: *Dr. Alice M. Smith-Gicklhorn*, head of the "Matrix Lab", *Dr. Martin K. Beyer*, the ICR group leader and "right hand" to *Prof. Bondybey*, and *Prof. Elena V. Savchenko* from the Verkin Institute for Low Temperature Physics and Engineering of the National Academy of Sciences of Ukraine. Special thanks to *Alice* from whom I have learnt many practical aspects of spectroscopy. Our common work in the lab and in analyzing data is an invaluable contribution to the results presented here. It is also extremely hard to put into a few words my thanks to *Martin*. His very practical, reliable and flexible approach to scientific and organizational problems was always stimulating and reflected directly on my successful work in this group. I also wish to express my deep gratitude to *Elena*, great teacher, and wonderful person. I appreciate every hour I have spent with her in the lab or on discussions. I really admire her patience in answering a whole bunch of not always wise questions.

I want to cordially thank *Dr. Brigitte S. Fox-Beyer*, who always likes to help and knows how to perfectly organize our work with the students in such a way that there are no collisions with our own plans. Work here would be very difficult without *Peter Kämmerer*, bearing in mind not only his great skills and knowledge of computers, but also his sense of humor. I much appreciate *Matthias Stecher* for his invaluable technical help in the lab and with the lab-classes. I would like to mention as well other members of our group whose very cooperative attitude makes everything much easier: *O. Petru Balaj*, *Dr. Zheng Sun* who works with me on the acetonitrile project, *Dr. Chi-Kit Siu* and *Iulia Balteanu*, as well as two former group members, *Dr. Bernd Urban* and *Dr. Dieter Kraus*. I want to thank *Dr. Martin Lorenz* who spent a few weeks introducing me into the mass-selection technique and FT spectrometer and helping us many times after he had left to industry; *Andreas Lammers* who “rescued” us fixing problems with old Aspect system. I want to thank *Mirko Gruber*, our “Werkstudent” who does a great job in the lab and hopefully will join our group in near future. I appreciate the common work on activation spectroscopy of rare gas solids, together with *Dr. Oleg N. Grigorashchenko* and *Galina B. Gumenchuk* from ILTPE in Kharkov.

I express my special gratitude to *Sabine Kullick*, our extremely helpful administrative assistant and secretary, who does not only keep us up to date with bureaucratic requirements but also takes care of all “sometimes really lost” foreign Ph.D. students.

Three years of experience within the Research Training Network on “Reactive Intermediates”, especially as a speaker of Young Researchers under the guidance of *Prof. John M. Dyke* from the University of Southampton and *Prof. Cornelis A. de Lange* from the University of Amsterdam, gave me a unique possibility to gain and develop presentation and organizational skills. Interaction with, *Prof. Philippe Bréchignac* and *Prof. Dolores Gauyacq* from Université de Paris-Sud, *Dr. Peter Watts* and *Dr. Andy J. Bell* from CBD Porton Down, *Prof. Stelios Couris* and *Prof. Theofanis N. Kitsopoulos from* FORTH, Heraklion, as well as Ph.D. students and postdoctoral fellows from their groups, was a great opportunity to exchange and implement new ideas in our work. I wish to express my special thanks to *Dr. Gökhan Baykut* from Bruker Daltonics for making the ESI project feasible, and *Prof. Maria de Lourdes Costa, Prof. Augusto Moutinho* as well as *Dr. Manuel Algarra* from the New University of Lisbon, and *Dr. Natalia Cordeiro* from the University of Porto for the fruitful collaboration on the spectroscopy of organic azides.

This is also a good opportunity to thank *Prof. Joseph Friedrich* from TU München, Weihenstephan and *Yuri Freiman* from ILTPE, Kharkov, *Prof. Dietrich Menzel* and *Dr. Peter Feulner* from TU München, who helped us to go through the tough task of organizing the Fourth International Conference on Cryocrystals and Quantum Crystals in Freising.

I gratefully acknowledge the electronics and machine workshops for their excellent work and troubleshooting advice.

Financial support by the Deutsche Forschungsgemeinschaft through the BO 945/18-2-3 grant, European Union through the Research Training Network on “Reactive Intermediates” (Contract No.: HPRN-CT-2000-00006) and the Fonds der Chemischen Industrie is gratefully acknowledged.

Finally I would like to express my gratitude to *Prof. Gerard Śliwiński*, head of the Department of Photophysics and Laser Technique in The Szewalski Institute of Fluid-Flow Machinery, Polish Academy of Sciences in Gdańsk, for introducing me to the photophysics of cryogenic solids. Work in his group, besides the lab experience and a few publications gave me the kick-off in this research area. I miss the fruitful and humourous discussions with all group members: *Dr. Adam Cenian* (and our adventure with medical lasers), *Dr. Mirosław Sawczak* with whom I shared the office in Gdańsk, *Dr. Rafał Jendrzejewski* as well as *Dr. Grażyna Rabczuk* and two Ph.D. students, *Marta Jankowska* and *Katarzyna Komar*. Special thanks to *Mirosław Piskulski* for his invaluable help in setting up the system for cryogenic matrices, as well as our laser specialists, engineers *Piotr Kukiełło* and *Ryszard Zaremba*.

I would like to thank *Prof. Nikolaus Schwentner* from Freie Universität, Berlin for the very fruitful collaboration, which also gave me an opportunity to work in his lab.

At this point I would like to express my deep and cordial thanks to *Sabine, Alice, Martin, Brigitte* and *Peter* who helped me, and later also my family, to get settled in Bayern.